Université Libre de Bruxelles

Service de Physique des Particules
Interuniversity Institute for High Energies

PhD Thesis

Study of Triple-GEM detectors for the CMS muon spectrometer upgrade at LHC and study of the forward-backward charge asymmetry for the search of extra neutral gauge bosons

Florian Zenoni

Supervisor Prof. Gilles De Lentdecker

April 2016

Florian Zenoni

Study of Triple-GEM detectors for the CMS muon spectrometer upgrade at LHC and study of the forward-backward charge asymmetry for the search of extra neutral gauge bosons

PhD Thesis, April 2016

Supervisor: Prof. Gilles De Lentdecker

Université Libre de Bruxelles

Interuniversity Institute for High Energies

Service de Physique des Particules

Boulevard de la Plaine, 2

1050 Brussels

PhD thesis jury members:

Giacomo Bruno (UCL)
Barbara Clerbaux (ULB) (secretary)
Anna Colaleo (INFN Bari)
Gilles De Lentdecker (ULB) (supervisor)
Laurent Favart (ULB) (president)
Michael Tytgat (UGent)

To Valeria Solesin,
Giulio Regeni,
and the best of youth

Abstract

This PhD thesis takes place in the CMS experiment at CERN's Large Hadron Collider (LHC). The LHC allowed the discovery of the Brout-Englert-Higgs boson in 2012, and is designed to run for at least 20 years, with an increasing luminosity that will reach by 2025 a value of $7.5 \cdot 10^{34}$ cm^{-2}s^{-1}, that is a yield five times greater than the one initially intended. As a consequence, the experiments must adapt and upgrade many of their components and particle detectors. One of the foreseen upgrades of the CMS experiment concerns the Triple Gas Electron Multiplier (GEM) detectors, currently in development for the forward muon spectrometer. These detectors will be installed in CMS during the second long LHC shutdown (LS2), in 2018-2019. The aim of this upgrade is to better control the event trigger rate at Level 1 for muon detection, thanks to the high performance of these Triple GEM detectors, in presence of very high particle rates (> 1 kHz/cm^2). Moreover, thanks to its excellent spatial resolution ($\sim$ 250 μm), the GEM technology can improve the muon track reconstruction and the identification capability of the forward detector.
The goal of my research is to estimate the sensitivity of Triple GEMs to the hostile background radiation in CMS, essentially made of neutron and photons generated by the interaction between the particles and CMS detectors. The accurate evaluation of this sensitivity is very important, as an underestimation could have ruinous effects of the Triple GEMs efficiency, once they are installed in CMS. To validate my simulations, I have reproduced experimental results obtained with similar detectors already installed in CMS, such as the Resistive Plate Chambers (RPC).
The second part of my work regards the study of the CMS experiment capability to discriminate between different models of new physics predicting the existence of neutral vector bosons called Z$'$. These models belong to plausible extensions of the Standard Model. In particular, the analysis is focused on simulated samples in which the Z$'$ decays in two muons, and on the impact that the Triple GEM detectors upgrades will bring to these measurements during the high luminosity phase of the LHC, called Phase II. My simulations prove that more than 20% of the simulated events see at least one muon in the CMS pseudo-rapidity (η) region covered by Triple GEM detectors. Preliminary results show that, in the case of 3 TeV/c^2 models,

it will be possible already at the end of Phase I to discriminate a Z'_{I} from a Z'_{SSM} with a significance level $\alpha > 3\sigma$.

Résumé

Cette thèse de doctorat a pour cadre l'expérience CMS auprès du grand collisionneur de protons du CERN, le LHC. Le LHC, qui a permis la découverte en 2012 du boson de Brout-Englert-Higgs, est destiné à fonctionner pour encore 20 ans, avec une luminosité qui croîtra progressivement pour atteindre d'ici 2025 la valeur de $7.5 \cdot 10^{34}$ cm^{-2}s^{-1}, c'est à dire environ cinq fois la valeur initialement prévue. Ceci a pour conséquence que les expériences doivent s'adapter et mettre à niveau une série de leurs composants et détecteurs. Une des prochaines mises à niveau de l'expérience CMS concerne les détecteurs Triple Gas Electron Multiplier (GEM) qui sont actuellement en développement pour la partie avant du spectromètre à muons de l'expérience. Ces détecteurs seront installés dans CMS durant le deuxième long arrêt du LHC, en 2018-2019, appelé LS2. Cette mise à niveau a pour but de contrôler les taux de déclenchement d'événements pour la détection de muons, grâce à la haute performance de ces détecteurs Triple GEM en présence de taux de particules extrêmement élevés (> 1 kHz/cm^2). De plus, grâce à sa très bonne résolution spatiale (~ 250 µm), la technologie GEM peut améliorer la reconstruction des traces de muons et la capacité d'identification du détecteur avant.

Le but de mon travail de recherche est d'estimer la sensitivité des Triple GEMs à l'environnement de radiation hostile dans CMS, essentiellement composé de neutrons et de photons produits lors des interactions entre les particules et les détecteurs constituant l'expérience CMS. L'estimation précise de cette sensitivité est très importante, car une sous-estimation pourrait avoir des effets désastreux pour l'efficacité des Triple GEMs une fois installés dans CMS. Pour valider mes simulations, j'ai également reproduit des résultats expérimentaux obtenus avec d'autres détecteurs similaires déjà installés dans CMS, tels que les Resistive Plate Chambers (RPC).

La deuxième partie de mon travail concerne l'étude de la capacité de l'expérience CMS à discerner différents modèles de nouvelle physique prédisant l'existence de bosons vecteurs, appelés Z$'$. Ces modèles font partie des extensions plausibles du Modèle Standard. En particulier, l'analyse se concentre sur des simulations dans lesquelles le Z$'$ se désintègre en deux muons, et sur l'impact que les mises à niveau avec les détecteurs Triple GEM apporteront à ces mesures tout le long de la phase de haute intensité du LHC. Mes simulations montrent que plus de 20% des événements simulés comptent au moins un muon dans la région en pseudo-rapidité (η) de CMS couverte par les détecteurs Triple GEM. Les résultats préliminaires démontrent que, dans le case de modèles à 3 TeV/c^2, il sera possible dès la fin de la Phase I de distinguer un Z$'_{\mathrm{I}}$ d'un Z$'_{\mathrm{SSM}}$ avec un niveau de signification $\alpha > 3\sigma$.

Acknowledgements

I would first like to thank Prof. Gilles de Lentdecker who welcomed me in his sparkling group, and guided me through the years of my doctoral studies; he also had the patience to read and correct my thesis with great care. Thanks also to Prof. Laurent Favart, who accepted to preside over my defense jury. I am grateful to all members of my thesis committee, Prof. Giacomo Bruno, Prof. Barbara Clerbaux, Dr. Anna Colaleo, and Prof. Michael Tytgat for their attendance to the private defense and their help for the improvement of the present document. Finally, this work was partially supported by the "David and Alice Van Buuren" funding.

I am in debt with Dr. Davide Pagano and Prof. Germano Bonomi for their early review of the introductive chapters, as well as for their precious share of experience related to the original contributions presented in this thesis. Concerning Chapter 6 content in particular, I would have never hoped to reach any level of control and mastery in Geant4 application development without the assistance and friendship of Prof. Bonomi first, and some years later of Dr. Cristina Riccardi and Alice Magnani. Thanks to Dr. Alfredo Castaneda for his important inputs. Also, Chapter 7 would have never seen the light of day without the crucial participation of Dr. Aidan Randle-Conde, Dr. Laurent Thomas, and Dr. Ryo Yonamine.

I would eventually like to express my sincere gratitude to the many persons that, by being close or distant, helped me to get through the day, every day. You know who you are.

Contents

1 Introduction

When Galileo Galilei gave support to the heliocentric theory, he generated intellectual, philosophical, and religious turmoil. Still, the spread of his ideas has been inexorable ever since. About two centuries after these controversies, James Clerk Maxwell wrote his famous set of equations on electromagnetism, which have been called "the second great unification in physics", after the first one realized by Isaac Newton. But the truth is that to deserve a scientific standing, a theory must be supported by evidence; the former examples are no exception. In fact, the Scientific Method basically rose as a paradigm the day Galilei took a Dutch invention, the telescope, and pointed it right at the Northern Italian sky. Electromagnetism equations would have got a poor appreciation today, if eight years after Maxwell's death, Heinrich Hertz had not discovered electromagnetic radiation at microwave frequencies. Therefore, it is no wonder that since the Modern Age, the scientific theories had determined the way humans have dealt with knowledge. Indeed, technology has also proven to be a key driver for advances in science. As we will see, this is especially true for particle physics.

Very often, progress makes small steps. It then consists in taking a proven technology, and pushing the limits a bit further. Once in a while though, a radical solution is needed, in order to offer something very different and able to improve the performance parameters by large amounts. Georges Charpak's contribution is one of such examples, and a prominent one. This Polish born scientist was awarded the Nobel Prize in 1992 "for his invention and development of particle detectors, in particular the multi-wire proportional chamber", developed in 1968. While physicists were previously struggling with the demanding bubble-chambers, the multi-wire proportional chamber enabled nothing less than modern particle physics, by providing the possibility for good spatial resolution and high trigger rates. Indeed, nowadays it is hard to imagine a particle physics experiment that would not use one of his concepts. It is true that silicon detectors are now faster than gas chambers, but the latter feature an important quality besides their high rate capability: they can equip very large detection planes. The four main experiments of the LHC (Large Hadron Collider), currently the world's most powerful particle accelerator, are using chambers that derive more or less directly from Charpak's invention. Therefore, without these developments, much of the LHC program would not be possible today.

The main principle behind this family of particle detectors is to collect and to amplify the electrons knocked out of a gas by charged particles as they pass through. A new idea, the GEM (Gas Electron Multiplier) from Fabio Sauli at CERN, continues this tradition. The GEM consists of a thin, metal-clad polymer foil, chemically pierced by a high density of holes (typically 50 to 100 per mm^2). On application of a difference of potential between the two electrodes, electrons released by radiation in the gas on one side of the structure drift into the holes, multiply and transfer to a collection region. Each hole acts as an individual proportional amplifier. The multiplier can be used as detector on its own, or as a pre-amplifier in a multiple structure; in this case, it permits to reach large overall gains in a harsh radiation environment. The main characteristics and performance of GEM detectors include the operation in most gas fillings, including pure noble gases, proportional gains above 10^5, energy resolution of 18% FWHM at 5.9 keV, a spatial resolution of 60 μm rms or better, a rate capability above 10^5 counts/mm^2·s, active areas up to 1000 cm^2, a flexible detector shape and readout patterns.

After having taken data since 2011 and undergone a two-year break started in 2013 and called first Long Shutdown (LS1), the second Long Shutdown (LS2) of the LHC will last for 18 months starting from January 2019. During this time, the injector chain will be upgraded, bringing the instantaneous luminosity at a value approaching or exceeding 2×10^{34} cm^{-2} s^{-1}. The so called LHC Phase I operation will end around 2024 with a total integrated luminosity of approximately 300 fb^{-1}. After that, a third long shutdown (LS3) will be operated to upgrade the LHC to its high-luminosity phase, up to 7.5×10^{34} cm^{-2} s^{-1}. Among all the sub-detectors of the various LHC experiments, this work has been carried out in the context of the CMS muon system. This set of gaseous detectors was originally designed as a highly hermetic and redundant system employing three detection technologies. Precision measurements and Level 1 (L1) triggering are provided by drift tubes (DT) in the barrel, covering acceptances up to $|\eta| < 1.2$, and cathode strip chambers (CSC) in the endcaps covering $1.0 < |\eta| < 2.4$. A redundant trigger and a position measurement in both barrel and endcap regions are provided by resistive plate chambers (RPC); however, they were not implemented beyond $|\eta| > 1.6$ due to concerns about their capability to handle the high background particle rates. After LS2, though, to achieve an acceptable L1 trigger rate for muons with $p_{\mathrm{T}} < 25$ GeV/c will be a difficult challenge. The addition of a set of muon detectors in the first endcap muon station will be a necessary improvement. This particular station is called GE1/1, and it will make use of the GEM technology. The goal is to maintain or even improve the forward muon triggering and reconstruction in the region $1.6 < |\eta| < 2.2$.

The performance of the detectors is highly dependent on the background particle rates. In fact, at new energy and luminosity regime, their high yield complicates

signal identification, and in extreme cases it may make detectors inoperable. This is especially true in the forward region: the expected background rate must then be accurately evaluated. The dominant contribution to the CMS cavern background is due to neutrons and secondary particles generated by neutron interaction with matter. Their energetic spectrum spans eleven orders of magnitude, and their time of flight reaches the order of seconds. The key quantity to estimate the impact of these particles is called sensitivity, that is the probability for a given type of particle to generate a spurious signal. The sensitivity of the GE1/1 chambers to neutrons, photons, electrons and positrons has been evaluated with a standalone simulation using the GEANT4 simulation toolkit, a Monte Carlo framework widely used to simulate the interactions between particles and materials. The detector has been modelled with a full material description. Particles of fixed energy and given type cross the volume of the chamber with incident angles reproduced according to the angular distribution in CMS obtained by a dedicated FLUKA simulation. This simulation is repeated for each particle type, scanning over their full range of energies. The convolution of the obtained sensitivity distribution with the energy dependence of the incident particles eventually provides the hit fraction probability of the GEM chamber. This quantity can be used to rescale the incident hit rate of background particles hitting on the surface of the detectors. The next stage – although beyond the scope of the present work – consists in the signal digitization, that uses a combination of the outcome of this standalone simulation and test beam data analysis.
The second part of the thesis is devoted to an analysis of simulated samples of a set of signals that have been so far indicated to benefit from the introduction of the GEMs in the muon system. Several models of a postulated beyond-the-Standard-Model boson, the Z', were then taken into consideration in three different CMS scenarios: Run 2, Run 3 and Phase II. The detection of a particular physical quantity, the forward-backward asymmetry, was the object of this study, as with increasing data it will represent a way for discriminating between several models of Z'.

The thesis is structured in the following way. Chapter 2 sketches a summary of the set of theories collectively known as Standard Model. This part provides the essential physics elements necessary to understand the fundamental objects and concepts being manipulated throughout the thesis. The experimental apparatus is being first outlined in Chapter 3 concerning the LHC main features; Chapter 4 is devoted to the discussion of the CMS experiment, together with an overview of the foreseen upgrades in the coming years. The GEM upgrade project, that forms the core context of this study, is presented in Chapter 5: the GEM technology is introduced, its state-of-the-art performance are shown and the motivations behind the upgrade are clearly defined. This is necessary to present the main personal contribution to the project in Chapter 6, consisting in the evaluation of the response of GE1/1 gaseous detectors to background particles such as neutrons, photons, electrons, and

positrons. As anticipated, the main tool exploited for this aim is GEANT4. After the validation of the physics libraries against data and other simulations found in literature, the geometry and layout of the detectors are implemented, and the distribution of the incident particles are given as an input to the software application. Eventually, Chapter 7 first shows the application of a analysis method to extract the forward-backward asymmetry from a sample of a dimuon signal at a mass of 3 or 4 TeV/c^2, with Drell-Yan and Z' samples. Then, this technique is applied to several Z' models in different integrated luminosity scenarios. Conclusions about the discriminating power of CMS between the considered Z' models at different stages of upgrades are eventually discussed.

2 The Standard Model

2.1 Introduction

Since the dawn of classical physics, the concept of unification has been a powerful and inspiring common thread. In 1687 Newton unified gravitation and dynamics through the statement of the equivalence of gravitational and inertial mass. Less than two centuries later Maxwell unified electric and magnetic phenomena, summarised in his famous set of equations. The latest step forward in this direction was the unification of electromagnetic and weak interactions, achieved in the late 1960s. This electroweak theory, which is a generalisation of quantum electrodynamics (or QED), together with the theory of strong interactions, known as quantum chromodynamics (QCD), are collectively referred to as the Standard Model (SM). It is one of the greatest achievements of the second half of the XX century in the field of particle physics and it is considered nowadays the theoretical cornerstone of our current understanding of fundamental particle interactions.
Formulated in the 1970s by Sheldon Glashow, Steven Weinberg and Abdus Salam, the Standard Model was framed by the experimental confirmation of the existence of the up and down quarks (SLAC, 1968, and later the other quark flavours also at BNL and FNAL), and supported by the discovery of the neutral weak currents caused by the Z boson exchange at CERN (Gargamelle, 1974), and the discovery of W and Z bosons themselves (UA1 and UA2, 1983). More recently, it gained the strongest credibility after the discoveries of the top quark (CDF and D∅, 1995) and the tau neutrino (DONUT, 2000) at FNAL, and eventually of the Higgs boson (ATLAS and CMS, 2012) at CERN.
The Standard Model provides not only the description of the electromagnetic, weak and strong nuclear interactions, but it also classifies all the known elementary particles, listed in Fig. 2.1.

There are two types of matter units, all of them being fermions: all fundamental fermions have spin $\frac{1}{2}$ (in units of $\hbar$) and are structureless at the smallest distances currently probed by the highest-energy accelerators. These particles are:

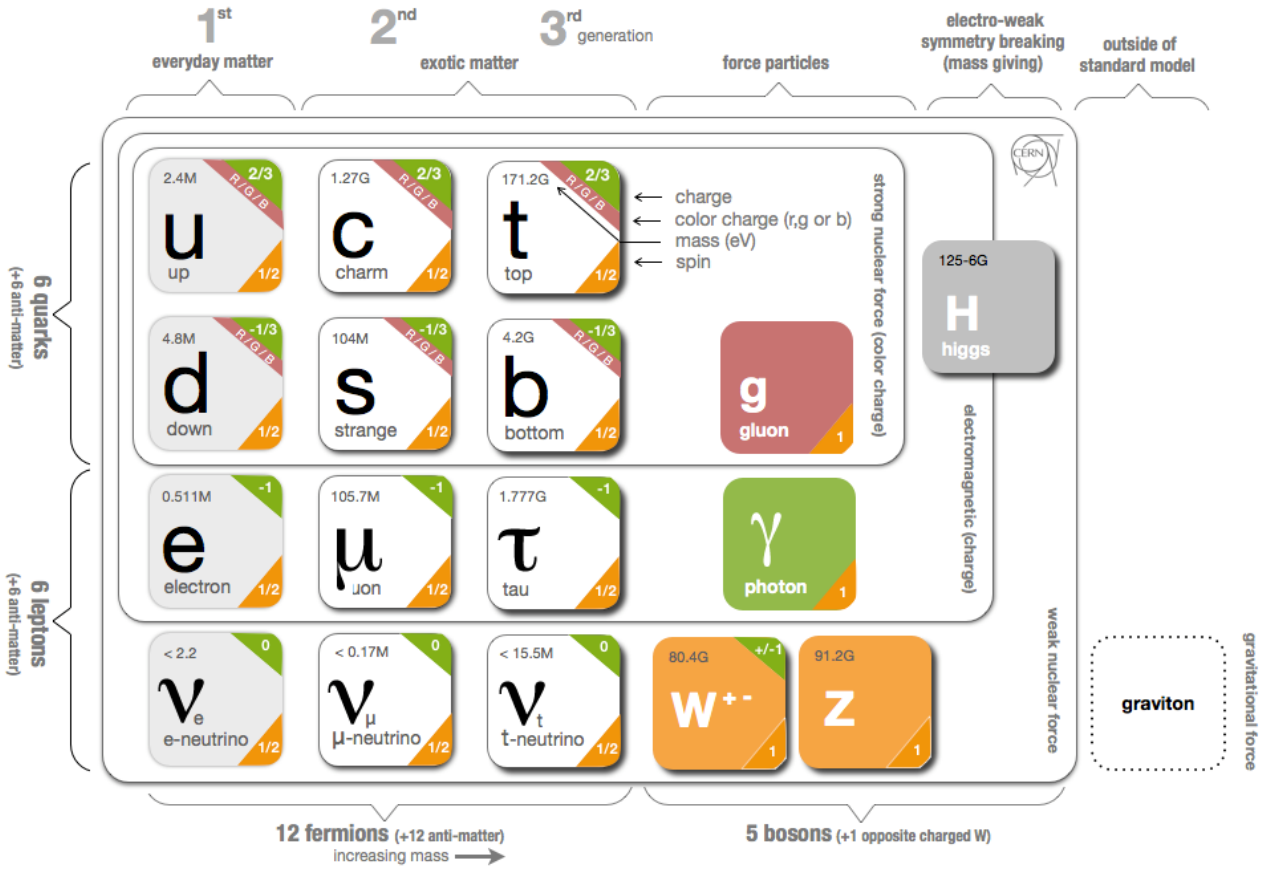

Fig. 2.1.: Schematic representation of the elementary particles described by the Standard Model, plus the hypothetical presence of the graviton, carrier of the gravitational force. This list consists of three generations of up- and down-type quarks, their antimatter partners, three generations of charged and neutral leptons, the gauge bosons and the Higgs boson. Credits: CERN

- three charged leptons which are subject to weak and electromagnetic interactions, together with corresponding neutrinos (also fermions), which only feel the weak interaction (neglecting the contribution of the gravitational force);

- three pairs of quarks, subject to all interactions, each coming in three colour states.

Fermions are grouped in three generations, or families. There are corresponding antiparticles to all these fermions. An antiparticle has the same mass as the one of its associate particle, but all its quantum numbers are reversed. Particle-antiparticle pairs can annihilate each other, producing two photons, but also W or Z bosons, or even gluons if the strong interaction is involved. All gauge bosons, which mediate the forces, have an integer spin. Known bosons are the photon (γ) for electromagnetism, the $W^{\pm}$ and Z for the weak interaction, and eight gluons for the strong interaction. In addition, the existence of the scalar boson predicted by Englert and Brout [1], Higgs [2], and Guralnik, Hagen, and Kibble [3] has been recently confirmed by the LHC experiments [4, 5].
Despite speculations about Grand Unified Theories, the electroweak model and QCD are distinct theories. Gravitation is still not included in the Standard Model, and is currently best described by Einstein's general theory of relativity (1915).
In this Chapter a brief theoretical treatment of the electroweak theory (Section 2.2) and the QCD (Section 2.3) will be provided. Developments about the Drell-Yan process (Section 2.4) and theoretical elements about extra Z bosons, known as Z' (Section 2.5), will also be given.

2.2 Electroweak unification

2.2.1 The gauge principle

As of today Maxwell's classical theory of the electromagnetic interaction (1864) still stands at the macroscopic scale. Maxwell's set of four partial differential equations together with the Lorentz force law form the foundation of classical electrodynamics, classical optics and electric circuits. Maxwell's equations are stated as follows:

$$\nabla \cdot \boldsymbol{E} = \frac{\rho}{\epsilon_0} \qquad \text{(Gauss' law)} \tag{2.1a}$$

$$\nabla \cdot \boldsymbol{B} = 0 \qquad \text{(Gauss' law for magnetism)} \tag{2.1b}$$

$$\nabla \times \boldsymbol{E} = -\frac{\partial \boldsymbol{B}}{\partial t} \qquad \text{(Faraday's law of induction)} \tag{2.1c}$$

$$\nabla \times \boldsymbol{B} = \mu_0 \left(\boldsymbol{J} + \epsilon_0 \frac{\partial \boldsymbol{E}}{\partial t} \right) \qquad \text{(Ampère's circuital law)} \tag{2.1d}$$

However, classical electrodynamics fails when it attempts to describe quantum phenomena such as the blackbody radiation, the photoelectric effect or the stability of the hydrogen atom. When merged to quantum mechanics though, this combination results in QED, in sufficient agreement with the experiment to be considered a paradigmatic theory.

The root of the amazing status of this theory relies on the intimate relation between dynamics and the symmetry principle. Symmetries are mathematical operations – or transformations – and their correspondent operators are also called invariances of the laws. In fact, it is possible to introduce new force fields that interact with the original particles in the theory in such a way that a local invariance (depending of individual space-time points) is conserved. Indeed, the only exact quantum number conservation laws are those which have such an associated dynamical theory force field, called gauge theory. The particular local invariance relevant to electromagnetism is the gauge invariance of Maxwell's equations, directly related to an invariance under local phase transformations of the electromagnetic quantum fields. All the interactions currently regarded as fundamental are precisely of this type. In fact, a generalisation of this phase invariance underlies also other gauge theories, such as the ones describing the weak and strong interactions.

In the following theoretical developments, a few classic textbooks were taken as reference [6, 7, 8]. Specific contributions are specified throughout.

In QED, the Lagrangian density for a free fermion of mass m is[1]

$$\mathcal{L} = \mathrm{i}\overline{\psi}\gamma^{\mu}\partial_{\mu}\psi - m\overline{\psi}\psi, \tag{2.2}$$

where ψ ($\equiv \psi(\boldsymbol{x}, t)$) is the Dirac spinor wavefunction and γ^{μ} are the 'γ matrices'

$$\gamma^{\mu} = (\gamma^0, \boldsymbol{\gamma}). \tag{2.3}$$

They have the following form in the Dirac basis:

$$\gamma^0 = \begin{pmatrix} I_2 & 0 \\ 0 & I_2 \end{pmatrix}, \qquad \gamma^k = \begin{pmatrix} 0 & \sigma^k \\ -\sigma^k & 0 \end{pmatrix}, \tag{2.4}$$

where k runs from 1 to 3, I_2 is the 2×2 matrix identity, and σ^k are the Pauli matrices. Eq. 2.2 is now required to be invariant under the local gauge transformation

$$\psi \longrightarrow \psi' = e^{\mathrm{i}q\alpha(x)}\psi, \tag{2.5}$$

[1] $\hbar = c = 1$ are set throughout.

where $x \equiv (\boldsymbol{x}, t)$ represents a space-time coordinate, $\alpha(x)$ is a function of position and time, and q is the fermion charge. The gauge transformation represents then an arbitrary phase change at every point in space and time. The spinors ψ and ψ' describe the same physics, since the probability densities $|\psi|^2$ and $|\psi'|^2$ are equal. Such a phase invariance is not possible for a free theory – as the derivatives now act on $\alpha(x)$ in the phase factor – but rather requires an interacting theory, involving a field whose interactions with the charged particles are precisely determined. In fact, the electromagnetic field must contemporaneously transform according to the gauge transformation:

$$A_\mu \longrightarrow A'_\mu = A_\mu - \partial_\mu \alpha(x). \tag{2.6}$$

Starting from Eq. 2.2, the replacement of the momentum operator $\mathrm{i}\partial_\mu$ in

$$\mathrm{i}D_\mu = i\partial_\mu - qA_\mu \tag{2.7}$$

is called covariant derivative, and it is a very simple prescription to obtain the wave equation for a particle in the presence of an electromagnetic field from the corresponding free particle equation. To obtain local gauge invariance, it is then necessary to introduce the A field in a well defined way. Such a particle is called a gauge boson. One way to identify the nature of such a boson is to consider the substitution performed in classical electrodynamics for the motion of a particle of charge $-e$ in an electromagnetic potential $A^\mu = (A^0, \boldsymbol{A})$:

$$p^\mu \rightarrow p^\mu + eA^\mu. \tag{2.8}$$

Eq. 2.8 suggests that the gauge boson represented by the field introduced in Eq. 2.7 is certainly the photon.

The substitution of the derivative with the covariant one leads to the Lagrangian for QED:

$$\mathcal{L} = \mathrm{i}\overline{\psi}(\gamma^\mu \partial_\mu - m)\psi - q\overline{\psi}\gamma^\mu A_\mu \psi - \frac{1}{4}F_{\mu\nu}F^{\mu\nu}, \tag{2.9}$$

where $F_{\mu\nu} = \partial_\mu A_\nu - \partial_\nu A_\mu$ is the field strength tensor. The first term in Eq. 2.9 represents the free fermion kinetic energy and mass, the second the interaction between the fermion and the electromagnetic field, and the last the kinetic energy of the field. As expected, there is no term for the mass of the photon, as it would break the gauge invariance.

The set of phase factors of the form $e^{\mathrm{i}\alpha}$, where α is any real number, form the element of a $\mathrm{U}(1)$ group, meaning the group of all unitary one-dimensional matrices. Thus we say that the electromagnetic gauge group is $\mathrm{U}(1)$. Such transformations can commute: $\mathrm{U}(1)$ is then called an Abelian group.

The link between the introduction of gauge bosons and electromagnetic phenomena – such as the Coulomb potential – stands in the fact that in a field theory a force arises from the exchange of quanta of the field potentials. For instance, the Rutherford

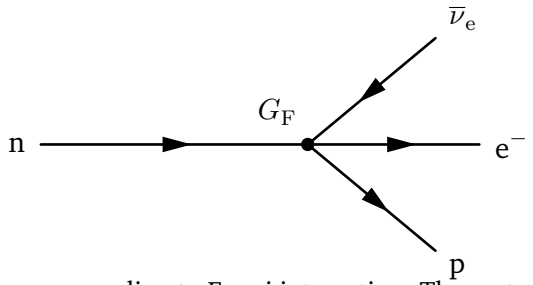

Fig. 2.2.: Neutron β decay according to Fermi interaction. The vertex coupling G_{F} is called Fermi's constant.

scattering is described as the exchange of a photon between two charged particles. In natural units the coupling constant of this simple process is found to be equal to

$$\alpha = \frac{e^2}{4\pi} \approx \frac{1}{137}, \tag{2.10}$$

and is called fine-structure constant.

The fundamental reinterpretation though is that, assuming covariant 4-momentum conservation, the intermediate photon states have a non-zero mass. In this case the photon is called 'virtual'.

In the case of a one-loop diagram (e.g. a one-photon emission and reabsorption process), the intermediate state summation over all momenta gives a divergent integral, instead of representing only a small correction (O(α^2)). The formal replacement of these infinities by their finite physical values is called renormalisation.

2.2.2 Weak interactions

The first attempt at a phenomenology of weak interactions dates back to Fermi (1933). For the β decay he postulated an effective four-fermion point-interaction, in analogy to an electromagnetic transition, the electron-neutrino pair playing the role of the emitted photon (see Fig. 2.2). However there are indeed evident dissimilarities between QED and this early view of the weak interactions: the existence of charged current processes, whose intermediate vector bosons are denoted by $\mathrm{W}^{\pm}$ (see Fig. 2.3), and the limited range of the interaction. In the neutron β decay, the

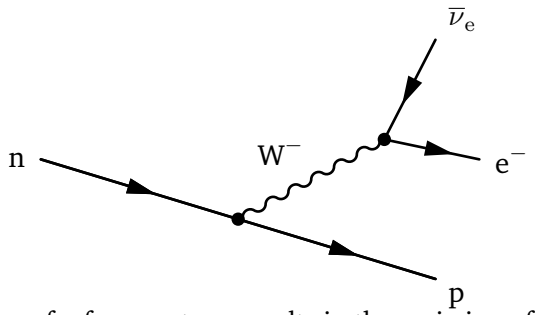

Fig. 2.3.: The β^- decay of a free neutron results in the emission of a proton, an electron and an electronic anti-neutrino. The intermediate emission of a virtual W^- boson is shown. The quark structure of the hadrons has not been represented.

matrix element can be reduced to a good approximation to a constant G_{F}, if all momentum dependence are neglected. Having dimensions of $[M]^{-2}$, its numerical value, determined from experiments on nuclear β decay, is given approximately by

$$G_{\mathrm{F}} \simeq 1.166 \times 10^{-5}\ \mathrm{GeV}^{-2}, \tag{2.11}$$

and is known as Fermi's constant.
The evidence of parity violation in weak interactions observed by Wu (1957) and predicted by Lee and Yang (1956) led to the conclusion that the currents participating in Fermi's current-current interaction are a mixture of vector, V_μ, and axial vector, A_μ currents. In fact, let us consider the cross reaction of the neutron β-decay:

$$\mathrm{pe}^- \rightarrow \mathrm{n}\nu_{\mathrm{e}}. \tag{2.12}$$

As stated before (see Fig. 2.2) Fermi proposed an analogy of the current-current invariant-amplitude for electromagnetic electron-proton scattering:

$$\mathcal{M} = G_{\mathrm{F}}(\overline{u}_{\mathrm{n}}\gamma^{\mu}u_{\mathrm{p}})(\overline{u}_{\nu_{\mathrm{e}}}\gamma_{\mu}u_{\mathrm{e}}). \tag{2.13}$$

This amplitude explains the properties of some features of the β-decay, such as the charge-raising or charge-lowering of the weak current, but not others. In fact it is proven that, assuming a universal weak theory, the most general β-decay interaction involving a four-particle coupling is a combination of vector (V) and axial vector (A) operators [9]. To describe and explain the parity violation found in experiments, the only change required in Fermi's original proposal is the replacement of γ^{μ} by $\gamma^{\mu}(1-\gamma^5)$, with $\gamma^5 \equiv i\gamma^0\gamma^1\gamma^2\gamma^3$. A mixture of γ^{μ} and $\gamma^5\gamma^{\mu}$ terms automatically violates parity conservation and leads to a theory of the form $V-A$. The experiments show that indeed only $\overline{\nu}_R$ and ν_L are involved in weak interactions, providing a clear violation of parity invariance. The $(1-\gamma^5)$ factors guarantee that the right-handed neutrinos do not contribute to the cross-section of a process such as $\nu_{\mu}\mathrm{e}^- \rightarrow \mu^-\nu_{\mathrm{e}}$. Therefore, the charge-raising weak current

$$J^{\mu} = \overline{u}_{\nu}\gamma^{\mu}\frac{1}{2}(1-\gamma^5)u_e \tag{2.14}$$

couples an ingoing negative helicity electron to an outgoing negative helicity neutrino (here we neglect the mass of the electron). Further, it can be shown that the charge-lowering weak current is the hermitian conjugate of Eq. 2.14:

$$J^{\dagger}_{\mu} = \overline{u}_e\gamma^{\mu}\frac{1}{2}(1-\gamma^5)u_{\nu}. \tag{2.15}$$

Weak interaction amplitudes are then of the form:

$$\mathcal{M} = \frac{4G_{\mathrm{F}}}{\sqrt{2}}J^{\mu}J^{\dagger}_{\mu}, \tag{2.16}$$

where the numerical factors depend on the normalisation of the operators. As anticipated, we then speak of the $V - A$ form of the weak current J^μ, in contrast to the V form of the electromagnetic current.

2.2.3 The electroweak theory

In QED one could reverse the argument and start from Eq. 2.9 to verify the gauge invariance under the combined gauge transformations. In the case of the electroweak theory, the gauge invariance is taken as an underlying dynamical principle. However, it needs a process of generalisation, in which the 'phase factors' involve matrix operators which do not in general commute with each other. Theories based on making such invariances local are called non-Abelian gauge theories. We shall now consider the specific theory associated with the names of Glashow, Salam and Weinberg, referred as the Standard Model of the electroweak interactions. It is indeed a non-Abelian gauge theory in which the local phase invariance is 'hidden' or 'broken', in order for the bosons to acquire mass.
The gauge fields must be able to allow us to alter the phase of the wavefunctions of all particles of a given charge independently at each space-time point, without any observable consequence. This must be possible over arbitrarily large space-time distances, apparently requiring the gauge quanta to be massless. Mathematically, the electromagnetic potential that satisfies the Maxwell equation

$$\Box A^\nu - \partial^\nu(\partial_\mu A^\mu) = j^\nu \tag{2.17}$$

is invariant according to

$$A^\mu \rightarrow A'^\mu = A^\mu - \partial^\mu \chi. \tag{2.18}$$

However, if A^μ represented a massive field, the relevant wave equation would be

$$(\Box + M^2)A^\nu - \partial^\nu(\partial_\mu A^\mu) = j^\nu. \tag{2.19}$$

This equation is manifestly not invariant under Eq. 2.18, and it is precisely the mass term $M^2 A^\nu$ that breaks the gauge invariance. Similar developments hold for non-Abelian analogues. However gauge invariance plays an essential role in ensuring renormalisability, so some kind of gauge invariance is required even for the case of massive vector quanta.
Despite the above argument about the masslessness requirement, the gauge invariance for massive gauge quanta is not lost, only hidden. Nambu (1960) suggested that the physical vacuum of a quantum field theory is analogous to the ground state of an interacting many-body system; it is simply the state of minimum energy, the stable (or equilibrium) configuration. It does not need to be one in which all the quantum fields have zero average value. It is then possible that in the true ground state of our

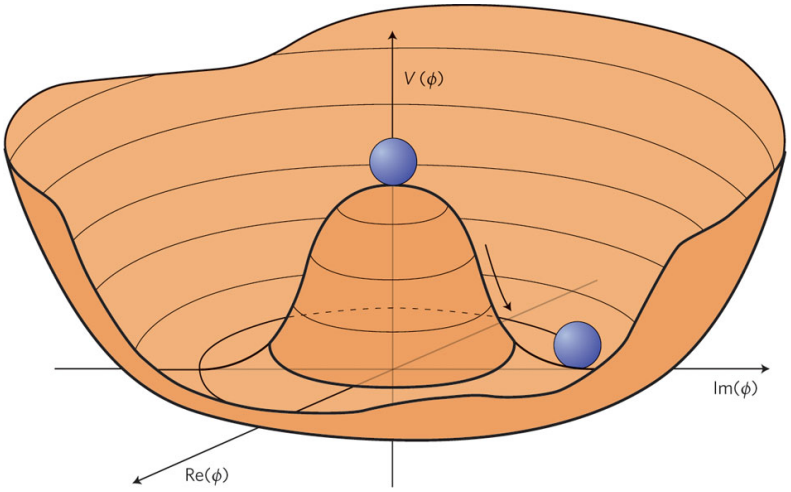

Fig. 2.4.: Shape of the Higgs potential for $\mu^2 < 0$ (see Eq. 2.21). The field free vacuum, when $\phi = 0$, corresponds to a local maximum, thus forming an unstable equilibrium. In a single point the potential reaches a minimum which represents a vacuum with a non-zero vacuum expectation value and a well defined phase. The system can still be rotated as a whole, so it is invariant under global but not under local rotations [10].

theory some field has a non-zero equilibrium state: this is an asymmetrical situation. The truly stable configuration of an interacting system can be lopsided even though the basic interactions between the constituents of the system are symmetrical. This situation, in which the ground state configuration does not display the symmetry of the Hamiltonian, is described by saying that the symmetry is 'spontaneously broken'. Let us consider a classical field:

$$\varphi = \frac{1}{\sqrt{2}}(\varphi_1 + \mathrm{i}\varphi_2). \tag{2.20}$$

We suppose that in the Lagrangian for our classical field system the potential V is given by

$$V(\varphi) = \frac{1}{2}\mu^2\varphi^*\varphi + \frac{1}{2}\lambda(\varphi^*\varphi)^2, \tag{2.21}$$

where the constants multiplying the two terms have been chosen for later convenience. The signs have been chosen so that V has the form sketched in Fig. 2.4; in particular: $\mu^2 < 0$. The minimum of the potential occurs at:

$$v = -\sqrt{-\mu^2/\lambda}. \tag{2.22}$$

This potential has a $\mathrm{U}(1)$ symmetry:

$$\phi \to \phi' = e^{i\alpha}\phi. \tag{2.23}$$

This corresponds to a rotation in the $\phi_1 - \phi_2$ plane. When $\phi_1 = \phi_2 = 0$ we actually have a maximum of V. The field configuration of minimum energy, which is therefore the equilibrium configuration, is an entire $locus$:

$$\phi_1^2 + \phi_2^2 = v^2. \tag{2.24}$$

There are therefore infinite possibilities for the stable configuration, but only one ground state is required. Once a particular point is chosen 'spontaneously', the $\mathrm{U}(1)$ symmetry is lost. We say that $\mathrm{U}(1)$ symmetry is 'broken'.
Possible leptonic transitions associated with the weak charged currents are $\nu_\mathrm{e} \leftrightarrow \mathrm{e}$, $\nu_\mu \leftrightarrow \mu$, etc. This suggests that these pairs should be regarded as doublets under the same group. From a mathematical point of view, the generalisation to non-Abelian invariances comes when more than one wavefunction, or state, is considered at a time. Introducing the two-component isospinor:

$$\psi^{(1/2)} \equiv \begin{pmatrix} \psi_A \\ \psi_B \end{pmatrix} \equiv \psi_A \chi_A^{(1/2)} + \psi_B \chi_B^{(1/2)}, \tag{2.25}$$

where

$$\chi_A^{(1/2)} = \begin{pmatrix} 1 \\ 0 \end{pmatrix}, \qquad \chi_B^{(1/2)} = \begin{pmatrix} 0 \\ 1 \end{pmatrix}. \tag{2.26}$$

If the two states ψ_A and ψ_B are regarded as truly degenerate, redefinitions are allowed, of the form:

$$\psi^{(1/2)} \to \psi^{(1/2)\prime} = \mathrm{U}\psi^{(1/2)}, \tag{2.27}$$

where U is a complex 2×2 matrix. The restrictions on U in the transformation define a set of matrices that constitutes the Lie group $\mathrm{SU}(2)$: the group of special, unitary 2×2 matrices.
Going back to the weak lepton transitions, a 'weak $\mathrm{SU}(2)$ group' is involved, called 'weak isospin'. We use the symbols t, t_3 for the quantum numbers of weak isospin, and make the specific lepton assignments

$$t = \frac{1}{2}, \qquad t_3 = \begin{cases} +\frac{1}{2} \\ -\frac{1}{2} \end{cases} \quad \begin{pmatrix} \nu_\mathrm{e} \\ \mathrm{e}^- \end{pmatrix}_\mathrm{L}, \ldots \tag{2.28}$$

where the dots indicate further generations. The subscript 'L' indicates that only the left-handed parts of the wavefunctions enter into these weak transitions. For this reason, the weak isospin group is usually referred to as $\mathrm{SU}(2)_\mathrm{L}$. For example, under a $\mathrm{SU}(2)_\mathrm{L}$ transformation

$$\begin{pmatrix} \nu_\mathrm{e} \\ \mathrm{e}^- \end{pmatrix}_\mathrm{L} \to \begin{pmatrix} \nu_\mathrm{e} \\ \mathrm{e}^- \end{pmatrix}_\mathrm{L}^{\prime} = \exp(\mathrm{i}\boldsymbol{\alpha} \cdot \boldsymbol{\tau}/2) \begin{pmatrix} \nu_\mathrm{e} \\ \mathrm{e}^- \end{pmatrix}_\mathrm{L}, \tag{2.29}$$

	I	t_3	Y	Q
ν_{e}	$1/2$	$1/2$	-1	0
$\mathrm{e}_{\mathrm{L}}^{-}$	$1/2$	$-1/2$	-1	-1
$\mathrm{e}_{\mathrm{R}}^{-}$	0	0	-2	-1
u_{L}	$1/2$	$1/2$	$1/3$	$2/3$
d'_{L}	$1/2$	$-1/2$	$1/3$	$-1/3$
u_{R}	0	0	$4/3$	$2/3$
d'_{R}	0	0	$-2/3$	$-1/3$

Tab. 2.1.: Electroweak quantum numbers of the first-generation fermions. The other generations follow an identical pattern.

where $\boldsymbol{\alpha}$ stands for the three quantities:

$$\boldsymbol{\alpha} = (\alpha_1, \alpha_2, \alpha_3), \tag{2.30}$$

and the three matrices $\boldsymbol{\tau}$ are the Pauli matrices:

$$\tau_1 = \begin{pmatrix} 0 & 1 \\ 1 & 0 \end{pmatrix}, \qquad \tau_2 = \begin{pmatrix} 0 & -\mathrm{i} \\ \mathrm{i} & 0 \end{pmatrix}, \qquad \tau_1 = \begin{pmatrix} 1 & 0 \\ 0 & -1 \end{pmatrix}. \tag{2.31}$$

In the 2×2 transformation there are now three 'phase angles' $\boldsymbol{\alpha}$ and there are non-commuting matrix operators (the $\boldsymbol{\tau}$'s appearing in the exponent).
The $\mathrm{SU}(2)$ schemes need to be enlarged by the inclusion of an additional $\mathrm{U}(1)$ gauge group, resulting in a $\mathrm{SU}(2) \otimes \mathrm{U}(1)$ group structure. The new Abelian $\mathrm{U}(1)$ group is associated with a weak analogue of hypercharge: the weak hypercharge Y. The third component of the weak isospin, hypercharge and electric charge Q (in units of e, the charge of the positron) are related by the formula

$$Q = t_3 + \frac{1}{2}Y. \tag{2.32}$$

The quantum number assignments for the first generation fermions are given in Tab. 2.1. Left-handed states have different quantum numbers than right-handed states. The right-handed fermions are all assigned $I = 0$, as they do not participate in the weak interactions with the W bosons. All right-handed components are singlet under the weak isospin group. The left-handed states $\mathrm{e}_{\mathrm{L}}^{-}$ and ν_{e} form the members of an $I = \frac{1}{2}$ doublet. Similarly, the u_{L} and d'_{L} form a doublet, where d' represents a mixture of d, s and b states. The gauge symmetry is written as $\mathrm{U}(1)_Y \otimes \mathrm{SU}(2)_{\mathrm{L}}$, where the subscript Y indicates that the $\mathrm{U}(1)$ symmetry operates on the hypercharge. We now need to make the global $\mathrm{SU}(2)$ invariance of Eq. 2.29 into a local one; the same for the $\mathrm{U}(1)_Y$ phase invariance. This new gauge group must accommodate a

massive neutral boson and, at the same time, a massless photon.
Let us now introduce the appropriate covariant derivative:

$$\partial^\mu \to \hat{D}^\mu = \partial^\mu + ig\boldsymbol{t}^{(t)} \cdot \hat{\boldsymbol{W}}^\mu + i(g'/2)Y\hat{B}^\mu, \tag{2.33}$$

where the fundamental constants g and g' are the weak 'charges' of $\mathrm{SU}(2)_\mathrm{L}$ and $U(1)_Y$ parts of the gauge group respectively. The numerical factors are purely conventional. The three $\hat{\mathrm{W}}^\mu$ are the $\mathrm{SU}(2)_\mathrm{L}$ gauge fields, while $\hat{B}^\mu$ is the new $U(1)_Y$ gauge field. Therefore, for the left-handed electron-type doublet (see Eq. 2.28) we have:

$$\left.\begin{array}{l}\text{left-handed leptons}\\ t = \frac{1}{2}\\ Y = -1\end{array}\right\} \quad \partial^\mu \to \hat{D}^\mu = \partial^\mu + ig\frac{\boldsymbol{\tau}\cdot\hat{\boldsymbol{W}}^\mu}{2} - \frac{ig'}{2}\hat{B}^\mu. \tag{2.34}$$

For the right-handed part of the lepton wavefunction, left untouched by $\mathrm{SU}(2)_\mathrm{L}$ transformations we have:

$$\left.\begin{array}{l}\text{right-handed leptons}\\ t = 0\\ Y = -2\end{array}\right\} \quad \partial^\mu \to \hat{D}^\mu = \partial^\mu + ig'\hat{B}^\mu. \tag{2.35}$$

Now we need to make three gauge fields massive – the $\hat{\mathrm{W}}^\pm$ and one associated with the neutral weak currents. It is then required to introduce some scalar field with at least three degrees of freedom, while also ensuring that some effective $\mathrm{U}(1)$ gauge symmetry stays unbroken, to represent the massless photon. We introduce a complex scalar doublet, known as the Higgs field, written in the form

$$t = \frac{1}{2}, \quad \hat{\varphi} = \begin{pmatrix} \frac{1}{\sqrt{2}}(\hat{\varphi}_1 + \mathrm{i}\hat{\varphi}_2) \\ \frac{1}{\sqrt{2}}(\hat{\varphi}_3 + \mathrm{i}\hat{\varphi}_4) \end{pmatrix}, \quad t_3 = \begin{cases} +\frac{1}{2} \\ -\frac{1}{2} \end{cases}. \tag{2.36}$$

We want the current induced in the vacuum to contain a part proportional to the gauge field, so that a non-zero vacuum expectation value of $\hat{\varphi}$ gives a mass to three of the gauge bosons. An appropriate choice for the phase of the scalar field's vacuum expectation value that breaks the invariance of the theory is the following:

$$\hat{\varphi} = \exp\left[\mathrm{i}(\boldsymbol{\tau}/2)\cdot\hat{\boldsymbol{\alpha}}(x)\right]\begin{pmatrix} 0 \\ \hat{P}(x) \end{pmatrix} \tag{2.37}$$

where three real phase field $\hat{\boldsymbol{\alpha}} = (\hat{\alpha}^1, \hat{\alpha}^2, \hat{\alpha}^3)$ appear, and $\hat{P}(x)$ is the real field. $\hat{\boldsymbol{\alpha}}$ and $\hat{P}$ are x-dependent, as the $\mathrm{SU}(2)_\mathrm{L} \times \mathrm{U}(1)_Y$ symmetry must be local. The fields $\hat{\boldsymbol{\alpha}}$ are excitations of the field along the potential minimum, i.e. changing the phase. They correspond to the massless Goldstone bosons of a global symmetry, in this case three for the three rotations of the SU(2) group. However, in a local gauge theory

these massless bosons can be eliminated by a local SU(2) rotation:

$$\hat{\varphi}' = \exp\left[-\mathrm{i}(\boldsymbol{\tau}/2)\cdot\hat{\boldsymbol{\alpha}}(x)\right]\hat{\varphi} = \begin{pmatrix} 0 \\ \hat{P}(x) \end{pmatrix} \tag{2.38}$$

A suitable choice of gauge leads without loss of generality to the following expectation value:

$$\langle\tilde{0}|\hat{\varphi}|\tilde{0}\rangle = \begin{pmatrix} 0 \\ v/\sqrt{2} \end{pmatrix}, \tag{2.39}$$

where v is a real constant. It represents excitations of the field independent of the phase, like the ball rolling down in Fig. 2.4 for a given phase and oscillating around the minimum, which represents one degree of freedom. The original field φ with four degrees of freedom has lost three degrees of freedom, which are recovered as the longitudinal polarisation of the three heavy gauge bosons.
We now introduce the currents associated with the complex isospinor $\hat{\varphi}$, where the ∂^μ have already been replaced by the appropriate $\hat{\varphi}$ covariant derivative (see Eq. 2.34). Requiring that the component of $\hat{\varphi}$ with non-zero expectation value has zero charge (which fixes $Y(\varphi) = 1$), the $\mathrm{SU(2)_L \times U(1)}_Y$ weak isospin current is

$$\hat{j}^{a\mu}(\hat{\varphi}) = \mathrm{i}g\left(\hat{\varphi}^\dagger\frac{\tau^a}{2}(\partial^\mu\hat{\varphi}) - (\partial^\mu\hat{\varphi})^\dagger\frac{\tau^a}{2}\hat{\varphi}\right) - \frac{g^2}{2}\hat{\varphi}^\dagger\hat{\varphi}\hat{W}^{a\mu} - gg'\hat{\varphi}^\dagger\frac{\tau^a}{2}\hat{\varphi}\hat{B}^\mu. \tag{2.40}$$

Considering the first two components of the relation, one is able to identify

$$M_\mathrm{W} = gv/2 \tag{2.41}$$

as the physical $\mathrm{W}^\pm$ mass. From this relation and our excellent knowledge of the value of the SU(2) coupling g from precision electroweak measurements, we have:

$$v = 246 \text{ GeV}. \tag{2.42}$$

The photon is obtained by an appropriate linear combination of the components, leading to the electromagnetic field equation:

$$\hat{A}^\mu = \sin\theta_\mathrm{W}\hat{W}^{3\mu} + \cos\theta_\mathrm{W}\hat{B}^\mu, \tag{2.43}$$

where θ_W is the Glashow-Weinberg angle defined as

$$\tan\theta_\mathrm{W} = g'/g. \tag{2.44}$$

Moreover the combination

$$\hat{Z}^\mu = \cos\theta_\mathrm{W}\hat{W}^{3\mu} - \sin\theta_\mathrm{W}\hat{B}^\mu \tag{2.45}$$

obeys a massive wave equation and represents a neutral vector boson Z^0 of mass

$$M_{\mathrm{Z}^0} = M_{\mathrm{W}} / \cos\theta_{\mathrm{W}}. \tag{2.46}$$

It is also possible to relate the coupling strengths of the weak and electromagnetic interactions:

$$g \sin\theta_{\mathrm{W}} = e. \tag{2.47}$$

We have just described how the masses of the bosons are generated by the Brout-Englert-Higgs mechanism. The way the masses of quarks and leptons are generated is however postulated. The SM simply states a coupling of the fermion and Higgs multiplets that respect the SU(2)×U(1) gauge symmetry. Then, when the Higgs field acquires its vacuum value, the fermions receive mass. No special structure is needed to produce mass terms of a very simple form [11].
It was previously stated that $\mathrm{u_L}$ takes part of a weak isospin doublet together with a mixture of d, s and b states called $\mathrm{d'_L}$. Let us consider for a moment only two generations of quark. We assume that the charged current couples rotated quark states

$$\begin{pmatrix} \mathrm{u} \\ \mathrm{d'} \end{pmatrix}, \qquad \begin{pmatrix} \mathrm{c} \\ \mathrm{s'} \end{pmatrix}, \tag{2.48}$$

where

$$\mathrm{d'} = \mathrm{d}\cos\theta_c + \mathrm{s}\sin\theta_c, \qquad \mathrm{s'} = -\mathrm{d}\cos\theta_c + \mathrm{s}\sin\theta_c. \tag{2.49}$$

This introduces an arbitrary quark mixing angle θ_c, known as the Cabibbo angle (1963). Such a parameter allows new couplings to accomodate observations like $\mathrm{K}^+ \to \mu^+\nu_\mu$ – the K^+ being made of u and $\bar{\mathrm{s}}$ quarks. The following unitary matrix U performs the rotation 2.49 of the d and s quark states:

$$U = \begin{pmatrix} \cos\theta_c & \sin\theta_c \\ -\sin\theta_c & \cos\theta_c \end{pmatrix}. \tag{2.50}$$

This allows the existence of charged (and flavour-changing) current couples u ↔ d′ or c ↔ s′ (left-handed) quark states. It also ensures that there are no s ↔ d′ transitions, which change flavour but not charge.
The extension of the mixing to the 3 families of lepton lead to a 3×3 mixing complex matrix containing three real parameters (Cabibbo-like mixing angles) and a phase factor $e^{i\delta}$. The complex elements $U_{i,j}$ have fundamental implications concerning CP invariance. The original parametrisation is due to Kobayashi and Maskawa (1973). The matrix extended to three families is known as CKM-matrix.
The constraints of unitarity of the CKM-matrix on the diagonal terms can be written as

$$\sum_k |V_{ik}|^2 = \sum_i |V_{ik}|^2 = 1, \tag{2.51}$$

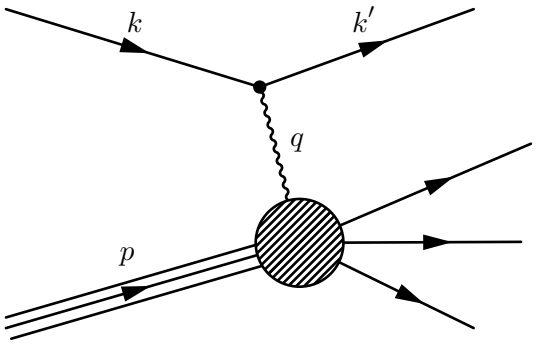

Fig. 2.5.: Lowest-order diagram for the inelastic electron-proton scattering. The letters represent the momentum carried by each particle, with $q = k - k'$. When $-q^2$ is large enough, the initial state proton breaks up and loses its identity.

for all generations i. Theoretically it is a consequence of the fact that all SU(2) doublets couple with the same strength to the vector bosons of weak interactions. It is a property known as weak universality.

2.3 The strong interaction

2.3.1 The parton model

Apart from gravitation, the interaction that was left out of the discussion so far is the strong interaction. The structure of hadrons when probed by deep inelastic electron scattering experiments is a topic of central importance: in fact, appropriate calculations lead to the evidence for the existence of quarks, the interactions of which are described by gauge theories. The occurrence of hadron jets in processes taking place at LHC energies can't be neglected either. A brief introduction to this physics sector is therefore needed.

Let us then consider the inelastic electron-proton scattering. The one represented in Fig. 2.5 shows the extreme case in which the momentum transferred by the virtual photon is so large that the proton breaks up. When probed by incident electrons with large momentum transfers $Q^2 \equiv -q^2$, the proton seems to behave like a sum of interactions on Dirac particles. It is the sign that inside such a complex system there are the true structureless particles undergoing the interaction: the quarks. Considering the momentum carried by the proton target p and the proton mass M, we define

$$\nu \equiv \frac{p \cdot q}{M}. \tag{2.52}$$

The two independent variables of the hadronic tensor $W^{\mu\nu}$, which parametrizes the form of the current at the end of the photon propagator, are q^2 and ν. Neglecting

the Z exchange and the interference term, the scattering hadronic tensor has the general following form:

$$W^{\mu\nu} = W_1 \left(-g^{\mu\nu} + \frac{q^\mu q^\nu}{q^2} \right) + W_2 \frac{1}{M^2} \left(p^\mu - \frac{p \cdot q}{q^2} q^\mu \right) \left(p^\nu - \frac{p \cdot q}{q^2} q^\nu \right). \quad (2.53)$$

As Q^2 increases above $\sim (0.7 \text{ GeV})^2$, the chance of elastic scattering is depressed, and the proton is more likely to break up. It turns out that the inelastic structure functions are independent of Q^2 at a given value of $\omega = 2q \cdot p/Q^2 = 2M\nu/Q^2$:

$$\begin{aligned} MW_1(\nu, Q^2) &\xrightarrow[\text{large } Q^2]{} F_1(\omega) \\ MW_2(\nu, Q^2) &\xrightarrow[\text{large } Q^2]{} F_2(\omega), \end{aligned} \quad (2.54)$$

suggesting that the interaction takes place on point-like subconstituent, behaving like free Dirac particles. The components of the proton structure are also called partons. They can each carry a different fraction x of the parent proton's momentum and energy. The parton momentum distribution $f_i(x)$ describing the probability that the struck parton i carries a fraction x of the proton's momentum p is such that:

$$\sum_{i'} \int dx \, x \, f_{i'}(x) = 1, \quad (2.55)$$

where i' sums over all the partons, not only the charged ones i which interact with the photon. It is possible to redefine $F_{1,2}$ as functions of the Bjorken x scaling variable (in fact x has the same definition than $1/\omega$ in Eq. 2.54, hence we only state that $x = 1/\omega$); this leads to the result that these are functions of only one variable, x. They are independent of Q^2 at fixed x, and therefore satisfy Bjorken scaling:

$$\begin{aligned} \nu W_2(\nu, Q^2) \to F_2(x) &= \sum_i e_i^2 \, x \, f_i(x), \\ MW_1(\nu, Q^2) \to F_1(x) &= \frac{1}{2x} F_2(x). \end{aligned} \quad (2.56)$$

The sum in Eq. 2.56 runs over the charged partons in the proton:

$$\frac{1}{x} F_2^{\text{ep}}(x) = \left(\frac{2}{3} \right)^2 [u^{\text{p}}(x) + \overline{u}^{\text{p}}(x)] + \left(\frac{1}{3} \right)^2 [d^{\text{p}}(x) + \overline{d}^{\text{p}}(x)] + \left(\frac{1}{3} \right)^2 [s^{\text{p}}(x) + \overline{s}^{\text{p}}(x)], \quad (2.57)$$

where the 'ep' apex refers to the electron-proton interaction, $u^{\text{p}}(x)$ and $\overline{u}^{\text{p}}(x)$ are the probability distributions of u quarks and antiquarks within the proton. The presence of charm and heavier quarks is here neglected. The comparison with the neutron counterpart of Eq. 2.57 and the assumption that the strong isospin symmetry holds

– suggesting that the neutron and proton quark content is related – provide the following equivalences:

$$\begin{aligned} u^{\mathrm{p}}(x) &= d^{\mathrm{n}}(x) \equiv u(x), \\ d^{\mathrm{p}}(x) &= u^{\mathrm{n}}(x) \equiv d(x), \\ s^{\mathrm{p}}(x) &= s^{\mathrm{n}}(x) \equiv s(x). \end{aligned} \tag{2.58}$$

We describe the proton as three-constituent or three-valence quarks $\mathrm{u_v u_v d_v}$ accompanied by many quark-antiquark pairs $\mathrm{u_s \overline{u}_s}$, $\mathrm{d_s \overline{d}_s}$, $\mathrm{s_s \overline{s}_s}$, etc. These are known as "sea" quarks. We call $S(x)$ the sea quark momentum distribution common to all quark flavours. Recalling the quantum numbers of the proton and the neutron and summing over the charged partons, one obtains

$$\begin{aligned} \frac{1}{x}F_2^{\mathrm{ep}} &= \frac{1}{9}[4u_{\mathrm{v}} + d_{\mathrm{v}}] + \frac{4}{3}S, \\ \frac{1}{x}F_2^{\mathrm{en}} &= \frac{1}{9}[u_{\mathrm{v}} + 4d_{\mathrm{v}}] + \frac{4}{3}S, \end{aligned} \tag{2.59}$$

where the 'en' apex refers to the electron-neutron interaction. The interpretation in terms of QCD (see below, Subsection 2.3.2) allows to generate the sea density as due to gluon splitting in $\mathrm{q\overline{q}}$ and gluon radiation from the valence quarks. Because of this effect $S(x)$ has a spectrum similar to bremsstrahlung at small x, so that the number of sea quarks grows logarithmically as $x \to 0$. Experimental data show that at values of Q^2 of a few GeV^2, in the scaling region, gluons carry about 50% of the proton momentum, which was unaccounted for by the charged quarks.
The description of the fundamental constituents of the proton is successful, but it is not sufficient to explain the interaction between these particles. A full-sized quantum theory is needed to frame the complexity of the ongoing strong interaction phenomena. This theory exists and is called Quantum Chromodynamics.

2.3.2 Quantum Chromodynamics

Quantum Chromodynamics (QCD) is that part of the SM that deals with the strong interaction. The fundamental actors of this theory are the quarks, whose interaction is mediated by massless gauge bosons called gluons. As reported in Fig. 2.1 six flavours of quark are known, together with their corresponding antiquark. The quarks seem to be exclusively bound in states of quark-antiquark (mesons) or of three quarks (baryons), though the confirmations of tetraquark exotic states [12] and the recent observation of a pentaquark would prove otherwise [13]. Due to the difficulty in accounting for the antisymmetry of some baryon wavefunctions – as required by Fermi-Dirac statistics – the quarks need to carry a new quantum number, called colour.
The colour also plays a dynamical role analogous to electric charge in QED. Since

there are three types of colours, the theoretical basis of QCD is the hypothesis of a local gauge invariance under transformation of the $\mathrm{SU(3)_c}$ symmetry group, of the form

$$\psi \rightarrow \psi' = \exp[\mathrm{i}\boldsymbol{\alpha}(x) \cdot \boldsymbol{\lambda}/2]\psi, \tag{2.60}$$

where $\boldsymbol{\alpha} = (\alpha_1, \ldots, \alpha_8)$ and the λ's are eight 3×3 matrices generators of the $\mathrm{SU(3)_c}$ group. It can be viewed as a generalised phase transformation, now with eight 'phase angles'. From the replacement of the partial derivative with the covariant one, it follows that the $\mathrm{SU(3)_c}$ covariant quark wave equation describing the colour interactions is such that

$$(\mathrm{i}\gamma^\mu \partial_\mu - m)\psi = g_s \frac{\lambda^\alpha}{2} \gamma^\mu A_\mu^\alpha \psi, \tag{2.61}$$

where m is the mass of the quark, g_s is a 'strong charge' and A^α ($\alpha = 1, 2, \ldots, 8$) is an octet of scalar 'gluon potentials'. This equation implies that quarks interact with massless vector particles, called gluons, in a similar way to electrons interacting with the photon. Here the quark changes its color by emitting or absorbing a coloured gluon. A new feature is that the gluons have three- and four-gluon self interactions. The parton model suggests that the effective interaction between the hadron constituents is weak. In fact, a fundamental feature of non-Abelian gauge theories (in appropriate circumstances) is 'asymptotic freedom': the effective coupling parameter between two particles is a function of the distance between them. The effective coupling goes to zero as the separation becomes very small, and such theories are called asymptotically (i.e. as $r \rightarrow 0$ or $Q^2 \rightarrow \infty$) free.
Following the perturbative approach used in QED, one introduces the 'strong' structure constant $\alpha_s = g_s^2/4\pi$ and its Q^2-dependent generalisation of $\alpha_s(Q^2)$.
The one-gluon exchange graph is corrected by a vacuum polarisation diagram involving a $\mathrm{q\overline{q}}$ loop, but in the same order (α_s) also a gluon loop contributions involving gluon self-interaction. One obtains:

$$\alpha_s(Q^2) = \frac{12\pi}{(33 - 2f)\ln(Q^2/\Lambda^2_{\mathrm{QCD}})}, \tag{2.62}$$

where Λ_{QCD} is the energy scale at which the perturbative approach behind the equation fails, that is when the confining forces dominate. Typical values of Λ_{QCD} lie in the range $100 - 200$ MeV. The corresponding confining region is about 1 fm. A decrease in $\alpha_s(Q^2)$ is then observed at large Q^2, as long as $f \leq 16$, where f is the number of quark families, the observed number of quark families being 3.

2.3.3 Breaking of scaling invariance

How does the gluon radiation from quarks contribute to the structure functions? As Q^2 is increased to, say, $Q^2 \sim Q_0^2$ the photon starts to "see" evidence for the point-like

valence quarks within the proton. If the quarks were non-interacting, the parton model would be satisfactory and this would be the end exact scaling would set in. QCD however predicts that on increasing the resolution ($Q^2 \gg Q_0^2$), we should observe a number of resolved partons sharing the proton's momentum. This number increases with Q^2. There is an increased probability of finding a quark at small x, and a decreased chance of finding one at high x, because high-momentum quarks lose momentum by radiating gluons.
The quark densities depend on Q^2, as photons with a large enough Q^2 probes a wider range of parton densities within the proton; we specify them as $q(x, Q^2)$. The Q^2 evolution of the quark densities is given by an integro-differential equation for $q(x, Q^2)$:

$$\frac{d}{d\log Q^2} q(x, Q^2) = \frac{\alpha_s}{2\pi} \int_x^1 \frac{dy}{y} q(y, Q^2) P_{qq}\left(\frac{x}{y}\right) + o(\alpha_s(Q^2)), \tag{2.63}$$

where

$$P_{qq}(z) = \frac{4}{3}\left(\frac{1+z^2}{1-z}\right) \tag{2.64}$$

represents the probability of a quark emitting a gluon and so becoming a quark with momentum reduced by a fraction $z = \frac{x}{y}$. Eq. 2.63 is called DGLAP evolution equation, while Eq. 2.64 is a splitting function. Eq. 2.63 expresses the fact that a quark with momentum fraction x could have come from a parent quark with a larger momentum fraction y which has radiated a gluon. Given the quark structure function at some reference point $q(x, Q_0^2)$, it is possible to compute it for any value of Q^2 using the DGLAP equation. At leading order, the variation of the quark density of Eq. 2.63 is also due to the convolution of the gluon density $g(y, Q^2)$ at a higher energy times the probability of finding a quark (of the given flavour) in a gluon.

2.3.4 Parton distribution functions

When two protons collide with a high center-of-mass energy ($\sqrt{s} \gg \Lambda_{\mathrm{QCD}}$), some of their partons can interact with each other. The probability density $f_{\mathrm{p}}(x_{\mathrm{p}}, Q^2)$ to find a parton p, with x being the fraction of the longitudinal proton momentum in the proton-proton center-of-mass frame, depends on the squared four-momentum transfer Q^2 between the partons of the collision, and is described by the parton distribution function (PDF). The PDF is different for each type of parton. Recently measured PDFs are reported in Fig. 2.6 for two different scales of the invariant momentum transfer Q^2 between the partons. The Fig. 2.6 shows how the shape of the function depends on the energy scale at which the interaction takes place. At leading order, to probe physics at a certain energy scale, the value for Q^2 would have to be taken in the range of the squared invariant mass M^2 of the system. This is why if one wants to study e.g. the Z boson, Q^2 must be in the order of M_{Z}^2, that is

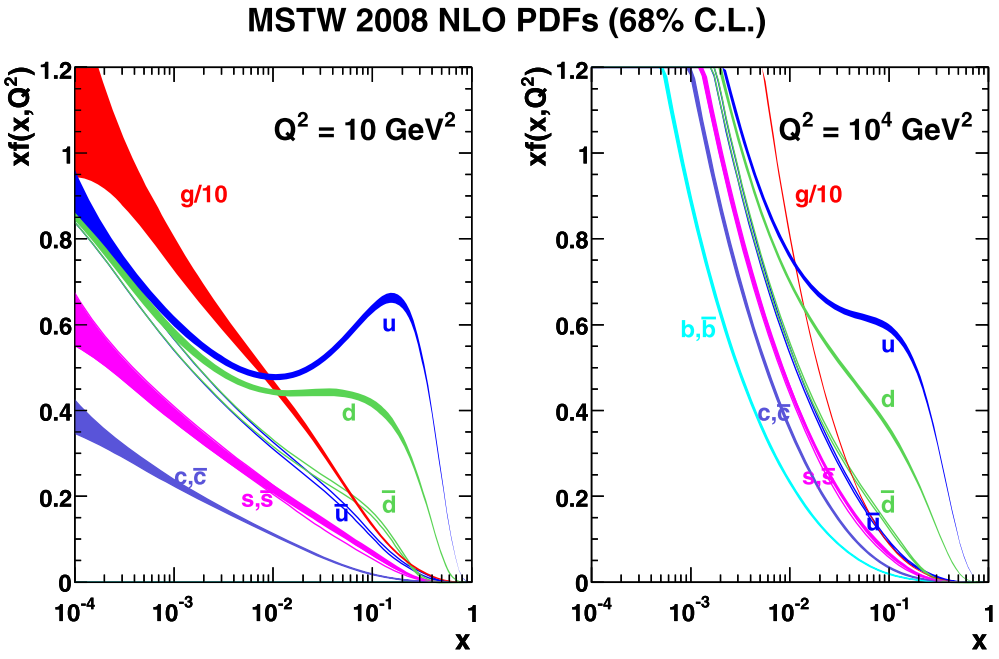

Fig. 2.6.: PDFs, including the one sigma uncertainty bands, for the partons in a proton for momentum transfers Q^2 of 10 and 10^4 GeV^2 [14].

$\sim 10^4$ GeV, as in the right plot of Fig. 2.6. However it must be noticed that the scale Q^2 at which the hard interaction takes place is not determined, as it is related to the presence of other high created masses, high transverse momenta or heavy quarks involved in the process.

2.4 The Drell-Yan process

The Drell-Yan process [15] plays an important role in determining the structure functions, and in testing the parton model and its QCD higher order corrections. In the context of this work, which will analyse dimuon resonances masses around 3 and 4 TeV, the Drell-Yan process represents a benchmark signal, as well as the main Standard Model contribution at such energies. It will play a useful role to prove that the analysis code is under control. Thus, the current case of interest is represented by a proton-proton collision producing a $\mu^+\mu^-$ pair along with unobserved hadrons X:

$$\mathrm{p} + \mathrm{p} \rightarrow \gamma^*/\mathrm{Z} + \mathrm{X} \rightarrow \mu^+\mu^- + \mathrm{X}. \tag{2.65}$$

The parton model assumes that in the limit

$$Q^2, s \rightarrow \infty, \tag{2.66}$$

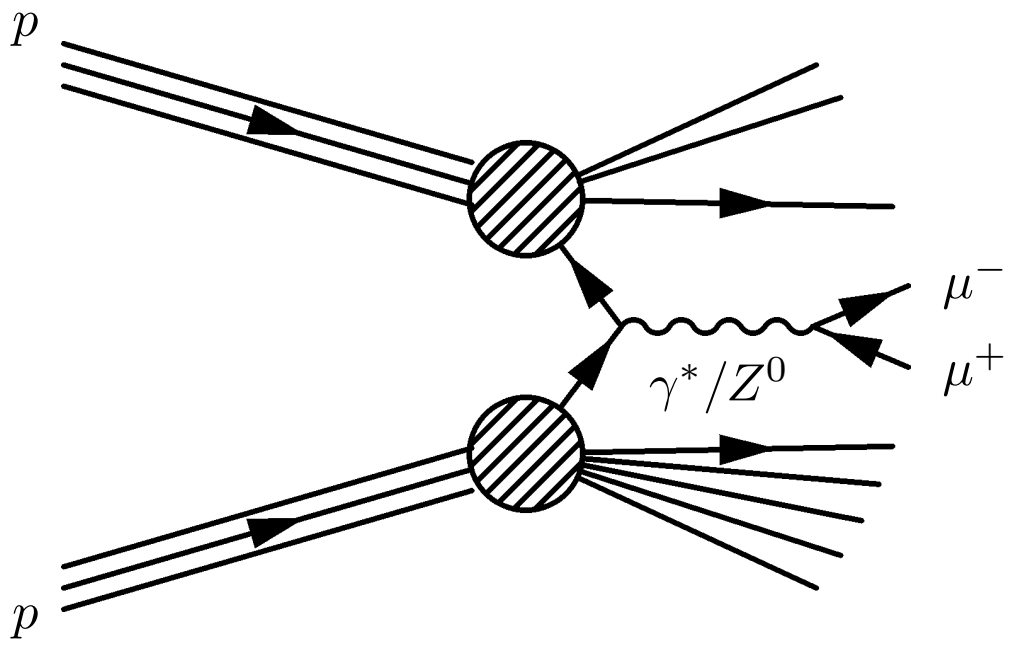

Fig. 2.7.: Drell-Yan process: when a quark, e.g., a down quark, from one proton and an antiquark, e.g., a down antiquark, from an oncoming proton collide, they can annihilate into a virtual photon (γ^*) or Z boson if the net electric charge is zero (or a W boson if the net electric charge is one). After briefly propagating, the photon/Z can split into a lepton and its antiparticle partner, for example into a muon and antimuon or electron–positron pair. Real collisions include the remnants of the scattered protons.

the dominant process is the lower-order process $\mathrm{q\bar{q}} \to \gamma^*/\mathrm{Z} \to \ell^-\ell^+$, as shown in Fig. 2.7, the remaining quarks and antiquarks emerging as hadrons. Theoretically this process is well known. Its signature consists of two high energy leptons (and the rest of the proton observable as forward activity) that suffer from low background in a hadron collider, providing a clean channel to perform precision measurements and to search for new physics.

In the Drell-Yan process, there are two fermions in the initial and final states with unknown polarization. The quarks and antiquarks exist in three different colors but only colorless pairs can form a photon or a Z boson. One must therefore sum the amplitude corresponding to any possible spin configuration, average on the spins on the incoming particles and require the quark and antiquark to carry an opposite color. At the leading order, the angular partonic cross-section of the Drell-Yan process is then given by

$$\frac{d\sigma_{\mathrm{q\bar{q}}\to\gamma^*/\mathrm{Z}\to\ell\bar{\ell}}}{d\Omega} = \frac{\alpha^2}{3} Q_\mathrm{q}^2 Q_\ell^2 \frac{1}{4s'} [c_1(1+\cos^2\theta) + c_2\cos\theta], \tag{2.67}$$

where $\sqrt{s'}$ is the total energy in the ultrarelativistic limit, α is the fine-structure constant, $Q_{\mathrm{q},\ell}$ are the quark and lepton electrical charges, θ is the angle between the

negative lepton and the quark directions of flight in the rest frame of the dilepton system, and c_1 and c_2 are given by

$$c_1 = 1 + 2\Re(\mathcal{R}) g_{V_\ell} g_{V_\mathrm{q}} + |\mathcal{R}|^2 (g_{V_\ell}^2 + g_{A_\ell}^2)(g_{V_\mathrm{q}}^2 + g_{A_\mathrm{q}}^2) \tag{2.68a}$$

$$c_2 = 4\Re(\mathcal{R}) g_{A_\ell} g_{A_\mathrm{q}} + 8|\mathcal{R}|^2 g_{V_\ell} g_{A_\ell} g_{V_\mathrm{q}} g_{A_\mathrm{q}} \tag{2.68b}$$

with

$$\mathcal{R} = \frac{1}{Q_\ell Q_\mathrm{q} \sin^2 2\theta_\mathrm{W}} \frac{s'}{s' - M_\mathrm{Z}^2 + i s' \Gamma_\mathrm{Z}/M_\mathrm{Z}} \tag{2.69a}$$

$$g_{V_{\mathrm{l,q}}} = I_{\mathrm{l,q}}^3 - 2Q_{\mathrm{l,q}} \sin^2 \theta_\mathrm{W} \tag{2.69b}$$

$$g_{A_{\mathrm{l,q}}} = -I_{\mathrm{l,q}}^3. \tag{2.69c}$$

M_Z and Γ_Z are the Z boson mass and width and $I_{\mathrm{l,q}}^3$ is the lepton or quark weak isospin. The last and second to last terms in Equations 2.68 correspond respectively to the Z boson and interference contributions. Only Eq. 2.68a has a contribution coming from the photon. After integration over $d\Omega$, the cross-section becomes:

$$\sigma_{\mathrm{q\bar{q}} \to \gamma/\mathrm{Z} \to \ell\bar{\ell}} = \frac{4\pi}{3\pi} \frac{\alpha^2}{s'} c_1. \tag{2.70}$$

At leading order, for the creation of a high mass resonance, the relation of the mass M to the longitudinal momentum fractions x_1 and x_2 carried by the partons is given by

$$M = \sqrt{x_1 x_2 s}, \tag{2.71}$$

where s is the squared center-of-mass energy of the colliding protons. To study physics at the TeV scale, with a collider with $\sqrt{s} = 8$ TeV, the average x of the partons has to be around 0.1. From the corresponding PDF, at such values the up quark and the down quark content exceeds the other quarks, which means that the interactions are dominated by the valence quarks and the gluons.
The QCD factorisation theorem allows to make the connection between the parton-level cross section and the hadronic one. One can obtain the pp cross-section for the DY process at leading order, by weighting the partonic cross-sections with the corresponding PDF $f_{\mathrm{q/p}}$:

$$\frac{d\sigma_{\mathrm{pp} \to \gamma^*/\mathrm{Z} \to \ell\ell}}{d\Omega} = \sum_q \int_0^1 dx_1 dx_2 \left[f_{\mathrm{q/p}}(x_1) f_{\bar{\mathrm{q}}/\mathrm{p}}(x_2) + (\mathrm{q} \leftrightarrow \bar{\mathrm{q}}) \right] \times \frac{d\sigma_{\mathrm{q\bar{q}} \to \gamma^*/\mathrm{Z} \to \ell\ell}}{d\Omega}. \tag{2.72}$$

2.5 Extra Z bosons

2.5.1 Introduction

From an experimental point of view the Z' is a resonance, more massive than the SM Z, observed in the Drell-Yan process $\mathrm{pp}(\mathrm{p\overline{p}}) \rightarrow \ell^+\ell^- + \mathrm{X}$. So far Z' searches have therefore been phenomenological in nature; indeed Chapter 7 will include the projected detection of the specific quantity known as forward-backward charge asymmetry of such an hypothetical particle in various stages of the CMS upgrades from a purely phenomenological point of view. A brief theoretical introduction to the extra bosons' postulated existence is therefore useful to add context to these searches. A simple compilation of different Z' is then provided in Sec. 2.5.2.

The mechanism of production tells that this new particle would be neutral, colorless and self-adjoint. Such a new state could be interpreted in different ways [16]. One can classify these possibilities according to the spin of the excitation: for instance, as a spin-0 $\tilde{\nu}$ in R-parity violating SUSY, as a spin-2 Kazuka-Klein (KK) excitation of the graviton as in the Randal-Sundrum (RS) model, or even a spin-1 KK excitation of a SM gauge boson from some extra dimensional model. A spin-1 particle could also be a carrier of a new force, that is a new neutral gauge boson arising from an extension of a SM gauge group. The spin could easily be measured with only a few hundreds of events by measuring the lepton angular distribution in the reconstructed Z' rest frame. There are a huge number of models which predict the existence of a Z', with different coupling to the other particles (mainly fermions). In general the Z' will have 24 distinct couplings: one for each of the two components SM fields, $\mathrm{u}_{\mathrm{L}_i}$, $\mathrm{d}_{\mathrm{L}_i}$, ν_{L_i}, $\mathrm{e}_{\mathrm{L}_i} + (L \rightarrow R)$ with $i = 1 - 3$ labelling the three generations. If the couplings are non-universal, i.e. family-dependent, this can lead in flavour changing neutral currents (FCNC) in low-energy processes. The constraints on this phenomenon are quite strong and are generated by fermion-mixing. Such a Z' must be of the order of 100 TeV or more, well outside the reach of the LHC. Then unless some special mechanism suppressing FCNC exists it is highly likely that a Z' accessible by the LHC energies will have generation-independent couplings. This means that the number of couplings is reduced from 24 to 8.

The number of independent couplings is further constrained by other sources. Let us consider the generator to which the Z' couples, T'. Considering T_i as the SM weak isospin generators of $\mathrm{SU}(2)_\mathrm{L}$, and $[T', T_i] = 0$, all members of any SM representation can be labelled by a common eigenvalue of T'. Therefore $Q^T = (\mathrm{u}, \mathrm{d})_\mathrm{L}$ and $L^T = (\nu, \mathrm{e})_\mathrm{L}$ will have identical Z' couplings, reducing their number from 8 to 6. In order to cancel anomalies new vector-like fermions are needed if one introduces new gauge bosons. This requires the presence of new fermions whose mass is comparable to that of the Z' itself. They could be decay products of the Z', having the effect of

modifying the various Z′ branching ratios and adding more coupling parameters to be determined.

2.5.2 Z' models

The number of models predicting a Z′ is rather large. The models usually fall into one of two baskets depending on whether or not they arise from a Grand Unification Theory (GUT) scenario. The models coming from the E_6 grand unification are a popular GUT scenario.

The standard SU$(3)_c\times$ SU$(2)_L\times$ U$(1)_Y$ model may be incorporated into a SU(5), with the known quarks and leptons in each family belonging to the representations $\mathbf{5}^*$ or $\mathbf{10}$ of the unifying group. These may be combined into a single 16-dimensional representation of SO(10), with the addition of a right-handed neutrino. The group SO(10) contains SU$(5)\times$ U(1) as a subgroup; we shall denote this U(1) by the subscript χ, and its corresponding gauge boson by Z_χ. The SU(5) model acquired a lot of popularity after its proposal in 1974, in particular because it predicted $\sin^2\theta_W = 0.375$ (at the unification scale), compatible with the measurements at that time [17]. For such a value, the renormalisation equations of the three couplings of the SM converge at $\mathcal{O}(10^{16}$ GeV). However $\sin^2\theta_W = 0.375$ is now ruled out by experiments and consequently the couplings do not converge. This is not true for supersymmetric cases that can still accomodate the current measurements. Unfortunately, a point that is not fulfilled in neither case is the stability of the proton. According to the SU(5) model the proton lifetime is $\sim 10^{29}$ years, smaller than the most recent experimental limits. Eventually the model cannot include massive neutrinos.

The SU(5) model has nevertheless been used at the starting point of a series of new models. For instance, a further embedding into E_6 is suggested by some string-theory models; the U(1) which arises when E_6 breaks down to SO$(10)\times$U(1) will be denoted by the subscript ψ, and its corresponding boson by Z_ψ. The 15 known fermions in each family of the SM belong to 27-plets of E_6, consisting of $\mathbf{16}$, $\mathbf{10}$, and $\mathbf{1}$ representation of SO(10). The $\mathbf{16}$, as mentioned, contains the standard fermions and a right-handed neutrino. The $\mathbf{10}$ contains weak isosinglet quarks and antiquarks of charge $\pm 1/3$, and weak doublets of leptons and antileptons. The $\mathbf{1}$ contains an isosinglet Majorana neutrino.

The most general Z′ within E_6 then may be parametrized as

$$\mathrm{Z}' = \mathrm{Z}_\psi \cos\theta + \mathrm{Z}_\chi \sin\theta, \tag{2.73}$$

where θ is treated as a free parameter. The particular values of θ corresponding to 'special' models are the following:

Model	$c_{\mathrm{V}}^{\mathrm{u}}$	$c_{\mathrm{A}}^{\mathrm{u}}$	$c_{\mathrm{V}}^{\mathrm{d}}$	$c_{\mathrm{A}}^{\mathrm{d}}$	c_{V}^{ℓ}	c_{A}^{ℓ}
Z'_{ψ}	0	0.300	0	0.300	0	0.300
Z'_{η}	0	0.380	−0.285	0.095	0.285	0.095
Z'_{χ}	0	0.233	−0.466	−0.233	0.466	−0.233
Z'_{I}	0	0	−0.368	−0.368	0.368	−0.368
$\mathrm{Z}'_{\mathrm{SSM}}$	−0.227	0.593	0.410	−0.593	0.045	−0.593

Tab. 2.2.: Vector (c_{V}) and axial-vector (c_{A}) couplings of the Z' boson to up quarks (u), down quarks (d) and the charged leptons (ℓ) for various models corresponding to different values of θ_{E_6}. The values are calculated according to the convention adopted in [18]. For comparison, the $\mathrm{Z}_{\mathrm{SSM}}$ couplings, which are identical to the Z boson couplings are also given.

(a) $\theta = 0$: Z'_{ψ}

(b) $\theta = -90^{\circ}$: Z'_{χ}

(c) $\theta = \sin^{-1}\sqrt{3/8} \simeq 37.76^{\circ}$: Z'_{η}

(d) $\theta = -\sin^{-1}\sqrt{5/8} \simeq -52.24^{\circ}$: Z'_{I}

The Z' couplings to up quarks, down quarks and charged leptons are given in Tab. 2.2 for these models.

In addition to the SM fermions and the right-handed neutrino, E_6 predicts, per generation, an additional neutral singlet, S^c, along with an electric charge $Q = -1/3$, color triplet, vector-like isosinglet, h, and a color singlet, vector-like isodoublet whose top member has $Q = 0$, H (along with their conjugate fields). These exotic fermions are quite heavy and as such they do not participate in Z' decays.

Finally, a commonly used 'standard candle' in experimental searches is a Z' that has couplings which are exactly the same as those of the SM Z, but is just heavier, and called the sequential to Standard Model Z' ($\mathrm{Z}'_{\mathrm{SSM}}$). A more realistic variant of this model is one in which a Z' has no couplings to SM fermions in the weak basis but the couplings are then induced in the mass eigenstate basis Z-Z' via mixing.

2.5.3 Status of the searches and present Z' constraints

A few experiments have already set constraints on different Z' models properties. Among the indirect searches, precise cross section measurements at the Z pole are sensitive to the existence of a new spin 1 particle, Z', with a significant mass mixing with the Z boson. Results from LEP1 have however not shown any deviation with respect to the SM expectation and were able to constraint the absolute value of a

Lower mass limit (GeV)	Z'_χ	Z'_ψ	Z'_η	Z'_{SSM}
ATLAS ($\sqrt{s} = 8$ TeV)	2620	2510	2850	2900
CMS ($\sqrt{s} = 8$ TeV)	-	2570	-	2900
ATLAS ($\sqrt{s} = 13$ TeV)	3080	2790	-	3400
CMS ($\sqrt{s} = 13$ TeV)	-	2600	-	3150

Tab. 2.3.: The 95% c.l. lower limits on the Z' mass for various models obtained by the analysis of the LEP 2 [22], ATLAS [25, 27], and CMS [26, 28].

mixing angle with an hypothetical Z' to be below 0.01 radian for many models [19]. The combination of Z pole precision observables obtained at LEP, SLC or Tevatron with other electroweak observables which include results from neutrino scattering or atomic parity violation experiments allows to set lower limits on the mass of the Z', typically between a few hundreds of GeV up to 1 TeV [20, 21].
Indirect constraints can also be derived from the study of electron-positron collisions with a center-of-mass energy beyond the Z pole but below the Z' mass. At the LEP2, the leptonic and hadronic cross sections and the forward-backward asymmetry were used to constraint Z' models [22]. Finally, among direct analysis, searches in the high mass tail of the Drell-Yan process have already been conducted at the Tevatron. The CDF and D∅ collaborations excluded a Z'_{SSM} in the dielectron channel below 963 GeV and 1023 GeV respectively [23, 24]. At the LHC, much stronger limits were set after 20.3 fb^{-1} of integrated luminosity in the dielectron channel and 20.5 fb^{-1} in the dimuon channel [25] at $\sqrt{s} = 8$ TeV. Similar limits were found by CMS [26]. The latest result include results of 13 TeV pp collisions, with 2.6 fb^{-1} of integrated luminosity in the dielectron channel and 2.8 fb^{-1} in the dimuon one. These values were included in Tab. 2.3.

2.6 Conclusions

In this Chapter a presentation of the Standard Model interactions was given, with a specific attention to the gauge symmetries. This introduction was necessary to illustrate a particular process, known as Drell-Yan, that will be used as a "Standard Model candle" in Chapter 6 to put the analysis code to the test. In fact, the analysis will be focused on different Z' models, and on the detection of one physical quantity known as the forward-backward asymmetry. These topics will be detailed in Chapter 7.

In the following Chapter a general overview of the Large Hadron Collider will be provided; nowadays this accelerator constitutes the main experimental setup in

which the features of elementary particles and fundamental interactions can be detected at energy scales never reached before.

3 The Large Hadron Collider

3.1 Introduction

CERN is a complex that includes six accelerators, formed by a succession of machines designed to increase the energy of particle beams. Each of these machines injects the particle beam into the next one, which takes over to bring it to an even higher energy. The last element of this chain is the Large Hadron Collider (LHC) [29]. CERN also operates a decelerator, called Antiproton Decelerator (AD), which reduces the velocity of antiprotons to about 10% of the speed of light, before delivering them to experiments doing research on antimatter.

The LHC is a two-ring-superconducting-hadron accelerator and collider. Its construction was approved in December 1994 by the CERN Council. The LHC re-uses the already existing 26.7 km tunnel of the former Large Electron-Positron (LEP) collider, constructed between 1984 and 1989 at the France-Switzerland border (see Fig. 3.1). The tunnel consists of eight straight sections and eight arcs. It was built at a mean depth of 100 m underground due to geological considerations, and at a slight gradient of 1.4%. Its depth varies between 175 m (under the Jura) and 45 m (towards Lake Geneva). There are two transfer tunnels, each 2.5 km long, connecting the LHC to the CERN accelerator complex that acts as injector. The LHC was built as a 14 TeV machine in a single stage.

Being a particle-particle collider, the LHC has two rings with counter-rotating beams. Only four of the possible eight interaction regions were equipped with detectors, in order to suppress beam crossings in the other four and prevent unnecessary disruption of the beams. Of these four interaction points, two were equipped with new underground caverns. Between 1996 and 1998, four experiments – ALICE, ATLAS, CMS and LHCb – were officially approved and started their construction work. Currently there are also smaller LHC experiments: TOTEM and LHCf, which focus on forward particles – protons or heavy ions that brush past each other rather than meeting head on when the beams collide. TOTEM uses detectors positioned on either side of the CMS interaction point, while LHCf is made up of two detectors which sit along the LHC beamline, at 140 m either side of the ATLAS collision point. MoEDAL uses detectors deployed near LHCb to search for the hypothetical magnetic monopole.

Energies of the order of the TeV can be guided essentially only through superconductivity. This phenomenon is able to occur at temperatures of 2 K and lower. Currently

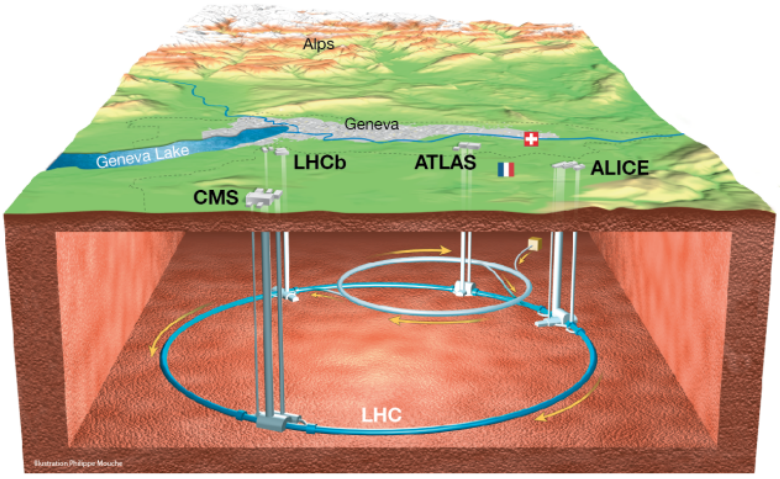

Fig. 3.1.: This figure shows the locations of the four main experiments (ALICE, ATLAS, CMS and LHCb) that take place at the LHC in the Geneva area straddling the France-Switzerland border (dashed line). Located between 45 m and 175 m underground, huge caverns of the size of a cathedral have been excavated to host the giant detectors. The SPS, the final link in the preacceleration chain, and its connection tunnels to the LHC are also shown [30].

each particle beam is accelerated up to the energy of 6.5 TeV [31], very close to the design value of 7 TeV. In addition, most of the other accelerators in the chain have their own experimental halls, where the beams are used for experiments at lower energies.

3.2 The injector complex

Here follows the path of a proton through the accelerator complex at CERN (see Fig. 3.2). First of all, protons are extracted from hydrogen stored in a gas cylinder by stripping orbiting electrons from the atoms. At this early stage the protons have an energy around 100 keV and are pulsed every 100 μs. They enter the 30 m long linear accelerator called Linac2, where they acquire an energy of 50 MeV. They are then ready to be injected into the PS Booster (PSB) synchrotron, that accelerates them to 1.4 GeV. The alternative electric field gives the bunch structure to the beam. When enough bunches are accumulated, the beam is fed to the Proton Synchrotron (PS), one of CERN's oldest accelerators, where it is accelerated to 25 GeV. Protons are then sent to the 6.9 km-long Super Proton Synchrotron (SPS) where they reach the energy of 450 GeV. They are eventually transferred to the LHC where they are accelerated for 20 minutes to their nominal energy of 7 TeV. Beams circulate for many hours inside the LHC beam pipes under normal operating conditions, and arrive in bunches.
In addition to protons, the accelerator complex also accelerates lead ions. Ions are

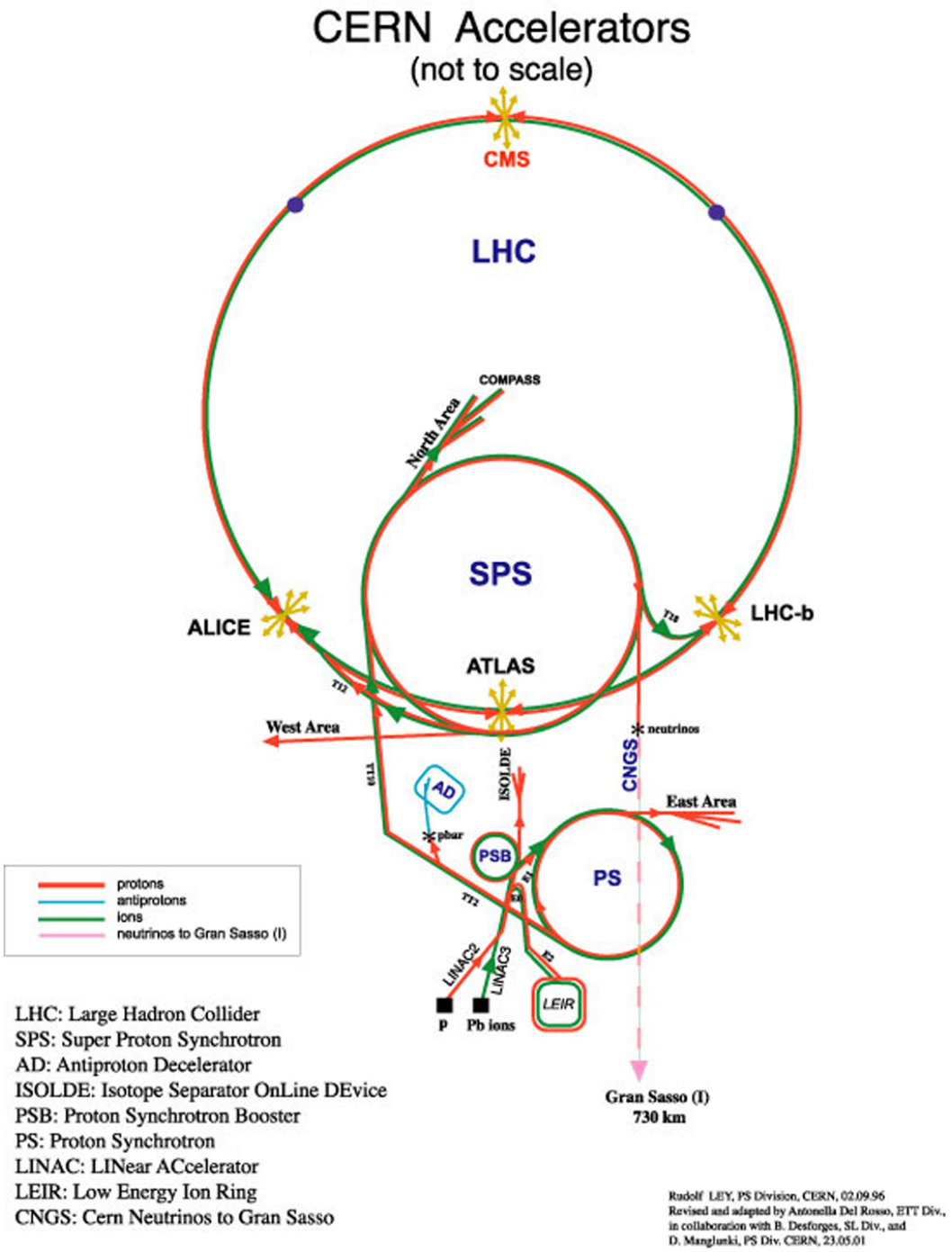

Fig. 3.2.: Accelerator complex of CERN: an overview of all accelerators of CERN [32]

produced from a highly purified lead sample heated to a temperature of about 500°C. The lead vapour is ionized by an electron current. Many different charge states are produced with a maximum around Pb^{29+}. These ions are selected and accelerated to 4.2 MeV/u (energy per nucleon) before passing through a carbon foil, which strips most of them to Pb^{54+}. The Pb^{54+} beam is accumulated, then accelerated to 72 MeV/u in the Low Energy Ion Ring (LEIR), which transfers them to the PS. The PS accelerates the beam to 5.9 GeV/u and sends it to the SPS after first passing it through a second foil where it is fully stripped to Pb^{82+}. The SPS accelerates it to 177 GeV/u and then sends it to the LHC, which accelerates it to 2.76 TeV/u.

3.3 Scientific motivations

As far as accelerator-based experiments are concerned – aside from some discrepancies such as the value of the muon $(g-2)$ [33] – the SM does an excellent job at explaining the variety of elementary particle phenomena. There is however a list of unanswered questions, some coming from observations, others from theory, which the LHC may help to answer:

- **Forces unification:** The Standard Model does not offer a unified description of all the fundamental forces. It is indeed difficult to construct a theory of gravity similar to those of the other forces.

- **Dark matter and dark energy:** We know from cosmological and astrophysical observations that all of the visible matter accounts for only 4.9% of the Universe [34]. The first hint of this important imbalance came in 1933, when astronomical observations and calculations of gravitational effects revealed the need for the existence of an unknown state of matter, named dark matter. Its gravitation effect could in fact explain the fact that galaxies spin faster than expected, and that its gravitation field deviates the light of objects behind it. On the other hand dark energy is estimated to form 70% of the Universe, and it appears to be associated with the vacuum in space. Its homogeneous presence in space and time would lead to a repulsive force that tends to accelerate the expansion of the Universe.

- **Baryon asymmetry:** The matter-antimatter asymmetry is another mystery. The strongest limits on the amount of antimatter in the Universe come from the analysis of the diffuse cosmic gamma-rays and the inhomogeneities of the cosmic microwave background (CMB).

- **Quark-gluon plasma:** Heavy-ion collisions will provide data onto the quark-gluon plasma (QGP) that is a state of matter in QCD that is hypothesized to exist at extremely high temperature, density, or both temperature and density. It is supposed to have existed in the early Universe.

- **Gauge hierarchy problem:** Despite being a compact description of elementary forces, the SM contains a large number of parameters. These include the SU(3)×SU(2)×U(1) gauge couplings – g_s, g and g' – the quark and lepton masses, the four CKM mixing angles, and two parameters from the Higgs field potential, or, equivalently, the Higgs mass and vacuum expectation value. These are already 18 free parameters. They could be increased to 62 parameters, including a complete specification of the model starting from the most general renormalizable Lagrangian with the SM gauge symmetry [11]. The problem is that these parameters cannot be predicted within the SM. In fact, the higher-order to all of these parameters are infinite and require renormalization. Even the qualitative form of the Higgs potential requires more structure than what is present in the SM. To cancel the quadratic divergences of the renormalized μ^2 parameter, new particles of mass of several TeV are expected. This difficulty is named "gauge hierarchy problem" and is sometimes presented as a motivation for new physics [35].

3.4 Performance goals

As previously stated, one of the main goals of the LHC is to reveal the physics beyond the Standard Model with centre of mass collision energies of up to 14 TeV. The number of events per second generated in the LHC collisions is:

$$N_{\text{event}} = L\sigma_{\text{event}}, \tag{3.1}$$

where σ_{event} is the cross section for the event under study and L is the machine instantaneous luminosity. L depends uniquely on beam parameters and can be written for a Gaussian beam distribution as:

$$L = \frac{N_{\text{b}}^2 n_{\text{b}} f_{\text{rev}} \gamma_r}{4\pi\epsilon_{\text{n}}\beta^*} F, \tag{3.2}$$

where N_{b} is the number of particles per bunch, n_{b} the number of bunches per beam, f_{rev} the revolution frequency, γ_r the relativistic gamma factor, ϵ_{n} the normalized transverse beam emittance, β^* the beta function at the collision point, and F the

geometric luminosity reduction factor due to the crossing angle at the interaction point (IP):

$$F = \left[1 + \left(\frac{\theta_c \sigma_z}{2\sigma^*}\right)^2\right]^{-1/2}, \tag{3.3}$$

where θ_c is the full crossing angle at the IP, σ_z the RMS bunch length, and σ^* the transverse RMS beam size at the IP [29]. Equation 3.3 assumes round beams, with $\sigma_z \ll \beta$, and with equal beam parameters for both beams. Rare events in the LHC collisions require high beam energies and intensities in order to be explored.
Both ATLAS and CMS aim to operate at a peak luminosity of $L = 10^{34}$ cm^{-2} s^{-1} for proton operation. LHCb is a lower luminosity experiment for b-physics, aiming at peak luminosity of $L = 10^{32}$ cm^{-2} s^{-1}, and TOTEM for the detection of protons from elastic scattering at small angles, aiming at a peak luminosity of $L = 2 \times 10^{29}$ cm^{-2} s^{-1}. The LHC will also be operated with ion beams, in addition to the proton beams. It has one dedicated ion experiment, ALICE, aiming at a peak luminosity of $L = 10^{27}$ cm^{-2} s^{-1} for lead-lead ion operation.

3.5 Performance limitations

There is a limitation on the maximum particle density per bunch related to the non-linear beam-beam interaction that each particle experiences when the bunches of both beams collide with each other. The beam-beam interaction is measured by the linear tune shift given by:

$$\xi = \frac{N_\mathrm{b} r_\mathrm{p}}{4\pi\epsilon_\mathrm{n}}, \tag{3.4}$$

where r_p is the classical proton radius ($r_\mathrm{p} = e^2/(4\pi\epsilon_0 m_\mathrm{p} c^2)$). Experience suggests that the linear beam-beam tune shift for each IP should not exceed 0.005. This limit together with the mechanical aperture of the LHC therefore limits the maximum bunch density to $N_\mathrm{b} = 1.15 \cdot 10^{11}$.
The nominal dipole field in the storage ring is 8.33 T, corresponding to an energy of 7 TeV. The stored energy in the LHC must be absorbed safely at the end of each run. This leads to limits for the maximum attainable beam energies and intensities. For instance, the total beam current of 0.584 A corresponds to a stored energy of approximately 362 MJ. One must add the energy stored in the circulating beam, and also the one coming from the LHC magnet system, that is approximately 600 MJ. Therefore, the total stored energy exceeds 1 GJ.
Another important limitation of the functioning of the LHC machine is the luminosity lifetime. In fact, the luminosity in the LHC is not a constant of the physics run. The degradation of intensities and emittances of the circulating beams provokes its

degradation. The main cause of this phenomenon is the beam loss from collisions. The initial decay time of the bunch intensity is:

$$\tau_{\text{nuclear}} = \frac{N_{\text{tot},0}}{L\sigma_{\text{tot}}k}, \tag{3.5}$$

where $N_{\text{tot},0}$ is the initial beam intensity, L the initial luminosity, σ_{tot} the total cross section ($\sigma_{\text{tot}} = 10^{25}$ cm^2 at 14 TeV) and k is the number of IPs. Assuming an initial peak luminosity of $L = 10^{34}$ cm^{-2} s^{-1} and two high luminosity experiments, Eq. 3.5 gives an initial decay time of $\tau = 44.85$ h. The result of the above expression has the following dependence in the beam intensity and luminosity as functions of time:

$$N_{\text{tot}}(t) = \frac{N_{\text{tot},0}}{1 + t/\tau_{\text{nuclear}}}, \tag{3.6}$$

$$L(t) = \frac{L_0}{(1 + t/\tau_{\text{nuclear}})^2}. \tag{3.7}$$

The luminosity decay time, when the luminosity drops by a factor $1/e$, is therefore:

$$\tau_{\text{nuclear},1/e} = (\sqrt{e} - 1)\tau_{\text{nuclear},0} = 29 \text{ h}. \tag{3.8}$$

However, the beam loss from collisions is not the only source of the decrease of luminosity lifetime. A net estimation of this quantity also depends on intra-beam scattering and rest-gas time constants. Approximating the overall decay by an exponential process the luminosity lifetime is then estimated to be

$$\tau_L = 14.9 \text{ h}. \tag{3.9}$$

The luminosity integrated over one run is:

$$L_{\text{int}} = L_0\tau_L \left(1 - e^{-T_{\text{run}}/\tau_L}\right), \tag{3.10}$$

where T_{run} is the length of the luminosity run. The collider efficiency depends on the ratio of the length of the run over the average turnaround time. The theoretical minimum turnaround time for the LHC is of the order of 70 minutes, but the pratical experience implies that it can go up to 7 hours. This time includes the cycles of the SPS and PS synchrotrons, the injection of pilot bunches, the readjustment of the machine settings, the ramping of the beam energy in the LHC, the check of all main systems, etc. Given the luminosity lifetime, the optimum run time is then 12 hours. Assuming 200 days of operation per year, the maximum total integrated luminosity per year varies from 80 fb^{-1} to 120 fb^{-1}, depending on the average turnaround time of the machine.

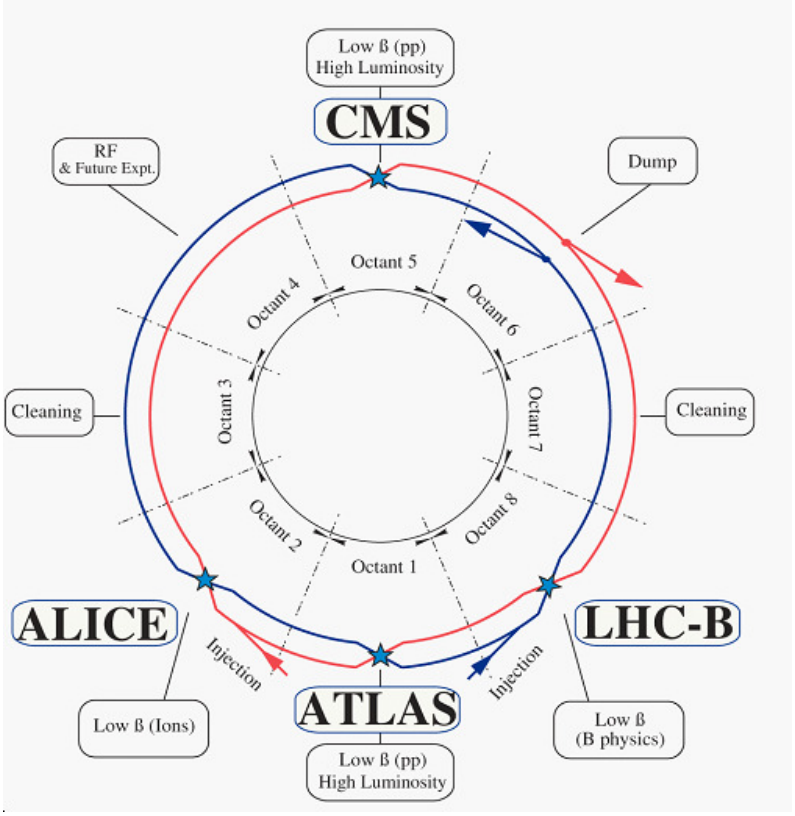

Fig. 3.3.: Schematic layout of the LHC including the main experiments [36].

3.6 LHC layout

The backbone of the LHC is based on the LEP tunnel geometry. It has eight arcs and eight straight sections. Each of the straight sections is approximately 258 m long and can serve as an experimental or utility insertion. The two high luminosity experiments are located at diametrically opposite straight sections (see Fig. 3.3): ATLAS is located at Point 1 and CMS at Point 5. Two more experimental insertions are located at Point 2 for ALICE and Point 8 for LHCb. These Points respectively include the injection systems for Beam 1 and Beam 2. The beam crossings are set on these four locations. Insertions at Points 3 and 7 each contain two collimation systems. The insertion at Point 4 contain one independent radio-frequency (RF) systems for each LHC beam. The straight section at Point 6 contains the beam dump insertion, where the two beams are extracted from the machine.

3.7 Magnets

The operation of the LHC relies on superconducting magnets at the edge of current technology. Large superconducting accelerators such as Tevatron (FNAL), HERA

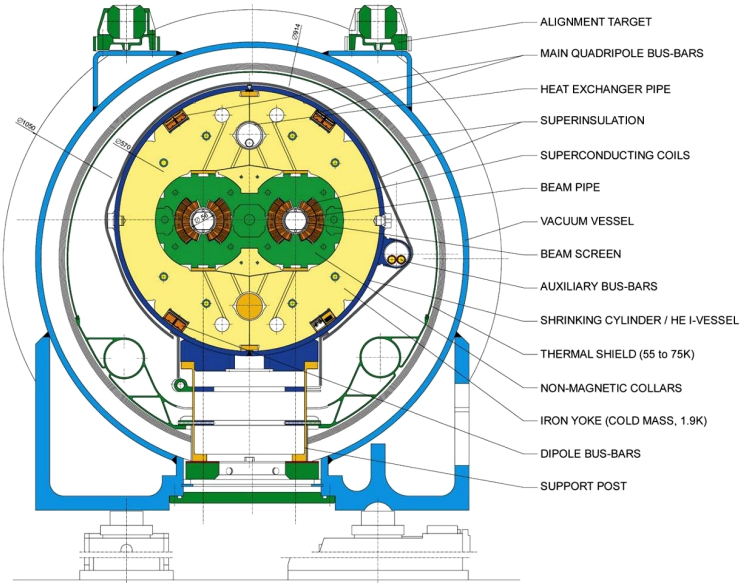

Fig. 3.4.: Cross-section of cryodipole (lengths in mm) [29].

(Desy) and RHIC (BNL) make use of classical NbTi superconductors, cooled by supercritical helium at temperatures slightly above 4.2 K, with fields that do not exceed 5 T. The LHC magnet system also uses the established technology based on NbTi Rutherford cables, but it cools the magnets to a temperature below 2 K, using superfluid helium, and is able to operate fields above 8 T. A consequence of this lowered temperature of operation is that a tighter control of movements and heat dissipation inside cables is requested. In fact, the heat capacity of the cable is reduced by an order of magnitude. As a result, for a given temperature margin, that is the difference between the critical temperature of the superconductor and the operating temperature, the energy deposition that can trigger a quench is reduced. A quench is the raise in magnet's temperature above a critical point, causing it to suddenly change from superconducting to "normal" conducting: a small part of the magnet can be heated from -271 to $700\,^{\circ}$C in less than one second. This is caused by a small number of beam particles hitting the magnet in one spot. The quench releases the stored energy of the magnet and its neighbour. As the electromagnetic forces directly depend on the square of the field, strong structures to retain the conductor motion are required.

Moreover, almost all of the LHC superconducting magnets have a "two-in-one" or "twin-bore" design, because of space limitations and budget restrictions (see Fig. 3.4). Because of this two-in-one design, the windings for the two beam channels include a common cold mass and cryostat, with a magnetic flux circulating in the opposite sense through the two channels.

The LHC ring accommodates 1232 main dipoles, having all the same basic design. This is required to guarantee the successful operation of the LHC. The relative variations of the integrated field and the field shape imperfections must not exceed

$\sim 10^{-4}$. The dipole magnets keep the beams on their circular path, while the 392 quadrupole magnets are used to keep the beams focused.

3.8 Conclusions

In this Chapter the main features of the LHC were briefly discussed, the scientific motivations behind its construction and the performance goals to be reached were shown. The following Chapter will focus on one of the multi-purpose experiments of the LHC: the Compact Muon Solenoid, which represents the experimental context of the present work. In particular the upgrade program of the next Long Shut Down and the plans for the High Luminosity Phase of the LHC will be brought into focus.

4 Compact Muon Solenoid

4.1 Introduction

The Compact Muon Solenoid (CMS) detector is a multi-purpose apparatus operating at the LHC. CMS is installed about 100 m underground close to the French town of Cessy, between Lake Geneva and the Jura Mountains. For the following description of the detector complex, one of the main related documents has been taken as reference [37]. Other sources are explicitly stated throughout the discussion.
An overview of the experiment's performance and layout is given in Sec. 4.2; a description of every subdetector is then included in Sections 4.3 and 4.4, with a particular emphasis on the muon system in Sec. 4.5. The trigger system is then reviewed (Sec. 4.6), and eventually an up-to-date overview of the CMS upgrades is provided (Sec. 4.7).

4.2 Overview

To meet the goals of the LHC physics program, the detector requirements for CMS are the following:

- Good muon identification and momentum resolution over a wide range of momenta and angles, a good dimuon mass resolution ($\sim 1\%$ at 100 GeV/c), and the ability to determine unambiguously the charge of muons with $p < 1$ TeV/c.

- Good charged-particle momentum resolution and reconstruction efficiency in the inner tracker. Efficient triggering and offline tagging of τ's and b-jets, requiring pixel detectors close to the interaction region.

- Good electromagnetic energy resolution, good diphoton and dielectron mass resolution ($\sim 1\%$ at 100 GeV/c), a wide geometry coverage, π^0 rejection, and efficient photon and lepton isolation at high luminosities.

- Good missing transverse energy and dijet-mass resolution, requiring hadron calorimeters with a large hermetic geometry coverage and with fine lateral segmentation.

The CMS detector – 21.6 m long and 14.6 m of diameter – has been precisely designed to meet these requirements. Its main distinguishing features are a high magnetic field solenoid, a full silicon-based inner tracking system, and a homogeneous scintillating crystals-based electromagnetic calorimeter.
The coordinate system of CMS has its origin centred at the nominal collision point inside the experiment, the y-axis pointing upwards, the x-axis pointing radially inward – that is, toward the center of the LHC ring. The z-axis is directed along the beam direction, and points toward the Jura mountains from LHC Point 5. The azimuthal angle ϕ is measured from the x-axis in the x-y plane and the radial coordinate in this plane is denoted by r. The polar angle θ is measured from the z-axis. The widely used pseudorapidity variable is defined as:

$$\eta = -\ln\left[\tan\left(\frac{\theta}{2}\right)\right]. \tag{4.1}$$

The momentum and energy transverse to the beam direction, denoted by p_{T} and E_{T}, respectively, are computed from the x and y components. The imbalance of energy measured in the transverse plane is denoted by $E_{\mathrm{T}}^{\mathrm{miss}}$.
As implied by its name, an important aspect of the CMS detector design regards the magnetic field configuration for the measurement of the momentum of all the charged particles, in particular the muons. To measure the momentum of high-energy charged particles with precision requires a large bending power. This leads to the choice of superconducting technology for the magnets.

The layout of CMS is shown in Figure 4.1. The detector is built around the 3.8 T superconducting solenoid being 13 m long, with an inner diameter of 6 m. It provides a bending power of 12 T·m before the muon bending angle is measured by the muon system. A 1.5 m iron yoke is used to collimate and restrain the magnetic field in space. Four muon stations are then positioned to ensure robustness and maximum coverage. In the barrel region each muon station consists of several layers of aluminium drift tubes (DT); in the endcap the station are equipped instead with cathode strip chambers (CSC). In both barrel and endcap regions, some stations are complemented with resistive plate chambers (RPC).
The bore of the magnet coil hosts the inner tracker and the calorimetry. The tracking volume consists in a cylinder of 5.8 m length and 2.6 m diameter. There are 10 layers of silicon microstrip detectors, which deliver the required granularity and precision to deal with high track multiplicities. Moreover, close to the interaction region are placed 3 layers of silicon pixel detectors to improve the measurement of the impact parameter of charged particle tracks, as well as the position of secondary vertices.
The electromagnetic calorimeter (ECAL) uses lead tungstate ($PbWO_4$) crystals with

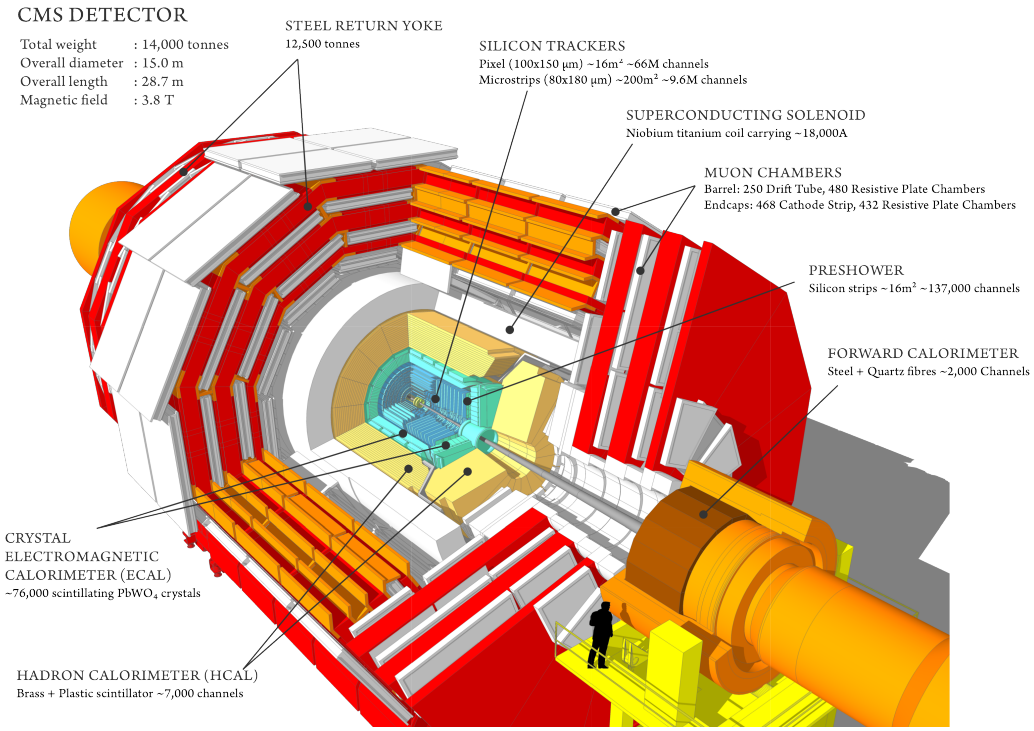

Fig. 4.1.: Cutaway view of CMS detector during Run 1 [38]

coverage in pseudorapidity up to $|\eta| < 3.0$. A preshower system is installed in front of the endcap ECAL for π^0 rejection. The energy resolution of the ECAL depends on three terms: a stochastic one (S), the noise (N), and a constant (C). This dependence shows the following form:

$$\left(\frac{\sigma}{E}\right)^2 = \left(\frac{S}{\sqrt{E}}\right)^2 + \left(\frac{N}{E}\right)^2 + C^2. \tag{4.2}$$

The ECAL is surrounded by the hadron calorimeter (HCAL) with coverage up to $|\eta| < 3.0$. It converts the scintillation light and channels the signal to photodetectors. A tail-catcher in the barrel region (HO) complements the central calorimetry, and the coverage is extended up to $|\eta| < 5.0$ with a iron/quartz-fibre calorimeter.
The superconducting magnet of CMS is able to store an energy of 2.6 GJ at full operation. The magnetic field flux is returned through a $10\,000$ t yoke comprising 5 wheels and 2 endcaps, composed of three disks each.

4.3 Inner tracking system

The LHC physics program demands a robust, efficient and precise reconstruction of the trajectories of charged particles with transverse momentum above 1 GeV/c for $|\eta| < 2.5$. The identification of electrons and muons is done by the tracker together with the electromagnetic calorimeter and the muon system, respectively. The inner

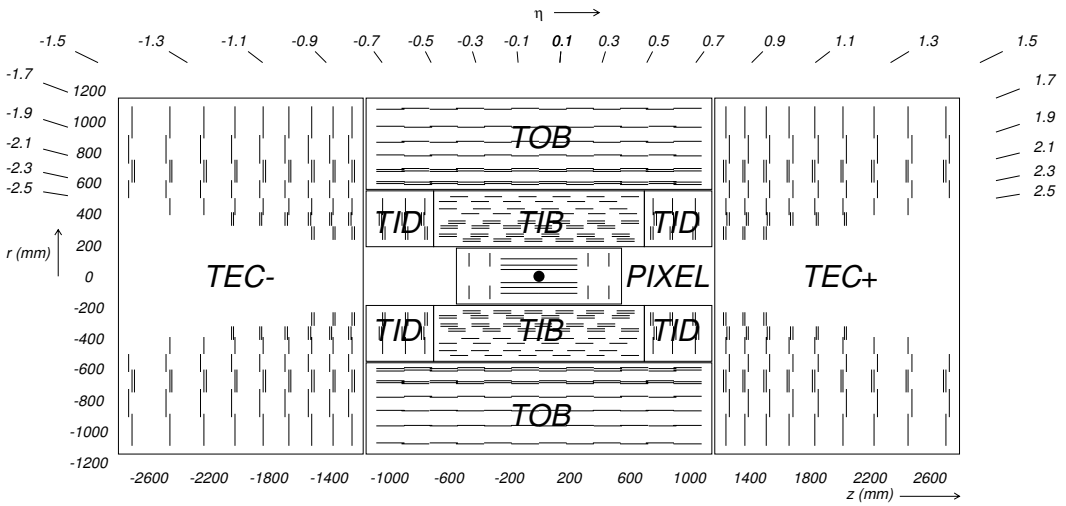

Fig. 4.2.: Cross section of the current CMS tracker, showing the nomenclature used to identify different sections. Each line represents a detector module. Double lines indicate back-to-back modules which deliver stereo hits in the strip tracker [37].

tracking system of CMS provides indeed a precise and efficient measurement of the trajectories of charged particles resulting from the LHC collisions. A precise reconstruction of secondary vertices is also provided. The tracker surrounds the interaction point and features high granularity and fast response, as in the LHC design luminosity of 10^{34} cm^{-2}s^{-1} there will be on average about 1000 particles from more than 20 overlapping proton-proton interactions traversing the tracker for each bunch crossing. The trajectories can therefore be identified reliably and attributed to the correct bunch crossing.

A scheme of the CMS tracker is shown in Figure 4.2. Overall, it is made of about 200 m^2 of active silicon. The tracker is composed of a pixel detector with three barrel layers at radii between 4.4 cm and 10.2 cm. Two disks of pixel modules complement them on each side. It covers an area of about 1 m^2 and has 66 million pixels. It provides precise tracking points in r-ϕ and z, allowing for a small impact parameter resolution that is important for good secondary vertex reconstruction. A similar track reconstruction in both r-ϕ and z directions allows a tridimensional vertex reconstruction in space, important for secondary vertices with low track multiplicity. The range $-2.5 < \eta < 2.5$ covered by the pixel detector matches the acceptance of the central tracker. The spatial resolution of the pixel detector is in the range of $15 - 20$ μm.

The silicon strip tracker and its 10 barrel detection layers occupy the radial region between 20 cm and 116 cm. Three different subsystems compose this detector. The Tracker Inner Barrel and Disks (TIB/TID) delivers up to 4 r-ϕ measurements on a trajectory, having a single point resolution of 23 μm for layers 1 and 2, and 35 μm for layers 3 and 4. The TIB/TID is surrounded by the Tracker Outer Barrel (TOB),

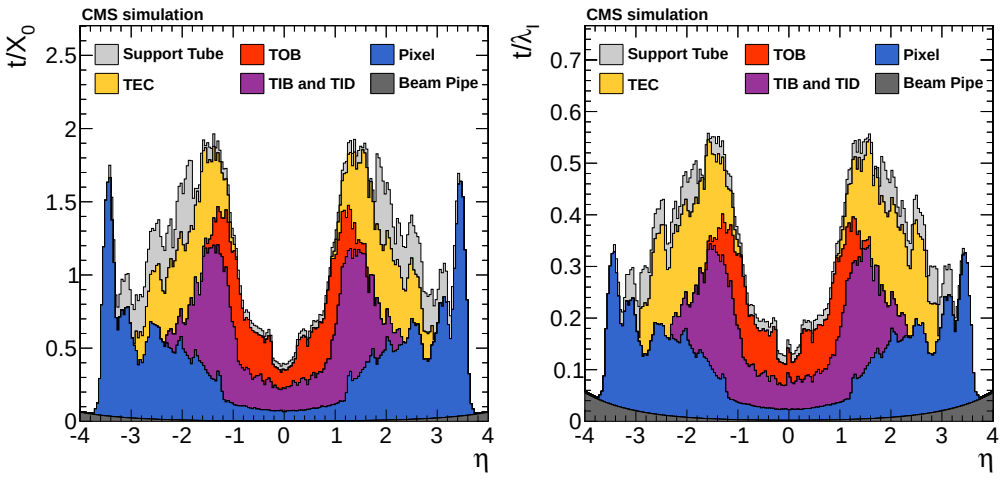

Fig. 4.3.: Total thickness t of the tracker material traversed by a particle produced at the nominal interaction point, as a function of pseudorapidity η, expressed in units of radiation length X_0 (left) and nuclear interaction length λ_I (right). The contribution to the total material budget of each of the subsystems that comprise the CMS tracker is shown, together with contributions from the beam pipe and from the support tube that surrounds the tracker [39].

providing 6 r-ϕ measurements with single point resolution of 53 μm for the first 4 layers, and 35 μm for layers 5 and 6. Beyond its z range are positioned the Tracker Endcaps (TEC+ and TEC-, according to the location along the z axis). Each TEC is composed of 9 disks, carrying up to 7 rings of silicon micro-strip detectors (320 μm thick on the inner 4 rings, 500 μm thick on rings 5-7) with radial strips of 97 μm to 184 μm average pitch. Thus, they provide up to 9 ϕ measurements per trajectory.
In addition, a second micro-strip detector back-to-back with a stereo angle of 100 mrad is mounted on the modules in the first two layers and rings of TIB, TID and TOB respectively, as well as rings 1, 2, and 5 of the TECs. It can then provide a measurement of the second coordinate (z and r for barrel and disks respectively). The achieved single point resolution of this measurement is 230 μm in TIB and 530 μm in TOB.

As anticipated, each LHC bunch crossing at design luminosity creates about 1000 particles hitting the tracker, on average. There is a conflict in the goal of minimizing the radiation lengths of the material, to limit multiple scattering, bremsstrahlung, photon conversion and nuclear reactions. The silicon detector technology has been selected by the CMS management, as it can offer the granularity, speed and radiation hardness requirements needed for a 10 years operation in a harsh environment, with some cost on the side of the radiation length. Indeed, the material budget of the tracker in units of radiation length is shown in Fig. 4.3. It goes from 0.4 X_0 at $\eta \approx 0$ to about 1.8 X_0 at $\eta \approx 1.4$, beyond which it falls to about 1 X_0 at $\eta \approx 2.5$.

The consequent hit rate density is of 1 MHz/mm^2 at a radius of 4 cm, falling to 60 kHz/mm^2 at a radius of 22 cm and 3 kHz/mm^2 at a radius of 115 cm. The

Radius (cm)	Fluence of fast hadrons (10^{14} cm^{-2})	Dose (kGy)	Charged particle flux (cm^{-2} s^{-1})
4	32	840	10^8
11	4.6	190	
22	1.6	70	6×10^6
75	0.3	7	
115	0.2	1.8	3×10^5

Tab. 4.1.: Expected hadron fluence and radiation dose in different radial layers of the CMS tracker (barrel part) for an integrated luminosity of 500 fb^{-1} (approximately 10 years). The fast hadron fluence is a good approximation to the 1 MeV neutron equivalent fluence.

needed radius so that the occupancy does not exceed 1% has to be below 10 cm for pixelated detectors. The size of 100×150 μm^2 in r-ϕ and z, respectively, provides an occupancy of 10^{-4} per pixel and LHC bunch crossing. At higher radii (20 cm $< r <$ 55 cm) it is possible to use silicon micro-strip detectors thanks to the reduced particle flux; the typical cell size is of 10 cm $\times$ 80 μm, providing an occupancy of no more than $2-3$ % per strip and LHC bunch crossing. In the outer region, where 55 cm $< r <$ 110 cm the strip pitch can be increased, also to limit the number of read-out channels.

The radiation damage due to the high particle fluxes in the LHC interaction regions has to be carefully taken into account. An integrated luminosity of 500 fb^{-1} corresponding to about 10 years of LHC operation lead to the fast hadron fluence and radiation dose in the CMS barrel tracker reported in Tab. 4.1. The substantial contribution to fast hadron fluence comes from hadronic interactions in the ECAL crystals of neutrons. It dominates the fluence in the outer tracker close to the ECAL surface. The radiation damage is one of the reasons why the tracker will need to be completely replaced for the next phase of the LHC, called High Luminosity LHC or Phase II.

For high momentum tracks the transverse momentum resolution is around $1-2\%$ up to $|\eta| \approx 1.6$, beyond which it degrades due to the reduced lever arm. At transverse momenta of 100 GeV/c, the transverse momentum resolution is dominated for $20-30\%$ by multiple scattering in the tracker material. The transverse impact parameter resolution is 10 μm for high p_{T} tracks, dominated by the resolution of the first pixel hit, while at lower momentum it is degraded by multiple scattering. The muon efficiency over most of the acceptance is about 99%, apart from where the gaps between the ladders of the pixel detector occur, and at high η due to the reduced coverage by the pixel forward disks. In general hadrons have a lower efficiency because of interactions with the material of the tracker.

It should appear clear by now that a consistent upgrade for the tracker is necessary to cope with the coming conditions of the LHC. The main requirements for Phase II include in fact a radiation tolerance up to an integrated luminosity of 3000 fb^{-1}, an increased granularity in order to ensure efficient tracking performance at high pileup (to maintain a channel occupancy near or below the 1% level), an improved ability to distinguish two close-by tracks, a reduced material in the tracking volume, and a more robust pattern recognition.

4.4 Calorimeters

4.4.1 Electromagnetic calorimeter

The composition of the electromagnetic calorimeter of CMS (ECAL) consists in $61\,200$ lead tungstate ($PbWO_4$) crystals mounted in the central barrel part, completed by 7324 crystals in each of the two endcaps. This closure makes the ECAL a hermetic homogeneous calorimeter. In front of the endcap crystals a preshower detector is placed. Avalanche photodiodes (APDs) are used as photodetectors in the barrel and vacuum phototriodes (VPTs) in the endcaps. They are fast, radiation tolerant and able to operate in the longitudinal 3.8 T magnetic field. The calorimeter is fast, has fine granularity and is radiation resistant, thanks to its high density crystals. The capability to detect the decay to two photons of the then postulated Higgs boson has been at the center of the ECAL design, together with a good energy resolution.
Having a density of 8.28 g/cm^3, a radiation length of 0.89 cm and a Molière radius of 2.2 cm, the $PbWO_4$ crystals are an appropriate choice for the LHC goals. They provide a fine granularity and a compact calorimeter. Their scintillation decay time is of the same order of magnitude as the LHC bunch crossing time: in fact, about 80% of the light is emitted within 25 ns.
The barrel part of the ECAL (EB) covers the range $|\eta| < 1.479$. The crystals are divided depending on a 360-fold granularity in ϕ and (2×85)-fold in η. The crystal dimensions are of 0.0174×0.0174 in $\eta - \phi$, that is 22×22 mm^2 in the front face of the crystal, and 26×26 mm^2 in the rear face. The crystal length is 230 mm, corresponding to $25.8\ X_0$.
The endcaps (EE) cover the range $1.479 < |\eta| < 3.0$. They consist of crystals of the same shape grouped in mechanical units of 5×5 crystals (called supercrystals, or SCs) organized in a carbon-fibre alveola structure. The rear face cross section of the crystals is 30×30 mm^2, while the front face is 28.62×28.62 mm^2, and the length is 220 mm, corresponding to $24.7\ X_0$.
For energies below about 500 GeV, the parametrization of the energy resolution is reported in Equation 4.2. We discuss hereby the different contributions.

- The stochastic term. The three basic contributions to the stochastic term are:

  1. Even-to-event fluctuation in the lateral shower containment. When the energy is reconstructed by summing an array of 5×5 crystals it is expected to be 1.5 % and a bit more (2 %) when using 3×3 crystals.

  2. A photostatics contribution of 2.1 %. It is given by:

$$a_{\mathrm{pe}} = \sqrt{\frac{F}{N_{\mathrm{pe}}}}, \tag{4.3}$$

     where N_{pe} is the number of primary photoelectrons released in the detector per GeV, that is $N_{\mathrm{pe}} \approx 4500$ pe/GeV in the barrel, and F is the excess noise factor which parametrizes fluctuations in the gain process (a value between 2 and 2.5).

  3. Fluctuations in the energy deposited in the preshower absorber (if present) with respect to what is measured in the preshower silicon detector.

- The constant term. It depends on the non-uniformity of the longitudinal light collection, intercalibration errors and leakage of energy from the back of the crystal.

- The noise term. The main contributions are electronics noise, digitization noise and pileup noise.

In test beams, using electron beams with momenta between 20 and 250 GeV/c, the following typical energy resolution was obtained by summing 3×3 crystals:

$$\left(\frac{\sigma}{E}\right)^2 = \left(\frac{2.8\%}{\sqrt{E}}\right)^2 + \left(\frac{0.12}{E}\right)^2 + (0.30\%)^2, \tag{4.4}$$

where E is expressed in GeV.

4.4.2 Hadron calorimeter

The hadron calorimeter (HCAL) of CMS is designed to measure the energy of the hadrons jets produced in the proton-proton interaction. It also plays a central role in the identification of neutrinos and exotic particles that do not interact with the detector and whose signature is a non zero transverse energy balance. Since the HCAL is placed inside the magnet, materials with short interaction lengths need to be used. A good hermiticity is also requested in order to accurately measure the transverse missing energy.

The HCAL is a sampling calorimeter consisting of a succession of layers of absorbers (mainly brass) and scintillator material. The central part (HB) which extends from $|\eta| = 0$ to $|\eta| = 1.3$ is made of 16 absorber plates. The innermost and outermost ones are made of stainless steel whereas the others consist of brass. The interleaved plastic scintillators are segmented into 32 regions in $|\eta|$ times 36 regions in ϕ, leading to 1152 towers 0.087×0.087 wide in $(\Delta\eta, \Delta\phi)$. On each side of the barrel, the two towers closest to the endcap transition region are also longitudinally segmented in two depths. Because of the barrel geometry, the number of interaction lengths of the HCAL varies between 5 ($|\eta| = 0$) and 10 ($|\eta| = 1.3$). This is sometimes too small to contain the full hadronic shower. In order to recover the end of the shower, the HCAL barrel is completed by an outer calorimeter (HO) surrounding the magnet, raising the total depth of calorimeter system to at least 12 interaction lengths.
The HCAL endcaps (HE) extend from $|\eta| = 1.3$ to $|\eta| = 3.0$. Its $\Delta\eta \times \Delta\phi$ granularity is 0.087×0.087 for $|\eta| < 1.6$ and around 0.17×0.17 for $|\eta| > 1.6$. As in the barrel the absorber is made of brass plates. The total depth of the endcap calorimetry is about 10 interaction lengths. The HCAL endcaps are longitudinally segmented into two depths for $|\eta| < 2.5$ and into three depths at higher $|\eta|$.
A forward calorimeter (HF) is also installed at 11.2 m from the interaction point that covers the $|\eta|$ range from 3.0 to 5.2. Due to the extreme particle fluxes in that region, a radiation hard technology had to be used. The choice fell on Cherenkov light detector made of quartz fibres. In addition to ensure a good hermiticity of the HCAL, this detector is used for the measurement of the instantaneous luminosity.

4.5 The muon system

4.5.1 Introduction

As it is implied by the experiment's name, the muon detection is at the heart of CMS. The robustness and reliability of the muon measurement is at the center of its design since the earliest stage. The muon system revolves around three functions: muon identification, momentum measurement and triggering. The solenoidal magnet and its flux-return yoke – along with the muon chamber themselves – are the essential tools to guarantee a good momentum resolution and trigger capability.
CMS can reconstruct the momentum and the charge of muons in the entirety of the kinematic range of the LHC. The muon system follows the shape of the solenoid magnet, and is divided in a cylindrical barrel section and two planar endcap regions. Three types of gaseous detectors are currently installed for muon identification, covering a total surface of $25\,000$ m^2 (see Figure 4.4). The gas-ionization technology was chosen since the detectors must be relatively inexpensive. Their relatively small data volume time response make them well appropriate for use in a hardware muon

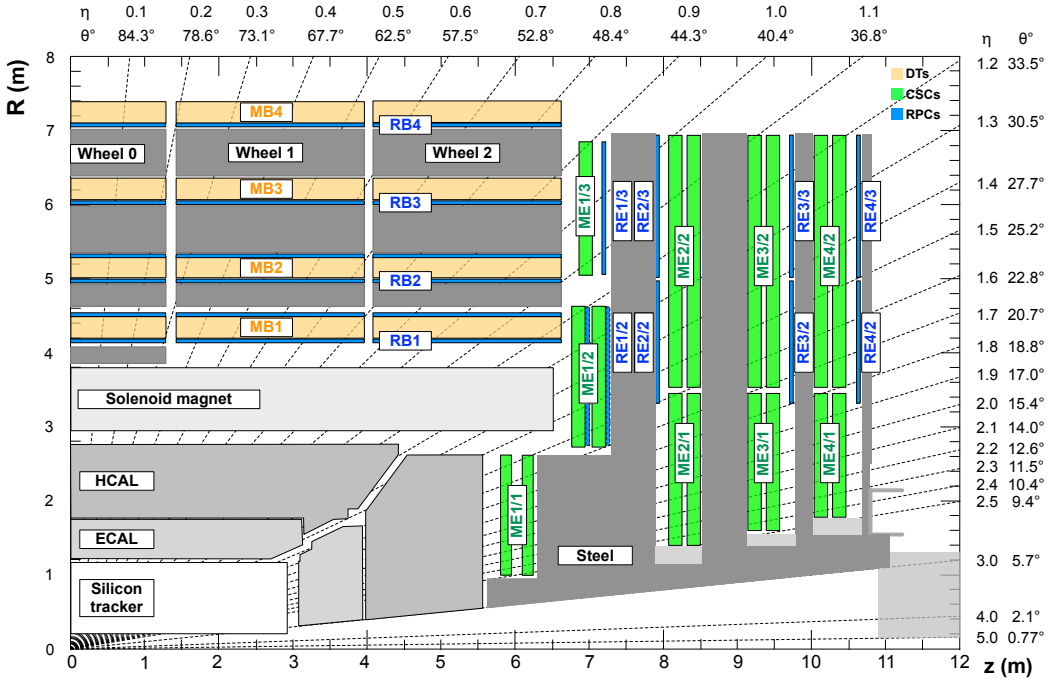

Fig. 4.4.: An $R - z$ cross section of a quadrant of the CMS detector with the axis parallel to the beam (z) running horizontally and radius (R) increasing upward. The interaction point is at the lower left corner. Shown are the locations of the various muon stations and the steel disks (dark grey areas). The 4 drift tube (DT, in light orange) stations are labelled MB ("muon barrel") and the cathode strip chambers (CSC, in green) are labelled ME ("muon endcap"). Resistive plate chambers (RPC, in blue) are in both the barrel and the endcaps of CMS, where they are labelled RB and RE, respectively [37].

trigger rather immune to high background particle densities.

For all the different technologies that will be hereby presented, the basic physical modules and independently-operating units are called "chambers". A "station" is an assembly of chambers around a fixed value of r in the barrel, or z in the endcap. There are 4 stations in the barrel and in each endcap, labelled respectively MB1-MB4 and ME1-ME4. Along z, the DTs and RPCs in the barrel are divided into 5 "wheels", with wheel 0 centred at $z = 0$ and wheels W+1 and W+2 in the $+z$ direction and W-1 and W-2 in the -z direction. Similarly in the r direction in the endcaps, there are "rings" of endcap RPCs and CSCs. The latter are labelled ME1/n-ME4/n, where integer n increases with the radial distance from the beam line.

The LHC is a bunched machine, in which the accelerated protons are distributed in bunches separated by one (or more) time steps of 25 ns, nominally. This coincides also with the minimum separation between bunch crossings, in which proton-proton collisions occur. Thus, a convenient time quantity for both the accelerator and the detectors is the bunch crossing (BX) "unit" of 25 ns. The ability of the muon chambers to provide a fast, well-defined signal is crucial for triggering on the muon tracks. To ensure unambiguous identification (ID) of the correct bunch crossing and the time coincidence of track segments among the muon stations, the local signal

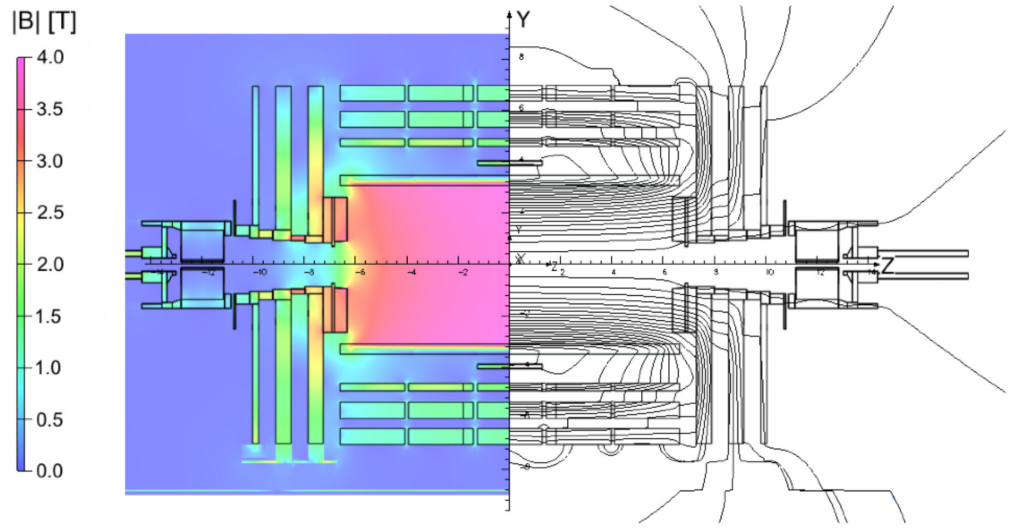

Fig. 4.5.: Map of the $|B|$ field (left) and field lines (right) predicted for a longitudinal section of the CMS detector by a magnetic field model at a central magnetic flux density of 3.8 T. Each field line represents a magnetic flux increment of 6 Wb [41].

must have a time dispersion of a few nanoseconds, much less than the minimum 25 ns separation of bunch crossings.
Tab. 4.2 summarises the functions and parameters of the muon systems as installed in CMS during the 2010 running period. The design specifications for spatial and time resolution coming from the CMS Muon TDR [40] are also listed. If not In the following sections the detectors performance is taken from [41], where otherwise not indicated.

4.5.2 Drift tubes chambers

Drift tube (DT) chambers with standard rectangular drift cells are used in the barrel, in the region $|\eta| < 1.2$, where the neutron-induced background is small (except in the outermost station MB4), the muon rate is low and the 3.8 T magnetic field is uniform and mostly contained in the steel yoke (see Fig. 4.5). DTs are divided into four concentric cylinder stations between the layers of the flux return plates and around the beam line, labelled MB1, MB2, MB3 and MB4. The first three inner cylinders contain 60 drift chambers each, and the outer one 70. The basic element of the DT is the drift cell, shown in Fig. 4.6. Four staggered layers of parallel cells form a superlayer (SL), the smallest independent unit of design. A chamber consists of 2 SLs that measure the muon coordinate in the r-ϕ bending plane, and an orthogonal SL that provides a measurement in the z direction, along the beam line. The fourth station, MB4, includes 70 drift chambers and does not contain the z-measuring planes. The chambers are limited in size in the longitudinal dimension

Muon subsystem	Drift Tubes (DT)	Cathode Strip Chambers (CSC)	Resistive Plate Chambers (RPC)
Function	Tracking, p_{T} trigger, BX ID	Tracking, p_{T} trigger, BX ID	p_{T} trigger, BX ID
$\lvert\eta\rvert$ range	0.0-1.2	0.9-2.4	0.0-1.6
No. of stations	4	4 (no ME4/2 ring)	4 (barrel) 3 (endcap)
No. of layers	8 (r-ϕ), 4 (z)	6	2 in RB1 and RB2, 1 elsewhere
No. of chambers	250	468	480 (barrel), 432 (endcap)
No. of channels	172000	Strips 220000, Wire groups (183000)	68000 (barrel), 41000 (endcap)
Design position resolution (σ) for perpendicular tracks	per wire 250 μm, r-ϕ (6/8 pts) 100 μm, z (3/4 pts) 150 μm	per chamber r-ϕ (6 pts) ME1/1, ME2/1 75 μm other CSCs 150 μm, r (6 pts) 1.9-6.0 mm	Strip size (on the order of a centimeter)
Design time resolution	5 ns (per tube)	6 ns (per anode)	3 ns (double-gap)

Tab. 4.2.: Properties and parameters of the muon system during the 2010 data-taking period. The design values of the position and time resolutions are from the CMS Muon TDR [40]. As explained in the above sections, these specifications were met or exceeded.

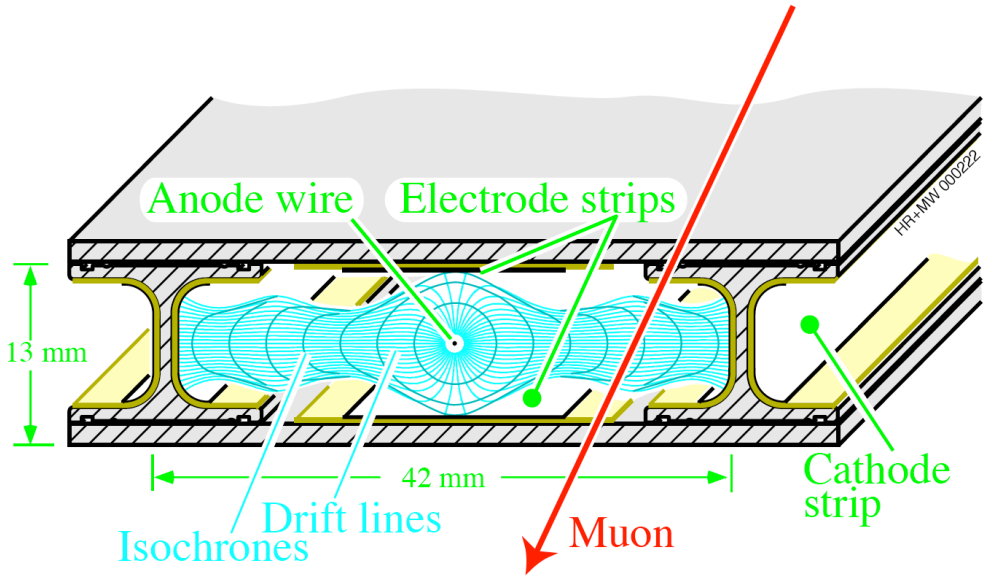

Fig. 4.6.: Sketch of a cell showing drift lines and isochrones. The plates at the top and bottom of the cell are at ground potential. The voltages applied to the electrodes are $+3600$ V for wires, $+1800$ V for strips, and -1200 V for cathodes [37].

by the segmentation of the barrel yoke, and are about 2.5 m long. On the transverse side, their length varies with the station, ranging from 1.9 m for MB1 to 4.1 m for MB4.

Dead spots in the efficiency are eliminated through half-cell offsets between neighbouring chambers. The low expected rate and the lower strength of the local magnetic field allows the usage of the DT as tracking detectors for the barrel muon system.

The wire length in the chambers is about 2.4 m if measured in a r-ϕ projection, and it is constrained by the longitudinal segmentation of the iron barrel yoke. The transverse dimension of the drift cell is 21 mm and corresponds to a drift time of 380 ns in a gas mixture of Ar (85%) and CO_2 (15%). The basic drift unit is a tube, to protect the chambers against damage from a broken wire and to decouple contiguous cells.

Redundancy is very important, to deal with the uncorrelated background hits (generated by neutrons and photons) having a much larger rate than that from prompt muons. Moreover at high momenta (≥ 40 GeV/c) the probability of electromagnetic cascades accompanying the parent muon becomes relevant. There are regions of η in which the combined effect of the ϕ and z discontinuities limits the number of stations crossed by a muon to only two. This is why a good tracking efficiency is important in each station. In the pseudorapidity range covered by four stations, that is $|\eta| < 0.8$, the efficiency to reconstruct a high p_{T} muon track with a momentum measured by the barrel muon system alone is better than 95%.

One SL has a time resolution of a few nanoseconds, giving excellent time-tagging

capability. This capability provides local, standalone and efficient bunch crossing identification. The Fast Pattern Recognition circuitry delivers also the position of the centre of gravity of the track segment and its angle in the SL reference system with precisions of 1.5 mm and 20 mrad, respectively. This information is used by the first-level muon trigger for the time and transverse momentum assignment.
The global resolution to be achieved by the mechanical precision of the construction of a chamber was of 100 μm in r-ϕ. Since the single wire resolution is better than 250 μm, the goal is achieved by 8 track points measured in the two ϕ SLs [42]. The precision requirement on the position of the field-shaping electrodes, including the wires, is about 300 μm [43].
According to the 2010 data performance analysis [41], and depending on the wheel and on the station considered, the DT chamber position resolution varies from ~ 80 μm to ~ 120 μm in the r-ϕ projection, and from ~ 130 μm to ~ 390 μm in the r-z projection. The resolution changes from inner to outer wheels because of the effect of the increased angle of incidence of muons. For r-z layers, the resolution is degraded in external wheels because of the increasing deviation from linearity of the space-time relationship between the hit position and the drift velocity, with larger angles of incidence (θ) of the particles. For r-ϕ SLs, the larger angle in external wheels results in longer paths inside the cells that increase the number of primary ionizations, leading to a slight improvement in the r-ϕ resolution.
The observed resolution is that expected from simulation, given the distribution of the incident angle for muons in CMS, and is in agreement with Muon TDR expectations. The overall time resolution of the DTs for a sample of prompt muon tracks with $p_{\mathrm{T}} > 10$ GeV/c is better than 2.6 ns.

4.5.3 Cathode strip chambers

In the endcap regions of CMS, the muon rates and background levels are higher and the magnetic field is large and non-uniform. In order to adapt to its environment and keep identifying muons when $0.9 < |\eta| < 2.4$, the muon system employs cathode strip chambers (CSC). The CSCs are multiwire proportional chambers consisting of six anode wire planes alternated with seven cathode panels. The direction of the wires is azimuthal, that is perpendicular to the strips, and is used to define the radial coordinates of the reconstructed tracks. They have fast response time, fine segmentation, radiation resistance [44] and can tolerate the non-uniformity of the magnetic field [45]. The CSC stations are four per endcap, with chambers positioned perpendicularly to the beam line and interspersed between the flux return plates. In each chamber the cathode strips run radially outward and provide a precision measurement in the r-ϕ bending plane, that is the position at which a muon or other charged particle crosses the gas volume. The anode wires are also read out in order to provide measurements of η and the beam-crossing time of a muon; the wires

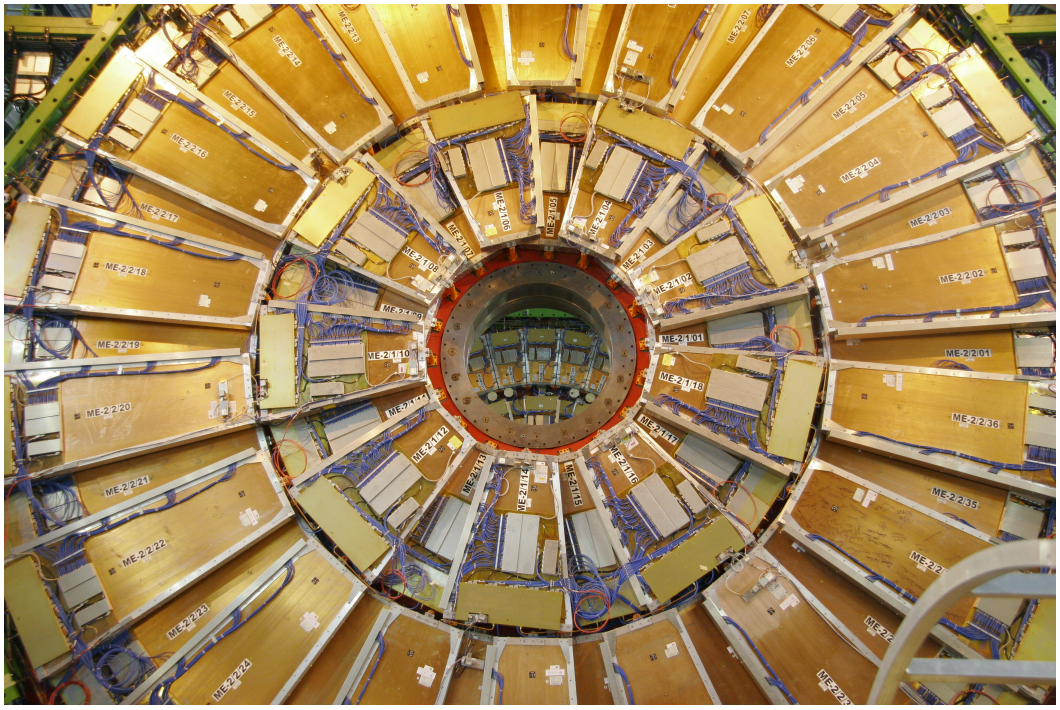

Fig. 4.7.: Endcap assembly on ground level during late 2007 [46].

provide a coarse measurement in the radial direction. The CSCs provide a robust pattern recognition for the rejection of non-muon backgrounds, and an efficient matching of hits to those occurring in other stations and in the CMS inner tracker. All chambers use a gas mixture of 50% CO_2, 40% Ar and 10% CF_4 (the properties of the gases concerning electron transport are discussed in Sec. 5.3.2).

CSCs are arranged in the CMS Endcap Muon system, and divided in groups as follows: 72 ME1/1, 72 ME1/2, 72 ME1/3, 36 ME2/1, 72 ME2/2, 36 ME3/1, 72 ME3/2, 36 ME4/1, and 72 ME4/2 for a total of 540 chambers. ME2/2 chambers are shown in Figure 4.7, during the endcap assembly. CSCs are trapezoidal and cover either 20° for stations 2, 3 and 4, or 10° in ϕ for the others. Each layer of CSC contains 80 cathode strips, each of which subtends a constant ϕ angle between 2.2 and 4.7 mrad and projects to the beamline. The anode wires have a diameter of 50 μm and are spaced by 3.16 or 3.12 mm in all chambers, except ME1/1 where they have 30 μm diameter and are 2.5 mm apart. They are ganged in groups of 5 to 16 wires, with widths from 16 to 51 mm, which limits the position resolution in the wire coordinate direction. All chambers, except for the ME3/1 ring, overlap and provide contiguous ϕ-coverage. A muon in the pseudorapidity range $1.2 < |\eta| < 2.4$ crosses 3 or 4 CSCs. In the endcap-barrel overlap range, $0.9 < |\eta| < 1.2$, muons are detected by both the barrel DTs and endcap CSCs. Muons with $|\eta| < 1.6$ are also detected by resistive plate chambers (RPC, see Sec. 4.5.5). Therefore the DT and CSC muon detector elements together cover the full CMS pseudorapidity interval

$|\eta| < 2.4$ with no acceptance gaps.
The required performance for the CSC includes the following:

- reliable and low-maintenance operation for at least 10 years at estimated random hit rates up to 1 kHz/cm^2;
- at least 99% efficiency per chamber for finding track stubs by the first-level trigger;
- at least 92% probability per chamber of identifying correct bunch crossings by the first-level trigger. Thanks to this efficiency per chamber and 3-4 CSCs on a muon track path, the correct bunch crossing number will be correctly assigned to the reconstructed muons in more than 99% of cases;
- about 2 mm resolution in r-ϕ at the first-level trigger;
- about 75 μm offline spatial resolution in r-ϕ for ME1/1 and ME1/2 chambers and about 150 μm for all others.

The position resolution measurements coming from the 2010 collisions data provide values of 58 μm for the ME1/1 station, and between 92 and 136 μm for the others. The requirements of the Muon TDR, that asked for 75 μm for the ME1/1 and ME1/2 chambers and 150 μm for the remaining ones (as reported in Tab. 4.2), are met.
The CSC hit time is based on the cathode signal, which is amplified, shaped and then sampled every 50 ns. The comparison with the known analytical form of the pulse shape delivered by the cathode electronics provides a measured single hit resolution of 5 ns. After the track reconstruction, the cathode hit times are combined with the anode hit times, and the Gaussian fit to the time distribution gives a resolution measurement of about 3 ns.

4.5.4 DT and CSC performance

As shown in Fig. 4.8, the muon momentum resolution of the standalone muon system is about 9% for small values of η and p for transverse momenta up to 200 GeV. This is due to multiple-scattering in the detector material between the muon stations. At 1 TeV the standalone momentum resolution varies between 15% and 40%. A combination with the inner tracker occurs through a global momentum fit, and improves the momentum resolution by an order of magnitude at low momenta: at such scales in fact, the momentum reconstruction is dominated by the tracker. At high momenta (1 TeV) the combined momentum resolution improves at about 5%. Independent measurements are nevertheless delivered by the muon system and the

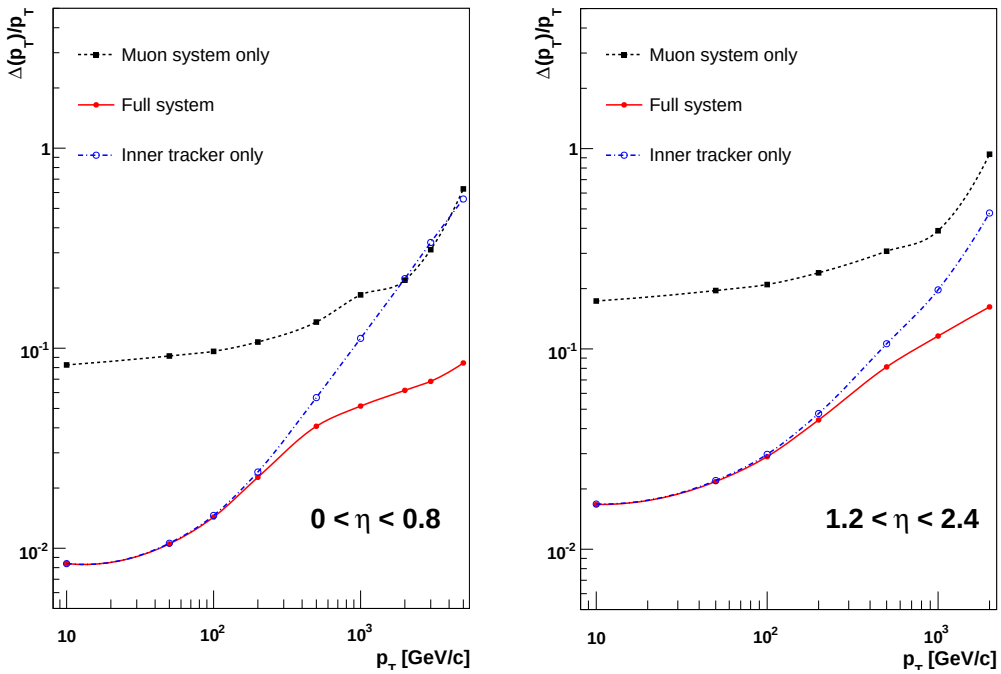

Fig. 4.8.: The muon transverse-momentum resolution as a function of the transverse-momentum (p_{T}) using the muon system only, the inner tracking only, and both. Left panel: $|\eta| < 0.8$, right panel: $1.2 < |\eta| < 2.4$.

inner tracker, for redundancy and cross-checking purposes. Offline reconstruction efficiency for the muons is typically 96-99% except in the gaps between the 5 wheels of the yoke (at $|\eta| = 0.25$ and 0.8) and the transition region between the barrel outer wheel and the endcap disks. Crucial properties of the DT and CSC systems are that they can each identify the collision bunch crossing that generated the muon and trigger on the p_{T} of muons with good efficiency, and that they have the ability to reject background by means of timing discrimination.

4.5.5 Resistive plate chambers

A third technology, the resistive plate chambers (RPCs), was added in both the barrel and the endcap regions. The main reason lies in the uncertainty in the eventual background rates and in the ability of the muon system to measure the correct beam-crossing time when the LHC reaches full luminosity. Not being wire detectors, RPCs add redundancy, along with being a complementary, dedicated triggering detector system. They provide a fast, independent and highly-segmented trigger with a looser p_{T} threshold over a large portion of the rapidity range ($|\eta| < 1.6$) of the muon system. The RPCs are gaseous parallel-plate double-gap chambers, operated in avalanche mode to ensure good operation at high rates. Each gap consists of 2 mm thick resistive Bakelite plates separated by a 2 mm thick gas gap. The outer surface of the bakelite plates is coated with a thin conductive graphite layer, and a voltage of

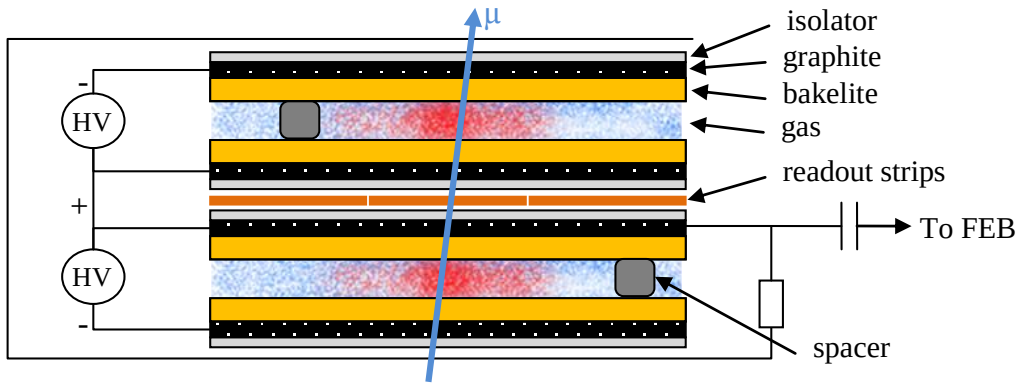

Fig. 4.9.: Cross-section of a double-gap RPC chamber [47].

about 9.6 kV is applied. The RPC are operated with a 3-component, non-flammable gas mixture that consists of 95.2% Freon ($C_2H_2F_4$, known as R134a), 4.5% isobutane (i-C_4H_10), and 0.3% sulphur hexafluoride (SF_6). The readout consists in common pick-up strips set between the chambers. This allows the single-gaps to operate at lower gas gain (that is, lower high voltage) with an effective detector efficiency higher than for a single gap. Fig. 4.9 shows a layout of a RPC.

The response they produce is fast, with good time resolution but worse position resolution than DTs or CSCs. In fact, a RPC is capable of tagging the time of an ionising event in a much shorter time than the 25 ns between two consecutive LHC bunch crossings.
The RPCs are organized in stations following a sequence similar to the DTs and CSCs. In the RPC barrel (RB) there are 4 stations, namely RB1, RB2, RB3 and RB4, while in the RPC endcap (RE) the 4 stations are RE1, RE2, RE3, and RE4. Six layers of RPCs are embedded in the barrel, two in each of the first two stations, and one in the last two stations. In the endcaps, each station is divided into three rings. Ring 1 was never instrumented, so the RPC system covers only the region up to $|\eta| = 1.6$.
Thanks to the redundancy in the first two stations, the trigger algorithm works even for low-p_{T} tracks that may stop before reaching the outer two stations. In the endcap region, each of the first three stations hosts a plane of RPCs in order for the trigger to use the coincidences between stations to reduce background, to improve the time resolution for bunch crossing identification, and to achieve a good p_{T} resolution [48].
Eventually, an alignment system measures the position of the muon detectors with respect to each other and to the inner tracker, and helps to optimize the muon momentum resolution.
To measure the position resolution of the RPC system, the coordinates of hits are extrapolated from DT and CSC track segments and compared with those of the reconstructed RPC hit. The hit position corresponds to the average coordinates of the strips fired by the muon. The RPC hit resolution depends on the strip width, the

cluster size and the alignment of the RPC chambers. The measured spatial resolutions lie between 0.8 and 1.3 cm. The cluster size measured in strip units decreases for increasing radial distance r from the beam line, following the increasing strip size. The time resolution of the RPC depends on a few factors. First, the intrinsic time resolution of the detector is known to be around 2 ns. Then, the time propagation along the strip contributes for another uncertainty of 2 ns. In addition, channel-by-channel differences generate a jitter on the order of 1-2 ns. The quadratic sum of these contributions gives an overall time resolution of ~ 3 ns. For muons with $p_{\mathrm{T}} > 10$ GeV the time of flight practically does not depends on the p_{T}, and does not give contributions to the time resolution [49].

4.6 Trigger system

4.6.1 Introduction

A sophisticated online event selection system is required to deal with a large number of minimum bias events (i.e. events triggered on minimum detector activity) per crossing, combined with small cross-sections of possible discovery signatures. In fact a collision rate of 40 MHz means that the aggregated data rate produced by CMS is about 100 GB/s [50]. The reduction of the data stream is achieved by the CMS trigger and DAQ system in two stages: The Level 1 trigger (L1) and the Higher Level Trigger system (HLT), as shown in Fig. 4.10. This section will first focus on the two layers of the CMS trigger system.

4.6.2 Level 1 trigger

The CMS L1 trigger has been designed to select proton-proton interactions whose final state includes signatures of new physics in the form of high transverse energy leptons, photons, jets, or high missing transverse energy. The L1 trigger system processes data in a pipeline fashion at a rate of 40 MHz; it has a design latency of 128 bunch crossings and an output rate of 100 kHz; the time latency is 3.2 μs. To perform the first level of online event selection, the current L1 is segmented in terms of detectors, as shown in the overview in Figure 4.11. The L1 trigger uses data from calorimeters and the muon system. Data are processed by the algorithms in pipeline fashion, using pattern recognition and fast summing techniques, without introducing dead-time. The algorithms use input data of reduced granularity and resolution. The calorimeters transmit energy sums, and data carrying information in order to characterise the origin of the energy deposition (electron/photon, tau, narrow jet, muon). Similarly, the muon system summarizes the hits in terms of track stubs. The

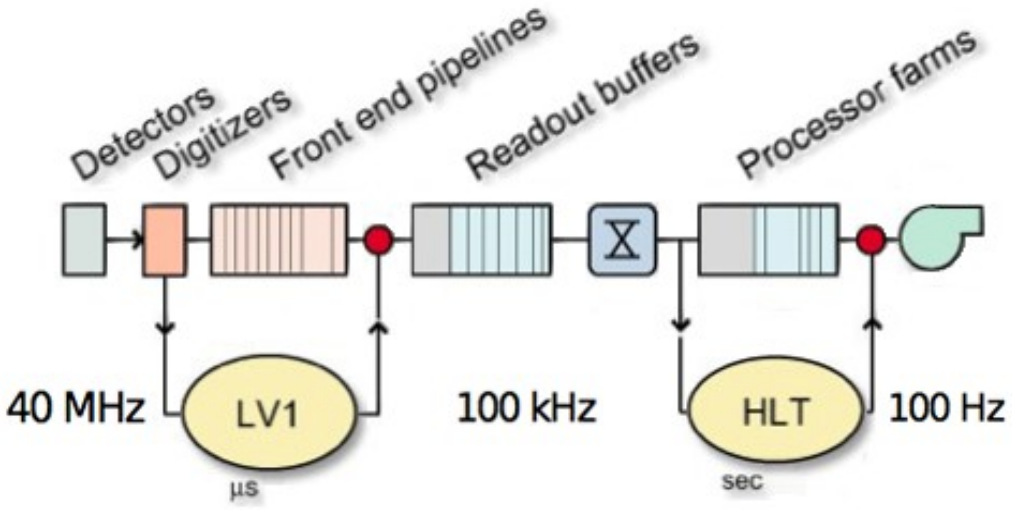

Fig. 4.10.: The CMS L1 trigger receives data from the calorimeter and the muon detectors and produces a yes/no decision a fixed number of crossings later. The delay is referred to as latency. Pipeline memories of depth equal to the trigger latency store the data on the detector until the L1 decision arrives. The HLT receives and processes complete events. The block diagram includes the data rates at each level [37].

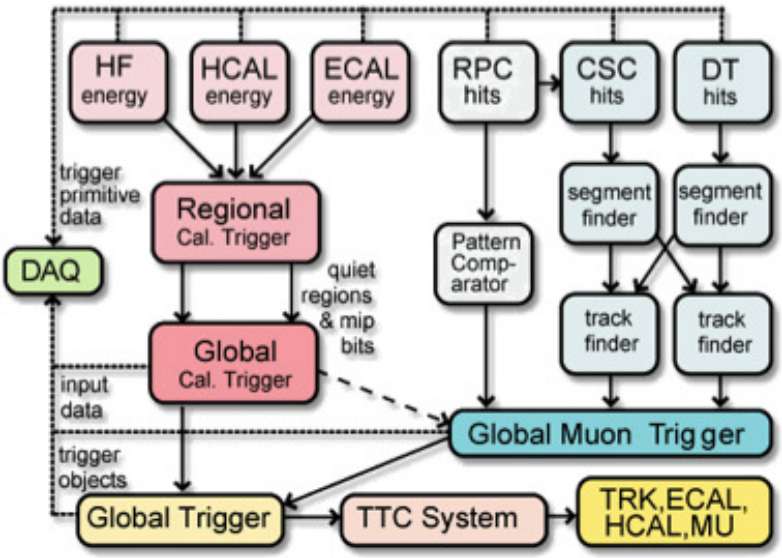

Fig. 4.11.: Overview of the current L1 Trigger System [37].

L1 output are quantities such as muon, electron, photon, tau and jet candidates along with jet counts and global transverse and missing transverse energy sums.
In this scheme, physics objects from different detectors can be combined only after arrival at the CMS Global Trigger. Thus, there is currently no possibility of combining information from different detectors to improve the performance of the L1 physics object reconstruction. Triggering at the first level is the most challenging part of the online data selection since it requires very fast custom designed electronics with a significant portion placed on the CMS detector. This introduces severe constraints in the front-end electronics design: among the rest, it must be radiation tolerant with limited power consumption. Lepton- and jet-finding algorithms run on large off-detector processors: their hardware is based on a mixture of discrete devices and FPGAs (Field Programmable Gate Arrays).

4.6.3 High Level Trigger

When a L1 accept occurs, data fragments from individual detectors are sent to the High Level Trigger (HLT), operating on a large computer farm of fast commercial processors, to build complete events. The algorithms have access to data from all CMS sub-detectors, including the tracker, with full granularity and resolution. The HLT reconstruction software is similar to what will eventually be used offline for CMS data analysis. Hence, the HLT algorithms, in contrast with the L1, calculate quantities with a resolution comparable to the final detector resolution. Information coming from different detectors can be combined at this stage. The HLT is then able to define its output objects very precisely and to significantly reduce background.
The HLT output quantities are similar to those of L1 but with far better resolution, purity and efficiency. Consistently with the L1 output, the maximum HLT input rate is 100 kHz and its output rate reaches 1 kHz. The reduced dataset collected for each event is about 1.5 MB, resulting in several hundreds of MB/s to be stored during each LHC run.

4.7 Overview of the upgrades

4.7.1 Introduction

In the first major physics run in 2011 and 2012, the LHC collider reached a peak luminosity of 7.7×10^{33} cm^{-2}s^{-1}, that is more than 75% of its design luminosity, and delivered an integrated luminosity of 30 fb^{-1} to each of its two general purpose experiments, ATLAS and CMS.
However, the LHC machine has a plan for achieving higher peak and integrated

luminosity, well above those for which CMS was designed. The CMS detector requires upgrades to preserve the efficiency, resolution, and background rejection of the detector at these high luminosities. The scientific goals now ahead of the LHC experiments concern precision Higgs studies and the search for new physics; both motivations bring indeed a powerful demand for higher luminosities.
A general schedule of the upgrades is presented in Sec. 4.7.2, while Sec. 4.7.3 shows the general challenges addressed by the Phase I upgrade plan. More specific sections are then devoted to the the upgrade plans for the main CMS detector systems and data acquisition system (Sec. 4.7.4 and 4.7.5).

4.7.2 Schedule of the upgrades

During Run 1 the LHC has delivered 30 fb^{-1} of data to CMS, since initiating collisions at $\sqrt{s} = 7$ TeV in early 2010. In 2012 the energy was raised to a new record of 4 TeV per beam, the instantaneous luminosity exceeded 7×10^{33} cm^{-2}s^{-1} and the average number of interactions per crossing, called pile-up, reached 21. In addition, CMS has collected 150 μb^{-1} of lead-lead and 31 nb^{-1} of proton-lead collisions.
The plans for the LHC luminosity upgrades are summarised in Fig. 4.12. The LHC is currently in the middle of its first cycle, called Phase I. The first long shutdown (LS1) has been closed and the LHC has already provided an energy in the center of mass $\sqrt{s} = 13$ TeV, on the way to the design energy of 14 TeV. The bunch-spacing has been reduced to 25 ns, the luminosity will reach the design value (10^{34} cm^{-2}s^{-1}) with 25 pile-up interactions, and the goal will be to integrate 100 fb^{-1} of pp data by the end of 2018. The second long shutdown (LS2) will take place starting from 2018 and will be used to upgrade the detectors for running at double the design luminosity and at an average pile-up of 50. The pixel detector will be replaced and the trigger upgraded during 2017 but CMS will utilize the present outer microstrip tracker throughout the Phase I period.
The next phase of planned LHC operation, referred to as the High Luminosity LHC (HL-LHC) or Phase II, will begin with the third long shutdown (LS3) in the period 2022-2023, where the machines and detectors will be upgraded to allow for pp running at a luminosity of 5×10^{34} cm^{-2}s^{-1} and an average pile-up of 140, with the goal of eventually accumulating 3000 fb^{-1} [51]. In particular, CMS will completely replace the tracking detector and will make many other changes to sub-detectors and the trigger and data acquisition systems [52].
The physics goals of the future LHC running in pp collisions are the following [53]:

- the properties of the scalar boson discovered in 2012 must be measured to the highest achievable precision, including the Higgs self-coupling, while additional Higgs bosons and exotic decays must be either found or excluded;

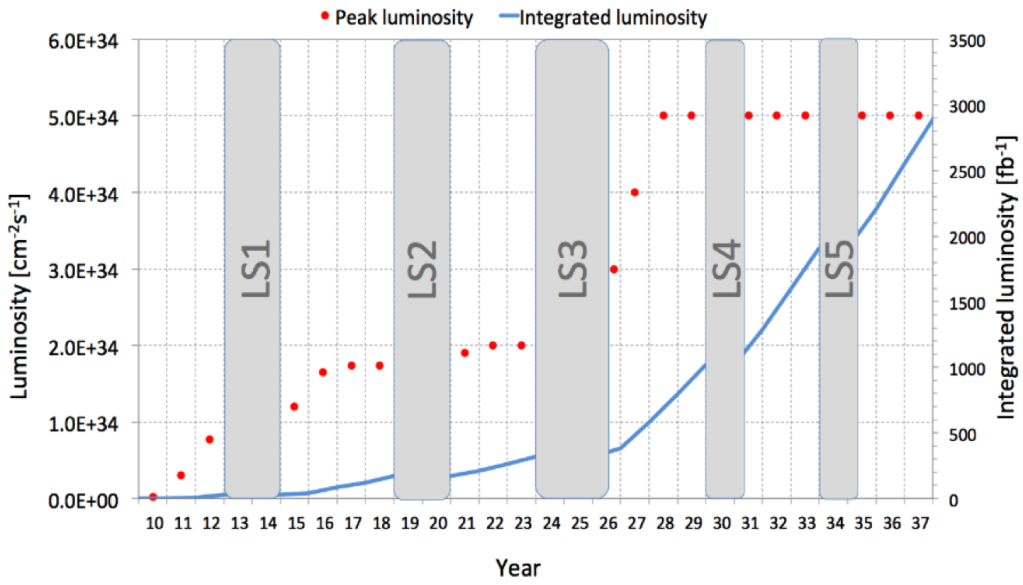

Fig. 4.12.: Projected LHC instantaneous and integrated luminosity as a function of time, throughout 2037. Preliminary dates for long-shutdowns (LS) are also indicated.

- the search for supersymmetric particles is intensified;
- the precision of top and electroweak measurements must continue to improve.

The CMS upgrades are designed to enable this physics by not only mitigating the effects of radiation damage and higher luminosity, but by maintaining the existing performance of the detector in key areas relative to the data taking at 13 TeV. The work foreseen involves muon detectors, hadron calorimeters, the pixel detector, the trigger and data acquisition, and the beam radiation monitoring and luminosity measurement system.

4.7.3 Challenges Addressed by the Phase I Upgrade Plan

At the end of the Phase I period, the peak luminosity is expected to exceed the design value by a factor of two. A series of problems must then be addressed to operate successfully throughout Phase I. A few challenges that the sub-detectors must face – mostly related with an high luminosity environment – will be listed hereby.

Collisions

Most of the interactions occurring in CMS are called “soft” or “peripheral”, as they are dominated by the non-perturbative regime: they do not make high mass states,

nor they are considered for the study of electroweak or beyond the standard model (BSM) physics. High mass states, that is "hard" collisions, are rarely produced. For successful analysis, the detector must discriminate with a sufficient efficiency between hard and soft collisions. The "pile-up" is the occurrence of many proton-proton interactions in a single crossing (typically 25). The presence of such pile-up makes the discrimination between types of collisions more difficult. The CMS L1 trigger performance will degrade at high luminosity. Upgrades to the muon system and the hadron calorimeters aim to preserve the L1 trigger capability.
When the pile-up occurs in the same crossing as the interesting triggered event, it is called "in-time pile-up". On the contrary, when there is signal contamination from preceding or following crossings, we speak of "out-of-time pile-up". This is caused by the intrinsic response of the sensor, or because the electronics takes longer than the 25 ns bunch crossing interval. The contamination is unlikely if the occupancy of a given channel is small: increasing the segmentation of a detector is therefore one way to counteract out-of-time pileup. To carry out more sophisticated time analysis is of course another way to proceed. Each of these tactics is employed in the proposed upgrades. Very slow particles, such as neutrons, can lead to out-of-time pile-up too.
Also integrated luminosity can affect the detectors resolution and efficiency. Ionizing radiations is one of the main sources of detectors damage. The development of radiation hard or radiation tolerant sensors and electronics was a major R&D effort for the LHC experiments. Most CMS detectors can sustain the integrated luminosity of Phase I with at most slight degradation. In two cases the replacement of damaged detectors will be necessary before Phase II: one is at the inner radius of the Forward Hadron Calorimeter (HF); the other is the replacement of the current 3-layer barrel (BPIX), 2-disk endcap (FPIX) system with a 4-layer barrel, 3-disk endcap system for four hit coverage.

Non-collisional background

There are also other phenomena or effects, not coming from the pp collision, that are a motivation for upgrade studies.

- beam halo: particles that migrate out of the beam and strike material such as a beam pipe or collimator and eventually produce muons that leave the LHC beam pipe and spread out. These particles are especially troublesome to large area systems such as the muon detectors.

- beam-gas interactions: protons in one of the beams can hit a residual gas molecule inside the vacuum pipe. The collision products may reach the detector

on a direct path or may strike other material producing more secondaries that eventually reach the detector.

- cosmic rays: cosmic rays are always passing through the detector. Occasionally, they will occur in time with a trigger and may be overlaid on the event and be recorded as part of the crossing data. Some may pass through the pixel detector and be close enough to beam spot to mimic genuine tracks from interactions.

- residual radiation: the particles passing through CMS can activate the elements of the detector producing various radionuclides. Their decay products may cause signals in some detectors.

4.7.4 Upgrades performed during LS1 on the muon system

Barrel Muon Drift Tubes

The work on the DTs is motivated by considerations about the lifetime of the experiment, and it includes the production of BTIM hybrid circuit, a device carrying four silicone-topped BTI ASICs (the front end barrel muon trigger device) bonded on a ceramic support. Eight BTIMs are placed on each Trigger Board (TRB). These devices suffer a high-mortality and the relocation of boards subject to radiation and high magnetic fields has been executed during LS1.
Also migrating to a more recent FPGA technology has optimized the production timescale to counter a spare TRBs crisis, and leaves space for possible modifications that may be needed for the future high luminosity operation. Once the migration to an FPGA is completed, its conversion to an ASIC can be reasonably fast.

Cathode Strip Chambers

The CSC upgrade finds its motivation in the safety of the muon trigger with respect to instantaneous luminosity. It includes the following:

- A fourth layer of chambers (ME4/2) was added during LS1. It helps reducing the accidental trigger rate and preserving a low p_{T} threshold expected at 30 GeV/c for the L1 muon trigger, as shown in Fig. 4.13. Without a proper measurement, low p_{T} muons contributing to the trigger rate cannot be eliminated with p_{T} cuts. Asking for three out of four stations to get a good momentum

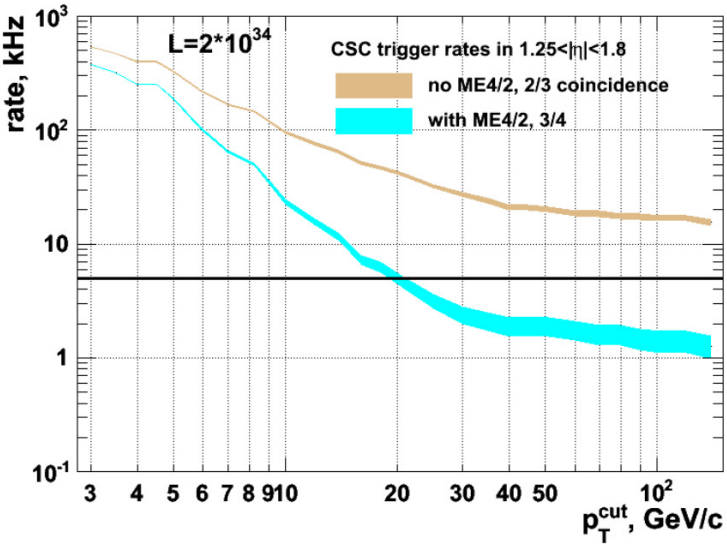

Fig. 4.13.: Simulation predictions for the contribution to the CSC inclusive muon trigger rate from the region $1.25 < |\eta| < 1.8$ as a function of trigger p_{T} threshold. The curves demonstrate that the CSC trigger performance critically depends on the ME4/2. The target single-muon trigger rate of 5 kHz is indicated by the horizontal line. With the upgraded ME4/2, the trigger p_{T} threshold can be maintained at 20 GeV/c, allowing for efficient triggering on W, Z, and top quark muonic decays. The W, Z, and top particles in turn are some of the best signals for Higgs, supersymmetric, and other sought-after particles [41].

measurement, it is possible to be both correct and efficient in identifying high-p_{T} muons in the trigger.

- Each strip of the ME1/1 station is now read independently, instead of being ganged into groups of three. This extends four-plane coverage of the region $2.1 < |\eta| < 2.5$.

- New muon trigger electronics has been deployed in view of the Phase I CSC Trigger Track-Finder upgrade to accomodate the new information from ME4/2 and ME1/1 [54].

From a physics perspective, not upgrading the current CSC system would have caused a dramatic decrease in the CMS acceptance in the range of $0.9 < |\eta| < 2.1$ for physics signatures with muons due to inefficiencies at increased luminosity and a complete shutdown of triggering capabilities in the region of $2.1 < |\eta| < 2.4$. Because muons are critical for most signatures of Higgs or new physics including supersymmetry, the CMS physics reach in those areas would have been severely diminished. Shutdown of the very forward region ($2.1 < |\eta| < 2.4$) would cause a substantial reduction in acceptance for signatures with one triggerable muon (e.g. SUSY, or $\mathrm{H} \to \tau\tau$ in the "golden" muon plus hadronic tau channel) and diminished acceptance

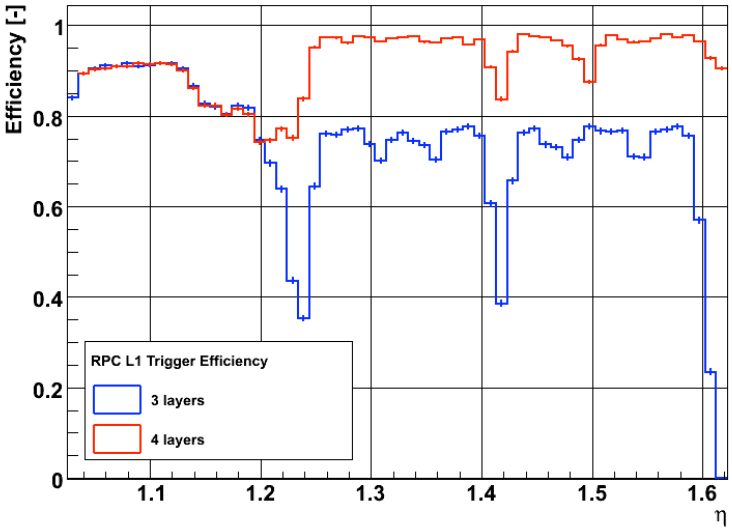

Fig. 4.14.: Simulated trigger efficiency as a function of η for different numbers of RPC layers [41].

for two-muon signatures (important channels occurring in the high $|\eta|$ region are discussed in Sec. 5.2). The very forward region is also critical for the measurement of $\sin^2\theta_{\text{eff}}$ [55] and PDFs using forward-backward asymmetry A_{FB} in Drell-Yan events [56] (the forward-backward asymmetry measurement will be discussed in detail in Sec. 7.2). Accurate knowledge of PDFs plays a key role in predicting Standard Model backgrounds in searches for new physics. Today's technologies allow us to remove these deficiencies and provide robust muon triggering and reconstruction up to $|\eta| = 2.4$.

Endcap Resistive Plate Chambers

In the original CMS project four RPC layers were foreseen in total for the endcaps, but due to insufficient funding availability, only 3 layers were built in the endcap which provided a limited rapidity coverage up to $|\eta| = 1.6$.
The upgrade on RPCs was led by motivations similar to those of the CSCs, that is the preparation to the impact of a high instantaneous luminosity. CMS has decided to split the upgrade project into two distinct phases:

- Phase I: completion of the low $|\eta|$ part ($|\eta| < 1.6$)
- Phase II: completion of the high $|\eta|$ part ($1.6 < |\eta| < 2.1$)

The coverage up to $|\eta| = 1.6$ has consisted in the addition of a fourth layer of RPC called RE4, which is now able to provide the finer timing and redundancy to the

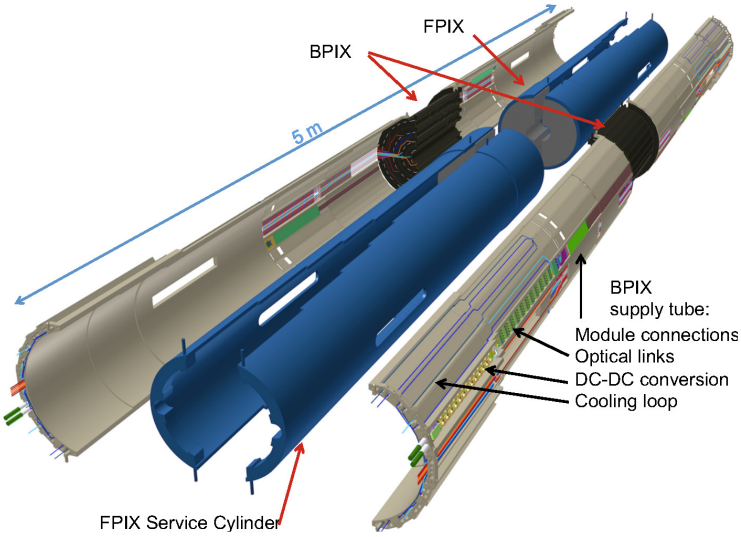

Fig. 4.15.: Exploded view of the upgraded pixel detector. The figure shows the positions of the different partitions FPIX and BPIX and their respective service cylinders. The necessary services, namely connections, optical links and DC-DC converters are located at high $|\eta|$ regions outside the tracking volume [58].

corresponding CSC station, and preserves a low p_{T} threshold. In Fig. 4.14 the simulated trigger efficiency as a function of $|\eta$ is shown in case of the present 3 layers and compared to the result for a 4-layer system. The advantage in extending the detector to include the fourth station is clearly evident. RE4 has been installed on the back of the YE3 yoke during LS1 [57], mounted independently of the CSC chambers.

4.7.5 Upgrades expected for the technical stop, LS2, and LS3

Tracker system upgrades

The pixel detector is a crucial component of the all-silicon CMS tracker. The upgrade plans aim to replace the present system with a four-layers/three-disks, low mass silicon pixel tracker capable of delivering high performance tracking in the high luminosity environment (up to 2×10^{34} cm^{-2}s^{-1}) of the LHC through LS3 [58]. The replacement will take place during the year-end technical stop of 2016/2017. In this way, CMS will profit from the LHC enhancement before the occurrence of LS2, thus maximizing the physics discovery potential.
A view of the upgraded four-layer pixel detector can be seen in Fig. 4.15. The upgrade is led by the following design choices, requirements and constraints:

- In running with 50 or more pile-up, to maintain the high efficiencies and low fake rates of the current pixel detector which is operating in relatively low pile-up;

- New pixel readout chip (ROC) to minimize data loss due to latencies and limited buffering in high luminosity running;

- Minimize degradation due to radiation damage;

- Optimized detector layout for 4-pixel-hit coverage over the η range with minimal innermost layer radius improving pattern recognition and track reconstruction;

- To reduce material, adopt two-phase CO_2 cooling and light-weight mechanical support, moving the electronic boards and connections out of the tracking volume;

- To reuse the current patch panel and off-detector services, cooling pipes, cables and fibres, adopt DC-DC power converters and higher bandwidth electronics;

- Reduce number of module types and interfaces simplifying production and maintenance;

- New smaller diameter beam pipe to accommodate the placement of the inner pixel layer closer to the interaction region.

The tracker must be completely replaced for Phase II. In fact, it will suffer significant radiation damage by LS3. The granularity of both the outer tracker and the pixel systems will be increased by a factor 4. In the outer tracker, the lengths of silicon sensor strips will be shortened without modifying the pitch. Design improvements will lead to a much lighter outer tracker, improving therefore the p_{T} resolution and providing a lower rate of γ-conversions. Moreover, the module design will provide track-stub information to the L1 trigger at 40 MHz for tracks with $p_{\mathrm{T}} > 2$ GeV/c, ensuring meaningful power rejection at the earliest stage of the event selection. The pixel system will implement smaller pixels and thinner sensors for improved impact parameter resolution and better two-track separation. The system coverage will be extended to almost $|\eta| = 4$, thanks to the addition of up to 10 additional pixel disks in each of the forward regions.

Calorimeter upgrades

The hadron calorimeter upgrade for Phase I is separated into two portions, one which applies to the HF and the other to the HB and HE calorimeters.

- Maintaining the design performance of the HF calorimeter in the presence of high-pileup is important for the CMS physics program [59]. Thanks to its large $|\eta|$ coverage, it plays an important role in identifying forward jets (important for Higgs boson coupling measurements), determining missing transverse energy (for BSM searches), and measuring the luminosity.
  The HF calorimeter uses Photomultiplier Tubes (PMTs) to collect the light from the quartz fibres. The replacement of the model of the PMTs will reduce the rate of anomalous signals, as rejection techniques are ineffective during operation at 25 ns bunch spacing. Other benefits are possible using the multi-anode output of the PMTs. Another important capability brought by the upgrade will be a TDC capability in the ADC chip.

- The HB and HE detectors used Hybrid Photodiode transducers (HPDs) which were chosen for their magnetic field tolerance and gain greater than 2×10^3. However the high voltage applied to these devices led to electrical discharges, which are a source of high-amplitude noise and a risk to the longevity of the phototransducers. The ideal replacement for the HPD is the Silicon Photomultiplier (SiPM).
  The SiPM is a multipixel Geiger-mode Avalanche Photodiode (APD) device which provides gains between 10^4 and 10^6 using an applied voltage less than 100 V and photon detection efficiencies in the range of 20% to 40%. The high performance of the SiPM devices, coupled with recent developments in data link technology, will allow a significant increase in depth segmentation in the HB and HE calorimeters. This segmentation will allow better tracking of hadronic shower development and better management of the radiation damage which will occur in the high-η region of the HE calorimeter, reducing the response of the individual tiles [53].

The electromagnetic and hadronic endcap calorimeters must be replaced as they will suffer radiation damage by LS3. The replacement is called the High Granularity Calorimeter (HGC). It includes excellent transverse and longitudinal segmentation, allowing detailed three dimensional images of showers. The sensors of the electromagnetic section have pads of variables sizes of less than 1.0 cm^2. This section has $25\ X_0$ and one hadron interaction length (λ). The hadronic part has a depth of 3.5λ, covering the hadronic shower maximum measurement. Thanks to the addition of a

"backing hadron calorimeter" of similar design to the current HE detector, the full calorimeter can reach an overall depth of $\sim 10\lambda$.

Muon system

In the region $1.5 < |\eta| < 2.4$ the muon system currently consists of four stations of Cathode Strip Chambers (CSC), as specified above. It is the only region of the muon detector that lacks redundant coverage despite being a challenging region for muons in terms of backgrounds and momentum resolution. To maintain good L1 muon trigger acceptance in this region it is therefore proposed to enhance these four stations with additional chambers that make use of new detector technologies with higher rate capability, as originally proposed by the design of CMS. The two first stations are in a region where the magnetic field is still reasonably high. Therefore, it has been chosen to install Gas Electron Multiplier (GEM) in the GE1/1 during LS2 to ensure good position resolution in order to improve momentum resolution for the standalone muon trigger and to improve the matching with tracks in the global muon trigger. Another muon station, named GE2/1, will be equipped during LS3 with GEM detectors similar to the ones in GE1/1. As anticipated, the two last stations will use low-resistivity Resistive Plate Chambers (RPC) with lower granularity but good timing resolution to mitigate background effects. In addition, plans concerning Phase II foresee the implementation of a GEM station called ME0 in the space that becomes free behind the new endcap calorimeters is being proposed in order to increase the coverage for muon detection to $|\eta| \approx 3$. Details about GEMs research, development and installation are provided throughout Chapter 5.

Trigger upgrades

Due to the increased detector occupancy at each beam crossing, toward the end of Phase I of the LHC when the luminosity will reach 2×10^{34} cm^{-2} s^{-1}, the L1 trigger systems will experience degraded performance of the algorithms presently planned to select 100 kHz of crossings from the input rate of 40 MHz (25 ns bunch spacing). The modifications proposed for the L1 Trigger systems for Phase I must deliver the L1A signal within the same time period of 3.2 μm as the present L1 Trigger systems since there is no possibility to increase this time until the present CMS tracker is replaced as part of Phase II [60].
Maintaining a 100 kHz L1 rate during Phase I operations will increase the burden on the DAQ, which will need to transport more than the LHC design luminosity data size of about 1 MB per event.

To compensate for problems caused by high event occupancy the new calorimeter trigger upgrade design must significantly improve the efficiency and rejection ability of the L1 trigger algorithms. This is done by:

- Increasing the granularity of the calorimeter trigger internal processing. The design of the upgrade calorimeter trigger completely exploits the full granularity of the ECAL and HCAL trigger towers in its calculations which enables improved algorithms that assure good performance up to twice the design luminosity or occupancy.

- Using the greatly increased flexible processing power in the new generation of FPGAs to implement sophisticated cluster algorithms that exploit the full trigger tower granularity.

- Using state-of-the-art micro-TCA (μTCA) Telecom technology [61] to support the increased bandwidth requirements imposed by the higher granularity of the trigger input data.

- Providing the option to further exploit the higher granularity for eventual matching with a L1 Tracking trigger in Phase II.

The muon trigger is a tracking trigger that measures the momentum of muons using the magnetic field in the steel yoke of the CMS solenoid; thus its resolution degrades with increasing momentum. The focus of the muon trigger upgrade is to improve its rate reduction capability without significantly affecting the efficiency.
The upgrade to the muon trigger will utilize the redundancy of the three muon detection systems earlier in the trigger processing chain so as to obtain a more performant trigger with higher efficiency and better rate reduction. The upgrade seeks to combine muon hits at the input stage to the Muon Track-Finder layer rather than at its output. This new Muon Track-Finder will ultimately replace the separate track-finders for DT and CSC muon triggers as well as the RPC pattern comparator trigger.
However, in addition to combining data from multiple muon systems in the same processors, more robust and sophisticated algorithms will be applied that are tolerant of the increased pile-up and make better use of the data from each muon system in the track-finding and p_{T} measurement. The entire muon trigger upgrade was commissioned during the 2015-16 Year-End Technical Stop, so the new trigger is now available for data-taking.

The CMS Upgrade Phase II Trigger R&D centers on two key components. The first one is the addition of a L1 tracking trigger for identification of tracks associated with calorimeter and muon trigger objects at L1. The second R&D focus point is to study

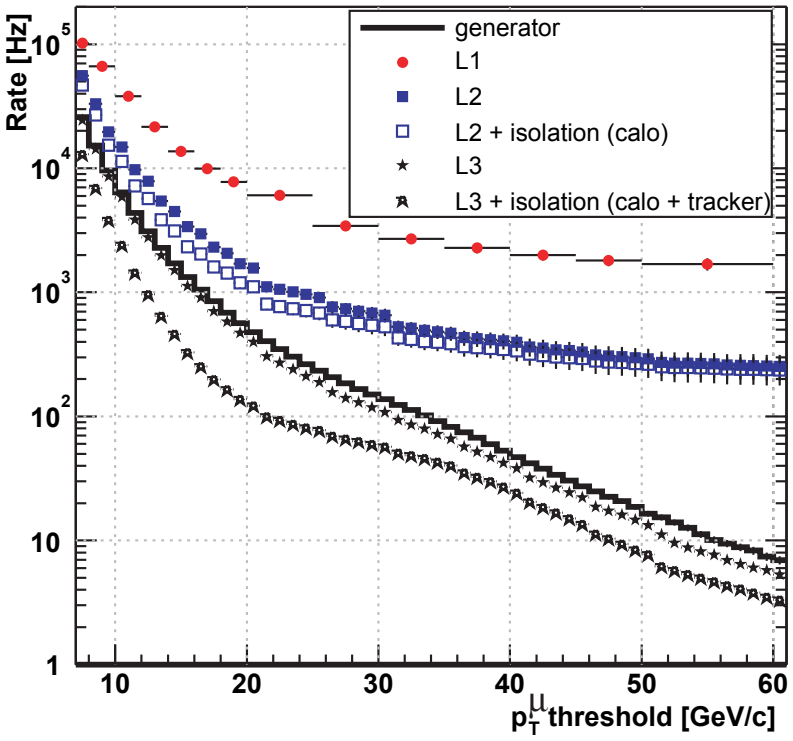

Fig. 4.16.: The HLT single-muon trigger rates as a function of the p_T threshold for a luminosity of 10^{34} cm^{-2} s^{-1}. The rates are shown separately for Level-1, Level-2, and Level-3, with and without isolation applied at Levels 2 and 3. The rate generated in the simulation is also shown [62].

the option of a significant increase of L1 rate, L1 latency and HLT output rate.

The single muon trigger rates as a function of the p_T threshold are shown in Fig. 4.16 for LHC design luminosity (10^{34} cm^{-2} s^{-1}). The rates are shown separately for L1 (L1 Trigger information only), Level-2 (HLT reconstruction using full-resolution muon system data only, with isolation calculated from full-resolution calorimeter data), and Level-3 (HLT track momentum and isolation calculated from silicon strip and pixel tracking data), with and without isolation applied at Levels 2 and 3. Also shown is the single muon rate predicted by the event generator. A threshold of 31 GeV/c reduces the single-muon Level-3 rate to 50 Hz with isolation (100 Hz without isolation).

For the Phase II upgrade it is planned to use track information at L1 and to combine it with the L1 calorimeter and L1 muon objects, similarly to the current implementation at HLT level.

Moreover, to enable the triggering on important hadronic objects in Phase II, the latency will be increased to 12.5 μs (compared to the current 3.2 μs and the ECAL-imposed limit of 6 μs if the tracking detectors are replaced) to provide sufficient time for the hardware track reconstruction and matching of tracks to muons and calorimeter information. The proposed L1-trigger acceptance rate is 500 kHz (compared to the current 100 kHz) for beam conditions yielding 140 PU, allowing comparable thresholds to those that will be used in a typical Phase-I trigger menu. To maintain

	LHC Run 1	LHC Phase I upgr.	HL-LHC Phase II upgr.	
Energy	7-8 TeV	13 TeV	14 TeV	
Peak Pile Up (av./crossing)	35	50	140	200
Level 1 accept rate (maximum)	100 kHz	100 kHz	500 kHz	750 kHz
Event size (design value)	1 MB	1.5 MB	4.5 MB	5.0 MB
HLT accept rate	1 kHz	1 kHz	5 kHz	7.5 kHz
HLT computing power	0.21 MHS06	0.42 MHS06	5.0 MHS06	11 MHS06
Storage throughput (design value)	2 GB/s	3 GB/s	27 GB/s	42 GB/s

Tab. 4.3.: DAQ/HLT system parameters.

comparable performance for 200 PU, the L1 rate must increase to 750 kHz. Any further increase would require an increase of the Pixel readout bandwidth.

The HLT farm currently contains processing power to handle 50% of the maximal data volume expected at 10^{34} cm^{-2}s^{-1}. The maximal first level trigger rate is 100 kHz, and will stay in all upgrade scenarios until the end of Phase I. Since the DAQ system has been designed under the assumption that the event size would be $\sim$ 1 MB, it follows that it is capable of building events at 100 GB/s. The HLT in Phase II will have to process an input rate of 500 kHz to 750 kHz, a factor 5 to 7.5 higher than in the present design. At the same time, it is proposed to increase the average output rate to the permanent storage by the same amount, to 5 kHz for 140 pileup events and 7.5 kHz for operation at 200 pileup events. These figures come from the increased L1 input rate, the increased event complexity due to the higher pileup conditions than the 2012 run, and the higher center-of-mass energy. CMS has adapted its framework to achieve event-level parallelism already at the beginning of Run 2, and algorithm-level parallelism in the following years.

During LS2 the HCAL system will replace their Front End Drivers (FEDs) with state of the art μTCA based FEDs. They are capable of delivering up to eight times more data than the current FEDs. The same will happen for the trigger system.
For an LHC operation at nominal energy, an enhancement of a factor 2 in the HLT processing power with respect to the pre-LS1 period is needed in order to deal with the expected data volume at 100 kHz. During LS1 the processing power of the HLT farm was indeed increased by a factor of 3 (taking into account some safety factor). The output rate will increase to 5 (7.5) kHz (compared to the current 0.5 to 1 kHz), for scenarios with PU 140 (200). The main parameters of the DAQ/HLT systems for Phase II, in comparison with the current system are summarized in Tab. 4.3.

4.8 Conclusions

In this Chapter a rather detailed presentation of CMS was provided. All detectors subsystems were introduced, from the inside out of the concentric structure of the experiment: the tracker, the calorimeters and the muon system. For every subsystem Section, an overview of the upgrade programs for Run 3 and even Phase II is included. One of the most relevant omissions concerns the in-depth description of the Muon Upgrade at high η, which foresees the addition of a new kind of detector technology in CMS: the Gas Electron Multiplier. Its ultimate goal is to guarantee at high η a performance in the muon detection at least as good as the one provided by Run 1, but at much harsher conditions of luminosity. Indeed, the next Chapter is entirely dedicated to the presentation and the status of this project.

5 GEM Upgrade Project

5.1 Introduction

Among the endcap region upgrades commissioned to sustain Phase II luminosity ($\sim\ 7.5 \times 10^{34}$ cm^{-2} s^{-1}) already discussed in Section 4.7.5, the one that is at the core of this thesis is the installation of an additional set of muon detectors, in the vacant $1.6 < |\eta| < 2.2$ region of the present RPC endcap system. In fact, during the CMS commissioning and construction, several concerns were raised on whether RPCs would be able to sustain the very hostile environment of the high $|\eta|$ region; it was decided not to instrument this area at all. A dedicated R&D program was launched in 2009 to study the feasibility of using micro-pattern gaseous detectors (MPGD), as this class of detectors can offer a spatial resolution of $\sim\ 100$ μm, a time resolution below 5 ns, a good overall detector efficiency above 98% and a rate capability of the order of 10^6 Hz/mm^2 (see Fig. 5.1).

Studies of characterization on 10×10 cm^2 MPGD prototypes [**2010arXiv1012.3675A**] have shown that the Micromegas [64] have a discharge probability of 10^{-4} per ionizing particle at a gain of less than 2000, and as a consequence a poor data quality, consistently with previous studies. The same discharge probability for the Triple Gas Electron Multiplier (GEM) prototype was 10^{-6} for gains up to $2 \cdot 10^4$. The GEM technology was then selected for further studies.
The station targeted for the upgrade instrumentation is set in the first endcap muon station, in order to maintain or even improve the forward muon triggering and reconstruction in that area. This muon station is called GE1/1, as G indicates the GEM technology, the letter E that this is an endcap muon station, the first "1" that it is part of the first muon station, and the second "1" that it is the first ring of muon chambers going outward in radius from the beam line.
The content of this chapter is partly based on the Technical Design Report produced by the CMS GEM Collaboration in view of the GE1/1 LS2 upgrade [65]. Other sources are specified throughout.
The physical and technical motivations that led to the proposal of instrumenting the RPC station in the range $1.6 < |\eta| < 2.2$ with Triple GEMs are detailed in Section 5.2. Then, Section 5.3 reports an overview of the detection principles that rule the GEM technology. It is followed by Section 5.4 that presents the needed requirements asked to the GEM chambers in the GE1/1 station to sustain the hostile CMS environment

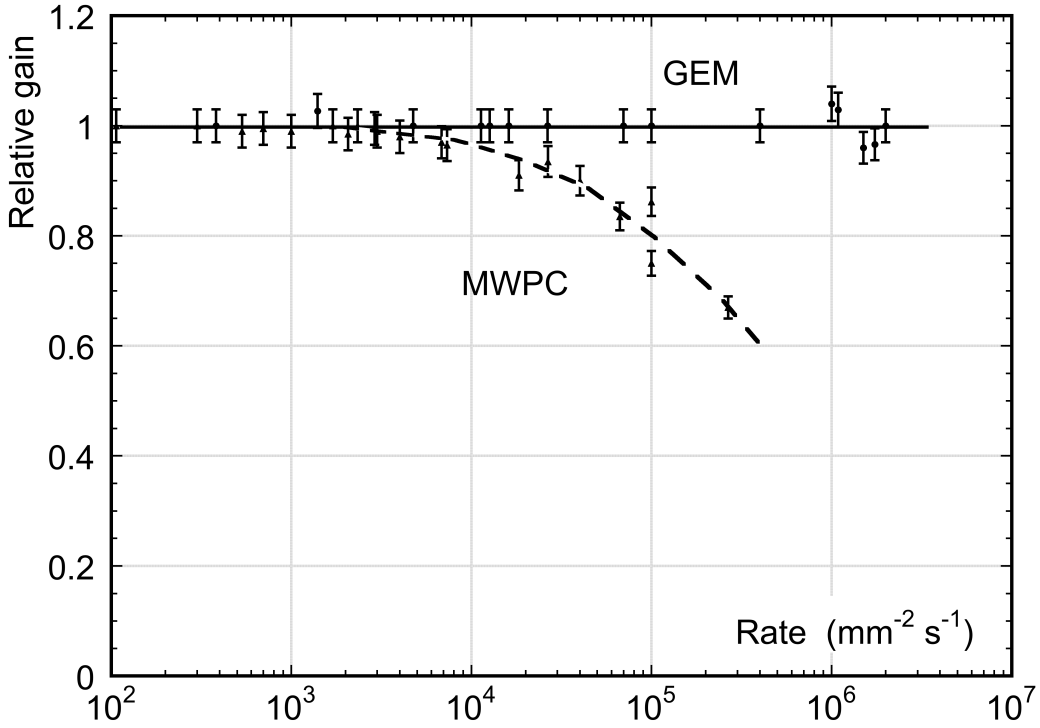

Fig. 5.1.: Normalized gas gain as a function of particle rate for MWPC and GEM [63].

in that area, to achieve redundancy at high $|\eta|$, and to guarantee a high reliability in triggering and tracking tasks. GE1/1 prototyping results obtained in the latest years are then summarised in Section 5.5. Eventually a brief overview on the GEM upgrades foreseen for LS3 and beyond is given in Section 5.6.

5.2 Motivations for the GE1/1 muon detector upgrade

The GE1/1 muon detector station is shown in the quadrant cross-section of CMS in Fig. 5.2. This station has tight geometrical constraints, due to the original CMS conception involving forward RPCs. GEM detectors are sufficiently compact and thin to respect these limitations. In addition to the needed profile, GEMs have the ability to operate at particle fluxes far above those expected in the forward region under HL-LHC conditions. Muon triggers simulations show that to keep a reasonable efficiency for muons with $p_{\mathrm{T}} < 25$ GeV/c already after LS2 implies unacceptable L1 trigger rate (see Fig. 5.4). This is the reason why the collaboration will not wait until Phase II to install the GEMs in the station. The L1 muon trigger will in fact benefit from the early installation of the GE1/1 station, before the installation of a new silicon tracker and its associated track trigger in LS3.
The contribution to the trigger rate within the GE1/1 coverage is very large – it accounts for ~ 6 kHz at a L1 p_{T} threshold of 20 GeV/c – and difficult to control, as the background rates increase with $|\eta|$. A positive impact of this additional chamber

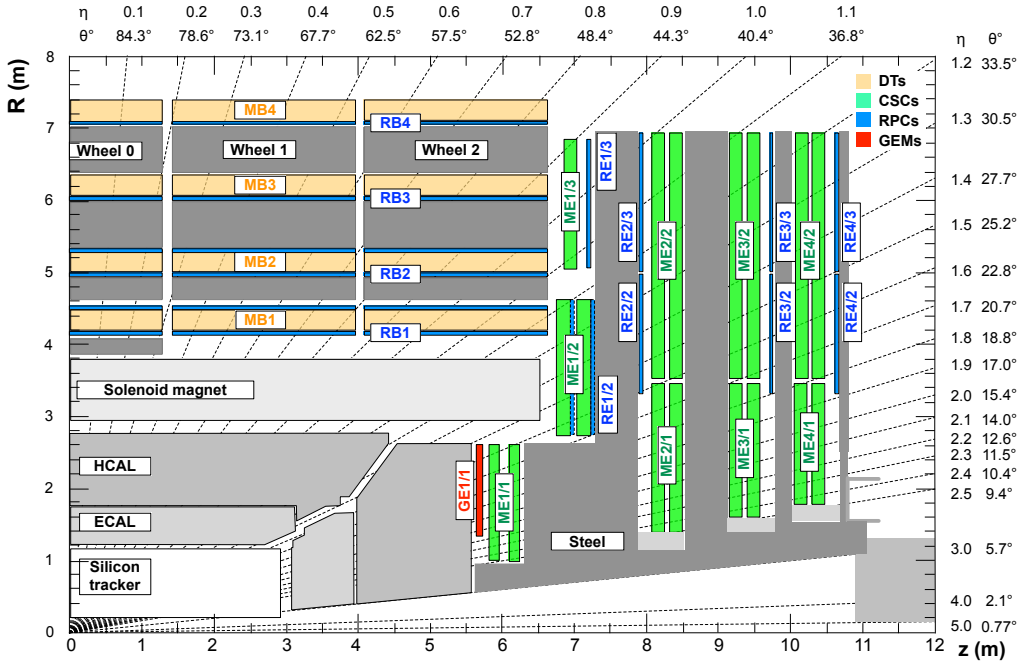

Fig. 5.2.: A quadrant of the $R - z$ cross-section of the CMS detector, highlighting in red the location of the proposed GE1/1 detector within the CMS muon system.

is that at the position of the first muon station the bending of the muons is the largest, and the GE1/1 chambers multiply by a factor of $2.4 - 3.5$ the path length traversed by muons over that of the 6 layers of the ME1/1 CSC chambers alone (11.7 cm), as shown in Fig. 5.3. This increased path improves the L1 stand-alone muon trigger momentum resolution, reducing its large contribution to the overall L1 muon trigger rate. Fig. 5.4 shows the improvement of the single muon trigger rate curves for the region $1.6 < |\eta| < 2.2$, before and after the GE1/1 upgrade.

The reason to keep low p_{T} values is to maintain high efficiencies for capturing physics processes featuring soft leptons. The upgrade will allow for instance to preserve a L1 single muon trigger threshold at $12 - 14$ GeV/c providing nearly full efficiency for offline muons with $p_{\mathrm{T}} > 18 - 20$ GeV/c. These physics processes range from new physics searches to measurements in the Higgs sector. In fact, the lowering of thresholds is possible not only for the inclusive L1 muon trigger, but also for the multi-object triggers involving muons in their selections. Striking examples are the studies of the Higgs coupling to the third generation leptons via $\mathrm{H} \to \tau^{+}\tau^{-}$. Among the various decay channels, the semileptonic $\tau\tau \to \mu\tau_h + X$ channel (where τ_h indicates a τ decaying hadronically) is especially considered due to its large branching fraction and clean signal, as long as these events can be efficiently triggered given the low average lepton p_{T}. In fact, most of the charged leptons being the decay product of a Higgs boson have a low p_{T}, and this is especially true for τ's (or for μ's coming from τ's), as a fraction of τ's energy converts in MET: there are two ν's per leptonic decay, and one per hadronic decay. During the analysis on Run 1 data the choice of

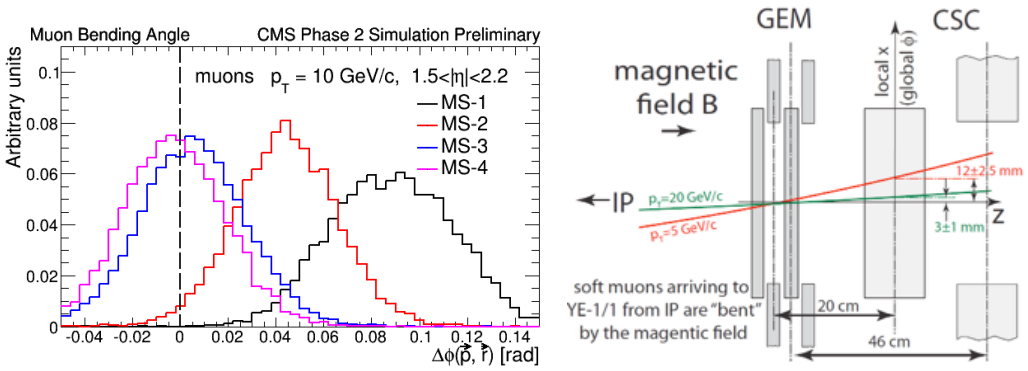

Fig. 5.3.: Left: Azimuthal bending angle of a simulated muon having a $p_{\mathrm{T}} = 10$ GeV/c with respect to normal vector to a CSC chamber, comparing the distributions for the four stations. Right: Sketch of a measurement of the bending angle with a pair of a CSC and a GEM chamber, showing discrimination between lower and higher momentum muons.

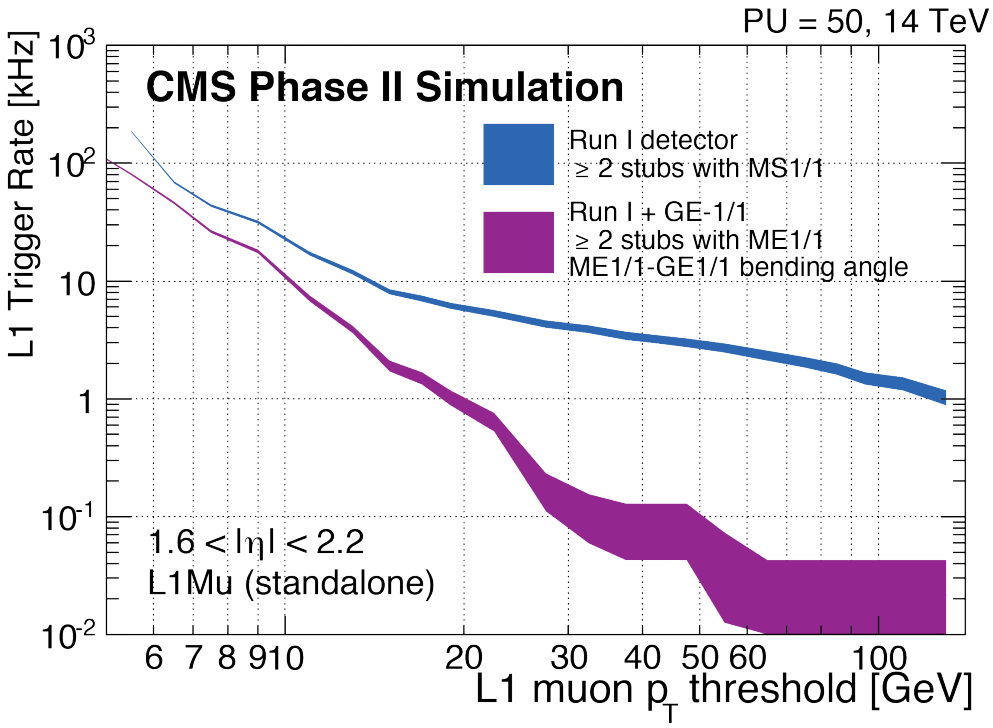

Fig. 5.4.: Level 1 muon trigger rates before and after the GE1/1 upgrade at a luminosity of 2×10^{34} cm^{-2} s^{-1}, for a constant efficiency of 94%. MS1/1 denotes the first endcap muon station Level 1 trigger in both cases, i.e. with CSC-only or with the combination CSC and GEM trigger information. With the addition of GE1/1, the bending angle between the two stations can be used and the trigger rate is reduced.

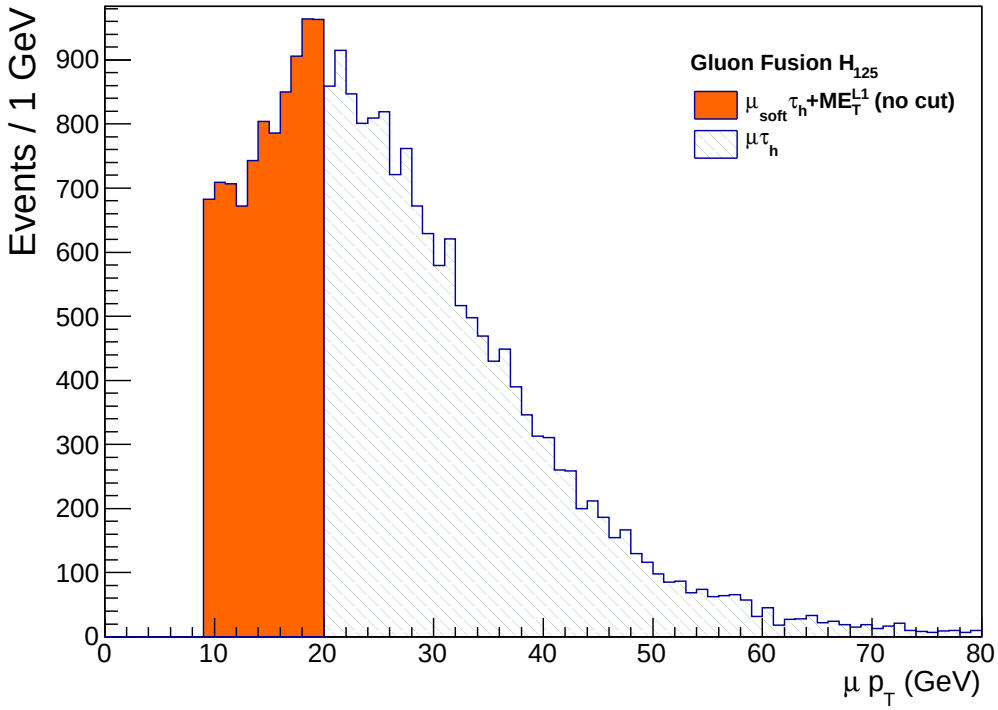

Fig. 5.5.: Distribution of muon's transverse momentum in a simulated sample of gluon fusion producing a Higgs boson with a mass of 125 GeV/c^2 without any cut in the missing transverse energy (MET). The orange area shows the region of the $\mu_{\text{soft}}\tau_h$ channel and the blue histogram represents the $\mu\tau_h$ channel region (above 20 GeV/c) [66].

the $\ell\tau_h$ pair implied of course cuts in the p_T distribution, among other identification and isolation cuts [66]. In the $\mu\tau_h$ channel, the requirement was $p_{\text{T}}(\mu) > 20$ GeV/c, and in the $\mu_{\text{soft}}\tau_h$ one it was $9 < p_{\text{T}}(\mu) < 20$ GeV/c. Fig. 5.5 shows how sensitive to the p_{T} cut is the $\mu_{\text{soft}}\tau_h$ channel: the possibility to lower the threshold down to 9 GeV/c increases indeed the signal acceptance by 57%. Successive data runs will need to rise the p_{T} cut in order to cope with increased luminosity. Simulations in which the Higgs boson is produced via Vector Boson Fusion (VBF) were generated at $\sqrt{s} = 14$ TeV. The effect on the signal acceptance is evaluated by varying the muon p_{T} threshold used in analysis selections in the range $5 < p_{\text{T}}(\mu) < 60$ GeV/c. Fig. 5.6 (left) shows the distribution for the reconstructed visible mass of the $\mu + \tau +$ MET system for $p_{\text{T}}(\mu)$ threshold of 15, 20 and 25 GeV/c. The results show that $\text{H} \rightarrow \tau_\mu\tau_h$ events increase their acceptance by 35% if the muon p_{T} threshold is lowered from 25 to 20 GeV/c, and an overall 68% increase if the thresholds are reduced from 25 GeV/c down to 15 GeV/c. The statistics populating the signal is limited even in a Phase II scenario, and this underlines the importance of maintaining the largest possible acceptance.

The new silicon tracker and the track trigger will be installed during LS3. This upgrade will lead to a "combined muon trigger", that is the coincidence of these

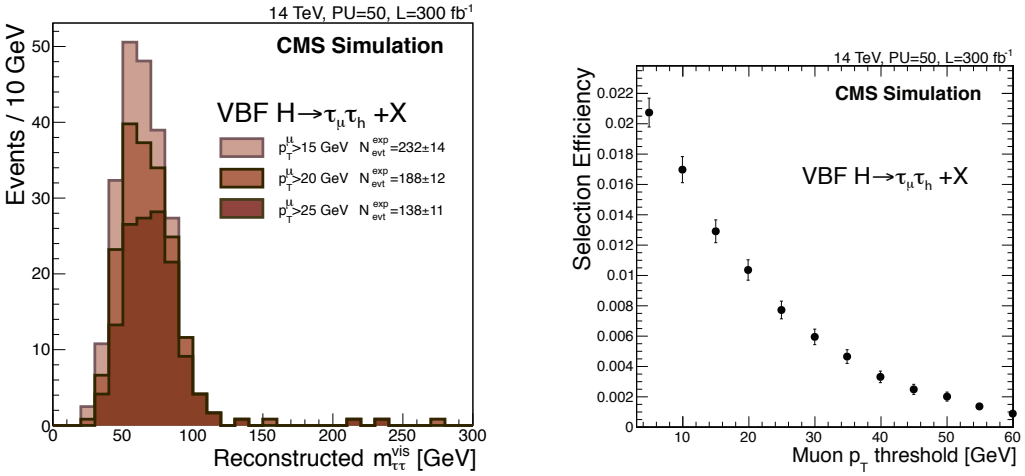

Fig. 5.6.: Left: distribution of the visible mass of the μ, τ_h, MET system for events surviving all analysis selections for the $H \rightarrow \tau\tau$ search in the VBF category in the $\mu\tau_h$ final state. The three distributions correspond to a sample with 300 fb^{-1} and the offline muon p_{T} threshold set to 15, 20 and 25 GeV/c. Right: full $H \rightarrow \tau\tau$ analysis selection efficiency for the $\mu\tau_h$ VBF category as a function of the chosen offline muon p_{T} threshold [65].

devices with the L1 muon trigger: the momentum resolution for most muons from primary event vertex will then be set by the very high resolution achieved by the track trigger. The new combined trigger object is called L1TkMu. The excellent momentum resolution of the tracker will eliminate the flattening of trigger-rate curve owing to mismeasured low-p_{T} muons. The muon stations will help maintaining excellent position matching with the track trigger. Nevertheless, the stand-alone muon trigger (L1Mu) will continue to be used for displaced muons and exotic particles; it will run in parallel with the combined muon trigger, to act as a backup to guarantee the highest possible muon trigger efficiency, but will be set at a higher p_{T} threshold. The importance of L1Mu will keep its importance during the HL-LHC runs, especially, as anticipated above, if one considers the sensitivity to scenarios of new physics predicting displaced muons arising from decays of new particles with finite lifetime. L1Mu is the only viable option to trigger tracks produced away from the beam spot, as the tracking trigger efficiency vanishes in those cases. The high occupancy environment of the HL-LHC is the main responsible for this difficulty.
The sensitivity of L1Mu to signatures with displaced leptons is illustrated by a SUSY theory with hidden sectors, in which the following reaction occurs:

$$h \rightarrow 2n_1 \rightarrow 2n_d\gamma_d, \tag{5.1}$$

where h is a SM-like Higgs boson with mass of 125 GeV/c^2 decaying into pairs of neutralinos n_1 and a dark photon of mass $m(\gamma_d) = 0.4$ GeV/c^2. The light γ_d decays into a collimated pair of muons produced away from the beamline and approximately pointing back at the beamspot. Fig. 5.7 compares the performance of L1TrkMu and L1Mu algorithms in reconstructing at least one of the muons with no p_{T} thresholds

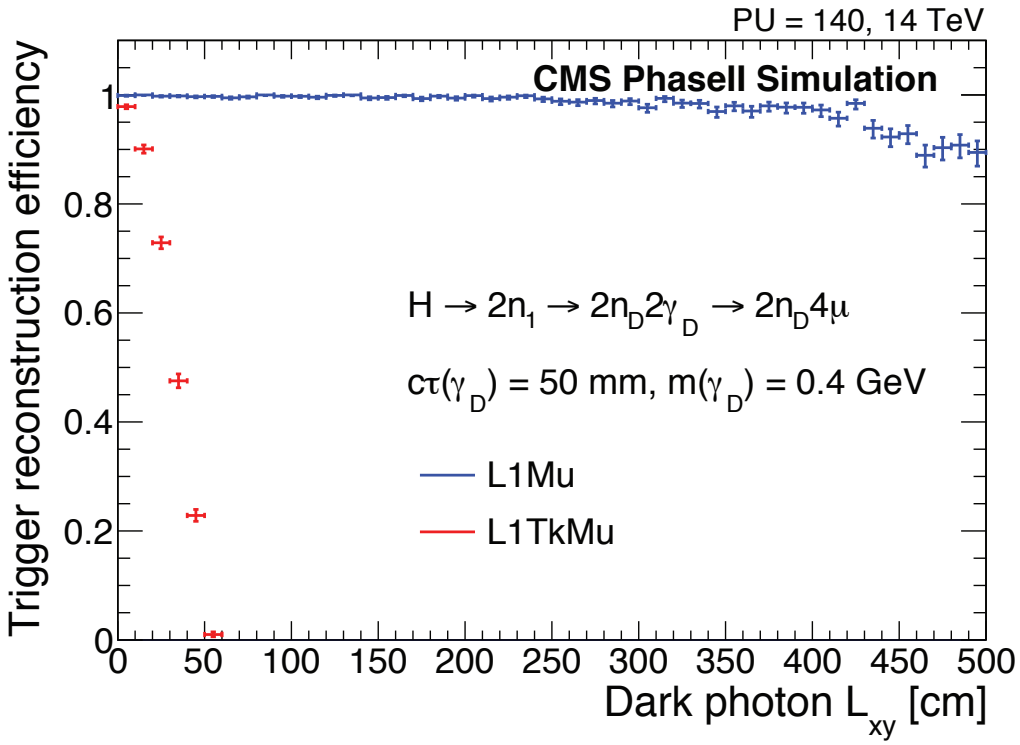

Fig. 5.7.: Probability of reconstructing at least one muon candidate produced in the decay of a light long-lived particle decaying to a pair of muons as a function of the distance between the decay vertex to the beam line in the transverse plane [65].

as a function of L_{xy}, that is the transverse displacement of the decay vertex from the beamspot. The sensitivity to signatures clearly requires an efficient standalone muon trigger.

GE1/1 is not the only proposed muon detector upgrade in the endcaps. The CMS Phase II muon upgrade plans include later installation, during LS3, of a second and third station of GEM detectors (GE2/1 and ME0, see Section 5.6), and third (RE3/1) and fourth (RE4/1) stations of improved RPC (iRPC) detectors [67]. The motivation to all these additions is to increase the average number of muon hits along a forward track, to make it comparable to the ones currently possible in the barrel region. A qualitative demonstration of the urgency of this issue is show in Fig. 5.8. The additional redundancy to the forward muon system is of course another motivation for this upgrade, as it would prevent the degradation in standalone muon momentum resolution (used in both the offline trigger and in the HLT) in case any of the ME1/1 detectors degrades with the increased radiation doses. In fact, over the course of Run 1, up to 10% of CSCs in station ME1/1 encountered operational problems, which were possible to solve only during LS1.

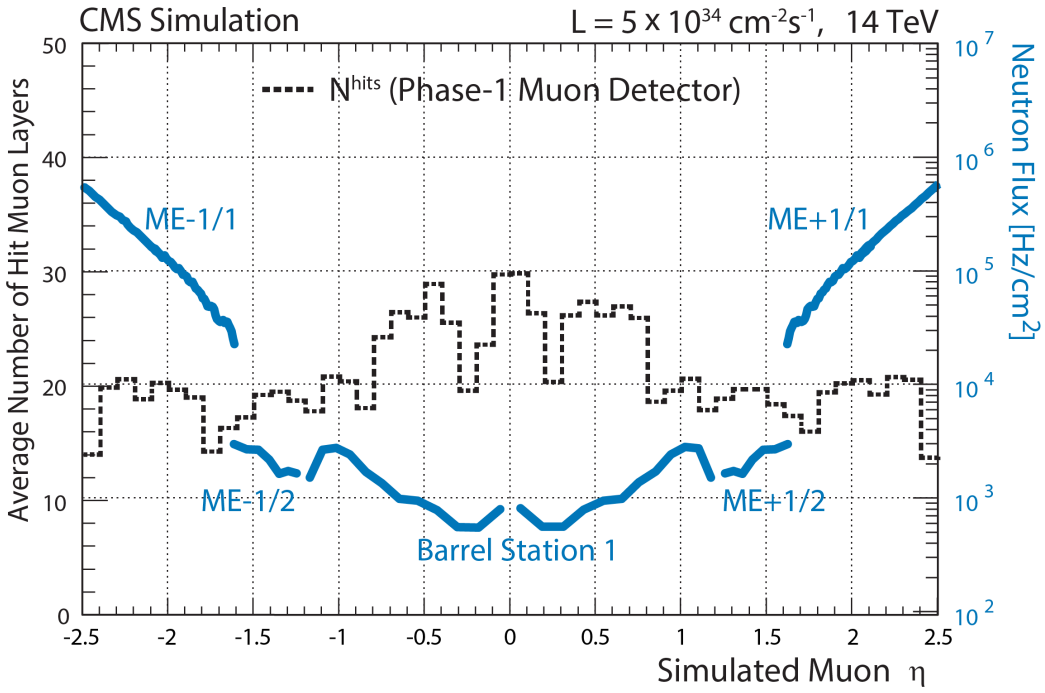

Fig. 5.8.: Histogram showing the average number of ϕ-measuring muon layers with reconstructed hits that are attached to a standalone muon track, for simulated muons from $Z \rightarrow \mu\mu$ as a function of $|\eta|$. It is compared to the flux of neutrons in Hz/cm^2 shown as coloured curves, which are the dominant cause of background hits, for the muon station first crossed by a muon with a given $|\eta|$ [65].

5.3 Overview of GEM Chambers

5.3.1 Technology overview and principles

The GEM [68] is a gaseous detector, and as such it relies on the detection of radiation crossing a gas mixture enclosed within electrodes with an electric field between them. When ionizing radiation passes through such a system, free charge is liberated in the form of electrons and ions moving under the action of the electric field to the respective electrodes. As any other MPGD operating in high fields, GEMs exploit the electron amplification to create a detectable signal. In this case the amplification occurs inside narrow holes that perforate a polyimide foil in a hexagonal pattern: this layer of material 50 µm-tick is called GEM foil. The GEM foil is clad on both sides with a conductive layer of copper 5 µm thick. It is chemically pierced with a high density of holes, typically 50 to 100 per mm^2. The hole sizes for the outer and inner radii are 70 µm and 50 µm and the pitch is 140 µm. The active area can be as high as 5000 cm^2. The standard fabrication of the perforated GEM foils involves photolitography techniques and the accurate alignment of two masks. However, to produce foils of such dimensions, the method has to be improved [69, 70]. To keep a good homogeneity of the hole geometry across the foil, the alignment error between

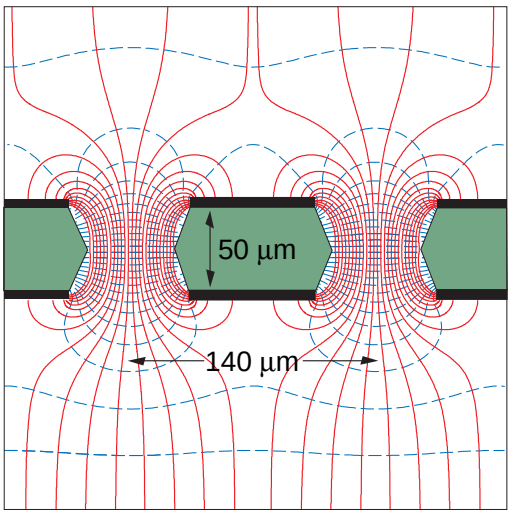

Fig. 5.9.: Schematic view and typical dimensions of the hole structure in the GEM amplification cell. Electric field (solid) and equipotential (dashed) lines are shown.

the two masks has to be kept within 10 µm. This condition is very difficult to respect when the linear dimensions of the GEM exceed ~ 40 cm. A possibility to overcome this problem is the use of single mask photolitography. In this way the GEM pattern is transferred only to one side of the raw material, therefore removing the need for alignment.

A voltage of a few hundred volts is applied across the two layers which creates a strong electric field ($60 - 100$ kV/cm) inside the holes, that act as independent proportional counters (see Fig. 5.9). Once the electrons acquire enough kinetic energy, they produce secondary ionization in the gas, causing an avalanche process. Most of the avalanche electrons then proceed into the lower gap, and can be collected on a passive electrode. A straight-forward solution to obtain lower high voltage and to avoid electrical breakdown problems is to set an arrangement of three cascaded GEM foils, commonly known as "Triple-GEM detector". Since the total charge amplification is equal to the product of the gains of the individual foils, it can then be as high as 10^5. In this way, one can reach much higher gains before discharges occur than in a single stage device, as shown in Figure 5.10 and 5.11. In GEM detectors the proportional multiplication and charge detection are performed on separate electrodes. This allow to prevent accidental discharges on the sensitive electronics with proper choice of the operating conditions. The signals induced on the readout board are very fast, because they are purely due to electrons, without any tails generated by the slow ion component. In fact, the ions from the gas amplification are pulled to and collected on the GEM foil surface while most of the electrons are extracted out of the GEM holes. Eventually, one can achieve two-dimensional projective readout thanks to thin multi-layer boards.

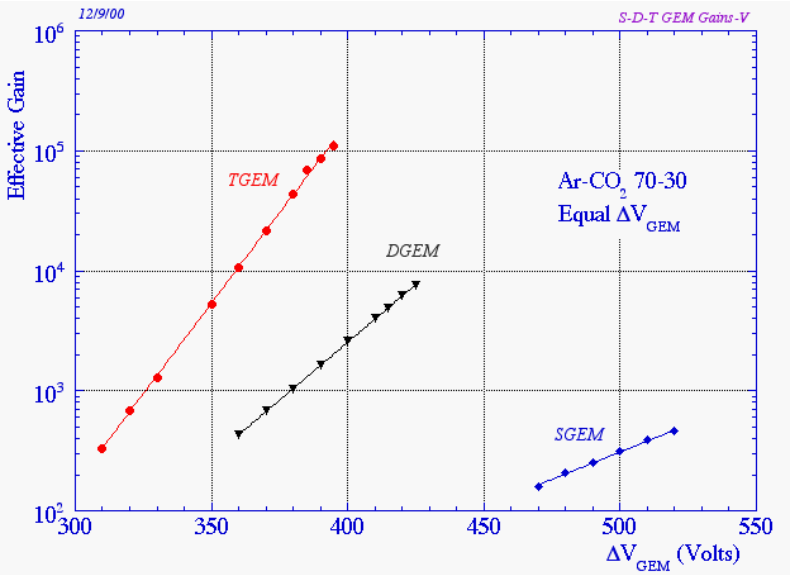

Fig. 5.10.: Gain on exposure to alpha particles of multiple GEM detectors [71, 72].

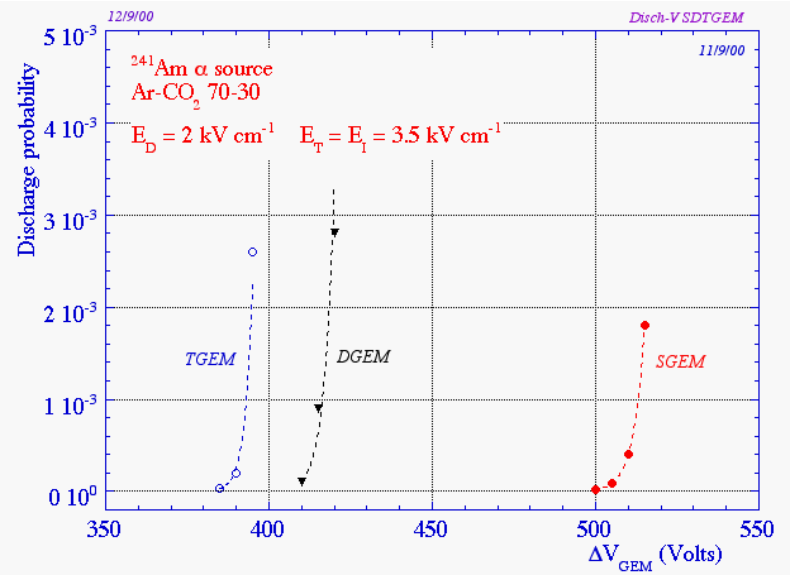

Fig. 5.11.: Discharge probability on exposure to alpha particles as a function of voltage applied to each GEM. The discharge in one GEM (usually the last in a cascade) may remain confined to the multiplier, or propagate to the next structure, with a probability that depends on the energy of the primary discharge [71, 72].

5.3.2 Electron transport

The requirements for high luminosity tracking at the LHC are stringent and represent a compromise between a fast gas mixture, small diffusion properties and a small Lorentz angle so that an event can be unambiguously associated to its bunch crossing, but large primary ionization statistics. The drift velocity would ideally be saturated or have a small variation with modifications in electric and magnetic fields. The mixture needs to be well quenched with no secondary effects like photon feedback and field emission giving a stable gas gain well separated from the noise of the electronics. Obviously financial constraints also need to be addressed in large gas systems, and a non-flammable, eco-friendly gas mixture is often a pre-requisite for safety.

The amount of free electrons and ions that are produced after an ionization event depend on the atomic number, density and ionization potential of the gas, and on the energy and charge of the incident particle. In the absence of electric field the electrons in a gas move randomly, undergoing collisions with the gas molecules with a Maxwell energy distribution, having an average thermal energy of $3/2kT$. When an electric field is applied, the electrons begin to drift in the field direction with a mean velocity v_d in addition to their random thermal velocity v. v_d represents the average distance covered by the drifting electron cluster per unit time. If the energy gained per mean free path is small compared with the electron energy, the electrons may still reach a steady distribution. The momentum transfer per collision is obviously not a constant, especially in excitation and ionization collisions between electrons and atoms, that cause a larger energy loss. This is testified for instance by Fig. 5.12: electrons with energies near the Ramsauer minimum in noble gases such as Ar have long mean free paths and consequently can gain more energy before experiencing a collision with the surrounding gas. The drift velocity is also dependent on pressure, temperature and can be modified by the presence of pollutants like water or oxygen. Poly-atomic molecular and organic gases behave differently from noble gases, as the former have many other modes of dissipating energy, such as molecular vibrations and rotations. These phenomena can play a role as important as those of electronic excitations. The mechanism of such interactions is complex, as shown by the cross-sections of CO_2 in Fig. 5.13. These collisions are produced at relatively small energies (0.1 to 1 eV) compared to excitation and ionization collisions. The main consequence is that the mean fractional energy loss is large, and the mean – or 'characteristic' – electron energy is low [73].

In a gas, electrons and ions drift along the electric field lines on average, but they are individually and symmetrically scattered by collisions with gas atoms and molecules. This is the origin of the effects called longitudinal diffusion of the drifting electron cloud (along the field lines), and the transverse diffusion (across the field lines).

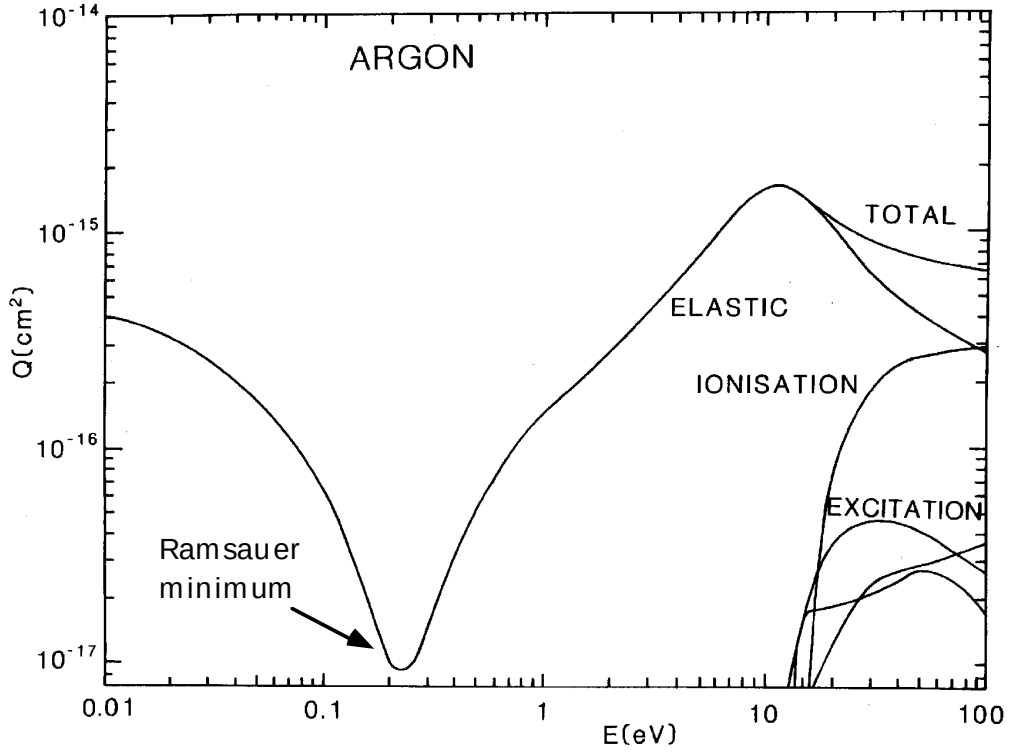

Fig. 5.12.: Cross sections for electron collisions in Ar [73].

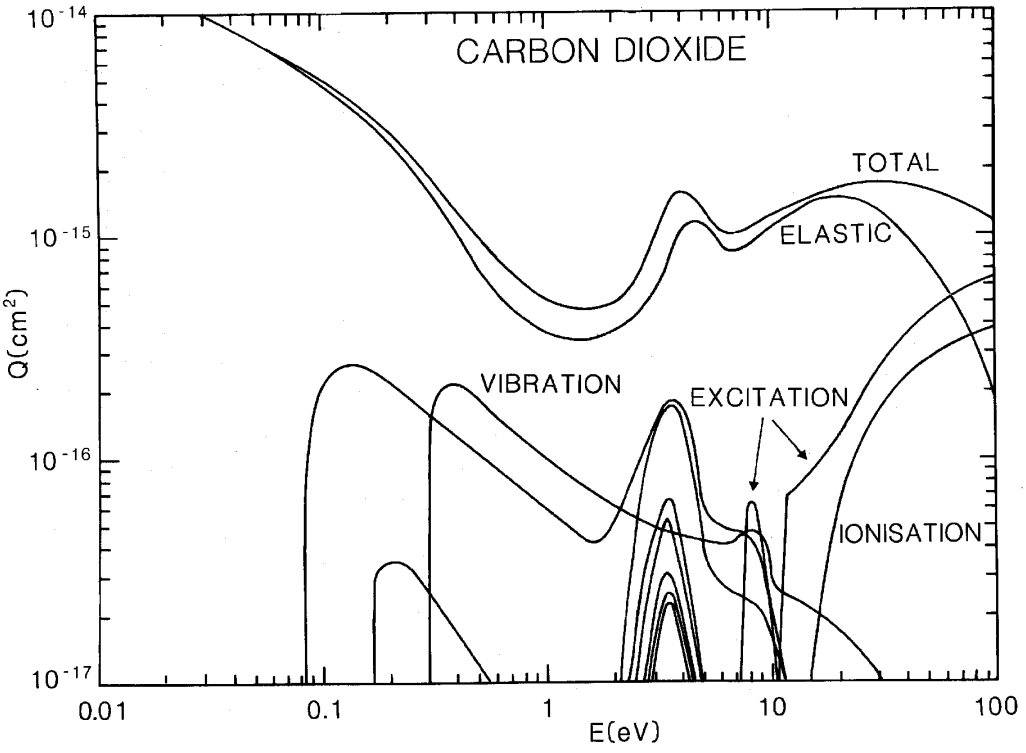

Fig. 5.13.: Cross sections for electron collisions in CO_2 [73].

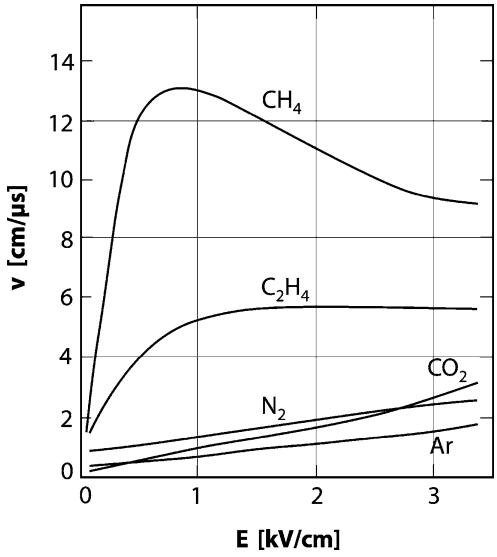

Fig. 5.14.: Drift velocity of electrons as a function of the electric field in several gases [74].

On a microscopic scale, the scattering processes are approximately Gaussian. In gases such as CO_2, called 'cold', where the electron energy is lower, the diffusion is small and the drift velocity is low and unsaturated at electric fields typically used in gaseous detectors. This implies a non-linear space-time relation. 'Hot' gases, such as argon, have stronger diffusion and even slower drift velocities (see Fig. 5.14 for a comparison among different gases), as the energy of the electron can only be dissipated through excitation and ionization. The threshold of these inelastic collisions are several eV high, therefore most of the collisions are elastic and the mean fractional energy loss is very small. In this case, the electron energy quickly rises above the Ramsauer minimum and the drift velocity is small. When noble gases are mixed with polyatomic gases having vibrational and rotational modes, the diffusion is reduced and the drift velocity is increased. Another parameter that is investigated in this field is the Townsend coefficient: it is defined as the inverse of the mean free path and corresponds to the number of ionizing collision per cm.

The 3.8 T CMS magnetic field at the location of the GE1/1 station, together with the angle between the electric field and the magnetic field, have effects on the charge transport inside the chambers. The component of the magnetic field perpendicular to the electric field (and the motion of the electron) clearly exerts a deflection effect: the electron moves in a helical trajectory resulting in a lowered drift velocity and transverse dispersion. This modifies for instance the arrival time of electrons in a proportional counter, and increases the spread in the drift time. The angle which the drifting electron cloud makes with the electric field is defined as the Lorentz angle of the particular gas, or gas mixture, under exam. It is usually large at small electric

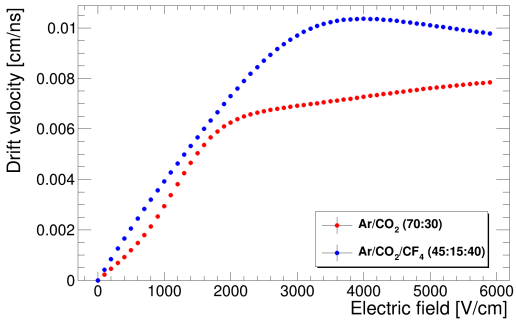

(a) Drift velocity as a function of the electric field for two possible gas mixtures.

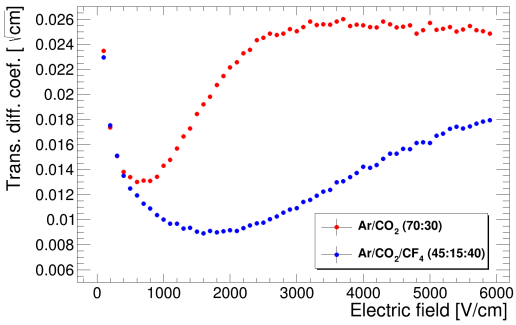

(b) Transverse diffusion coefficient as a function of the electric field for two possible gas mixtures.

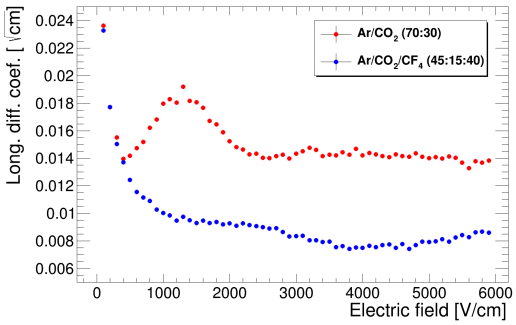

(c) Longitudinal diffusion coefficient as a function of the electric field for two possible gas mixtures.

Fig. 5.15.: Diffusion parameters of electrons in two different gas mixtures simulated with GARFIELD [75]. Credits: Federico Lucchetti, Thierry Maerschalk

fields but falls to smaller values for larger electric fields and is approximately linear with increasing magnetic field.

The Ar:CO_2:CF_4 45:15:40 gas mixture has been successfully employed with GEM detectors in the LHCb experiment [76] and Ar:CO_2 70:30 in the TOTEM experiment [77]. Being non-flammable gas mixtures, these two are candidates for operating in the GE1/1 station in CMS. The Ar:CO_2:CF_4 45:15:40 mixture combines a high drift velocity due to its high CF_4 content with a small Lorentz angle, similar to that of Ar:CO_2. The angle between the magnetic and electric field reaches a maximum of 8° in the GE1/1 station. The effect of the deviation caused by the Lorentz force over 7 mm of drift in the GE1/1 chamber is therefore less than 1 mm in the azimuthal direction. The diffusion in Ar:CO_2:CF_4 is the lowest of the two mixture options, due to higher polyatomic gas content (both CO_2 and CF_4 have vibrational modes that lower the diffusion). Moreover, the Lorentz angle is small, similar to that of Ar:CO_2. GEM simulations performed with GARFIELD [78] and supported by measurements [79] show that the addition of the CF_4 gas makes the mixture significantly faster, with a drift velocity approaching or even exceeding $\sim$ 10 cm/µs, depending on the gas mixture proportions, whereas Ar:CO_2 mixture provides a value not greater

than $\sim$ 8 cm/μs for the same applied voltage (see Fig. 5.15a). This molecule enables high-rate capability due its high drift velocity but it suffers from electron attachment. GARFIELD simulations were also used to study the transport parameters of the two gas mixtures: the transverse diffusion coefficient (see Fig. 5.15b) and the longitudinal diffusion coefficient (see Fig. 5.15c). Coefficients are related to diffusions by the following relation:

$$\sigma_{\mathrm{D}} = c_{\mathrm{D}}\sqrt{L}, \tag{5.2}$$

where σ_{D} is the diffusion, c_{D} is the diffusion coefficient, and L is the drift length. For an electric field of 2.4 kV/cm – a realistic value for the Triple GEM – the transverse diffusion coefficient in particular is found to be $\sim 0.025\ \sqrt{\mathrm{cm}}$ for Ar:CO_2, while for Ar:CO_2:CF_4 it is seen to be $\sim 0.01\ \sqrt{\mathrm{cm}}$. The effect of the magnetic field is to reduce the transverse diffusion coefficient with respect to its direction, while the longitudinal coefficient is unchanged.
It must be noticed that CF_4 has a high environmental impact, and thanks to European Union policies, it will not be produced any more in the next several years, leading to the rise of gas price and difficulties with stock supplies. Potential alternatives to CF_4 have been tested by the GEM Collaboration, and results have been released at the end of 2015 [80]. However, it must be underlined that even if an alternative will not be found, Ar:CO_2 70:30 provides the current baseline gas for operation, as it provides time and efficiency performances within the CMS requirements.

5.4 GE1/1 upgrade

5.4.1 Overview

The GE1/1 station is proposed to host 72 chambers per endcap, covering 10° in ϕ each, therefore providing full azimuthal coverage. The chosen technology, as stated above, is Gas Electron Multipliers (GEMs) for charged-particle detection. The Triple GEM foil gap configuration is $3/1/2/1$ mm (drift, transfer 1, transfer 2, induction gap sizes) [81].
The amplified charge induces a signal on the electrodes that are finely segmented in the muon bending direction (ϕ), so that the detector is position-sensitive. There are 384 segmentations in ϕ, meaning that each strip covers 450 μrad.
In the GE1/1 system the GEMs are arranged in pairs in order to form a so called "super-chamber". Two measurements planes are then provided, complementing the existing ME1/1 system and maximizing the detection efficiency. The super-chambers are trapezoidal in shape and alternate in ϕ between long ($1.55 < |\eta| < 2.18$, large base $= 510$ mm, small base $= 279$ mm, height $= 1283$ mm) and short ($1.61 < |\eta| <$

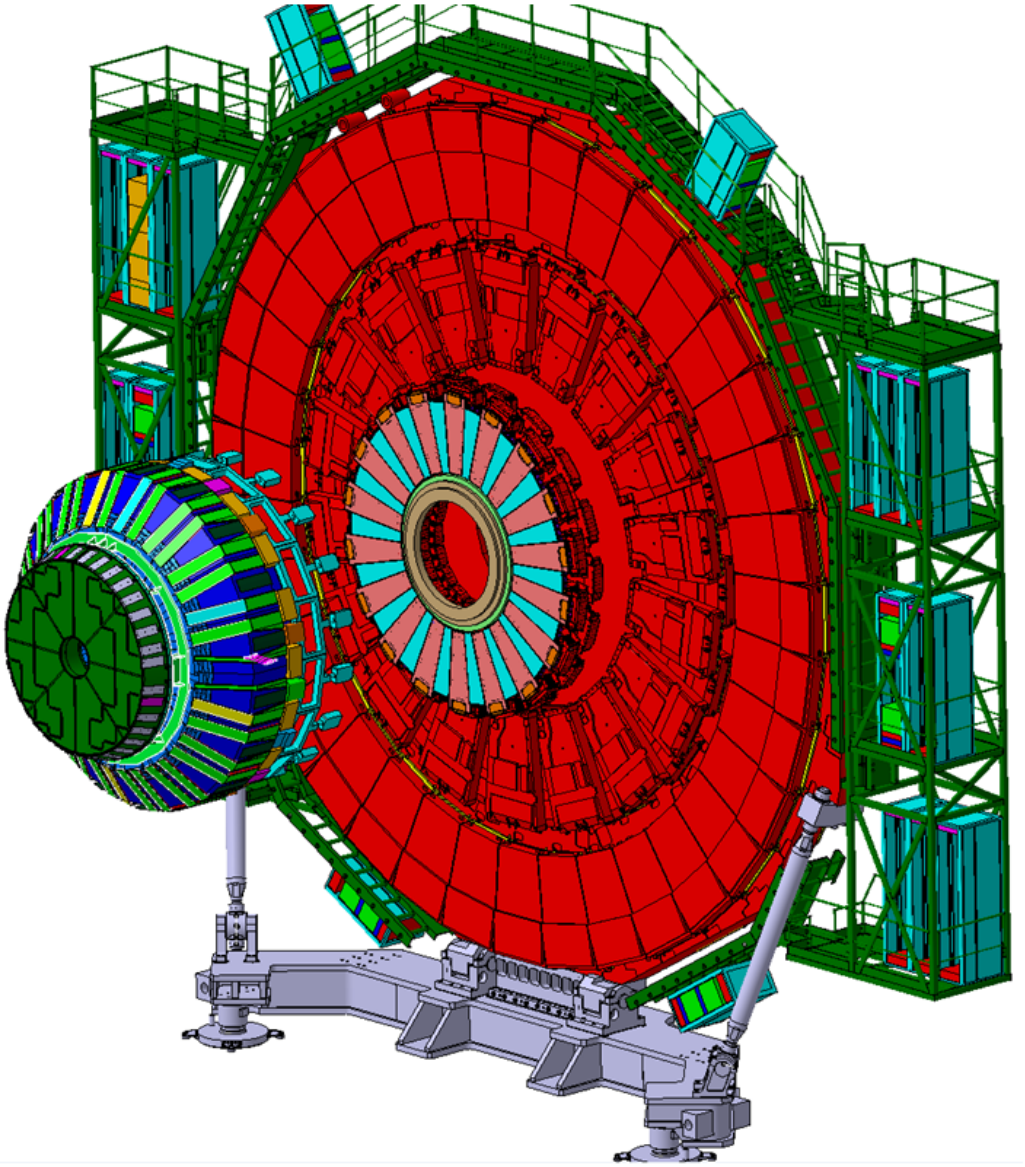

Fig. 5.16.: First CMS muon endcap station where the inner ring is equipped with 18 long (pink) and 18 short (light blue) Triple GEM superchambers.

2.18, large base = 445 mm, small base = 220 mm, height = 990 mm) versions, as required for mechanical reasons. The GE1/1 $|\eta|$ coverage usually quoted as $1.6 < |\eta| < 2.2$ is therefore only an approximation. The 100 mm slots foreseen for the GEM installation are set in the gap between the hadron calorimeter and the CSC ME1/1 chambers in the part of YE1/1 commonly referred to as the "nose", represented in Fig. 5.16. A first trial installation of a first set of "dummies' (not containing any detectors, nor any electronics) into one of the inner endcaps was successfully performed during the summer of 2013; a second trial installation with the second set was done in March 2014 [82].

The GEM chambers are segmented in three sections in ϕ and eight in $|\eta|$ creating 24 individual detector segments. Each of these segments is further subdivided into 128 strips and read out by 128-channels application-specific integrated circuits (ASICs), called VFAT3. After being induced on the electrodes, the small charge signals are amplified, digitized, and further processed by the ASICs. This new front-end ASIC design is based on the previously used binary-readout VFAT2 chip [83]. It is developed to match the required particle rates and trigger precision. The VFAT can provide a programmable, fast OR function on the input channels depending on the region of the sensor for triggering. The chip offers adjustable thresholds, gain, and signal polarity, plus a programmable integration time of the analog input signals. The signal sampling of the VFAT chips is driven by a 40 MHz internal clock.
From the VFAT chips, the data are then sent to the GEM Electronics Board (GEB), which provides the connection to the GEM strips (besides delivering power and communication signals to and from the VFAT hybrid). The data from the GEB are trasmitted to one FPGA board, called the GEM OptoHybrid (OH), located on the far end of the GEM module. Optical fibres will be used to transmit the data between the GEM electronics and the off-detector DAQ system; they are then processed by a local trigger algorithm and transferred to the L1 endcap muon track finder. The GEM trigger data are designed to be sent to the CSC Trigger Mother Board (TMB) through a dedicated additional fibre. Here, the GEM data will be combined with the CSC data to make combined local muon stubs. Radiation tolerant optical communications are ensured by CERN-based common projects such as the GBT chip set [84], Versatile link [85] and GLIB [86]/MP7 [87] μTCA systems.

5.4.2 Triple-GEM geometry

It was already discussed in Sec. 5.3 that the GEM detector is a thin metal-coated polymer foil perforated with a high density of holes, each hole acting as a multiplication region. It was also shown that Triple-GEM detectors, made with three GEM foils in cascade, ensure high gains and safe operation at low voltage.
The CMS Triple-GEM has a trapezoidal-shaped active area of $0.3 - 0.5$ m^2 with a $3/1/2/1$ mm (drift/transfer 1/transfer 2/induction) field gap configuration (see Fig. 5.17 for a sketch of the detector showing a full amplification event). If an ionization occurs in the drift gap, the free electron is accelerated by an electric field and undergoes three stages of amplification through as many GEM foils. In the CMS endcap, Triple-GEM's will be installed in pairs in order to form a super-chamber. For space saving concerns, two configurations are foreseen: in the first, called 'odd', the read-out electronics of the two chambers face the inner part of CMS, towards the point of interaction; in the second, called 'even', their orientation is symmetric with respect to the first one. As a super-chamber covers $10°$ in ϕ, there will be 144

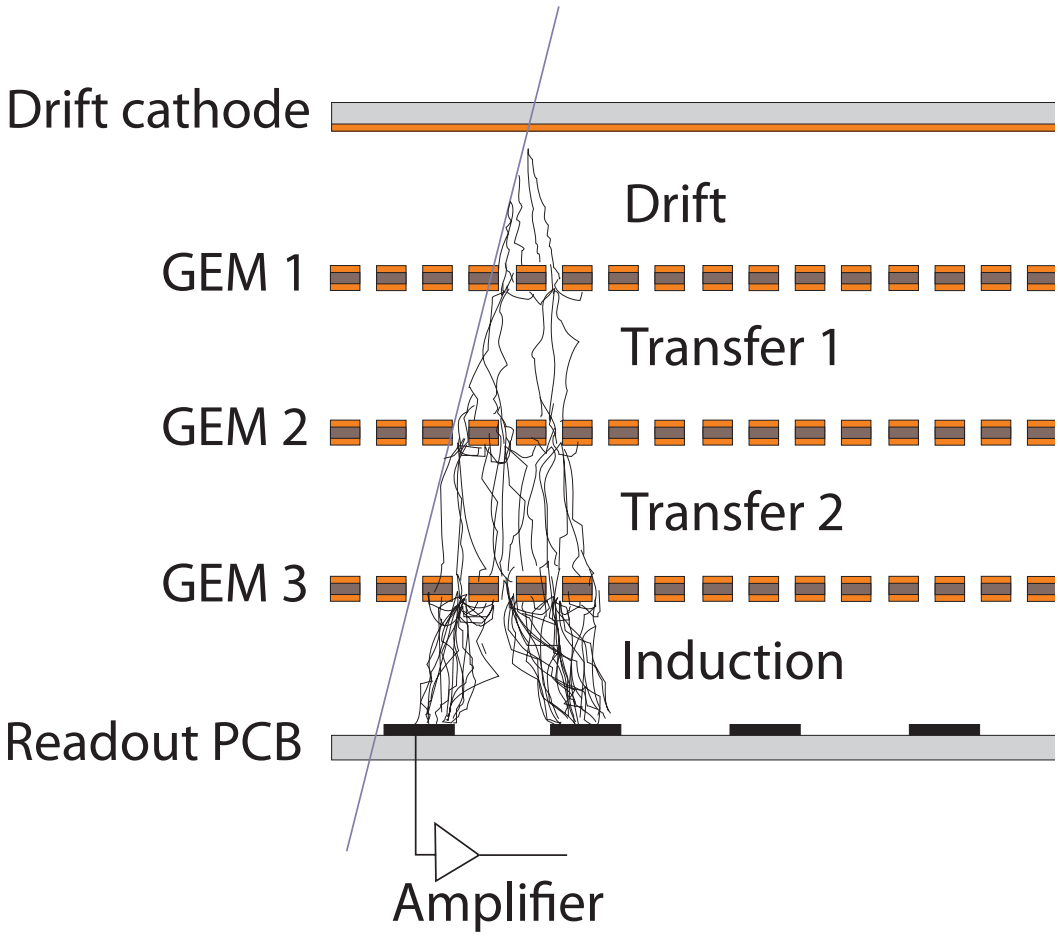

Fig. 5.17.: Sketch of a Triple-GEM chamber (not to scale). Free electrons coming from ionization processes that appear in the drift gap undergo three stages of amplifications thanks to the GEM foils. The gain is typically ~ 20 per stage, and the difference of potential applied on each foil is ~ 400 V.

chambers in total, considering the two endcaps (36 chambers times 2 chambers per super-chamber times 2 endcaps). An exploded view of the detector is shown in Fig. 5.18, and includes covers, thermal screen, optohybrids, readout boards and GEM foils.

5.4.3 Requirements on GE1/1 performances

A series of requirements are imposed on the detection performance of the GE1/1 chambers by the physics performance presented in the above sections:

- Maximum geometric acceptance within the given CMS envelope: in fact, maximum acceptance allows maximum physics yield.

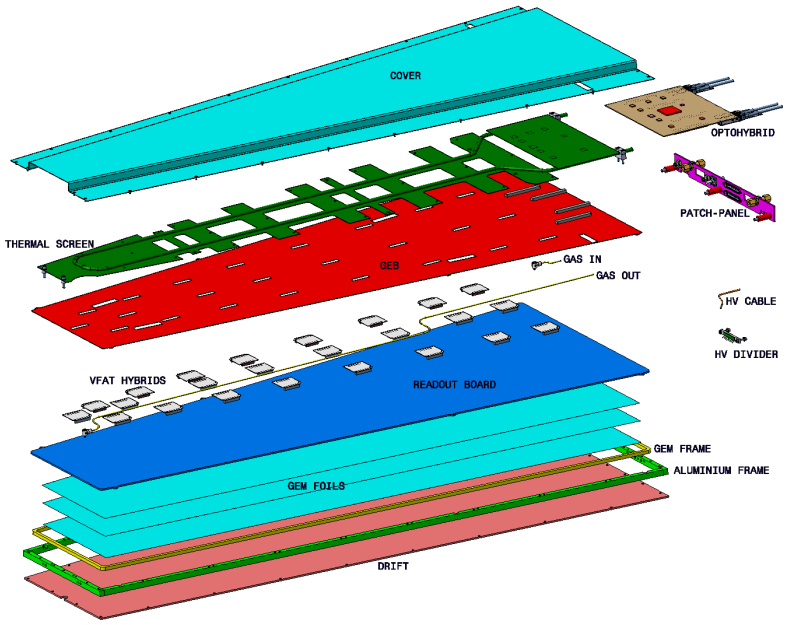

Fig. 5.18.: GE1/1 Triple-GEM exploded view

- Rate capability of 10 kHz/cm^2 or better: this requirement is obtained multiplying by a safe factor of two the maximum expected hit rate in this station, that is about 5 kHz/cm^2 for Phase II running at 14 TeV and 5×10^{34} cm^{-2}s^{-1}.

- Single-chamber efficiency of 97% or better for detecting minimum ionizing particles: when two chambers will be connected with a logical OR, a "super-chamber" will have an efficiency above 99.9%.

- Angular resolution[1] of 300 µrad or better will enable the trigger to discriminate high-p_{T} muons from low-p_{T} muons reliably when combining the angular muon position measured in GE1/1 and ME1/1. The azimuthal precision of 300 µrad corresponds to a 0.8 mm resolution in the azimuthal $\hat{\phi}$ direction at the outer radius of the GE1/1 chambers ($r = 2.6$ m).

- Timing resolution of 10 ns or better for a single chamber: this timing can be combined with the one coming from the CSCs, such a resolution is sufficient to match GE1/1 hits to ME1/1 stubs in time with a 25 ns bunch crossing time.

- Gain uniformity of 15% or better across a chamber and between chambers: this ensures the absence of biases in triggers or reconstruction due to the geometry.

- No gain loss due to ageing effects after 200 mC/cm^2 of integrated charge: the charge expected to be integrated for a GE1/1 chamber at the highest $|\eta|$ over 20 years of operation is about 100 mC/cm^2.

[1] Strips are radial, therefore the spatial resolution is stated as an angular resolution in ϕ.

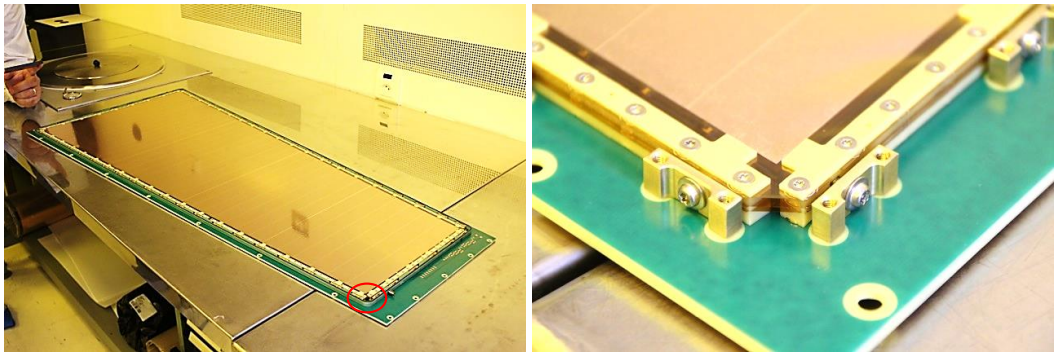

Fig. 5.19.: Left: GE1/1 prototype with GEM foil stack tensioned against brass pull-outs, mounted onto drift board, and surrounded by outer frame. The active chamber volume is now ready to be closed with the readout board. A detail (red circle) of the stack is given that shows the gap between inner frame sections in one corner and the pull-outs (right).

The chamber design has additional technical constraints and requirements:

- The chambers will need to operate with gases having low global warming impact (see Section 5.3.2 for a discussion).

- The multiple scattering caused by the material budget must not affect the muon track measurement in the GE1/1-CSC trigger. The latter needs to remove CSC ghosts with multiple muon hits in a CSC chambers; therefore, a small enough readout segmentation in $|\eta|$ is needed.

- Eventually, as previously stated, the super-chambers' size must respect the available slot in the muon endcap nose, less than 10 cm thick.

The decision to implement GEM technology in the CMS experiment is supported by the more-than-a-decade operation of GEM detectors in several major high energy and nuclear physics experiments, such as COMPASS, PHENIX, STAR, TOTEM, and LHCb. In TOTEM, triple-GEMs operate at a hit rate of ~ 12 MHz/cm^2 with no ageing effect nor any change in material properties or performance. In LHCb, the rate is ~ 1 MHz/cm^2; in COMPASS, they operate at ~ 2.5 MHz/cm^2 with no degradation of gain, efficiency, energy and time resolution [88].

5.4.4 Assembly overview of GE1/1 chambers

The assembly and sealing of the detector are entirely mechanical, in the sense that no glue is applied at any stage. This allows to open a detector again for repairs, if needed. The three GEM foils are sandwiched at their edges between four layers of a thin frame made of epoxy. The stack is held together by numerous stainless steel

screws, penetrating all frame layers. The GE1/1 is assembled with manual control so that the GEM foils can be tensioned as uniformly as possible. This is possible thanks to small brass posts ("pull-outs") that are tightened manually. A large outer glass-epoxy frame is placed around the tensioned GEM stack and the brass pull-outs provide the border of the gas volume (see Fig. 5.19). The frame provides a solid barrier that is only penetrated by two small holes in diagonally opposed corners to provide the gas inlet and outlet for the chamber.
The drift board features a single drift cathode on its inner side and a solid ground plane on the outside of thde chamber. It provides connections to external high voltage supply lines via HV noise filtering circuitry. The readout board is interfaced to the radial readout strips. The VFAT2 hybrids plug on the readout board from the outside. The VFAT2 hybrids also plug into a second full-size PCB, the GEM Electronics Board (GEB), directly attached on top of the readout PCB. The GEB is in charge of carrying the digital output signals from all VFAT2 hybrids to the wide end of the chamber for processing and transporting to the Trigger/DAQ.
Finally, an aluminium frame is mounted on the drift board all around the outer edge. An aluminium sheet with a thin central chimney along the long axis of the chamber is attached to that aluminium frame to cover the entire assembly from the readout side, providing solid protection for the on-chamber electronics and utilities.

5.5 GE1/1 prototyping results

The performances of GE1/1 prototypes were studied in a series of beam tests at CERN in 2010 [89], 2011 [81], 2012 [90], and at Fermilab in 2013 [91]. At CERN, the detectors were operated with the Ar:CO_2:CF_4 45:15:40 gas mixture and read out with binary-output VFAT2 front-end chips, while in Fermilab beam tests employed Ar:CO_2 70:30 and chambers were read out with analog APV25 front-end chips [92] that produce full pulse height information. The measured performances of the most important detector parameters are illustrated hereby. Different prototypes belonging to different GEM generations were used. As they operate at different tensions, the results may not be directly comparable.
There are currently six versions, or 'generations', of GEM chambers, from GE1/1-I, the first 1 m-class GEM detector ever constructed and operated (2010), to the current version. The gas gain was measured by irradiating the chamber with a high-rate X-ray generator. The gain measurements are shown for a GE1/1-IV (the first one produced without gluing any component) in Fig. 5.20 for both Ar:CO_2 70:30 and Ar:CO_2:CF_4 45:15:40 counting gases. The chambers were operated at different high-voltages applied to the drift electrode. The plot also includes the observed hit rates for a fixed rate of incident photons coming from a Cu target X-ray gun. In both mixtures the hit rates suggest the beginning of the plateau of efficiency, well

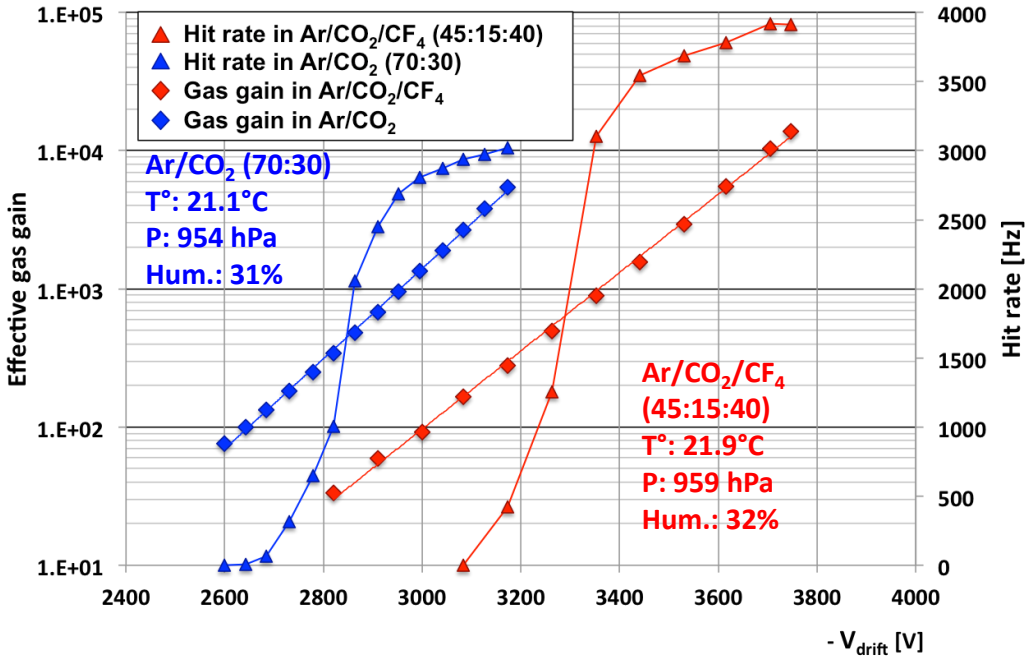

Fig. 5.20.: Measured gas gains (diamonds) and hit rates (triangles) as a function of high voltage applied to the drift electrode of a GE1/1-IV detector. Measurements with Ar:CO_2 70:30 (blue) and with Ar:CO_2:CF_4 45:15:40 (red) gas mixtures are displayed. The log scale (left) applies to the gain while the rates are plotted on a linear scale (right) [65].

before voltages at which the discharges occur. In particular the Ar:CO_2:CF_4 mixture allow to operate gains exceeding 10^4. The study of the response uniformity over the detector also implies the use of an X-ray generator, placed at a distance of about 1 m. The data show that the response varies not more than 15% across the detector. Efficiency measurements for charged particles show a plateau efficiency of 98% for pions when operated with Ar:CO_2:CF_4 and readout with VFAT2 chips.

As mentioned in Sec. 5.4.3, the required angular resolution of 300 µrad is an upper limit required by the trigger. It is however a resolution requirement that combines the intrinsic ME1/1 resolution, the ME1/1 and GE1/1 chamber alignments, in addition to the intrinsic GEM resolution. This is why the latter must be significantly better than 300 µrad to respect the trigger limit. GE1/1-IV Measurements at the 2012 CERN test beam operated with a Ar:CO_2:CF_4 counting gas and a binary-input VFAT2 chips. For tracking studies, this detector was positioned on a movable table in front of a GEM detectors with 2D Cartesian readout. The results show a distribution of the residuals with a width of 268 ± 2 µm (see Fig. 5.21). This is called "exclusive residual" as the track positions do not include GE1/1 in the track fit: this width represents then an upper limit (that is, an overestimation) on the intrinsic chamber resolution. This result is obtained from sector 6 of the chamber at radius $r \approx 1.95$ m. The residual in the $\hat{\phi}$ direction corresponds therefore to an angular resolution of

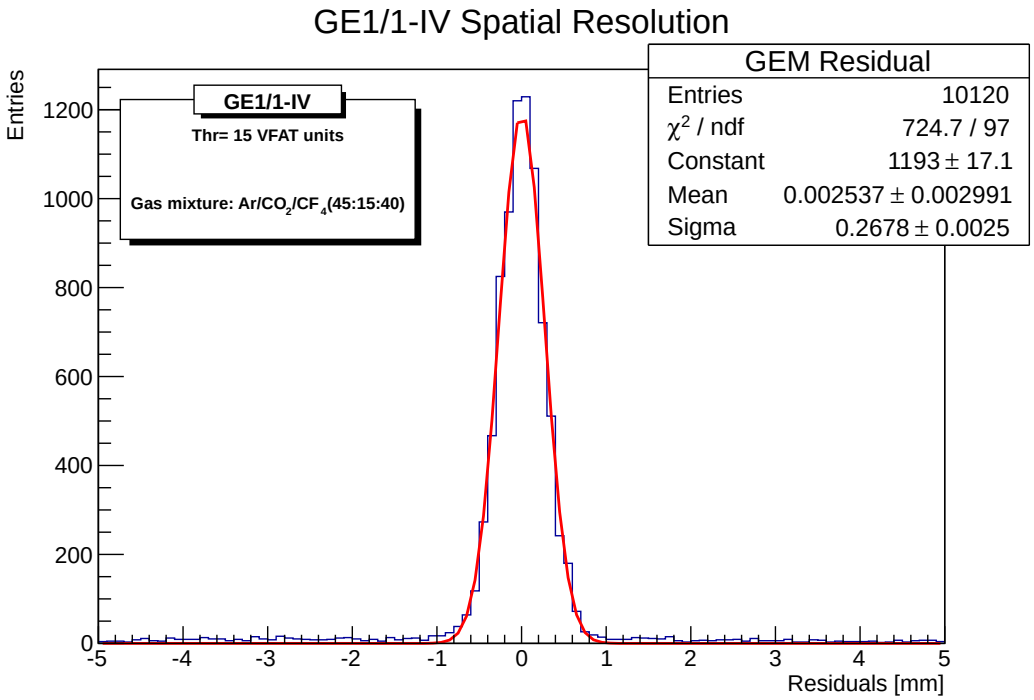

Fig. 5.21.: Exclusive residuals in azimuthal $\hat{\phi}$-direction measured with a pion beam at CERN on a GE1/1-IV chamber.

137 ± 1 µrad, which is close to the expected intrinsic resolution for a binary readout as the angular strip pitch is 455 µrad, approximately given by:

$$\frac{\text{angular strip pitch}}{\sqrt{12}} = \frac{455\ \mu\text{rad}}{\sqrt{12}} = 131\ \mu\text{rad}. \tag{5.3}$$

When taking the 2013 results coming from the Fermilab test beam facility and combining exclusive and inclusive residuals – which underestimate the intrinsic resolution by biasing the track reconstruction – in a geometric mean, one obtains:

$$\sigma_{\text{resolution}} = \sqrt{\sigma_{\text{incl.residual}} \times \sigma_{\text{excl.residual}}} = 132\ \mu\text{rad}. \tag{5.4}$$

The timing resolution of a 10×10 cm^2 Triple-GEM prototype for Ar:CO_2 70:30 and $3/2/2/2$ mm gap configuration is 8 ns. It is possible to improve it by a factor of two, using Ar:CO_2:CF_4 45:15:40 and $3/1/2/1$ mm gap configuration, to reach 4 ns. The timing performance of a GE1/1-III prototype operating Ar:CO_2:CF_4 45:15:40 is actually 6 ns; for this configuration, 97% of all hits occur within the correct 25 ns clock cycle (see Fig. 5.22). For two GE1/1 chambers united in one super-chamber, we would expect a resolution of 6 ns$/\sqrt{2} = 4$ ns. We expect an overall timing resolution of 8 ns for a super-chamber operated with Ar:CO_2 70:30.

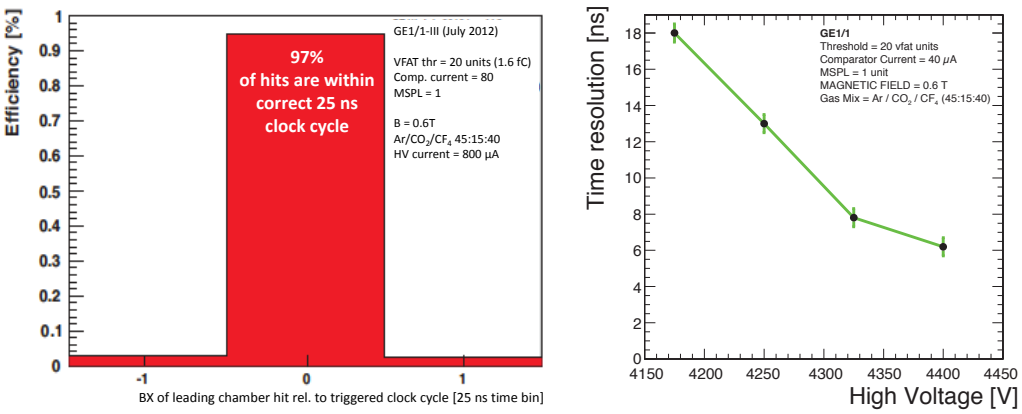

Fig. 5.22.: Timing measurements for a GE1/1 prototype with VFAT2 readout in a beam with 25 ns bunch crossing time. Left: Fraction of hits measured in bunch crossings relative to the trigger clock cycle. Right: Timing resolution VS drift voltage.

The discharge probability was measured to be on the order of 10^{-5} to 10^{-3} per ionizing particle, in the high gain range of $4 - 6 \times 10^5$. These conditions are well beyond those that will be used in CMS. Extrapolating these experimental data to more realistic conditions gives a discharge probability of about 10^{-12} to 10^{-11}. Regarding the rate capability, the gain stays constant over four orders of magnitude of incident particle rate up to 100 MHz/cm^2. This is four orders of magnitude higher than the rate the GE1/1 detector will need to sustain in the forward muon region of CMS.

The performance of GE1/1 prototypes has also been tested in magnetic fields. The CMS M1 superconducting magnet provided a magnetic field up to 1.5 T. Results show that the cluster size is not affected by the magnetic field, while the cluster position is displaced, in good agreement with simulations performed by GARFIELD. Not even the performance of the time resolution is affected by the presence of the magnetic field. In conclusion, the magnetic field does not influence the performance of the GE1/1 detector.

5.6 GEM upgrade in Phase II

5.6.1 GE2/1 station

Without any intervention, the level of performance achieved during Run 1 cannot be sustained throughout Phase II, because of the much harsher environment at a luminosity reaching and exceeding 10^{34} cm^{-2} s^{-1}. Therefore, an extended program of upgrades is foreseen to counter the higher instantaneous and integrated luminosity, the possible detector degradations, and changes to the trigger (in particular the

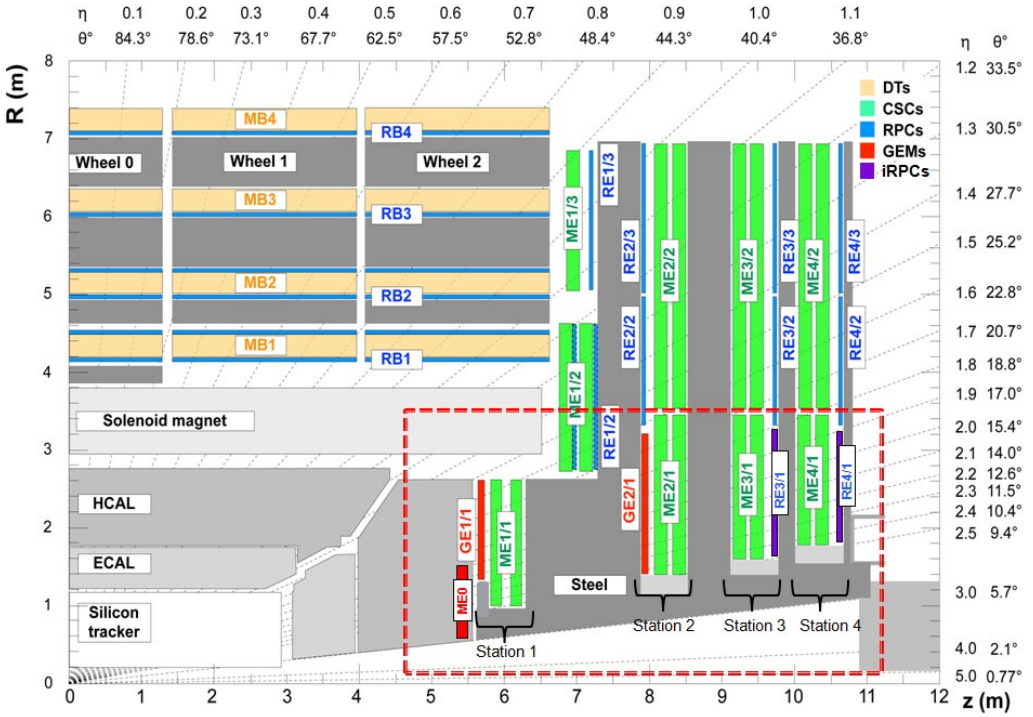

Fig. 5.23.: A quadrant of the muon system, showing DT chambers (yellow), RPC (light blue), CSC (green), as well as Phase I upgrade GE1/1 GEM detector (red). The locations of the new forward muon detectors for Phase II are contained within the dashed box and indicated in red for GEM stations (ME0 and GE2/1) and dark blue for improved RPC stations (RE3/1 and RE4/1).

increase in L1 latency and rate).

The muon upgrade for Phase II was partially presented in Section 4.7.5. Three types of upgrades related to as many types of muon detectors were illustrated: Drift Tubes (DT), Cathode Strip Chambers (CSC) and Resistive Plate Chambers (RPC). The main part of the muon system was installed in 2007, and since then, during LS1, the large chambers in the fourth endcap disk were installed (ME4/2, RE4/2 and RE4/3). For Phase II, it will be crucial to keep the efficiency of the L1 muon triggers high, and at the same time collecting the largest possible fraction of interesting signals with low p_{T} thresholds.

The muon upgrades proposed for Phase II can be summarized in three categories:

- upgrades of existing muon detectors and electronics to sustain a more severe environment,
- addition of muon detectors in the range $1.6 < |\eta| < 2.4$ to guarantee the redundancy and improve the trigger and reconstruction capabilities,
- extension of muon detector coverage up to $|\eta| = 3$, to match the new endcap calorimeter and to exploit the pixel tracking extension.

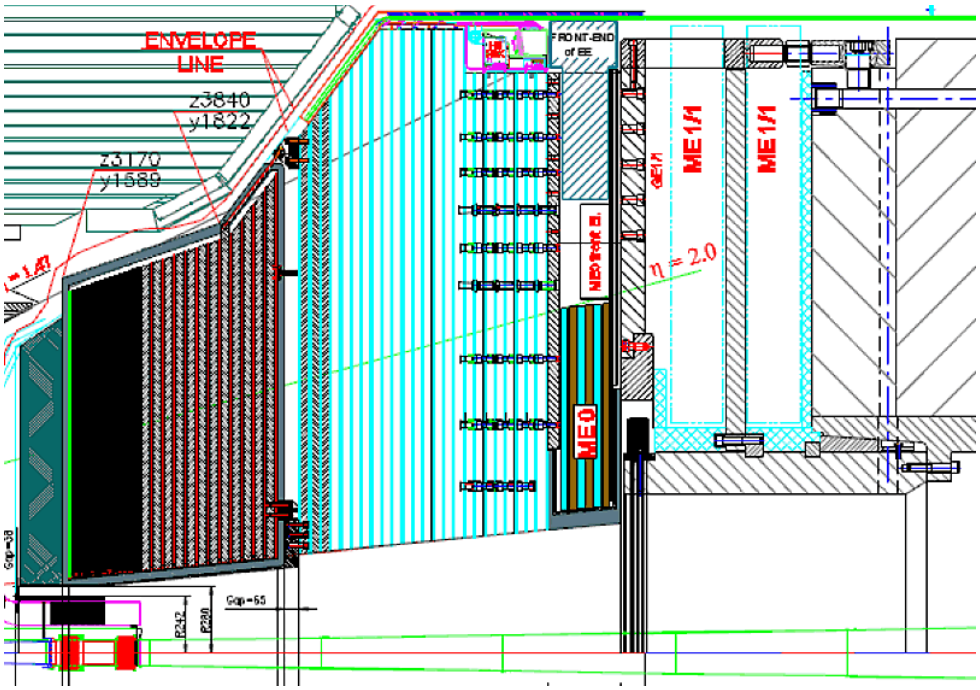

Fig. 5.24.: A cross-section of the endcap region including ME0 placed behind the endcap calorimeters at $523 < z < 554$ cm and extending from $2.0 < |\eta| < 3.0$. Space behind the calorimeter at larger radii will be used to accomodate mechanical elements and endcap calorimeter services [51].

In addition to the already mentioned GE1/1 station, proposed for LS2 installation, the GE2/1 station is currently under study, and is meant to correspond to the CSC chambers in station ME2/1, as shown in Fig. 5.23. Thirty-six GE2/1 super-chambers will cover the endcaps, therefore covering each 20° in ϕ. The interested $|\eta|$ range is $1.65 - 2.4$. The detectors are about 1.2 m long and 0.8 m wide on the outer side of the trapezoid. The chambers are segmented in eight rings in r and six sectors in ϕ; each sector is segmented into 128 radial strips readout by a single front-end ASIC. The strip pitch evolves from about 0.5 mm to 1.2 mm, subtending an angle of 0.45 mrad between strips. Considering a binary read-out, the expected spatial resolution varies then from 140 to 350 µm from inner to outer radius. The L1 trigger combines four strips adjacent in ϕ into a single trigger strip, reducing the trigger segmentation to 1.8 mrad [51].

5.6.2 ME0 station

The new endcap calorimeter will free a space of ~ 30 cm, as shown in Fig. 5.24. This area will host the ME0 station, whose extension is proposed to lie in the range $2 < |\eta| < 3$. This set-up takes into account the neutron shielding that will be required at the inner radius. The main goal of this detector will be to provide a good muon

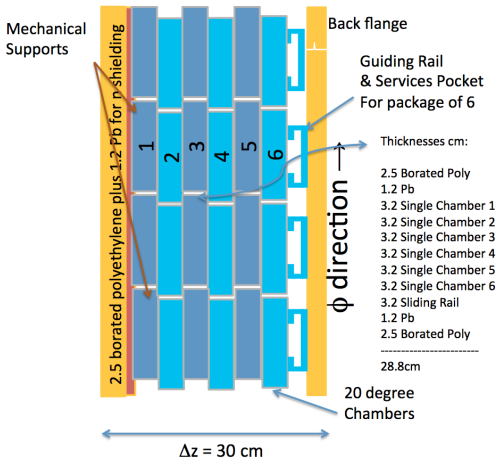

Fig. 5.25.: Preliminary layout of approximate 100° of a 6-layer ME0 layout in ϕ-z view, using 20° Triple GEM chambers in the 30 cm space made available behind the new Endcap Calorimeters [51].

ID in offline analysis. The proper rejection of neutron background is done through a design that includes six layers of GEM chambers, in addition to appropriate neutron and photon shielding (borated polyethylene and lead). The units of ME0 detector will be made of 20° wedges with an inner radius of 300 mm and an outer radius of 1495 mm. The final design is still under study, but will be certainly based on the layout shown in Fig. 5.25.

5.7 Conclusions

The main features of the GE1/1 upgrade project were outlined in this Chapter. The necessity to equip the high $|\eta|$ station and advantages brought by the GEM technology were detailed. The Chapter did not fail to include a few concrete physical scenarios, such as the important $\mathrm{H} \rightarrow \tau_{\mu}\tau_{h}$ channel, that would benefit from a high $|\eta|$ upgrade and an increase in acceptance. The GEM technology overview was provided, as well as up-to-date result coming from several test-beams ran in the last years.

Now the time is ripe to face the established work in the domain of the response of the Triple GEM detectors to the background particles hitting the GE1/1 chamber. This is indeed an important parameter able to tell if a detectors are able to cope with the harsh environment of the next stages of the LHC. A GEANT4 simulation has been created to give the required answer. The next Chapter will be entirely devoted to this matter.

6 Estimation of Triple-GEM sensitivity to background particles through a GEANT4 simulation

6.1 Introduction

The interaction between particles and matter is at the core of every particle physics experiment. The complexity of the experiment design requires more and more techniques of Monte Carlo simulation, to give a prediction about the detection of a signal of interest. When small cross-sections are involved and rare signals are searched, the prediction of the background rates becomes a priority. The particle environment of the CMS cavern is a very complex one due to the large quantity of detectors and surrounding passive material present in the apparatus. Dedicated research groups exist with the unique goal to give an accurate description of the rate, energy, and angle distributions of such particles [93]. A common tool used to estimate the hit rate of the particles in a detector, given the geometry of the source is GEANT4. It is a Monte Carlo tool established since more than a decade, constantly tested with experimental data and improved by the GEANT4 collaboration. The application whose results are presented in this Chapter has been built from scratch; it includes the geometry of the Triple GEM detectors for the GE1/1 upgrade and the description of the background environment at the GE1/1 station coordinates in CMS. Specific efforts were made in order to validate as much as possible with data the prediction given by the application. When this has not been possible, critical comparisons with simulation found in literature were performed.

The Chapter is structured in the following way. Sec. 6.2 includes common knowledge about electromagnetic interaction between radiation and matter. The interaction of photons is detailed in Sec. 6.3, while elements of neutron physics are given in Sec. 6.4. A presentation of the GEANT4 toolkit is available in Sec. 6.5, and the way physical processes are included and reproduced according to the existing models is reviewed. Several CMS background-related distributions are included in Sec. 6.6. Eventually, the methodological approach of the results shown in Sec. 6.7 includes a validation and comparison study of the GEANT4 results obtained in this work with

data and past simulations, followed by a presentation of the obtained results. An estimation of the systematic errors is also provided.

The most common information about radiation-matter interaction reported in this Chapter are taken from a few classic textbooks [94, 95]. Other sources are specified throughout.

6.2 Charged particles interaction with matter

6.2.1 Heavy particles

Since the celebrated Geiger–Marsden experiment (1909), the knowledge of the interactions of radiation encountering matter is the basis of all particle detection devices. In this section and the following ones, a concise theoretical introduction will be provided. For this scope let us first consider the passage of charged particles through matter. The principal features that characterize such an interaction are:

- a loss of energy by the incident particle, and
- a deflection of the particle from its incident direction.

These effects are essentially the result of inelastic collisions with the atomic electrons of the material, and elastic scattering off nuclei. These processes have a cumulative effect, that is translated at a macroscopic scale in the two principal effect mentioned above. However, they are in no way the only existing reactions. Other processes – although extremely rare compared to the previous ones – include the emission of Cherenkov radiation, nuclear reactions and *bremsstrahlung*. Among all the electromagnetic processes, the inelastic collisions ($\sigma \approx 10^{-17} - 10^{-16}$ cm^2) are almost exclusively responsible for the energy loss of heavy particles (i.e. heavier than electrons) in matter: the energy is transferred from the particle to the atom, exciting or even ionizing the latter. Soft collisions only results in excitations, and hard collisions transfer sufficient energy to cause ionization. In some of the hard reactions, the electron itself is able to cause secondary ionization; such high-energy recoil electrons are known as δ-rays.
Elastic scattering off nuclei may also happen, although not as frequently as electron collisions. Due to the masses of the nuclei, very little energy is usually transferred. The kinetic energy transfer is in fact equal to:

$$\Delta T = T \frac{4Mm}{(M+m)^2} \cos^2 \phi, \tag{6.1}$$

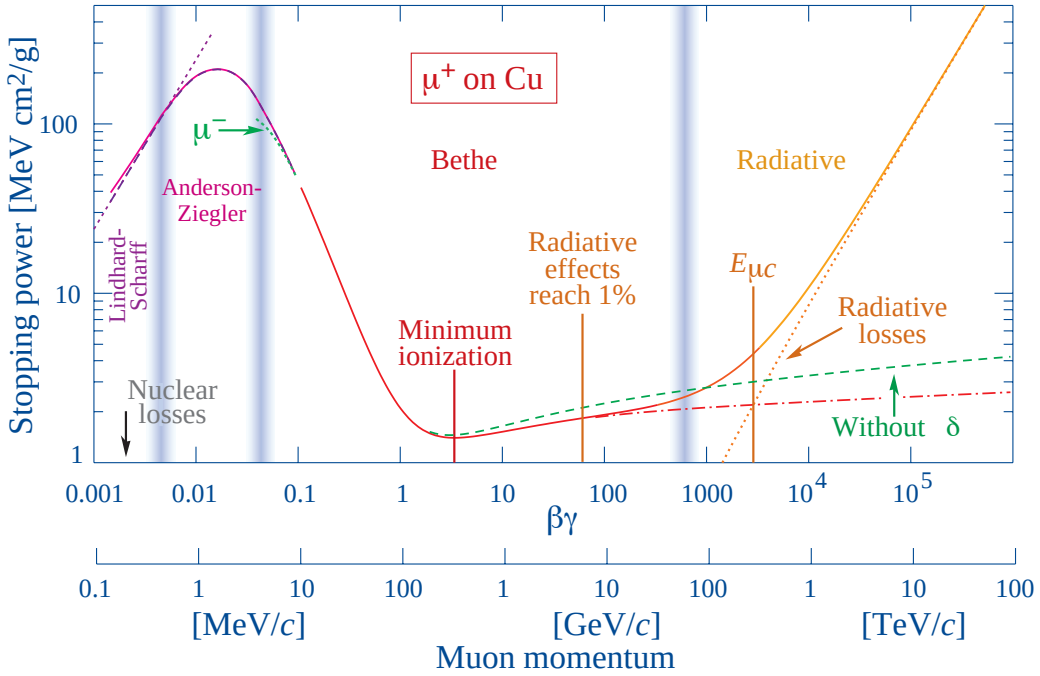

Fig. 6.1.: Stopping power for positive muons in copper as a function of $\beta\gamma = p/Mc$. Solid curves indicate the total stopping power. The short dotted lines labelled "μ^-" illustrate the Barkas effect, the dependence of stopping power on projectile charge at very low energies. In the radiative region, dE/dx is not a simple function of β any more [63].

where T is the initial kinetic energy, M is the mass of the colliding nucleus at rest, m is the mass of the incident particle, and ϕ is the angle of the recoil nucleus after the collision, defined with respect to the incident direction of the projectile. The maximum transfer of energy occurs when $\phi = 0$.

The quantum-mechanical calculation of the stopping power (i.e. the average energy loss per unity path length) has been performed by Bethe, Bloch and other authors. The formula computed in terms of momentum transfer is the following:

$$-\frac{dE}{dx} = 2\pi N_{\mathrm{a}} r_{\mathrm{e}}^2 m_{\mathrm{e}} c^2 \rho \frac{Z}{A}\frac{z^2}{\beta^2}\left[\ln\left(\frac{2m_{\mathrm{e}}\gamma^2 v^2 W_{\max}}{I^2}\right) - 2\beta^2 - \delta - 2\frac{C}{Z}\right], \qquad (6.2)$$

where $2\pi N_{\mathrm{a}} r_{\mathrm{e}}^2 m_{\mathrm{e}} c^2 = 0.1535$ MeV·cm^2/g, $r_{\mathrm{e}} = 2.817 \times 10^{-13}$ cm is the classical electron radius, m_{e} is the electron mass, $N_{\mathrm{a}} = 6.022 \times 10^{23}$ mol^{-1} is Avogadro's number, I is the mean excitation potential, Z and A are respectively the atomic number and the atomic weight of the absorbing material, ρ is the density of the absorbing material, z is the charge of the incident particle (in units of e), β is the v/c of the incident particle, $\gamma = (1-\beta^2)^{-1/2}$, δ is the density correction, C is the shell correction, and $W_{\max}$ is the maximum energy transfer in a single collision. Details about the mean excitation potential, the shell and density corrections are available in literature [94, 96].

As shown in Fig. 6.1, at non-relativistic energies higher than the "break" at $\beta\gamma \approx 0.1$,

dE/dx is dominated by the overall $1/\beta^2$ factor and decreases with increasing velocity until about $v \approx 0.96c$ (or $\beta\gamma \sim 3$), where a minimum is reached. At this point the particles are known as minimum ionizing. Beyond this mark, the term $1/\beta^2$ becomes almost constant and dE/dx rises again due to the logarithmic dependence of the Bethe-Bloch formula, although the effect is suppressed by the density correction.
For $0.01 < \beta < 0.05$ there is no satisfactory theory. For protons, Andersen and Ziegler [97] have developed phenomenological fitting formulae. For particles moving more slowly than $\approx 0.01c$ (that is the velocity of the outer atomic electrons), the electronic stopping power is proportional to β. Eventually, for even lower energies, *e.g.* for protons of less than several hundred eV, non-ionizing nuclear recoil energy loss dominates the total energy loss [98].

6.2.2 Fast electrons

Although Eq. 6.2 was derived for the case of Rutherford scattering of heavy particles it also holds for incident electrons at low energy. The scattering of electrons in matter is more complex because electrons have a small mass, and consequently relativistic corrections become important for kinetic energies as low as several hundred keV. In addition electron's paths suffer large deviations because its mass is equal to that of the orbital electrons with which it is interacting. Therefore, a much larger fraction of its energy can be lost in a single interaction. Electron-nuclear interactions can sometimes occur, and suddenly change the electron direction. The energy loss due to ionization and excitation – a physical quantity similar to the one shown in Eq. 6.2 – becomes.:

$$-\left(\frac{dE}{dx}\right)_{\mathrm{c}} = \frac{2\pi e^4 N_{\mathrm{a}} Z}{m_0 v^2}\left(\ln\frac{m_0 v^2 E}{2I^2(1-\beta^2)} - (\ln 2)(2\sqrt{1-\beta^2}-1+\beta^2) + (1-\beta^2) + \frac{1}{8}(1-\sqrt{1-\beta^2})^2\right), \tag{6.3}$$

where $m_0 = m_{\mathrm{e}}$ is the mass of the particle, and the other symbols carry the same meaning that in Eq. 6.2.
Another difference from heavy charge particles is that the energy can be lost by radiative processes, such as *bremsstrahlung*, from any position along the electron track. The linear energy loss caused by this radiative process is:

$$-\left(\frac{dE}{dx}\right)_{\mathrm{r}} = \frac{N_{\mathrm{a}} E Z(Z+1)e^4}{137 m_0^2 c^4}\left(4\ln\frac{2E}{m_0 c^2} - \frac{4}{3}\right). \tag{6.4}$$

The m_0^2 factor in the denominator of the multiplicative term suggests that the contribution of radiative losses is negligible for heavy charge particles. Radiative losses are most important for high electron energies and for absorber materials of

large atomic number. The ratio of the specific energy losses is given approximately by:

$$\frac{(dE/dx)_{\mathrm{r}}}{(dE/dx)_{\mathrm{c}}} \approx \frac{EZ}{700}, \tag{6.5}$$

where E is expressed in MeV.

6.2.3 Positrons

The Coulomb interactions are present for either positive or negative charge of the particle, and the impulse and energy transfer for particles of equal mass are about the same. For this reason, there is no difference in the tracks of positrons and electrons in an absorber. However, at the end of the positron track annihilation occurs and radiation is emitted, corresponding to two 0.511 MeV photons. These photons are very penetrating compared with the range of the positron, and can cause a deposition of energy far from the original position track.

6.3 Interaction of photons

6.3.1 Introduction

There are three major types of possible interaction mechanisms that play a role in radiation measurements: photoelectric absorption, Compton scattering, and pair production. These processes result in disappearance or scattering at a large angle of the incident photon. Fig. 6.2 shows the cross-section of main photon interactions in a volume of argon. These effects are discussed in the following.

6.3.2 Photoelectric absorption

The effect in which a photon disappears by transferring all its energy to an atom is called photoelectric absorption, and was first correctly explained by Einstein in 1905, contributing to the quantum revolution in physics. In place of the photon, the atom ejects a electron (called photoelectron) from one of its bound shells. The most probable origin of the photoelectron is the K shell of the atom, which is the most tightly bound. The resulting energy of the photoelectron is:

$$E_{\mathrm{e}} = h\nu - E_{\mathrm{b}}, \tag{6.6}$$

where E_{b} is the binding energy of the photoelectron in its shell of origin. If the energy of the photon is greater than a few hundred keV, the photoelectron will carry

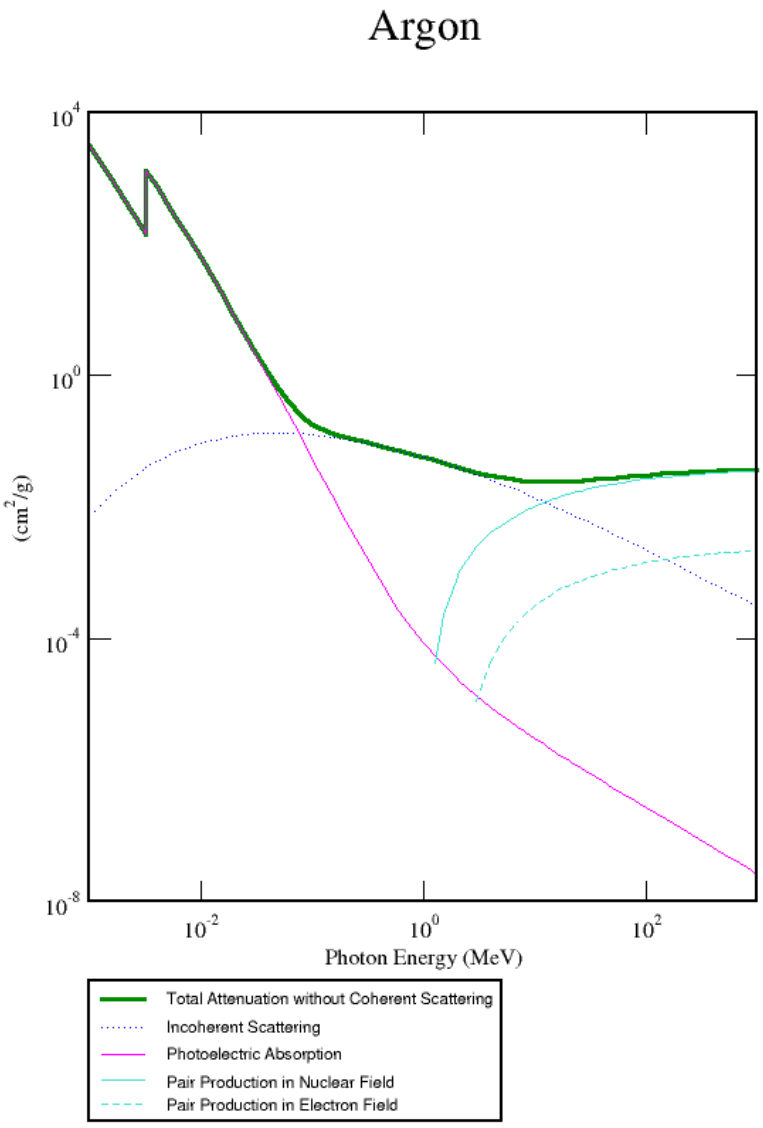

Fig. 6.2.: Normalised cross-section expressed in cm^2/g of the main photon interaction in a volume of argon. The Compton effect is called here "incoherent scattering". The total cross-section is also represented [99].

off the majority of it.
A consequence of the photoemission is the creation of an ionized atom with a vacancy in one of its bound shells. Such a vacancy is immediately filled through the capture of a free electron coming from other shells of the atom. One or more X-ray photons may be generated as a consequence. They can escape the detector, or be reabsorbed through photoelectric absorption, causing the emission of an Auger electron.
Photons of relatively low energy undergo a photoelectric process as the predominant interaction. A rough approximation for the probability of photoelectric absorption per atom, over all ranges of E_γ and Z is

$$\tau \approx \text{constant} \times \frac{Z^n}{E_\gamma^{3.5}}, \tag{6.7}$$

where the exponent n varies between 4 and 5 over the E_γ region of interest. The process is therefore enhanced for absorber materials of high atomic number Z.

6.3.3 Compton scattering

Compton scattering consists in the deflection of the incoming photon through an angle θ, after the interaction with the absorbing material. Only a portion of the photon energy is therefore transferred to the electron, assumed to be initially at rest. The transferred energy can vary from zero to a large fraction of the incident one, according to the angle of scattering. The conservation of energy and momentum (neglecting the atomic binding of the electron and assuming that the electron is free) lead to the following relation:

$$h\nu' = \frac{h\nu}{1 + \frac{h\nu}{m_0 c^2}(1 - \cos\theta)}, \tag{6.8}$$

where $h\nu'$ and $h\nu$ are respectively the energy of the final and incident photon, $m_0 c^2$ is the rest-mass energy of the electron (0.511 MeV), and θ is the angle between the incident and scattered directions. Even in the extreme $\theta = \pi$, some of the original energy is kept by the incident photon. The probability of Compton scattering per atom of the absorber increases linearly with Z. The differential scattering cross-section, known as the Klein-Nishina formula, gives the angular distribution of scattered photons:

$$\begin{aligned}\frac{d\sigma}{d\Omega} = Z r_0^2 \left(\frac{1}{1 + \alpha(1 - \cos\theta)}\right)^2 \left(\frac{1 + \cos^2\theta}{2}\right) \\ \left(1 + \frac{\alpha^2 (1 - \cos\theta)^2}{(1 + \cos^2\theta)[1 + \alpha(1 - \cos\theta)]}\right),\end{aligned} \tag{6.9}$$

where $\alpha \equiv h\nu/m_0c^2$ and r_0 is the classical electron radius. The angular distribution indicates a strong tendency for forward scattering at high values of the photon energy.

6.3.4 Pair production

The process of pair production becomes energetically possible when the photon energy exceeds 1.02 MeV, that is twice the rest-mass energy of an electron. The interaction must take place in the Coulomb field of a nucleus. As the created positron will annihilate after slowing down in the medium, two annihilation photons are normally produced as secondary products of the interaction. There is no simple expression for the probability of pair production per nucleus, although its magnitude has an approximate dependence with the square of the absorber atomic number.

6.3.5 Coherent scattering

In the coherent, or Rayleigh, scattering there is neither excitation nor ionization of the atom, and the incident photon maintains its original energy after the scattering event. Only the direction of the photon is changed, and the probability for this process is significant only for photon energies below a few hundred keV for common materials, and is most prominent in high-Z absorbers. The practical importance of this process is rather negligible, and will be ignored in the following discussions, as no energy is transferred.

6.3.6 Photon attenuation

The result of a transmission experiment, where monoenergetic photons are collimated into a narrow beam and strike a detector after passing through an absorber of variable thickness, is a simple exponential attenuation for the photons (caused by absorption or scattering). The probability of occurrence per unit path length in the absorber of each of the interaction processes is fixed. The sum of the probabilities is then simply:

$$\mu = \tau(\text{photoelectric}) + \sigma(\text{Compton}) + \kappa(\text{pair}), \tag{6.10}$$

and is called the linear attenuation coefficient. The number of transmitted photons I is expressed as a function of the number without an absorber I_0 as:

$$I = I_0 e^{-\mu x}. \tag{6.11}$$

The mass attenuation coefficient is widely used, as it includes the dependence from the density ρ of the medium:

$$\text{mass attenutation coefficient} = \frac{\mu}{\rho}. \tag{6.12}$$

The mass attenuation coefficient does not change with the physical state of a given absorber. The resulting coefficient for a compound or mixture of elements is obtained from a weighted sum:

$$\left(\frac{\mu}{\rho}\right)_{\mathrm{c}} = \sum_i w_i \left(\frac{\mu}{\rho}\right)_i, \tag{6.13}$$

where the w_i factors represent the weight fraction of element i in the compound or mixture. The attenuation law for photons now takes the form:

$$I = I_0 e^{-(\mu/\rho)\rho x}, \tag{6.14}$$

where the product ρx, the mass thickness of the absorber, is now the significant parameter that determines its degree of attenuation.

6.4 Elements of neutron physics

6.4.1 Neutron interactions

As neutrons have no electric charge, they cannot interact through the Coulomb force, just as the photons. A neutron typically interacts with a nucleus of the absorbing material, but it can travel through many centimetres of matter without undergoing any type of interaction. When it interacts though, the neutron either disappears to be replaced by one or more secondary radiations, or the energy or direction of the neutron is changed significantly. The resulting secondary radiations are almost always heavy charged particles, in contrast to photons. What generates them is either a neutron-induced nuclear reaction, or the nuclei of the absorbing material itself, having gained energy as a result of neutron collisions.
The probabilities of the different types of neutron interactions are strongly dependent on the neutron energy. Neutron are indeed usually sorted by energy range, as follows:

- Thermal neutrons are in thermal equilibrium with the ambient temperature, that is they have an energy lower than 0.5 eV (where the "cadmium cut-off" takes place), a most probable energy of $kT = 0.025$ eV, where k is the Boltzmann constant, and a mean energy of $3/2\,kT = 0.038$ eV.

- Epithermal neutrons have an energy between 1 eV and 10 keV.

- Fast neutrons have an energy between 10 keV and 20 MeV.
- High-energy neutrons have an energy between 20 MeV and 1 GeV.
- Relativistic neutrons have an energy above 1 GeV, corresponding to the mass energy of a nucleon (≈ 940 MeV), for which relativistic effects become non-negligible.

Neutrons undergo several processes, which depend, as anticipated, on the neutron energy and the properties of the target material. Elastic collisions of neutrons with substantial transfer of kinetic energy occur only in low-A and hydrogenous materials such as water, concrete and polyethylene. In fact, according to Equation 6.1, if the target nucleus is composed of one proton (^{1}H) of mass m_p, thus $M = m_\mathrm{p} \approx m_\mathrm{n}$, the maximum energy transfer is $\Delta T_\mathrm{max} \approx T$ and the mean energy transfer is $\Delta T_\mathrm{max} \approx T/2$.
Inelastic scattering in the case of neutrons is in fact a neutron capture followed by the emission of a neutron with a lower energy and in a different direction than the initial neutron. The absorber nucleus is potentially left in an excited state and can decay through photon channels. If on the contrary the nucleus is left in its ground state, it is then considered the same as an elastic scattering.
The capture process is then very similar to an inelastic scattering, except there are other particles than one neutron in the final state. It can involve the emission of an electron, positron, proton, photon (in which case the process is called radiative capture), deuteron, triton, α particle, or more than one neutron. The energy of the incident neutron then needs to exceed some threshold specific to the capture reaction. The secondary particles are called prompt if the decay time is very short; if on the contrary it is very long, up to thousands of years, the material is considered as activated.
The infamous fission process takes place in high-Z materials when the neutron capture leads to the nucleus break-up, producing heavy fragments and nucleons with high kinetic energy.
Eventually, spallation reactions occur when the neutron is energetic enough to interact with individual nucleons inside the absorber nucleus. An intra-nuclear cascade inside that nucleus may occur and produce different kinds of high-energy particles (see Sec. 6.4.3 for more details).

6.4.2 Neutron cross-sections

Accurate neutron cross-section databases are obtained by combining experimental results, and theoretical or empirical computations. Several collaborations take care of producing this information. The main existing libraries are the US Evaluated Nu-

clear Data File (ENDF) by the National Nuclear Data Center (NNDC, by Brookhaven National Laboratory), the European Joint Evaluated Fission and Fusion Library (JEFF, coordinated by the Nuclear Energy Agency), and the Japanese Evaluated Nuclear Data Library (JENDL, by the Japan Atomic Energy Agency). Each of these agencies publish up-to-date databases on their website. Most of the libraries give the neutron cross-sections over the range from thermal to 20 MeV, but recently-added ENDF and JEFF libraries extend to 150 MeV for some isotopes.
Fig. 6.3 shows elastic and inelastic cross-section for low-, medium-, and high-Z materials. Elastic scattering is often the dominant component to the total cross-section. However, thermal neutrons may be captured by atomic nuclei and, depending on the nature of the target nucleus, capture reaction (low-Z materials) or nucleus fission (high-Z materials) may occur. Over the thermal and epithermal ranges, capture processes are characterized by a decreasing cross-section following a $1/v$ law, where v is the neutron velocity. For non-elastic processes such as inelastic scattering, capture and fission, strong discrete peaks called resonance peaks occur at neutron energies specific to a particular nuclide because of the quantum properties of the nucleus. For non-fissionable nuclei, the radiative capture is the only component to the non-elastic cross-section over the thermal and epithermal ranges, while other capture reactions occur only above energy thresholds in the fast-neutron energy range.

6.4.3 Intra-nuclear cascade models

Nuclear reactions of high-energy heavy particles are very complex processes. When proton or neutrons carry 450 MeV of kinetic energy, their de Broglie wavelength is of the order of the average distance between nucleons ($\sim$ fm $= 10^{-15}$ m). Above this energy, the interactions can be described as individual nucleon-nucleon collisions [100]. In fact, experimental nucleon-nucleon cross-sections are used whenever possible. However, interference between nucleons can be important and affect the particle-nucleon interaction [101]. If the transferred energy is larger than ~ 150 MeV the nucleon involved in the interaction can escape from the nucleus. Below this energy, in turn, it may collide with other nucleons, leading to the so-called intra-nuclear cascade (INC), represented in Fig. 6.4. Non-nucleon particles such as the pion may also be produced during the cascade and escape from the nucleus. The first standard Monte Carlo simulation methods for INC were implemented by Bertini in 1968 [102]. After the INC, the energy is distributed over the nucleus in a non-equilibrium state, which is difficult to evaluate. The exciton model [101] is then used to describe a pre-equilibrium phase, in which intra-nuclear collisions give rise to an increasing number of excited particles and holes (the excitons), accompanied by nucleon emission, eventually leading to an equilibrated but excited nucleus [103]. The remaining excited nucleus emits, through a process known as evaporation, particles such as photon, neutron, proton, deuton, triton, and α. The evaporation

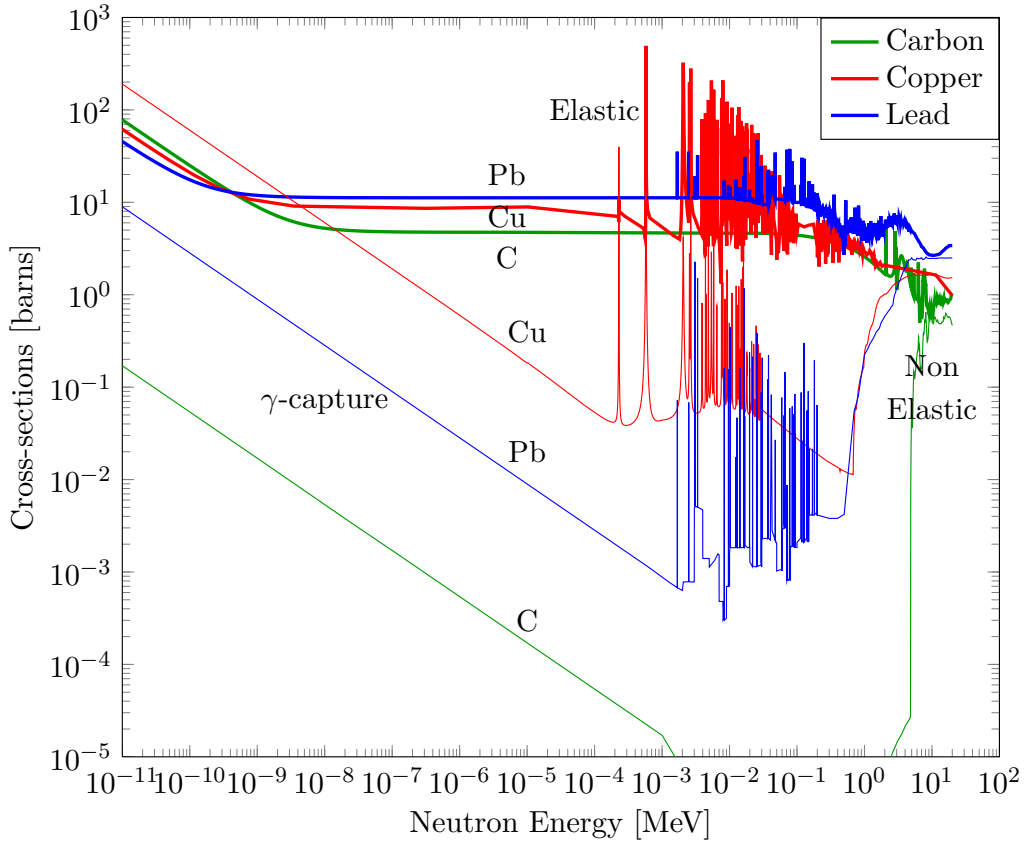

Fig. 6.3.: Neutron cross-sections for C ($Z = 6$) in green, Cu ($Z = 28$) in red and Pb ($Z = 82$) in blue, ENDF library. Reproduced from NNDC.

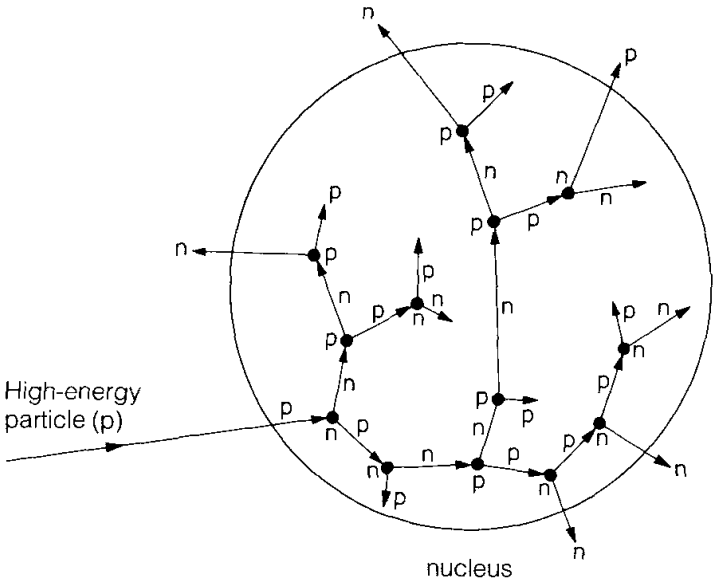

Fig. 6.4.: Schematic view of reaction cascades in nuclei set off by high-energy particles (p = proton, n = neutron) [105].

is described by a model originally developed by Weisskopf [104] that assumes complete energy equilibration before particle emission, and re-equilibration of excitation energies between successive evaporation emissions. As a consequence, the angular distribution of emitted particles is isotropic. The emission of particles is computed until the excitation energy fall below a cut-off. In some extreme cases, such as in light nuclei or if the excitation energy is much larger than the binding energy, break-up models can be applied and the nucleus explodes into neutrons and protons. Intranuclear cascade and pre-equilibrium, evaporation, fission and decay phases are usually known as spallation reactions.
Significant progress was made in this field in the last fifty years. The increasing understanding of nuclear properties and particle physics allows the use of more accurate models for each stage of the cascade: nucleons distribution inside the nucleus, quantum effects, quantum dynamics, exciton and evaporation models, transition models between each stage, etc.

6.5 GEANT4 toolkit

6.5.1 Introduction

GEANT4 is an object-oriented simulation toolkit that provides a diverse, wide-ranging, yet cohesive set of software components to be used for simulating the passage of particle through matter [106, 107]. Among GEANT4 features are modularity

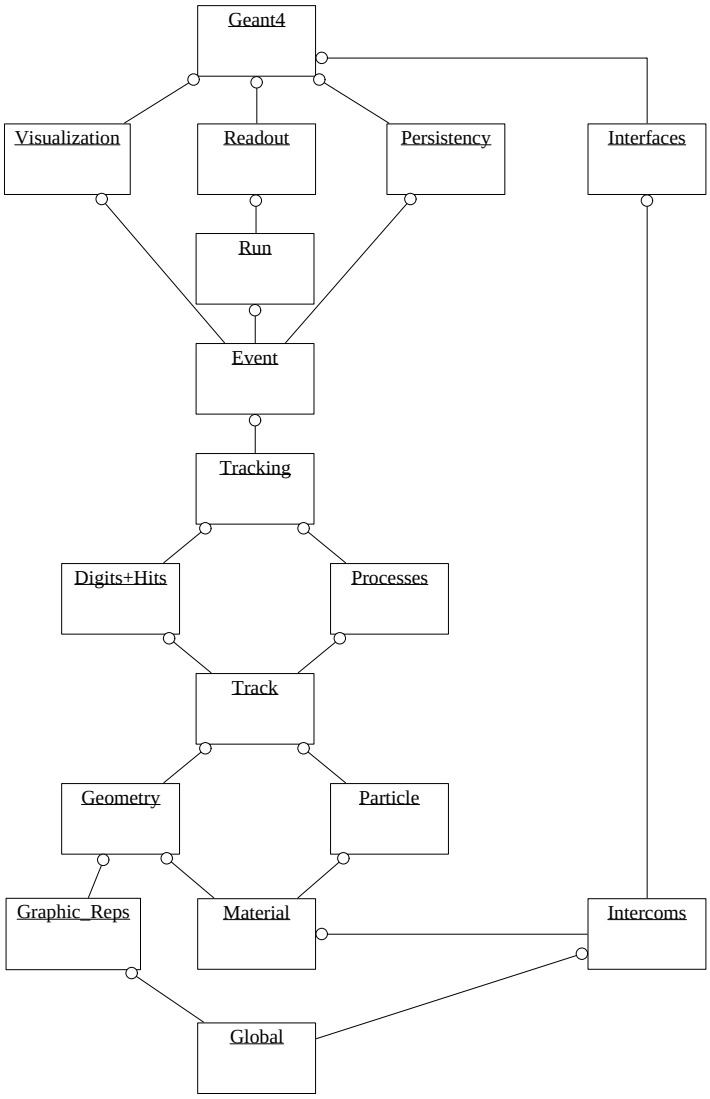

Fig. 6.5.: Top Level Category Diagram of the GEANT4 toolkit. The open circle on the joining lines represents a using relationship; the category at the circle end uses the adjoined category [106].

and flexibility, and the fact that its implementation of physics is transparent and open to user validation. The main domains of the simulation of the passage of particles through matter are the following: geometry description, particle definition, navigation and tracking, physics models for electromagnetic (EM), hadron and optical interactions, event scoring, input/output and visualization. Fig. 6.5 illustrates the modular and hierarchical structure for the toolkit, where domains are linked by a uni-directional flow (i.e. non circular) of dependencies. Categories at the bottom of the diagram are used by virtually all higher categories.

GEANT4 uses an internal database of isotopes, elements and materials. Most of the data is obtained from the NIST database [108]: natural isotope compositions, isotope masses, mean ionization potentials for elements and materials, material densities and atomic composition of materials. For all the simulations presented

in this study the GEANT4 version 10.1 patch 2, that was the most recent when this work was performed, was used. The version 10.2 was released on December 4th 2015. Among other improvements, it affects the energy response in hadronic showers, introduces a new model for nuclear gamma de-excitation, and extends the treatment of low-energy neutrons (below 20 MeV) to charged particles: proton, deuteron, triton, ^{3}He and alpha, with energies up to 200 MeV. Future developments of the work presented hereby will certainly need to face these updates.

6.5.2 Physics simulation

Standard electromagnetic physics

EM interactions of photons and charged particles with matter are implemented in two electromagnetic packages. The Standard EM package includes simulation of ionization, bremsstrahlung, gamma conversion and other EM interactions of particles with energies from 1 keV up to 10 PeV. The Low-energy EM package includes alternative models for simulation of photon, electron, hadron and ion interactions. It also includes models for simulation of atomic relaxation and other atomic shell effects, besides unique models for biological systems. The interactions described by this package go down to 100 eV. The difference between proton stopping powers for different materials provided by the Standard EM package and the evaluated data is well inside 2%, which is less than systematic uncertainty of the data [107].

Hadron physics

QCD is the well-established theory of strong interactions, but most of the hadron interactions that occur when particles cross matter happen in the non-perturbative region of the theory, where the cross-sections are not computable. This is why, in GEANT4 applications, hadron interactions are handled by different models which cover the high, medium and low energy domains. The current standard set of models for high energy physics includes the quark-gluon string (QGS) [109], the Fritiof model (FTF) [110], the Bertini-style cascade [103] and the Binary cascade [111]. These models are theory-based – as opposed to pure parametrization – and explicitly conserve energy-momentum and most quantum numbers.
The QGS model is used in the approximate range 15 GeV - 50 TeV, and its simulation predictions are in good agreement with experimental data at high energies [112]. However, as the validity of lower energy cascade models cannot go higher than 10 GeV, a parametric model was previously used to fill the gap, resulting in discontinuities in some of the physics observables [113]. This is why the alternative

FTF model gained more and more interest in the recent years, as it extends into the intermediate energy range as low as 3 GeV. Therefore, it can directly overlap with cascade models. This model has a good agreement with the nuclear reaction data of projectiles of momenta between 3 and 15 GeV/c [114].
The Bertini-style cascade handles incident protons, neutrons, pions, kaons and hyperons up to 10 GeV, as anticipated. Among the features it includes, three of these are: classical scattering without matrix elements, free hadron-nucleon cross sections and angular distributions taken from experiments, and step-like nuclear density distributions and potentials. The projectile enters the nucleus and is then transported along straight lines through the nuclear medium and interacts according to the mean free path determined by the free hadron-nucleon total cross section. As cascade collisions occur, an excited residual nucleus is built up. In the final stage, nuclear evaporation happens as long as the excitation energy is large enough to remove a neutron or α particle from the nucleus. Photon emission then occurs at energies below 0.1 MeV. The agreement with data is reasonable at low energies (100-200 MeV) and is very good at 800 MeV; at 3 GeV the predictions are good at forward and backward angles [112].
The Binary cascade model is an alternative to the Bertini-style cascade: it is an hybrid between a classical cascade and a full quantum-molecular dynamics model. It is meant to simulate incident protons and neutrons with $0 < E_{\text{kin}} < 3$ GeV, pions with $0 < E_{\text{kin}} < 1.5$ GeV, and light ions with $0 < E_{\text{kin}} < 3$ GeV/A, but it works reasonably well up to 10 GeV. In particular, the Binary cascade better describes production of secondary particles produced in interactions of protons and neutrons with nuclei, when compared with Bertini-style cascade.
Cascade models are generally not valid for energies below a few tens of MeV. Below some A-dependent cut, the residual nucleus and exciton system are passed to the GEANT4 precompound model which handles the nuclear de-excitation. It is valid in the range below 200 MeV, for any excited nucleus. Modern data are used to improve the competition between particle emission and internal transition between exciton states [115]. The control goes directly to the precompound model if the primary particle is below 45 MeV.
Other models exist, in order to fill in the gaps in coverage and extend the capabilities of the package:

- The high precision neutron model for energies from thermal to 20 MeV. This model interfaces GEANT4 to the low energy nuclear data from Evaluated Nuclear Data File (ENDF) libraries, developed at the Lawrence Livermore National Laboratory (LLNL). During the simulation, the cross-sections based on the materials in the geometry are initially requested; the neutrons are then tracked according to their mean free path; eventually, the library is consulted for the final state products of the reaction [115].

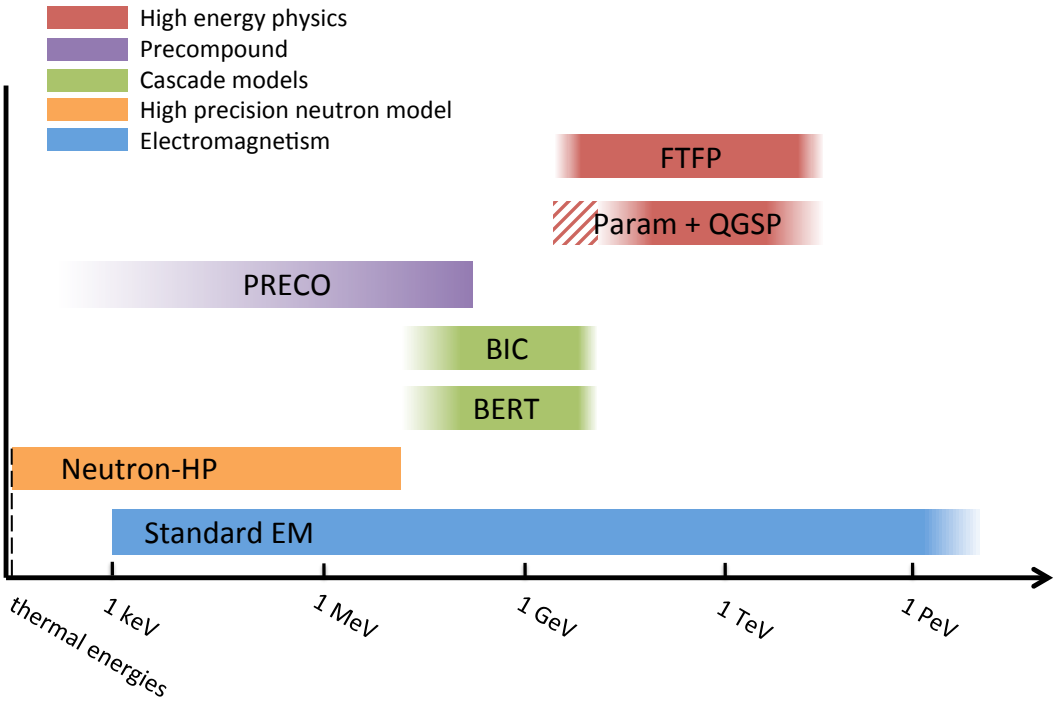

Fig. 6.6.: Qualitative summary of the coverages in energy of the main models involved in this work. They are grouped in different colors, depending on the role they carry: high energy physics library, precompound model, cascade model, high precision neutron model, and electromagnetic library. The dashed area represents the parametrised model covering the gap between QGSP and the cascade models. Notice that to avoid discontinuities in the simulation response over a wide range of energies, the models must overlap each other. The gradients of color provide qualitative information about the agreement of the various models with data.

- Several elastic scattering models optimized for various energy ranges.
- Several types of nuclear de-excitation codes, including fission, Fermi breakup and multi-fragmentation.

The coverages in energy of the main models used in this work have been summarised in Fig. 6.6.

6.6 CMS Background evaluation

6.6.1 Introduction

The energy and luminosity regime of the LHC during Phase II are reflected in a higher collision rate, and therefore in an extreme radiation environment. The signal identification is complicated by high background particle rates. The impact on the performance of the detectors is significant and, in extreme cases, it can lead them to

be inoperable: the high occupancy and hit rate can lead to inefficiencies in detector response, degraded resolutions and momentum mismeasurements. It can also cause an unacceptably high rate of track misreconstructions which will contribute to the trigger rate; not to mention that a high flux of incident particles can lead to radiation damage of the front-end electronics. When a new detector is planned to be installed in a region of the experiment, an accurate evaluation of the expected background rates is therefore crucial. This is true in particular for the forward region of CMS, where the main signal is given by muons and the backgrounds are especially high. The main contribution to the CMS cave backgrounds are the neutrons, together with the secondary particles coming from the neutrons interaction with matter. The neutron background has a long lifetime, as neutrons can propagate for several seconds without interacting. They are produced in primary pp interactions, and their main source for the muon system are the interactions in the beam pipe and lower endcap, the hadron forward calorimeter, the shielding and the collimator region. Most of the background photons are produced in thermal neutron capture and the photon energy is characteristic of the capturing nucleus. Background electrons and positrons come from the following reaction chain:

$$\text{thermal neutron} \rightarrow \gamma \rightarrow \mathrm{e}^{+}\mathrm{e}^{-}, \tag{6.15}$$

where the thermal neutron is captured by a nucleus and the emitted photon undergoes one of the possible electromagnetic reactions. The resulting electrons and positrons are able to produce detectable amounts of ionization in gaseous detectors.

6.6.2 Evaluation of the backgrounds due to long-lived neutrons

The energy and angle distributions at the CMS GE1/1 station of the neutron, photons, electron and positron background particles were obtained through a dedicated FLUKA simulation [116, 117, 118]. Among other features, FLUKA allows the evaluation of the fluxes of long-lived neutrons and secondary particles produced in interactions of neutrons with the material of the subdetectors and surrounding materials. Secondary particles capable of reaching GE1/1 chambers are typically produced at the edges of the volumes surrounding the enclosures where chambers are positioned. Once rescaled by the appropriate response of the detector, these fluxes eventually provide the hit rate (see Sec. 6.7).
The CMS geometry has been interfaced to the FLUKA package, including a detailed description of the dimensions and material composition of each of the detector subsystems. The version of the geometry that was used to estimate the particle flux is the one corresponding to Run2 configuration: it accounts for the improvements to the central beampipe and to the muon chamber shielding. The beam energy has been set-

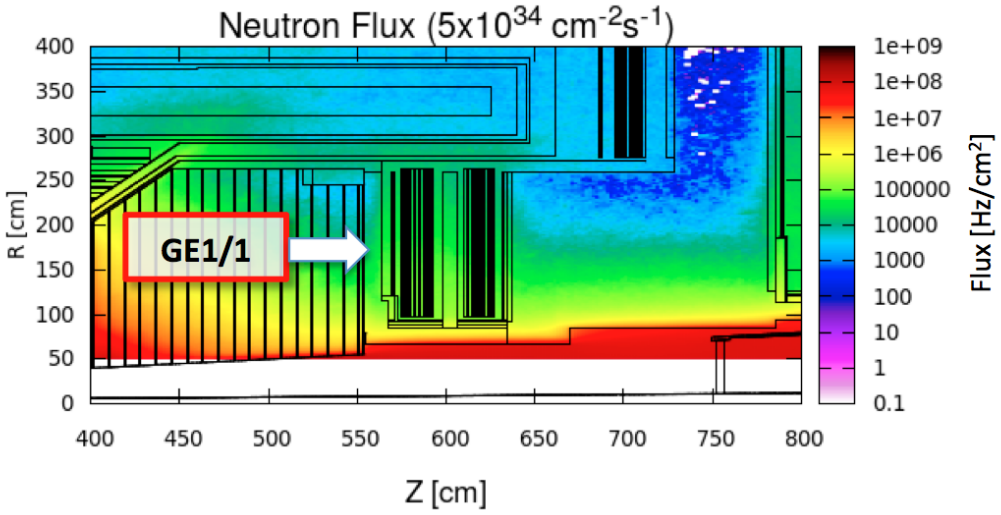

Fig. 6.7.: 2D flux map for neutrons normalized to an instantaneous luminosity of 5×10^{34} cm^{-2}s^{-1} and overlaid on the diagram showing the detector elements.

up at 7 TeV; the structure of minimum bias events is estimated using extrapolations from experimental data at lower energy. The energy cut-off for neutrons has been set at 10^{-14} GeV; below this energy, the particles are no longer tracked. Other cut-offs are: 1 keV for hadrons, 3 keV for photons, and 30 keV for electrons and positrons. Photons, electrons and positrons may have significantly higher cut-offs depending on the detector region. Some of the results of the simulation are shown in Fig. 6.7 and 6.8.

Tab. 6.1 reports the simulation predictions for the flux of background particles through the volume where the GE1/1 chambers will be installed. The (r, z) coordinates correspond to the bottom, lower middle, higher middle, and the top parts of the chamber. From these results, one can estimate the total neutron fluence and the total radiation dose accumulated by the GE1/1 chambers. After accumulating 3000 fb^{-1} of integrated luminosity, the total dose amounts to 1 kGy at the highest eta region of the detector.

6.7 GEANT4 simulations

6.7.1 Introduction

The GE1/1 response to the background environment, that will be called from now on 'sensitivity', is evaluated using a dedicated standalone GEANT4 simulation. The sensitivity is the probability for a given type of particle to generate a spurious signal in the detector. It depends on the particle energy and the direction it crosses the

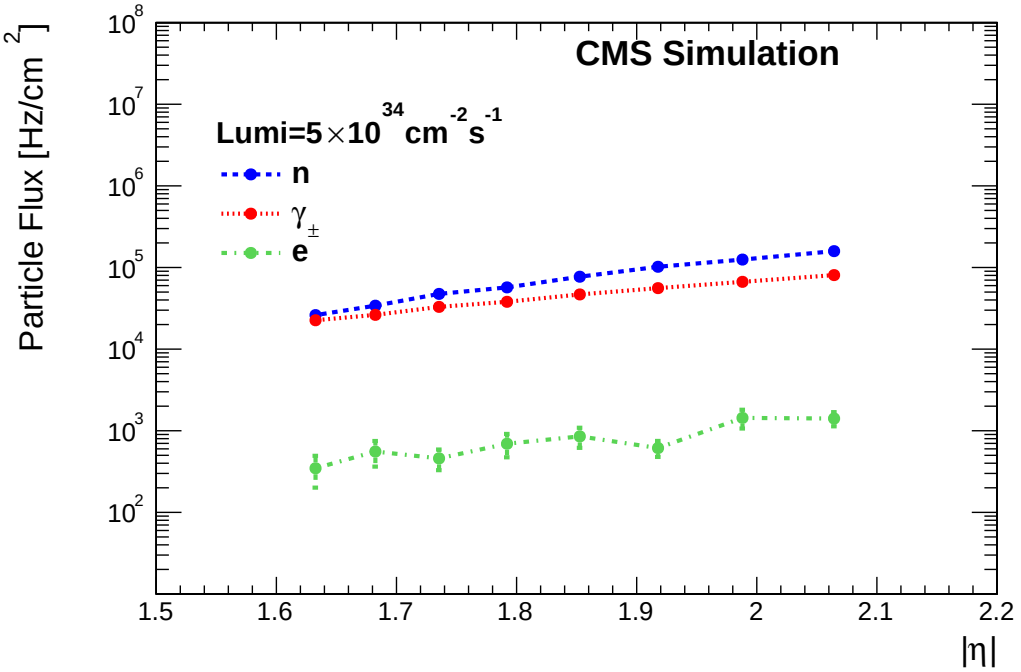

Fig. 6.8.: Particle flux for GE1/1 region as a function of the pseudorapidity range assuming an instantaneous luminosity of 5×10^{34} cm^{-2}s^{-1}.

chamber. When neutrons or photons enter a GEM chamber, they interact with the material of the detector and generate secondary particles that can reach the gas gaps and begin an avalanche process that will eventually induce a signal on the strips. Electrons and positrons can either reach the gas gaps, or cause electromagnetic showers by interacting with the inner structure of the chamber, generating secondary particles. The particle-dependent energy ranges of the simulated CMS background are shown in Fig. 6.9; the energy ranges considered in GEANT4 reflect this estimation and were chosen as reported on Tab. 6.2.

6.7.2 Evaluation of the Physics Lists

While GEANT4 does not offer one single model to cover the entire variety of physical processes, as each model has certain limitation in its validity, the models, however, can be combined to cover practically any use-case. In particular, as reported in Tab. 6.2, the current application needs to satisfy a particularly large range of energies (e.g.: eleven orders of magnitude for the neutrons). This concept is known as a physics list (PL), where every two adjacent models may have an overlap in their validity range. While the fabrication of a PL is, in principle, a choice of a user, the GEANT4 toolkit is distributed with a number of pre-fabricated PLs, for the convenience of many user applications.
The motivations that exist behind every model, already illustrated in Sec. 6.5.2,

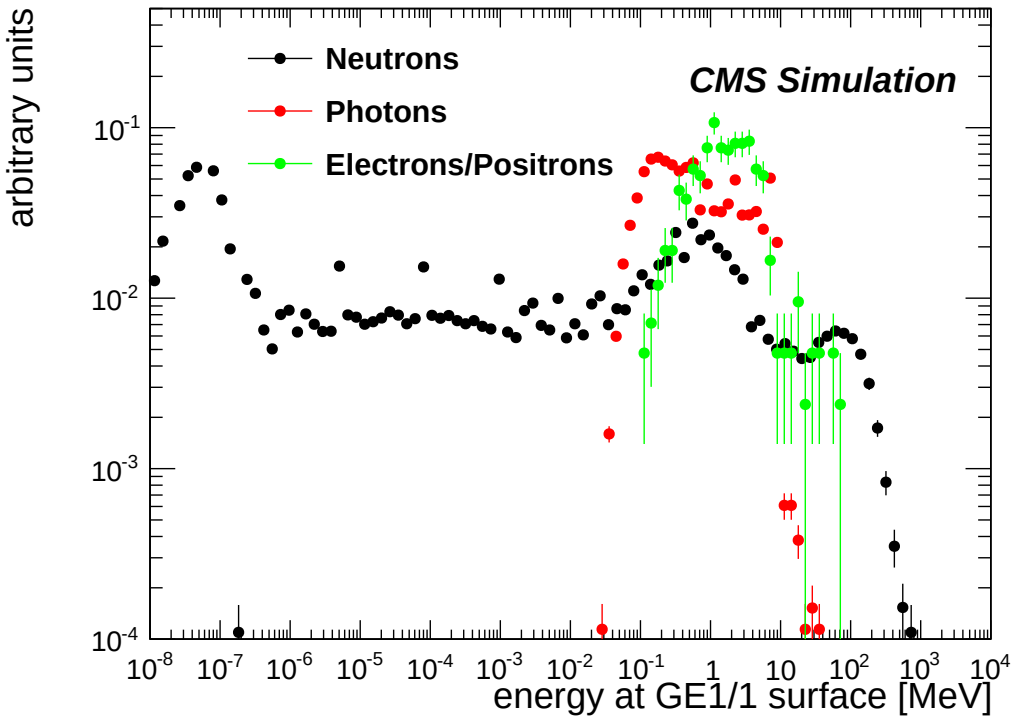

Fig. 6.9.: Energy spectrum of incident particles crossing the GE1/1 chambers predicted by FLUKA. The distributions are normalized to 1; this explains the fact that the y axis is dimensionless. The simulation reproduces the conditions for a LHC luminosity of 5×10^{34} cm^{-2}s^{-1}.

Particle type	r (cm)	z (cm)	Flux (Hz/cm^2) for $\mathcal{L} = 5 \times 10^{34}$ cm^{-2} s^{-1}	Flux uncert. (%)
Neutrons	150	560	$1.5 \cdot 10^5$	1.5%
	170	560	$1.0 \cdot 10^5$	1.7%
	190	560	$0.6 \cdot 10^5$	1.9%
	210	560	$0.4 \cdot 10^5$	2.3%
Photons	150	560	$7.6 \cdot 10^4$	1.8%
	170	560	$5.6 \cdot 10^4$	2.0%
	190	560	$4.1 \cdot 10^4$	2.1%
	210	560	$3.0 \cdot 10^4$	2.3%
Charged	150	560	$1.3 \cdot 10^3$	16.4%
	170	560	$9.8 \cdot 10^2$	21.4%
	190	560	$6.2 \cdot 10^2$	24.0%
	210	560	$5.2 \cdot 10^2$	26.0%

Tab. 6.1.: FLUKA predictions for the particle fluxes through the volume where the GE1/1 chambers are to be installed. Flux values are provided for each particle type and four point in the (r, z) coordinates. The energy cut-off for neutrons has been set at 10^{-14} GeV; below this energy, the particles are no longer tracked. Other cut-offs are: 1 keV for hadrons, 3 keV for photons, and 30 keV for electrons and positrons. Photons, electrons and positrons may have significantly higher cut-offs depending on the detector region. The flux uncertainty is purely statistical.

Particles	Energy range (MeV)
neutrons	$10^{-8} - 10^3$
photons	$0.029 - 100$
electrons/positrons	$0.15 - 75$

Tab. 6.2.: Energy ranges of every type of simulated particle, reflecting the incoming flux provided by FLUKA and reported in Fig. 6.9.

constitute a necessary but not sufficient information to proceed with the choice of a specific combination or models. The best way to discriminate between different PLs is to validate simulations with existing experimental measurements. While very few measurements of the Triple-GEM response to background particles exist, in the past decade many measurements were done with RPCs, and are therefore available in literature. This is especially important to evaluate the simulation of a detector geometry when hadron physics is involved, as the standard electromagnetic simulation libraries are well established. There is no reason to assume that GEANT4 is unable to provide the correct physics modelling in the range of our interest, but it is nevertheless important to demonstrate that the current application is reliable, as it must extract and correctly analyse the involved physical quantities. Besides, it is possible that a particular model is better suited than an other for our particular case of interest.

Unlike GEANT3, in GEANT4 there are no tracking cuts. All particles produced are tracked down to zero range. Crucial parameters to be set are then the production cuts, expressed in unity of distance: to be created inside a material, a secondary particle must be able to perform inside that same material a distance at least as large as the chosen cut. For all the simulations performed the production cuts were set as follows:

particle	production cut
γ	1 μm
e^-	1 nm
e^+	1 μm
p & nuclei	0

The cut involving protons and other nuclei is crucial to compute the correct hadron sensitivity in a gaseous detector. In fact, in the physical case any nucleus can undergo elastic scattering, move into a gas gap and be accelerated by the electric field as any other positive ion, ripping out an electron from an atom and initiate an avalanche. Therefore, putting the production threshold at the lowest possible value is the way to take these cases into account in the computation of sensitivity. For PLs using neutron-HP and since version 10.1, this is a standard cut. It must be observed that, when converted to an energy value for each material, the production threshold is not arbitrarily small but has a hard coded minimum value for photons, electrons, and positrons. This value is equal to 990 eV; the production cuts that are set here reach this lower limit most of the time. In the case of protons and other nuclei the minimum value is set instead at 0 eV.

6.7.3 Electromagnetic physics validation

The current GEANT4 application response was first compared with the experimental electromagnetic cross-sections of a single material coming from NIST's XCOM Photon Cross Section Database [99]. The number of photons not absorbed by a layer of a thickness x follows the exponential law already shown in Eq. 6.11. This expression corresponds therefore to the number of photons not interacting in the layer of material. It was already discussed that a convenient way to express Eq. 6.11 is usually to replace μ with μ_ρ, where $\mu_\rho \equiv \mu/\rho$ is the mass absorption coefficient, expressed in cm^2/g, and ρ is the density of the material (see Eq. 6.14). To be able to span over a large range of energies, the validation efforts of the code have been focused on a 3 mm layer of the Ar:CO_2:CF_4 mixture ($45\% : 15\% : 40\%$). Even though most of the interactions occur in the solid components of the detector, if one considers the interaction probability of photons in the case of dense targets, it quickly saturates to 1, allowing no meaningful comparison between data and simulations.

Then, using a gaseous target, it is possible to make use of the mass absorption coefficient – also called total attenuation without coherent scattering – provided by the above mentioned reference and elaborate it in the following definition of sensitivity $S(x)$:

$$S(x) = 1 - e^{-\mu_\rho \rho x}, \tag{6.16}$$

which eventually represents the probability of interaction in a layer of material of length x. The gas mixture density is taken from GEANT4 databases at STP conditions. The tested model is `G4EmStandardPhysics`, included in the largest fraction of PL. A million events were generated per energy value. The comparison between GEANT4 and experimental data is shown in Fig. 6.10, and proves an excellent agreement between data and simulations over six order of magnitudes. The shown error bars are only statistical; the statistical uncertainties associated to the XCOM numbers are of the order of 5%, and are dominated by the ones on the photoelectric effect and the Compton scattering.

6.7.4 Hadron physics validation

Comparisons with GEANT3 simulations

The first attempt to make comparisons neutron sensitivity over a wide range of energies is done by considering the results coming from several GEANT3.21 simulations [119] available in literature [120, 121, 122] and the ones from the current GEANT4 application. The way neutrons were treated in GEANT3 is not directly comparable with state-of-the-art GEANT4 applications, so differences in the materials response are to be expected. The reason why so many results involving GEANT3 simulations are found in literature is that it has represented the state-of-the-art of the simulations packages until the mid-2000s. Many of the results obtained in preparation to the LHC machine and other experiments were done in such framework. Thereafter not all of them were updated through GEANT4. It should also be noticed that GEANT4 is not a simple update of GEANT3, it is not a simple rewriting in objected-oriented language, but a full new program based on brand new physical models and experimental data. Nowadays, a greater trust is assigned in GEANT4 results, that keep being validated and enhanced when necessary.
The references focus on simulations of the neutron sensitivity of RPC detectors in double-gap configuration with common readout strips. The gas mixture is 3% iC_4H_{10} + 97% $C_2H_2F_4$. From the simulation point of view RPC detectors are similar to the GEMs in many aspects: they are both gaseous detectors and the way the event is defined in the code is the same, namely that each charged particle produced in the gas gaps induces a signal into the read-out strips; if more than one charged particle reaches the gas gap, only the first one is assumed to produce a signal during the

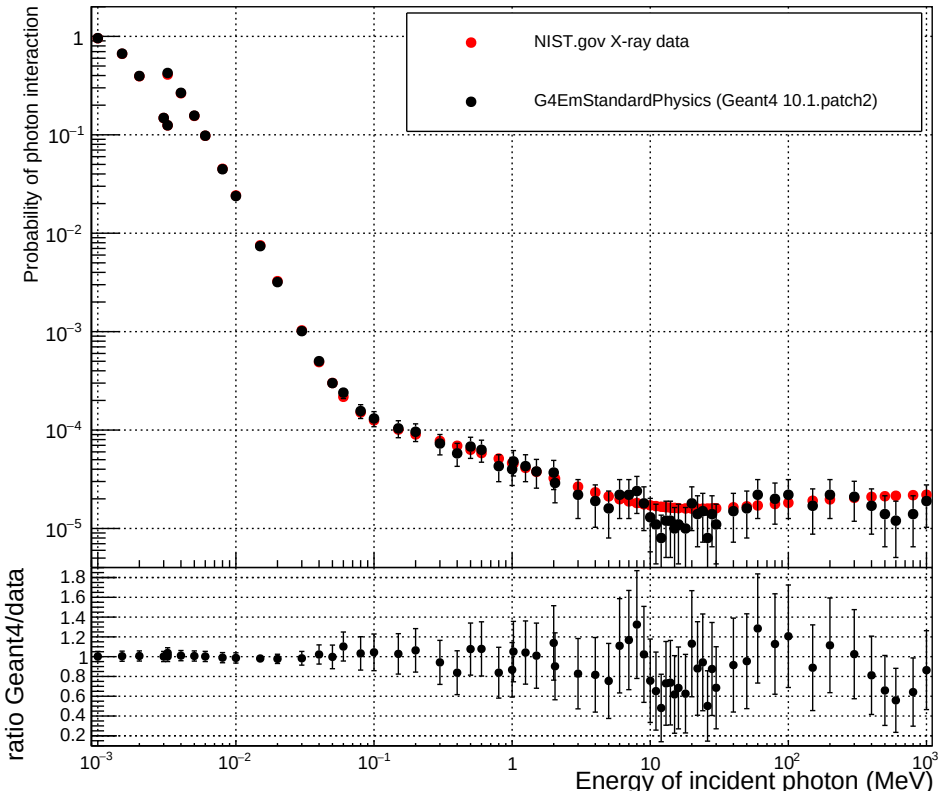

Fig. 6.10.: Upper plot: interaction probability of incident photon impinging normally on 3 mm of Ar:CO_2:CF_4 mixture ($45\% : 15\% : 40\%$) at STP conditions, obtained with `G4EmStandardPhysics` model. The error bars indicate a 95.45% confidence level. Lower plot: ratio between the GEANT4 simulation and the data coming from the NIST XCOM database. The ratio is almost always confident with the unity within 2σ. The resonance occurring at 3.202 keV corresponds to the K photoelectric absorption edge of argon.

Material	Thickness (cm)
Aluminium	0.06
Polyethylene	0.03
Bakelite	0.2
Gas	0.2
Bakelite	0.2
Aluminium	0.01
Bakelite	0.2
Gas	0.2
Bakelite	0.2
Polyethylene	0.03
Aluminium	0.06

Tab. 6.3.: Thickness of RPC materials used in the simulation reported in [120].

GEANT4 event, and hypothetical following ones provide no further contribution in that frame. Several configurations are reported, depending on the chosen reference, and were given as input to the GEANT4 application. Whenever possible materials were taken from the GEANT4 material database, instead of being redefined.
Starting chronologically from reference [120], the setup consists in a RPC of area 20×20 cm^2. The thickness of RPC materials used in the simulations are reported in Tab. 6.3. For a layout of the RPC detector, refer to Fig. 4.9. Neutrons were transported by GEANT3.21 using the FLUKA interface for higher energies [123] and MICAP interface [124] at low energies ($E_{\mathrm{n}} < 20$ MeV). In the current GEANT4 simulations, in turn, different PL were tested, in the light of the considerations on the hadron models reported in Sec. 6.5.2.
First of all, the PL `FTFP_BERT_HP` has been chosen, as it is recommended for high energy physics [115, 125]. It includes among other features:

- all standard electromagnetic processes,
- hadron Fritiof (`FTF`) string model (> 5 GeV) – although these energy yields are never reached in the current context, so to use Fritiof or QGSP model makes no difference –,
- `G4Precompound` (`P`) model used for hadron de-excitation,
- Bertini-style (`BERT`) cascade for hadrons (< 5 GeV),
- high precision data-driven model (`HP`), able to track neutrons down to thermal energies, and

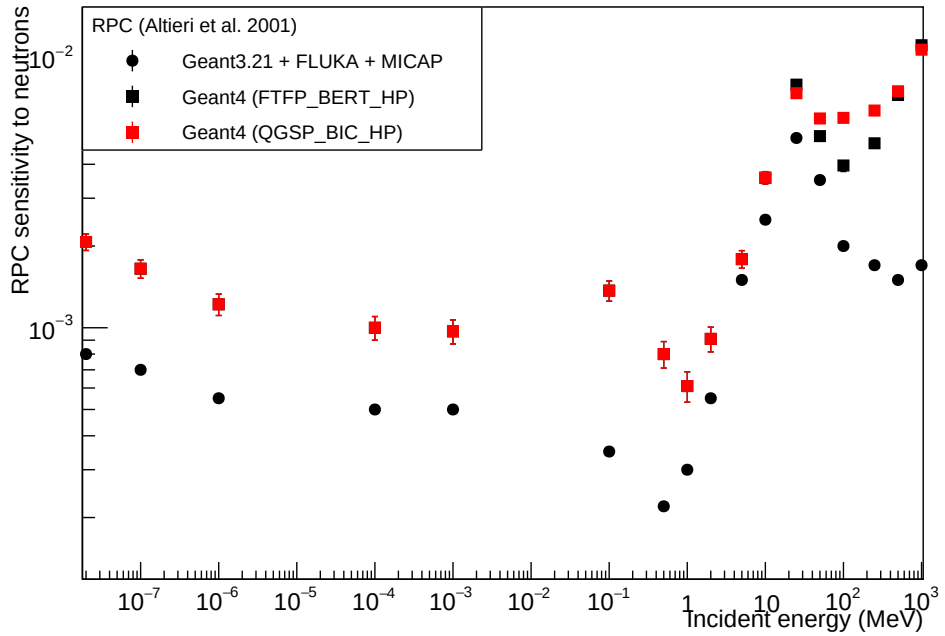

Fig. 6.11.: Comparison of GEANT3.21 simulations from [120] and GEANT4 simulations with two different physics lists, for a RPC setup (see Tab. 6.3). The shown error bars are of statistical nature. Statistical errors of GEANT3.21 simulation are unknown.

- `G4NDL4.5` data libraries; G4NDL data mainly come from the ENDF/B-VII library which is developed and maintained by the Cross Section Evaluation Working Group (CSEWG) (`http://www.nndc.bnl.gov/csewg/`). The original data files may be accessed at the National Nuclear Data Center webpage, `http://www.nndc.bnl.gov/`. G4NDL data also comes from the JENDL library which is developed and maintained by Nuclear Data Evaluation Center of Japan Atomic Energy Agency (`http://wwwndc.tokai-sc.jaea.go.jp/index.html`). The original data files may be accessed at the Japanese Evaluated Nuclear Data Library web page: `http://wwwndc.tokai-sc.jaea.go.jp/jendl/jendl.html#jendl-sp`.

The other option has the aim to investigate the Binary cascade in the $E_{\mathrm{n}} > 20$ MeV range, as it reportedly behaves better for low energy protons and neutrons [126]. A suitable PL is `QGSP_BIC_HP`. As anticipated, the quark-gluon string model (`QGS`) plays no role in this application as the former is optimized for the range 15 GeV - 50 GeV. The comparison of the double-gap sensitivities for a parallel beam of neutrons is shown in Fig. 6.11.

The sensitivity in the low-energy region ($E_{\mathrm{n}} < 10^{-5}$ MeV) is mostly due to the photons coming from (n, γ) capture reactions whose cross-section rises at lower

neutron energies ($\sigma \propto 1/\sqrt{E_{\rm n}}$). At higher energies ($E_{\rm n} > 1$ MeV) the sensitivity rises rapidly and reaches a maximum as a consequence of protons produced by elastic scattering on H and by (n,p) reactions on C, O and Al. As expected the two GEANT4 simulations provide identical results below 20 MeV, as the only library involved in this range is `HP`, common to both PL. For both setups the agreement with GEANT3.21 stays within a factor of ~ 3 up to ~ 1 MeV. The main hypothesis behind this important difference is the inadequacy of the old libraries in treating low energy neutrons. Above the energy of ~ 50 MeV, the divergence is such that the behaviour of 10-year old FLUKA is probably not comparable to GEANT4 any more. Concerning the difference between the two PL, a higher sensitivity is visible around 100 MeV when the Binary cascade is involved.

The next reference analysed is [121], that has the merit to report also two experimental points with neutron beams. The first one involves spontaneous fissions of a ^{252}Cf source. During fission events there is on average an almost isotropic emission of 3.8 prompt neutrons having an average energy of ~ 2 MeV and 10.3 prompt gammas. In this case simulation results were used to separate neutron and photon contribution in the experimental data and eventually extract the neutron and photon sensitivities. The second point lays at 20 MeV; the neutron production was based on the reaction ^{9}Be + d $\rightarrow$ n + X, using a 50 MeV deuterons beam accelerated by the Louvain-la-Neuve cyclotron on a 1 cm beryllium target. The average neutron energy is 20 MeV. The simulated geometry of this RPC is shown in Tab. 6.4. The comparison for a parallel beam of neutrons is shown on Fig. 6.12, together with the two experimental points. Regarding the comparison between GEANT versions, it is possible to make the same conclusions already presented for Fig. 6.11. The difference in sensitivity with respect to the experimental data should be interpreted not only as the possible – and expected – existence of a systematic error in the GEANT4 estimation of the neutron sensitivity at such scales, but also as an indication of the fact that a possible uncertainty concerning the geometrical setup of the test beams has not been taken into account. The latter information is sadly impossible to estimate. In conclusion, the data points do not support any discrimination between the candidate PLs `FTFP_BERT_HP` and `QGSP_BIC_HP`.

Going on to reference [122], the thickness of RPC materials used in the simulations are reported in Tab. 6.5, and include two different setups of area 20×20 cm^2. The differences between them consist in the usage of aluminium instead of copper, for grounded material and strips, as well as the thickness of every polyethylene layers (0.01 cm vs. 0.060 cm). Sketches of the two simulated RPC setups are shown in Fig. 6.13. The comparison of the double-gap sensitivities for a parallel beam of neutrons is shown in Fig. 6.14 and 6.15. It is possible to make observations consistent with the comparisons already made in Fig. 6.11 and Fig. 6.12 even though the gap between GEANT versions for higher energies is even larger in the current case, while

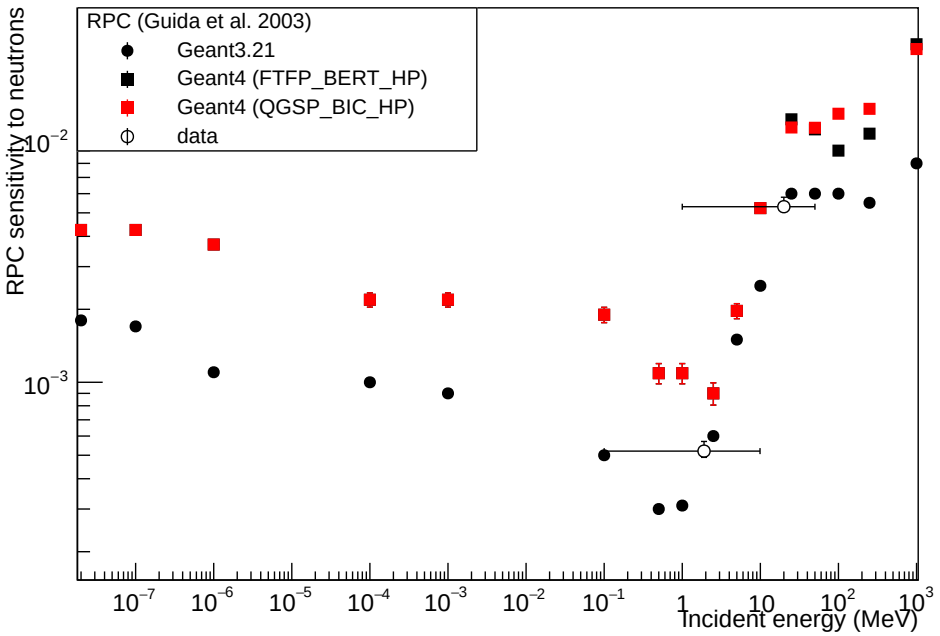

Fig. 6.12.: Comparison of GEANT3.21 simulations from [121] and GEANT4 simulations with two different physics lists, for a RPC setup (see Tab. 6.4), together with two experimental points. The shown error bars relative to GEANT4 are of statistical nature. Statistical errors of GEANT3.21 simulation are unknown. The horizontal error bars related to the experimental points are due to the spread of the neutron energy source.

Material	Thickness (cm)
Wood	1.0
Copper	0.0019
Polyethylene	0.038
Graphite	0.002
Bakelite	0.2
Gas	0.2
Bakelite	0.2
Graphite	0.002
Polyethylene	0.038
Copper (strips)	0.0019
Polyethylene	0.038
Graphite	0.002
Bakelite	0.2
Gas	0.2
Bakelite	0.2
Graphite	0.002
Polyethylene	0.038
Copper	0.0019
Wood	1.0
Aluminium	0.25

Tab. 6.4.: Thickness of RPC materials used in the simulation reported in [121].

the discrepancies for low energy neutrons have strongly decreased, and are now consistent with a qualitative 30% systematic error between GEANT3.21 and GEANT4 simulation response (A. Ribon, personal communication, 11 March 2015).

Comparisons with GEANT4 simulations

More recent references report GEANT4 simulations, although with PLs today considered as obsolete and not available any more. Therefore, if one wants to check the validity of his own code by comparing with results in literature, he cannot reproduce a completely faithful application, but has to adapt using present PLs. This corresponds to what is done in the following, taking the reference [127]. The implemented RPC geometry is almost identical to the one shown for Setup II in Tab. 6.5, with the exception that all copper layers have a thickness of 0.005 cm instead of 0.001 cm. The neutron sensitivity was estimated thanks to two different PL packages. The first one is the GEANT4 Standard-energy package [106], describing the interactions of electrons, positrons, photons, and charged hadrons in the energy range between 1.0 keV and 100 TeV. This package assumes that the atomic electrons are quasi-free while the atomic nucleus is fixed; we currently know that the latter assumption, when applied to the sensitivity of gaseous detectors to low

Setup I material	Thickness (cm)	Setup II material	Thickness (cm)
Aluminium (GND)	0.06	Copper (GND)	0.001
Polyethylene	0.01	Polyethylene	0.060
Graphite	0.002	Graphite	0.002
Bakelite	0.2	Bakelite	0.2
Gas	0.2	Gas	0.2
Bakelite	0.2	Bakelite	0.2
Graphite	0.002	Graphite	0.002
Polyethylene	0.01	Polyethylene	0.060
Aluminium (strips)	0.01	Copper (strips)	0.001
Polyethylene	0.01	Polyethylene	0.060
Graphite	0.002	Graphite	0.002
Bakelite	0.2	Bakelite	0.2
Gas	0.2	Gas	0.2
Bakelite	0.2	Bakelite	0.2
Graphite	0.002	Graphite	0.002
Polyethylene	0.01	Polyethylene	0.060
Aluminium (GND)	0.06	Copper (GND)	0.001

Tab. 6.5.: Thickness of RPC materials used in the simulations [122]. In the first setup RPC with aluminium ground plates and strips were used, while in the second configuration both ground and strips were made of copper.

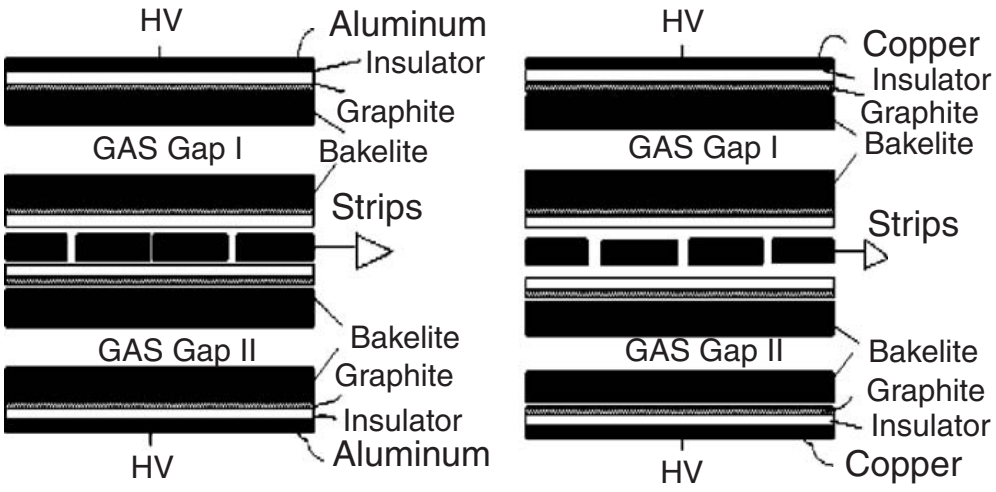

Fig. 6.13.: Schematic view of the two simulated RPC setups from [122].

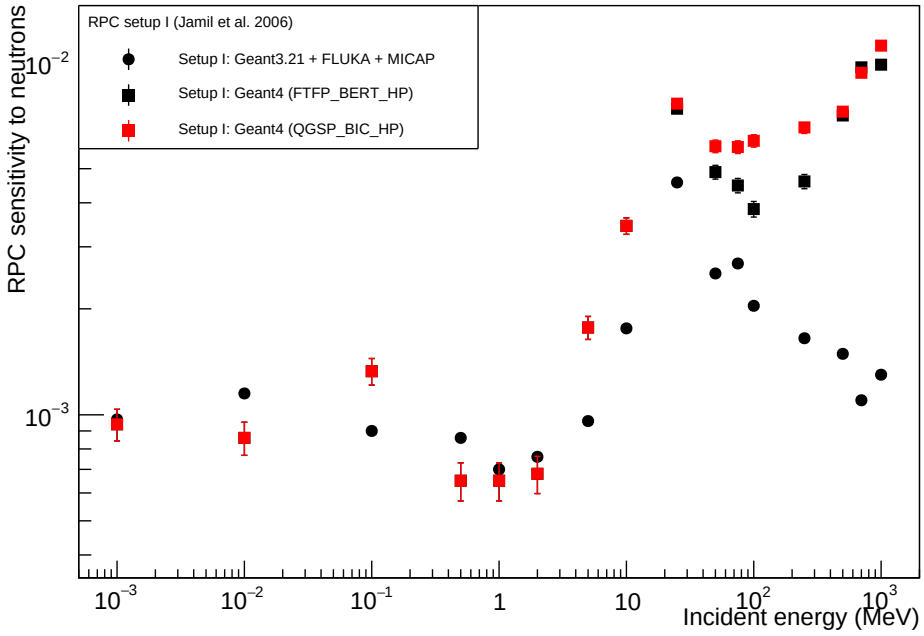

Fig. 6.14.: Comparison of GEANT3.21 simulations from [122] and GEANT4 simulations with two different physics lists, for RPC setup I (see Tab. 6.5). The shown error bars are of statistical nature. Statistical errors of GEANT3.21 simulation are within 1%.

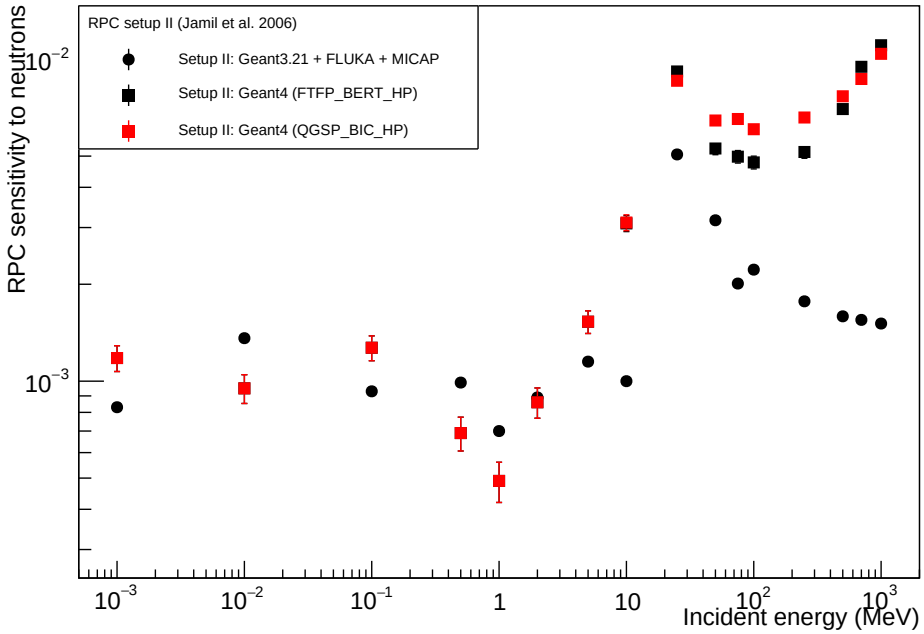

Fig. 6.15.: Comparison of GEANT3.21 simulations from [122] and GEANT4 simulations with two different physics lists, for RPC setup II (see Tab. 6.5). The shown error bars are of statistical nature. Statistical errors of GEANT3.21 simulation are within 1%.

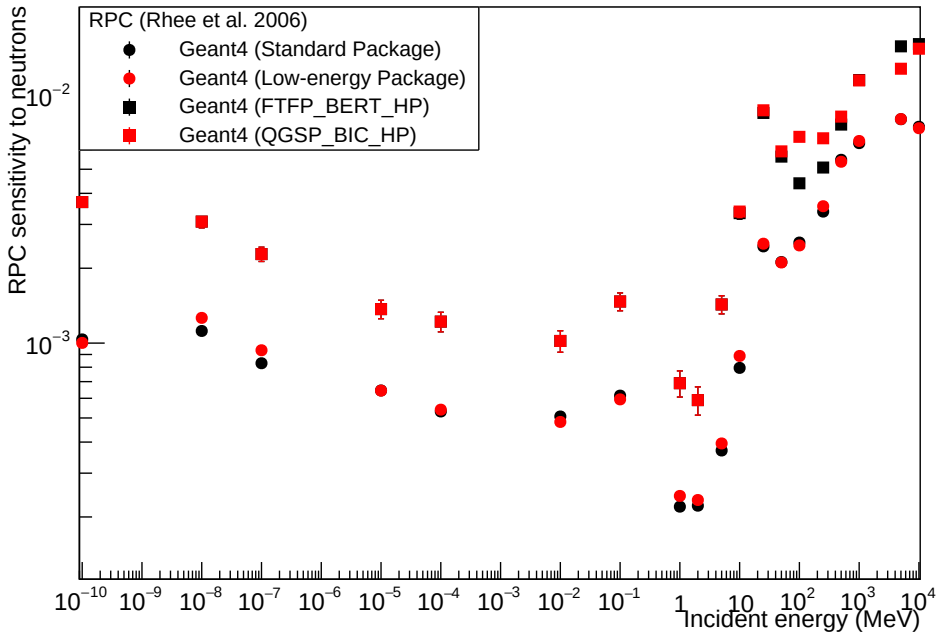

Fig. 6.16.: Comparison of GEANT4 simulations from [127] with old libraries and GEANT4 simulations with two different physics lists, for an RPC setup similar to setup II in Tab. 6.5. The shown error bars are of statistical nature. Statistical errors of reference simulation are within 1%.

energy hadrons, is certainly false. The second package investigated was the GEANT4 low-energy package, that extends the range of accuracy of electromagnetic interactions down to 250 eV, by exploiting evaluated data libraries for the calculation of cross-sections and the sampling of the final state for the modelling of photon and electron interactions with matter. The reason why no dedicated neutron library was employed in the reference is unknown. The comparison is shown in Fig. 6.16. Taking into account the fact that the geometry is almost identical to the one providing the plots in Fig. 6.15, one can appreciate how different is the trend of the curve above 20 MeV between a GEANT3 simulation involving MICAP for higher energies (see also Fig. 6.11) and an early GEANT4 version. Net of the factor ~ 3, the trend is confirmed by the current simulation. Another study by the same authors [128] seems to support the hypothesis that early versions of GEANT4 lacking specific neutron libraries tend to underestimate RPC's response to neutrons, at least for the range $1\ \mathrm{MeV} < E_\mathrm{n} < 50$ MeV.

Validations with experimental data

The failure of a practical way to discriminate between two state-of-the-art PLs by looking at decade-old simulations leads to the research of ulterior experimental data,

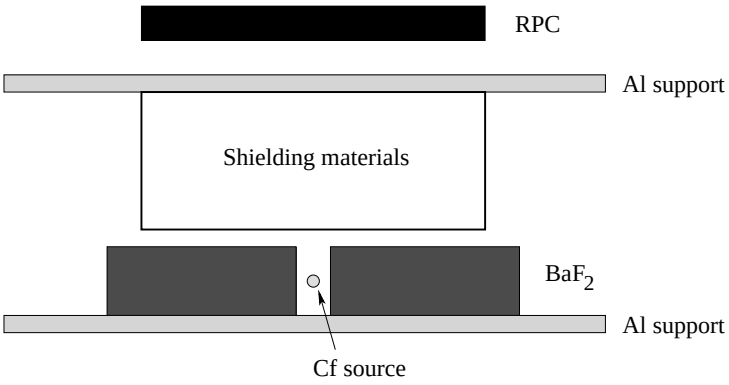

Fig. 6.17.: A schematic view of the experimental setup configuration [129].

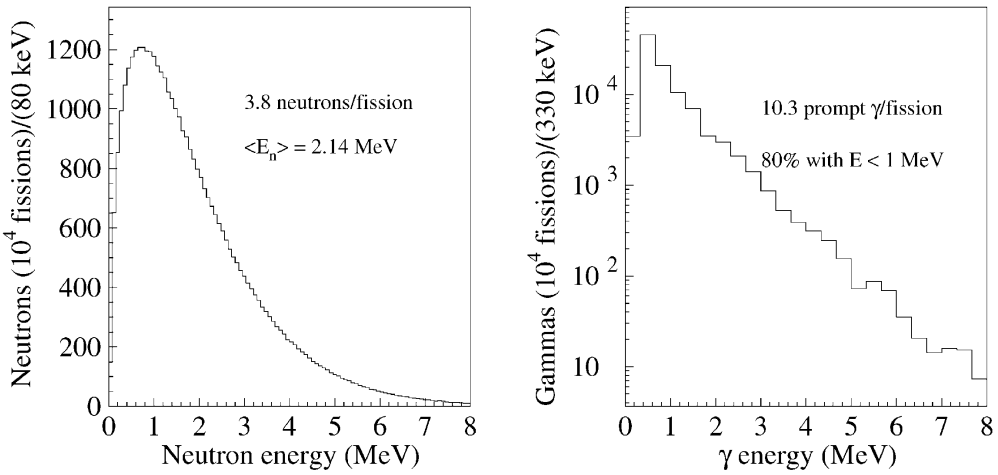

Fig. 6.18.: Neutrons and prompt gammas energy spectra from ^{252}Cf spontaneous fission events [129].

and possible experimental setups to implement in the GEANT4 simulation. This was partially done and reported in Fig. 6.12, but thanks to reference [129] it was possible to increase the variety of tests. The experimental setup described in the reference is shown in Fig. 6.17.

A double gap RPC was placed 30 cm away from a ^{252}Cf source. The fission events were detected with two BaF_2 scintillators, sensitive to the source prompt gamma radiation. Lead and polyethylene slabs were used to change the relative number of gammas and neutrons that reached the detector surface. The experimental result is a measurement of the probability to reveal the ^{252}Cf fissions with the RPC detector. The events were counted in coincidence with a trigger signal within a 50 ns time window; this is taken into account in the simulation, as well as the spectrum of the ^{252}Cf fission, shown in Fig. 6.18. The geometry of the RPC coincides with the one described in Tab. 6.4. There are four shielding configurations, all of them described in Fig. 6.19. The results are reported in Fig. 6.20 as a function of the number of

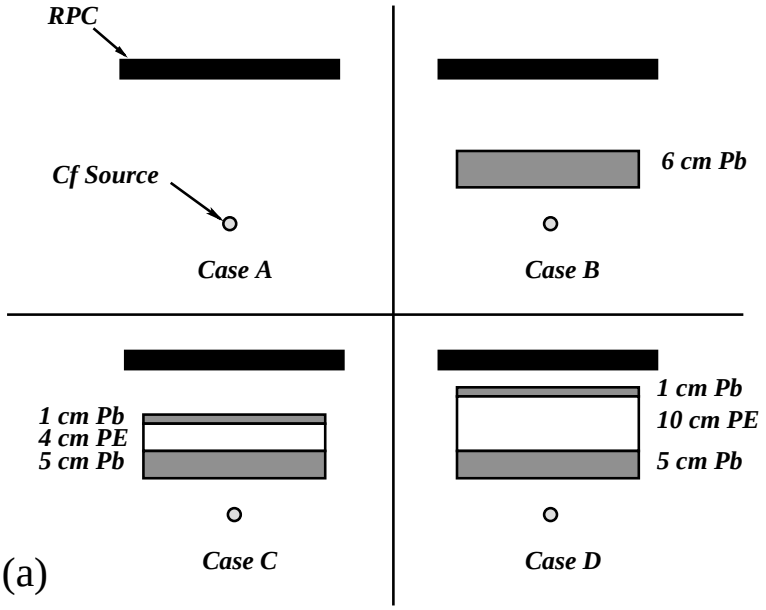

Fig. 6.19.: Description of the four shielding configurations, made with lead and polyethylene (PE) slabs of different thickness. The lead has an attenuation effect mainly on the photons ans leaves the neutrons component almost unchanged [129].

effective neutron interaction lengths X_{eq}. Considering the energy spectrum of ^{252}Cf, two observations are necessary. The first one is that the largest contribution in the signal formation in the RPC certainly comes from the photon source. The second is that the prompt neutrons spectrum shown in Fig. 6.18 (not exceeding 10 MeV), reveals that only the `HP` libraries of the PL considered so far will contribute to the description of the RPC response to neutrons. This is why only one of these PLs – namely, `FTFP_BERT_HP` – has been included in the comparison plot in Fig. 6.20. To offer another term of comparison, the PL `QBBC` is here introduced [126]. `QBBC` has been created for space applications, radiation biology, and radiation protection. It includes combinations of `BIC`, `BIC-Ion`, `BERT`, `QGSP` and `FTFP` models and has higher precision than the others for many hadron-ion and ion-ion interactions in a wide energy range. The difference in the behaviour of the two PLs will come exclusively from the neutron contribution, as they share the same standard electromagnetic libraries. The plot in Fig. 6.20 shows that the `HP` libraries seems to be more accurate in the description of neutron response for energies smaller than a few tens of MeV. It must be noted that no systematic error based on the incomplete description of the experimental setup, or on the unknown density of particular materials (*e.g.* the wood), has been evaluated. It may be one of the reasons why the values at the lowest interaction length do not lie in the same confidence interval as the experimental result.

In conclusion, the usage of the `HP` library is to be preferred for neutron energies smaller than 20 GeV. However, it was not possible to motivate a preference between

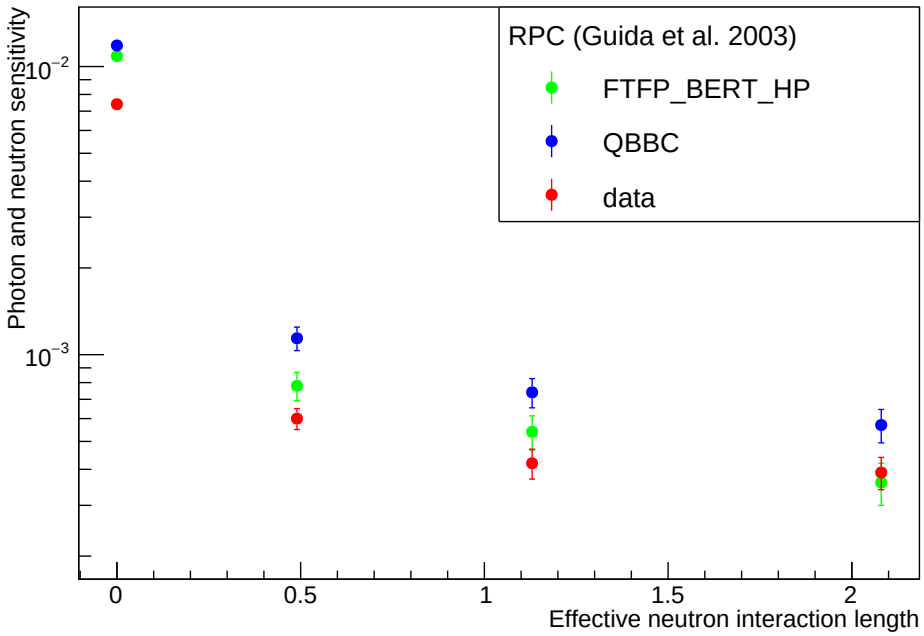

Fig. 6.20.: Sensitivity of the RPC defined in Tab. 6.4 to the decaying products of a ^{252}Cf source, as a function of the effective neutron interaction lengths of several attenuating layers, in the experimental setup illustrated in Fig. 6.19. The error shown on the values coming from GEANT4 simulations are statistical. The data points are taken from reference [129].

`FTFP_BERT_HP` and `QGSP_BIC_HP`. Therefore, the decision in this work involves the usage of `FTFP_BERT_HP`, with a systematic error that will be evaluated in Sec. 6.7.7.

6.7.5 Simulated geometry

The appropriate materials and the geometry of a Triple-GEM super-chamber were input to the code. We assumed the following Triple-GEM gas mixture: 45% Ar - 15% CO_2 - 40% CF_4, as well as the possible other option 70% Ar - 30% CO_2. Materials and their thickness for one of the two single chambers present in the super-chamber are shown in Tab. 6.6. Every GEM detector is subdivided in sectors in both the ϕ and η directions, with every sector containing 128 readout strips on which charge is induced by the passage of an ionizing particle through the detector volume. In the GEANT4 simulation, such sectors are not reproduced. The control, read-out, and power to and from the hybrids on which are mounted the front-end chips is delivered via electric signals running through a large printed circuit board called the GEM Electronic Board (GEB) covering the entire detector surface. The GEB and the hybrids that carry the read-out chips, called VFAT2, are included in the simulated geometry, and their material budget are reported respectively in Tables 6.7 and 6.8. Fig. 6.21 shows a portion of the GEB, together with the optohybrid and a series of

VFAT2 read-outs.

The full super-chamber geometry therefore consists of twice the reported material budget, plus a 3.7 mm thick air spacer between the two chambers. A U-shaped pipe filled with water and few copper plates, whose goal is to cool the super-chamber, are added in the geometrical description. These components can be seen in the super-chamber picture modelled in GEANT4 in Fig. 6.22. The response to both orientations – 'odd' and 'even' – were simulated.

The dimensions of the chamber are those corresponding to the ones of the large chambers that will be installed in GE1/1 station; the shape is trapezoidal, and the smaller base being 279 mm, the larger base 510 mm and the height 1283 mm. No electric field is included in the simulation, therefore no signal amplification process actually takes place. This is approximation is acceptable, as it is compensated by the hypothesis that any charged particle that reaches the gas gap can induce a signal.

function	material	thickness
GEM cover	aluminium	1 cm
Cooling pipe	copper	⌀16 mm
Pipe content	water	⌀12 mm
Cooling plates	copper	1 mm
VFAT2	see Tab. 6.8	1.6 mm
VFAT pedestal	air	5.5 mm
GEB	see Tab. 6.7	1 mm
Readout board (1)	copper	35 µm
Readout board (2)	FR-4	3.2 mm
Readout board (3)	copper	35 µm
Inducing gap	Ar:CO_2(:CF_4)	1 mm
GEM foil (1)	copper	5 µm
GEM foil (2)	Kapton	50 µm
GEM foil (3)	copper	5 µm
Transfer 2 gap	Ar:CO_2(:CF_4)	2 mm
GEM foil (1)	copper	5 µm
GEM foil (2)	Kapton	50 µm
GEM foil (3)	copper	5 µm
Transfer 1 gap	Ar:CO_2(:CF_4)	1 mm
GEM foil (1)	copper	5 µm
GEM foil (2)	Kapton	50 µm
GEM foil (3)	copper	5 µm
Drift gap	Ar:CO_2(:CF_4)	3 mm
Drift board (1)	copper	35 µm
Drift board (2)	FR-4	3.2 mm
Drift board (3)	copper	35 µm

Tab. 6.6.: Thickness of Triple-GEM materials used in the simulation - first configuration

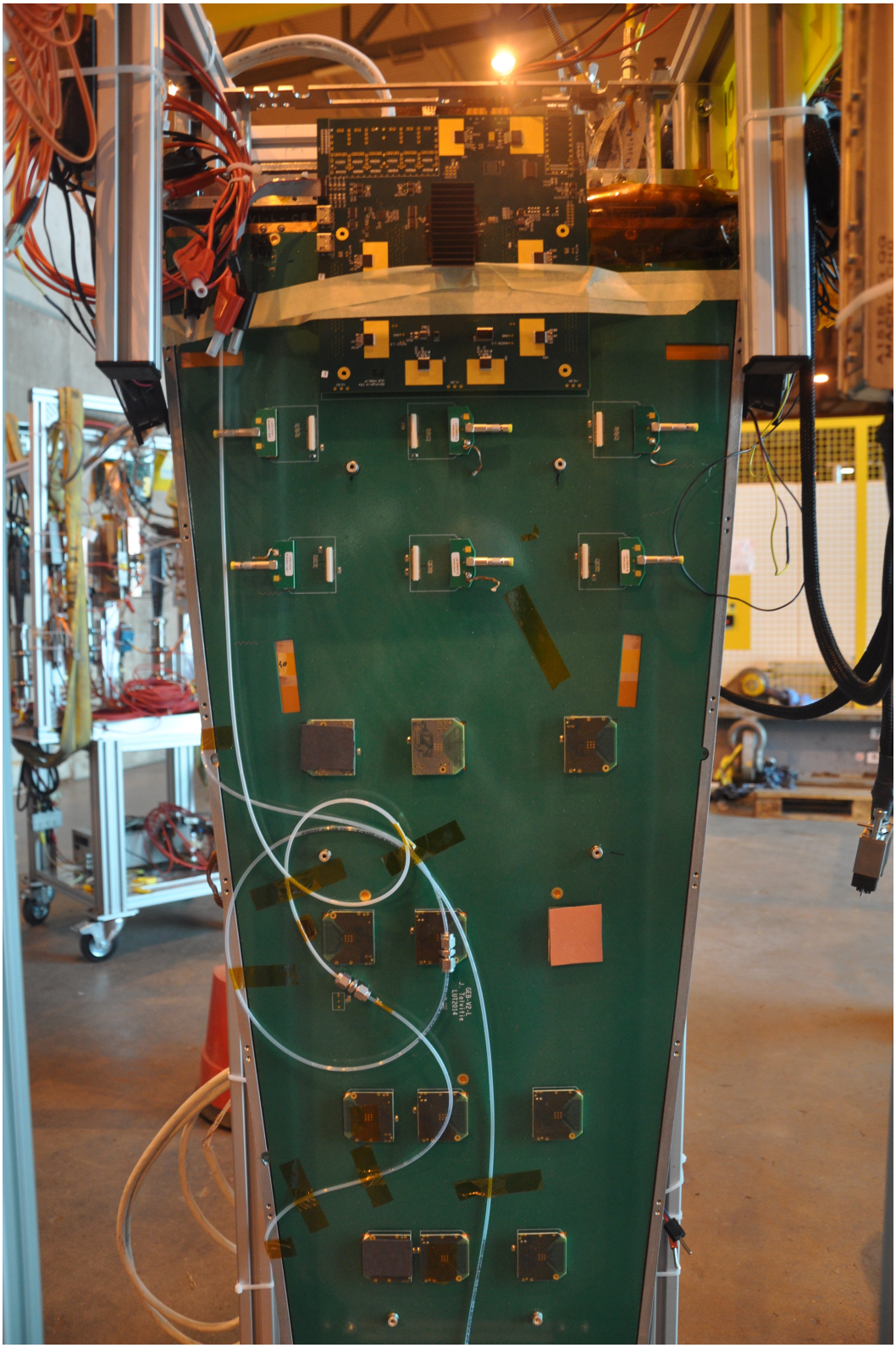

Fig. 6.21.: Picture including a portion of the GEB, together with the optohybrid (upper side of the board) and a series of VFAT2 read-outs connected to the GEB itself. Courtesy of Thomas Lenzi.

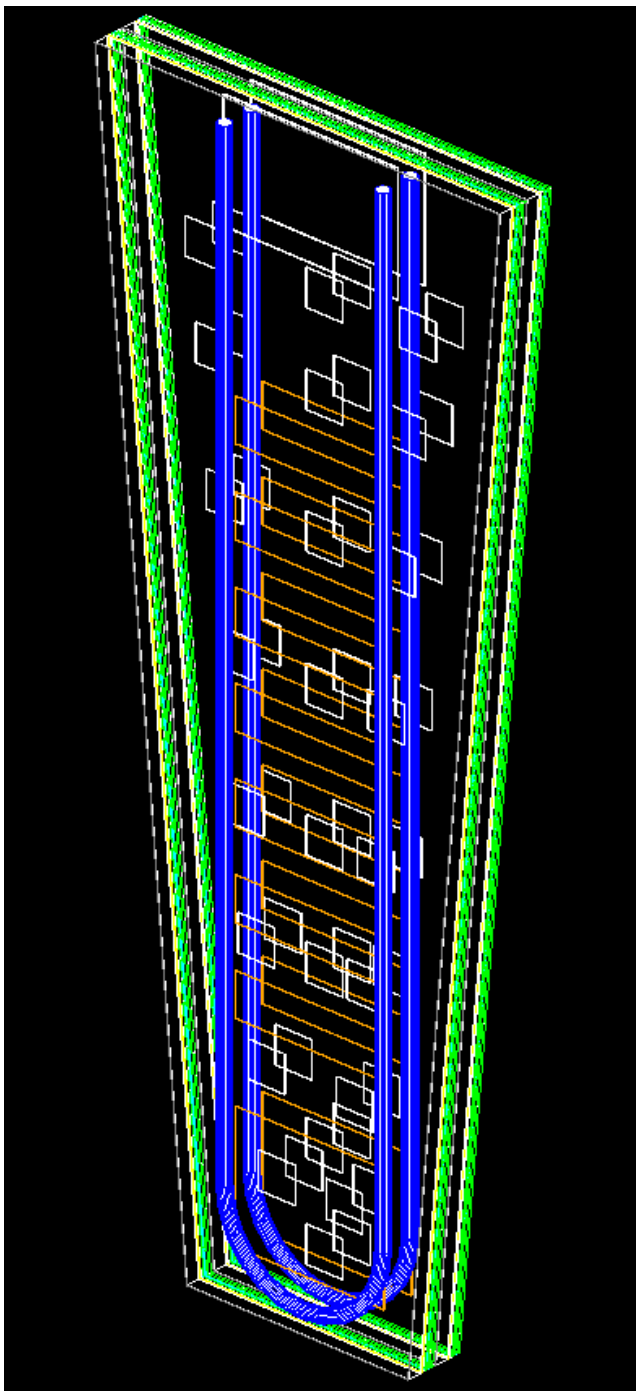

Fig. 6.22.: Super-chamber model in GEANT4. The cooling pipe is highlighted in blue, while cooling copper plates' borders are in orange. The white shapes represent the VFAT2 hybrids as well as the optohybrid. The separation between the green layers shows the air gap between two single chambers.

material	thickness
Copper plane	35 μm
Insulator (FR-4)	218 μm
Routing plane (FR-4)	17.5 μm
Insulator (FR-4)	150 μm
Copper plane	17.5 μm
Insulator (FR-4)	120 μm
Copper plane	17.5 μm
Insulator (FR-4)	150 μm
Routing plane (FR-4)	17.5 μm
Insulator (FR-4)	218 μm
Copper plane	35 μm

Tab. 6.7.: GEM electronic board's material budget

material	thickness
copper	17.5 μm
insulator (FR-4)	310 μm
copper	17.5 μm
insulator (FR-4)	310 μm
copper	17.5 μm
insulator (FR-4)	310 μm
copper	17.5 μm

Tab. 6.8.: VFAT2's material budget. The insulator thicknesses were averaged.

6.7.6 Definition of Triple-GEM sensitivity

The sensitivity is defined in the following way:

$$\text{sensitivity} = \frac{N_{\text{signals}}}{N_{\text{crossing particles}}}. \tag{6.17}$$

$N_{\text{crossing particles}}$ is easy to implement in the simulation code, as it corresponds to the request for the incident particle to cross the volume of the detector, no matter if it interacts or not. On the contrary, N_{signals} deserves a more articulate discussion. In the case of the double-gap RPC, the recipe was taken from the strategy given in literature, and consisted in the presence of a charged particle in one of the two gas gaps. The presence of four different gaps in a Triple-GEM increases the number of possibilities of sensitivity definition. Luckily, more information is provided by independent GARFIELD simulations [75]. In fact, these results show that the maximum charge deposition exceeding a given threshold occurs mostly in the drift and the transfer 1 gaps. The probabilities are the following:

Gas Gap	Probability of signal origin
Drift	$\sim 80\%$
Transfer 1	$\sim 17\%$
Transfer 2 + Induction	$\sim 3\%$

These results lead to the possible statement that in the GEANT4 simulation, the algorithm determining if an event generates a detectable hit consists in looking for the presence of a charged particle either in the drift gap, either in the transfer 1 gap; this condition is to be intended as a logical OR. The advantages of this definition are twofold: it is easy to implement, and it has precedents in literature, as already stated. On the other hand, it can be charged with lack of realism: it represents an upper limit to sensitivity, as it does not take into account any threshold effect, included the one dictated by the electronics.
The other option is to keep the condition concerning the selection of the gas gaps, but to ask indeed for the deposited energy by ionisation (E_{dep}) times the Triple-GEM gain G to exceed the charge threshold imposed by the electronics on the strips. That is:

$$E_{\mathrm{dep}} \times G > \mathrm{Threshold}. \tag{6.18}$$

This principle is certainly more realistic, but it requires more offline analysis. Both techniques have been tested.

6.7.7 Convolution with background flux

There are two kind of distributions coming from FLUKA predictions of the background environment of GE1/1. The first one was already shown in Fig. 6.9 and concerns the energy spectrum of the particles crossing the GE1/1 detector. The second one focuses on the angular distributions of the particles, in the form of direction cosines. The two distributions are decorrelated from each other. The direction cosines of a vector are the cosines of the angles between the vector and the three coordinate axes. That is, if $\mathbf{v}$ is a Euclidean vector in three-dimensional Euclidean space $\mathbb{R}^3$:

$$\mathbf{v} = v_x\mathbf{e}_x + v_y\mathbf{e}_y + v_z\mathbf{e}_z, \tag{6.19}$$

where $\mathbf{e}_x$, $\mathbf{e}_y$, $\mathbf{e}_z$ are the standard basis in Cartesian notation, then the direction cosines are:

$$\alpha = \cos x = \frac{\mathbf{v}\cdot\mathbf{e}_x}{|\mathbf{v}|} = \frac{v_x}{\sqrt{v_x^2+v_y^2+v_z^2}}, \tag{6.20}$$

$$\beta = \cos y = \frac{\mathbf{v}\cdot\mathbf{e}_y}{|\mathbf{v}|} = \frac{v_y}{\sqrt{v_x^2+v_y^2+v_z^2}}, \tag{6.21}$$

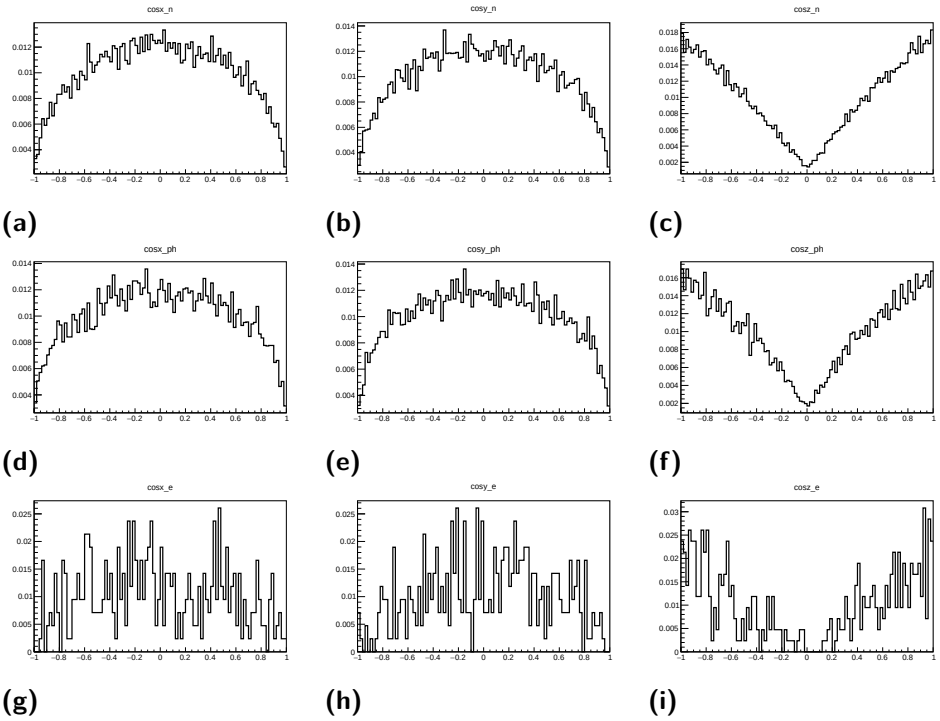

Fig. 6.23.: Direction cosines for each kind of considered particle (neutron, photon, electron and positron), according to definitions of Eq. 6.20, 6.21, and 6.22. The first line shows neutron distributions, the second line photon distributions, the third one electron and positron distributions. The first row concerns $\cos x$, the second $\cos y$, the third $\cos z$.

$$\gamma = \cos z = \frac{\mathbf{v} \cdot \mathbf{e}_z}{|\mathbf{v}|} = \frac{v_z}{\sqrt{v_x^2 + v_y^2 + v_z^2}}. \tag{6.22}$$

It follows that by squaring each equation and adding the results:

$$\cos^2 x + \cos^2 y + \cos^2 z = 1. \tag{6.23}$$

The GEANT4 simulation integrates into its `PrimaryGeneratorAction` class the angular distributions, in order to take into account as much as possible the available information about the scenario of interest. The generated distributions are shown in Fig. 6.23. Their populations are the following: neutrons distribution has 46258 events; photons distribution has 26280 events; electrons and positrons distribution has 422 events. In contrast to the single read-out double-chamber RPC, the Triple-GEM super-chamber has two independent readouts. Therefore, one has to consider the sensitivity of two separate detectors inserted in a super chamber layout. Besides, there are two existing super-chamber configurations, called “odd” and “even”. The former has the cooling system facing the interaction point, while the latter’s orientation is reversed (see Fig. 6.24). In any cases, detector A’s position is internal; B’s is external. The simulation were performed according to the available direction cosines, and are collectively shown for odd an even layouts, respectively in Fig. 6.25

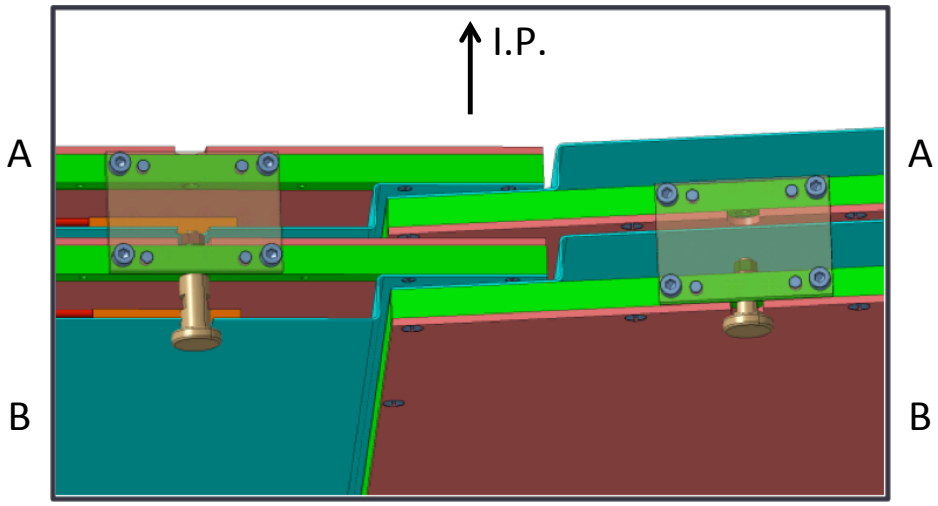

Fig. 6.24.: Layout of Triple-GEM super-chambers. On the left, the GEBs and the cooling system are looking at the external of CMS; this is the "even" configuration. On the right, the GEBs and the cooling system are looking toward the interaction point; this is the "odd" configuration. Chamber A is always the most internal one; they are both on the top of the picture.

and 6.26. The physical processes causing such sensitivity yields will be discussed. It is nevertheless possible to anticipate that concerning the photon curve, the peak at energies around 100 keV is due to the photoelectric effect, and that the sensitivity to positrons is greater than the one to electrons below 1 MeV because of positron annihilation. At such incident energies, it is safe to assume that a positron and an electron are converted into a photon having an energy equal to the combined mass of the leptons, that is 1.022 MeV. Indeed, Fig. 6.25 and 6.26 show that this positron sensitivity plateau has the same yield as the photon sensitivity at 1 MeV. At energies greater than ~ 10 MeV, both curves tend to saturate at 100%, as expected for charged particles in a gaseous detector with full efficiency.

The convolution of this curves with the unitary distributions shown in Fig. 6.9 provides new histograms. To integrate these histograms – that is by simply adding all the bin contents – is ultimately equivalent to obtain the ultimate hit probability to the different kind of particles in the GE1/1 station. The hit yields are reported in Tab. 6.9 for PL `FTFP_BERT_HP` and in Tab. 6.10 for PL `QGSP_BIC_HP`. As expected some differences appear only when hadronic processes are involved. As there is no argument to decide which of the two PLs is the closest to experimental data, the average of the two results will be taken as the final value and their difference as a contribution to the systematic error.

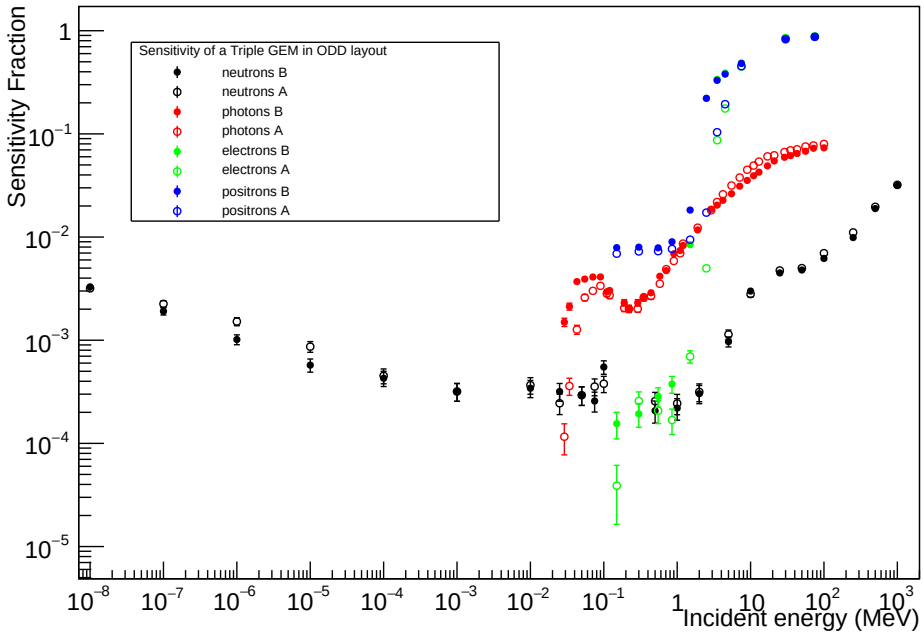

Fig. 6.25.: Sensitivity of a Triple GEM chamber "A" and "B" in an odd super-chamber layout, as a function of the incident energy of several particles.

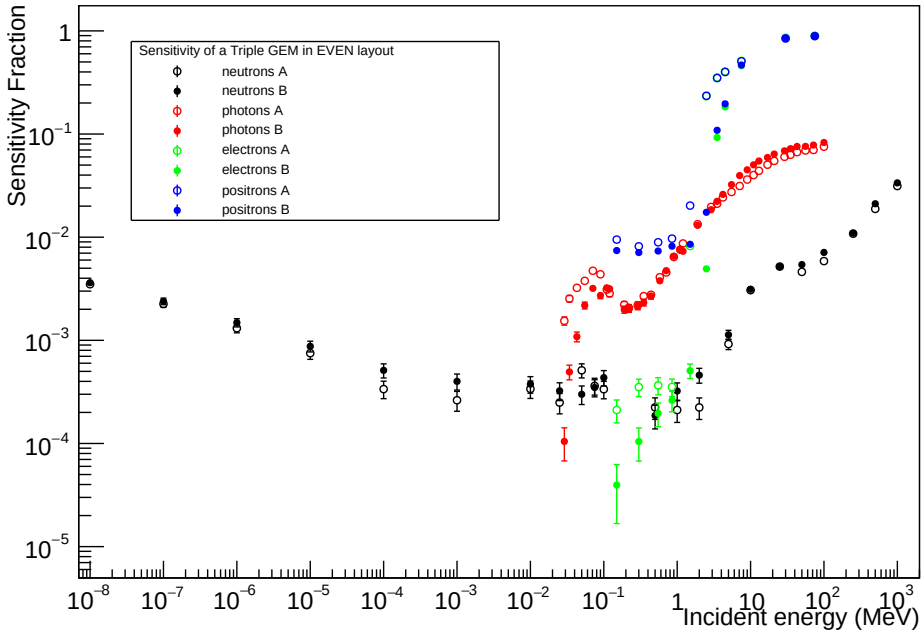

Fig. 6.26.: Sensitivity of a Triple GEM chamber "A" and "B" in an even super-chamber layout, as a function of the incident energy of several particles.

BERT_HP	neutrons	photons	electrons	positrons
even A	$0.00159(5)$	$0.0087(1)$	$0.12(1)$	$0.13(1)$
even B	$0.00174(5)$	$0.0092(1)$	$0.064(9)$	$0.072(9)$
odd A	$0.00160(5)$	$0.0090(1)$	$0.062(8)$	$0.071(8)$
odd B	$0.00149(5)$	$0.0084(1)$	$0.12(1)$	$0.12(1)$

Tab. 6.9.: Hit probabilities for Triple-GEM "A" and "B" in even and odd configuration, using PL FTFP_BERT_HP. The error is only statistical and includes the uncertainty on the sensitivity and on the incident flux. Different contributions to the systematic uncertainty will be evaluated in the following sections.

BIC_HP	neutrons	photons	electrons	positrons
even A	$0.00164(5)$	$0.0087(1)$	$0.12(1)$	$0.13(1)$
even B	$0.00179(5)$	$0.0092(1)$	$0.064(9)$	$0.072(9)$
odd A	$0.00163(5)$	$0.0090(1)$	$0.062(8)$	$0.071(8)$
odd B	$0.00155(5)$	$0.0085(1)$	$0.12(1)$	$0.12(1)$

Tab. 6.10.: Hit probabilities for Triple-GEM "A" and "B" in even and odd configuration, using PL QGSP_BIC_HP. The error is only statistical and includes the uncertainty on the sensitivity and on the incident flux. Different contributions to the systematic uncertainty will be evaluated in the following sections.

6.7.8 Simplified geometry

The hit probabilities depend on the level of description of the GE1/1 detector material budget. To provide a better feeling on this dependence, the hit probabilities were computed by choosing a simplified geometry, that includes only the bare detector and disregards the front-end electronics as well as the cooling system (tube and plates). Following the exact same workflow detailed above, one obtains the results shown in Tab. 6.11. With respect to the results shown for instance in Tab. 6.9 the neutron values drop by approximately 30%, establishing by far the largest difference among the considered particles. In fact the neutron hit rate drops as the cooling copper plates acted as a target for the production of neutron-induced secondary particle. Photons, electrons, and positrons, in turn, involve exclusively electromagnetic processes, and as such they are partially shielded by these same copper layers in the complete geometry. Consistently, the consequence in adopting the simplified geometry is to increase the hit rate due to these particles. A difference common to all particles with respect to the complete geometry is that, adopting a simplified layout, chambers A and B have values compatible with each other within a interval of 2σ. Indeed the removal of layers that accentuate the asymmetry of the super-chamber impacts the difference in the A and B chambers: it is now much reduced compared with the results shown so far.

BERT_HP	neutrons	photons	electrons	positrons
even A	0.00116(3)	0.0100(1)	0.13(1)	0.13(1)
even B	0.00116(3)	0.0102(1)	0.10(1)	0.10(1)
odd A	0.00131(4)	0.0103(1)	0.10(1)	0.11(1)
odd B	0.00120(4)	0.0098(1)	0.13(1)	0.13(1)

Tab. 6.11.: Hit probabilities for Triple-GEM "A" and "B" in even and odd configuration, using PL FTFP_BERT_HP, and a simplified GE1/1 geometry that excludes the front-end electronics and cooling system. The error is only statistical and includes the uncertainty on the sensitivity and on the incident flux.

	neutrons	photons	electrons	positrons
no holes	0.00050(1)	0.00755(8)	0.18(2)	0.18(2)
holes	0.00051(2)	0.00749(8)	0.18(2)	0.18(2)

Tab. 6.12.: Comparison of the hit probability with and without taking into account the modelling of the holes in GEM foils.

6.8 Estimation of the sensitivity

6.8.1 Modelling of the holes in the GEM foils

The average diameter of a hole in a GEM kapton foil is around 60 μm. Since the hole pitch is 140 μm, a short computation shows that the GEM holes occupy $\sim 17\%$ of the foil surface. This could have an impact on the simulation of the sensitivity of the Triple-GEM. To find out, a reduced 10×10 cm^2 version of the chamber has been simulated, with a simplified geometry (no GEB, no VFAT, etc.). Photons and neutrons have been generated according to their angle distribution in the GE1/1 station. The results presented in Fig. 6.27 and Fig. 6.28 clearly show that the impact due to the presence of the holes, if any, is negligible. Due to the significantly different time duration of the simulations, due to the microscopic details brought by the numerous holes, all consecutive results are obtained with a geometry having GEM foils consisting of full kapton material. Hit probabilities are shown in Tab. 6.12 and prove that the ultimate impact of the presence of the GEM foils holes is therefore negligible.

6.8.2 Choice of the gas

Starting from 2017, the CMS policy will ban all greenhouse gases used in detectors, such as $C_2H_2F_4$, CF_4, and SF_6. Unless an alternative is found, the GEM collaboration will then be forced to abandon the Ar:CO_2:CF_4 (45:15:40) mixture, and switch to the Ar:CO_2 (70:30) one. The experimental impact of this change has already been

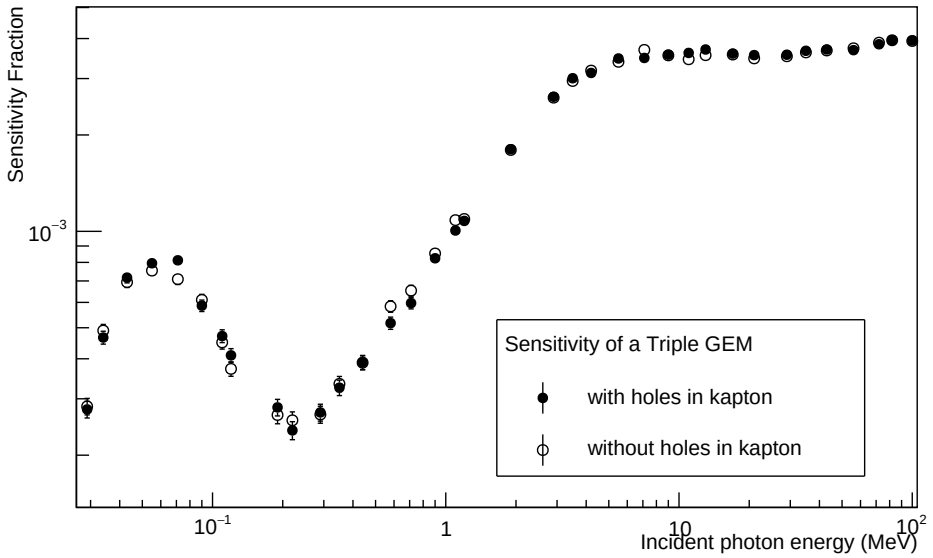

Fig. 6.27.: Triple-GEM sensitivity to photons as a function of incident energy generated according to the angle distribution in the GE1/1 station, provided by FLUKA. The plot shows a comparison with and without taking into account the modelling of the holes in the kapton foils. The respective yields are well within each other statistical error.

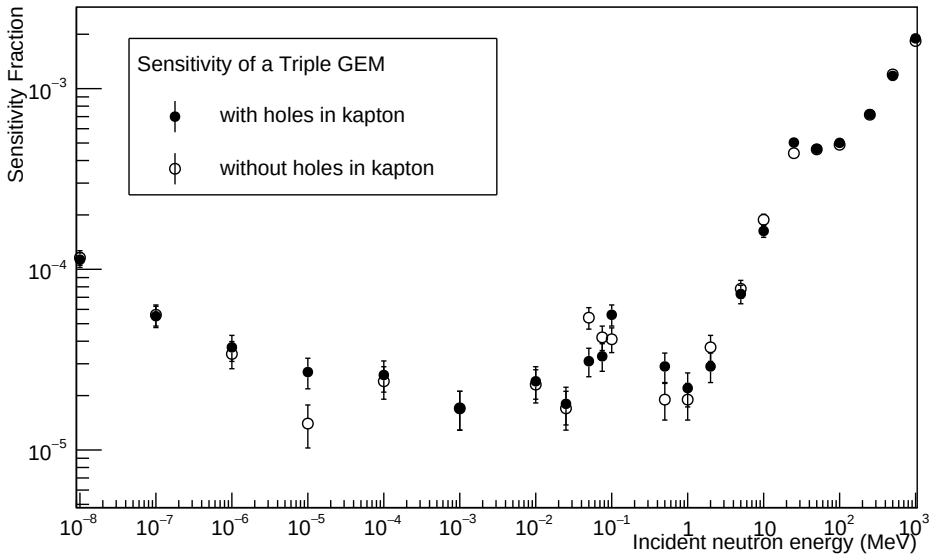

Fig. 6.28.: Triple-GEM sensitivity to neutrons as a function of incident energy generated according to the angle distribution in the GE1/1 station, provided by FLUKA. The plot shows a comparison with and without taking into account the modelling of the holes in the kapton foils. The respective yields are well within each other statistical error.

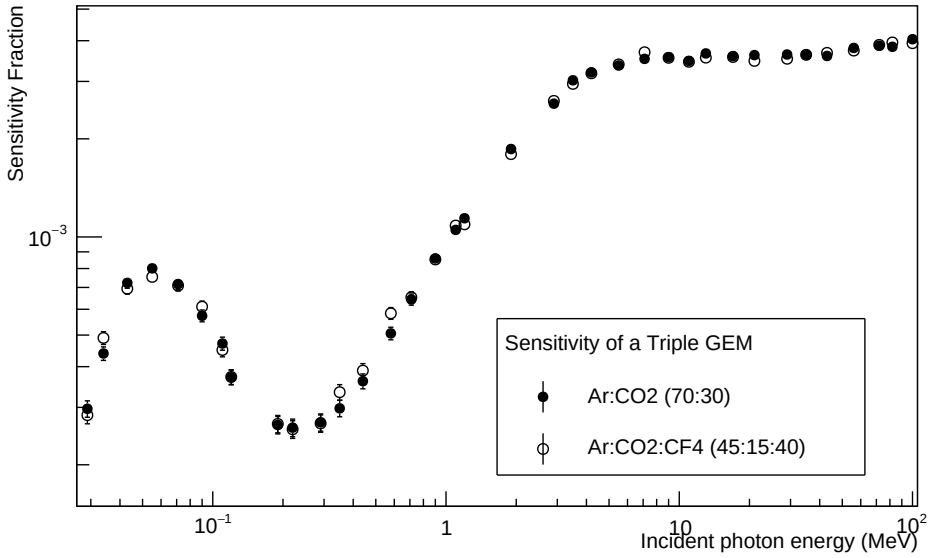

Fig. 6.29.: Triple-GEM sensitivity to photons as a function of incident energy generated according to the angle distribution in the GE1/1 station, provided by FLUKA. The plot shows a comparison with Ar:CO_2 (70:30) gas mixture and the Ar:CO_2:CF_4 (45:15:40) one. The respective yields are well within each other statistical error.

	neutrons	photons	electrons	positrons
Ar:CO_2:CF_4 $(45:15:40)$	$0.00050(1)$	$0.00755(8)$	$0.18(2)$	$0.18(2)$
Ar:CO_2 $(70:30)$	$0.00043(2)$	$0.00748(8)$	$0.18(2)$	$0.18(2)$

Tab. 6.13.: Comparison of the hit probability as a function of the gas mixture. The Ar:CO_2:CF_4 line corresponds to the first line of Tab. 6.12.

discussed in Sec. 5.3.2. Does the output of the GEANT4 simulation depend on the nature of the chosen gas mixture? To find out, a comparison was performed using a 10×10 cm^2 Triple-GEM geometry and computing the sensitivity to photons and neutrons for each of the two cases. The results are shown in Fig. 6.29 and Fig. 6.30. The qualitative difference is certainly negligible for photons, but not for neutrons. This is due to the fluorine contribution given the presence of resonance peaks in the (n,tot) cross-section in the sub-MeV range, absent in carbon and oxygen. Ultimate hit probabilities for GE1/1 region are shown in Tab. 6.13; due to the uncertainty of the foreseen gas mixture during Run 3 and following, they reveal the appearance of a contribution to the systematic error in the case of the sensitivity to neutrons.

6.8.3 Energy threshold

As anticipated in Sec. 6.7.6, it is interesting to check if the method to compute the sensitivity that involves uniquely the presence of a charged particle in the gas

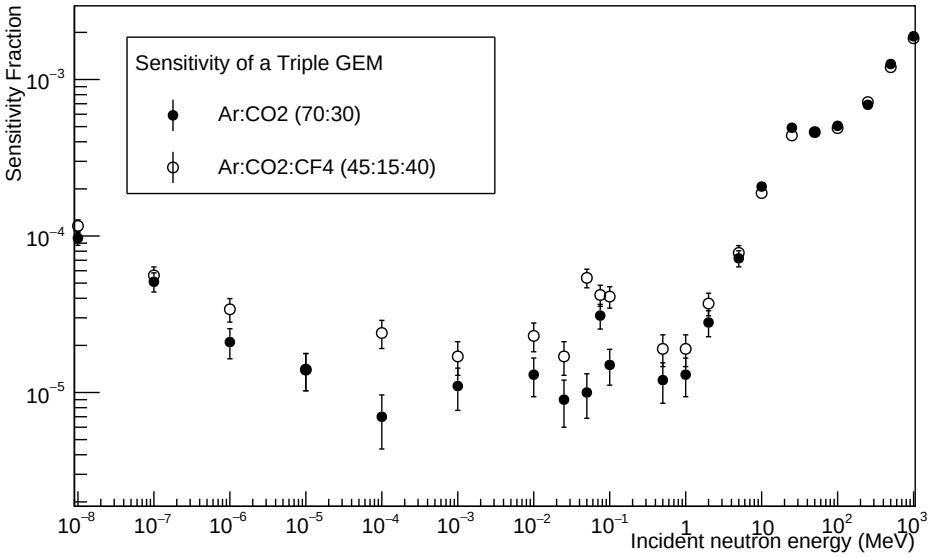

Fig. 6.30.: Triple-GEM sensitivity to neutrons as a function of incident energy generated according to the angle distribution in the GE1/1 station, provided by FLUKA. The plot shows a comparison with Ar:CO_2 (70:30) gas mixture and the Ar:CO_2:CF_4 (45:15:40) one. The qualitative difference between the curves is not negligible.

gaps is confident with the method accounting the charge threshold induced on the strips imposed by the electronics. The present test requires the knowledge of the threshold itself and the Triple-GEM gain at a certain current (or high voltage). This current has to stand on the detector efficiency plateau. This information is given by the efficiency as a function of the current, measured during the October 2014 test-beam campaign at CERN, shown in Fig. 6.31. The chosen gain is equal to 1800, and corresponds to a current value lying at the beginning of the plateau and equal to 660 μA (approximately 3300 V). The threshold (thr) on the electronics is equal to 1.6 fC. In order for the signal to be detected, the minimum number of electrons inducing a charge on the strips is therefore:

$$N_{\mathrm{min}} = \frac{\mathrm{thr}}{Q_{\mathrm{e}}}, \tag{6.24}$$

where Q_{e} is the positron charge.
As previously stated, the main assumption of the simulation is that only the drift and the transfer 1 gap are involved in the formation of the signal. An ionisation occurring in the drift gap – or in general a charged particle appearing there – undergoes the full amplification chain; in other words, it is amplified with the total gain. The minimum number of electrons to be produced in the drift gap is therefore:

$$N_{\mathrm{d}} = \frac{N_{\mathrm{min}}}{G}. \tag{6.25}$$

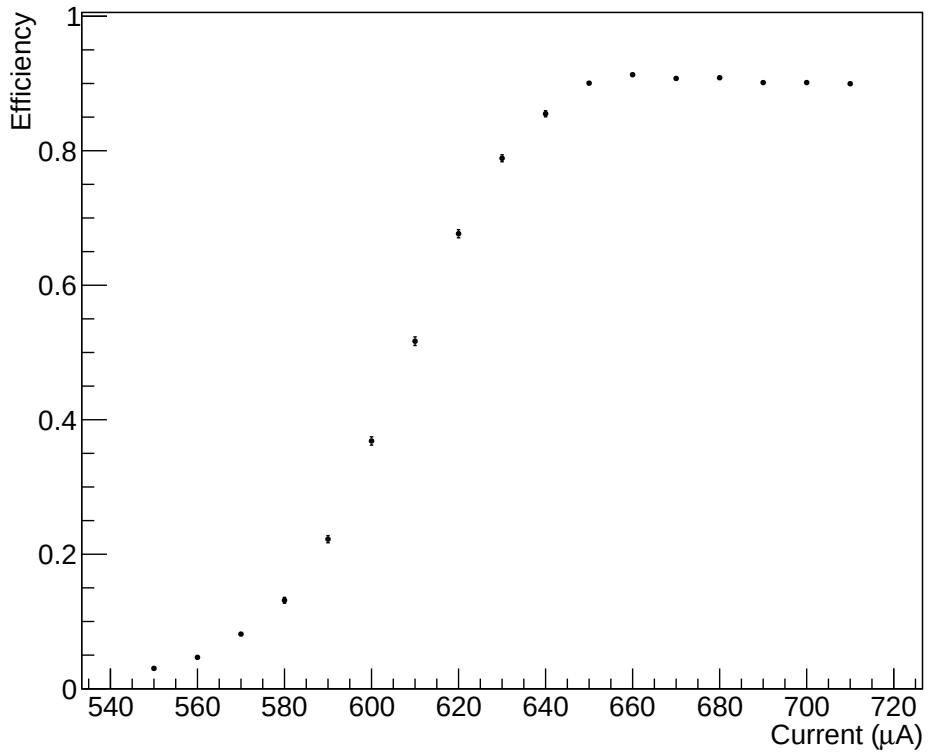

Fig. 6.31.: Detection efficiency of a Triple-GEM as a function of the current for a beam of muons having a momentum of 150 GeV/c, measured in the October 2014 test-beam campaign at CERN. Credits: Thierry Maerschalk.

	neutrons	photons	electrons	positrons
even A	$0.00149(5)$	$0.0086(1)$	$0.13(1)$	$0.13(1)$
even B	$0.00162(5)$	$0.0091(1)$	$0.070(9)$	$0.073(9)$
odd A	$0.00148(5)$	$0.0089(1)$	$0.068(8)$	$0.072(8)$
odd B	$0.00138(4)$	$0.0083(1)$	$0.12(1)$	$0.12(1)$

Tab. 6.14.: Hit probabilities for Triple-GEM A and B in even and odd configuration according to the algorithm involving the deposited energy by ionisation. The error is only statistical.

Assuming that each amplification stage gives the same contribution, this same minimum number in the transfer 1 gap is:

$$N_{\mathrm{t1}} = \frac{N_{\mathrm{min}}}{\left(\sqrt[3]{G}\right)^2}. \tag{6.26}$$

The minimum deposited energy that generates a detectable signal to be released in the gas gap is:

$$E_{\mathrm{dep}} = N_{\mathrm{d/t1}} \cdot U_{\mathrm{gas}}, \tag{6.27}$$

where U_{gas} is the average energy potential for a gas mixture. Of course E_{dep} is gas gap- and gas-dependent. Moreover, it carries the assumption that all of the charge is induced on one single strip, that is, if the cluster size (cs) is 1. A more general relation is then:

$$E_{\mathrm{dep}}^{\mathrm{corrected}} = \mathrm{cs} \cdot E_{\mathrm{dep}}. \tag{6.28}$$

For the Ar:CO_2:CF_4 ($45\% : 15\% : 40\%$) gas mixture, the average energy potential is [73]

$$U_{\mathrm{gas}} = (0.45 \cdot 26 + 0.15 \cdot 34 + 0.40 \cdot 54)\ \mathrm{eV} = 38.4\ \mathrm{eV}. \tag{6.29}$$

This ultimately allows to estimate the sensitivity of the Triple-GEM according to the alternate algorithm based on the deposited energy by ionisation. The yields for a cluster size equal to 1 are reported in Tab. 6.14. If compared with Tab. 6.9, the results show little to no difference in the cases of photons, electrons and positrons. On the contrary, a difference is visible in the neutron case, although confident within 2σ. To keep a fixed cluster size equal to 1 when evaluating the sensitivity is not a realistic option. This is why the sensitivity yields were evaluated for a cluster size included between 1 and 2, to give an estimation of the dependence from this experimental parameter. After being convoluted with the incident flux, they provide as usual the hit probabilities for each kind of particle. The results are shown in Fig. 6.32. The cluster size number can be converted to equivalent yield of threshold on the induced charge: to set a cluster size equal to 2 mathematically corresponds to twice the charge induction on a single strip. If the threshold on a strip is 1.6 fC, two fired strips imply a total charge of 3.2 fC. This equivalence is reflected in the horizontal axes of Fig. 6.32. The results prove a very weak dependence on the exact

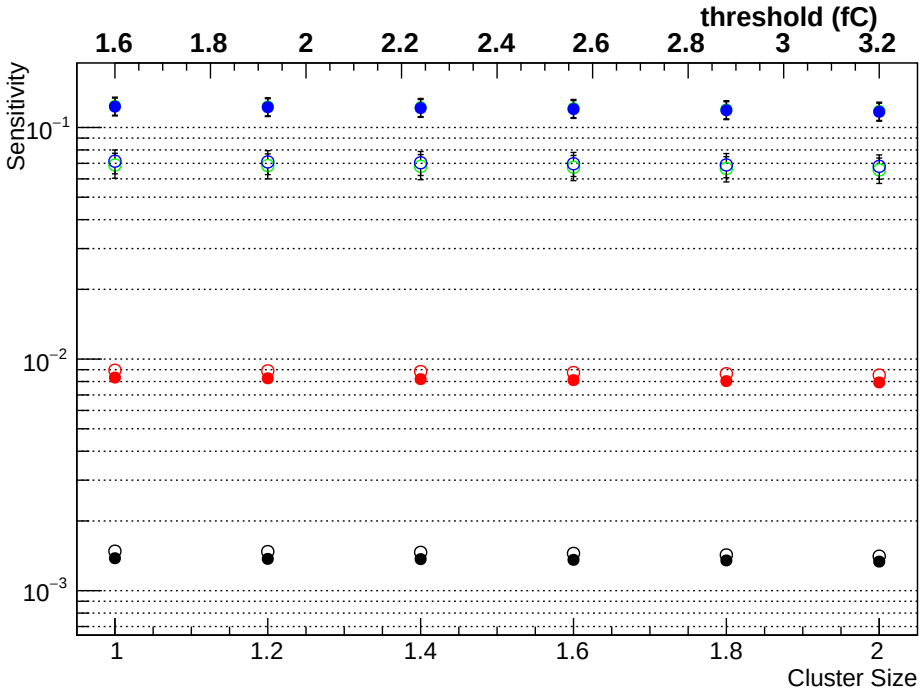

Fig. 6.32.: Hit probabilities for a Triple-GEM in the odd configuration. The color code and the marker shape follows the same legend as in Fig. 6.25 and 6.26: empty bullets represent the A chamber, while full bullets represent the B chamber. Black points refer to neutrons, red to photons, green to electrons, and blue to positrons. The error bars are statistical.

value of the threshold, as long as it lies on the same order of magnitude. The reason for this is straight-forward to understand looking at Fig. 6.33 and 6.34 that show the deposited energy as a function of the incident neutron energy, in the drift and in the transfer 1 gap respectively, in the case of neutrons for the "odd" configuration. Considering that a threshold of 1.6 fC is equivalent to a deposition of $2 \cdot 10^{-4}$ MeV for the drift gap and $3 \cdot 10^{-4}$ MeV for the transfer 1 gap, Fig. 6.33 and 6.34 show that the applied cut is negligible if one considers the average deposited energy.

6.8.4 Evaluation of the angle distribution impact uncertainty

As previously stated, the angle distribution of the particles impinging on the surface of the GE1/1 detectors is given by a FLUKA simulation. The statistical precision of the distribution is given by the number of particles resulting from the collision simulation. This means that due to the nature of the background origin, the number of electrons and positrons is limited to few hundreds. This could be solved by processing larger samples of simulations.

What will be evaluated in this section is the systematic uncertainty related to the angle distribution itself. Due to the ultimate goal of this study, that is the estimation of the background hit rate on GE1/1, the risk is that the detector's response is

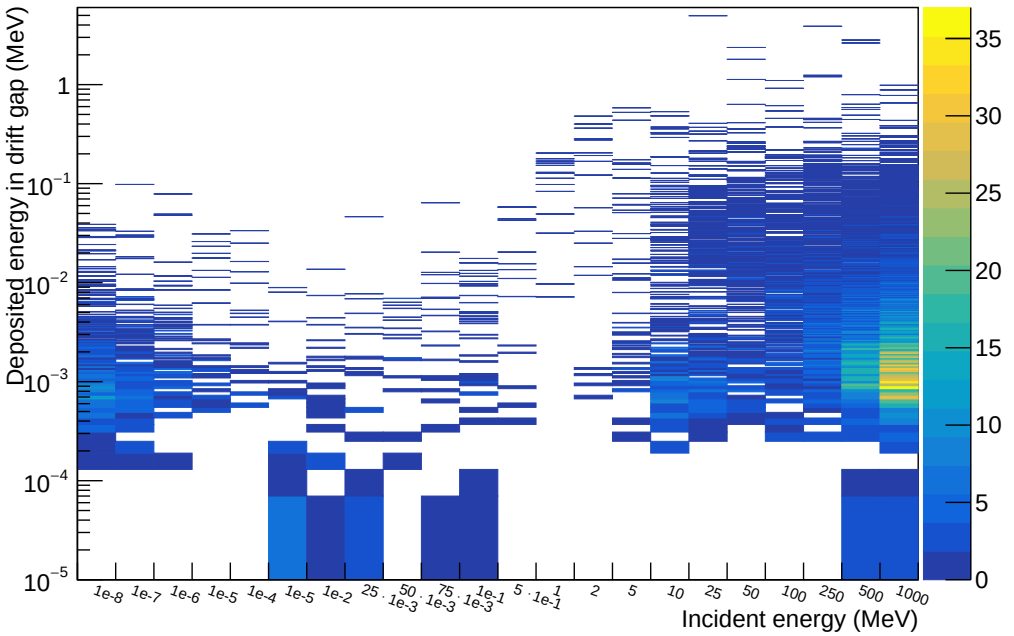

Fig. 6.33.: Deposited energy in the drift gap as a function of the incident energy of neutrons, for the "odd" configuration. The z-axis indicates the number of events per bin.

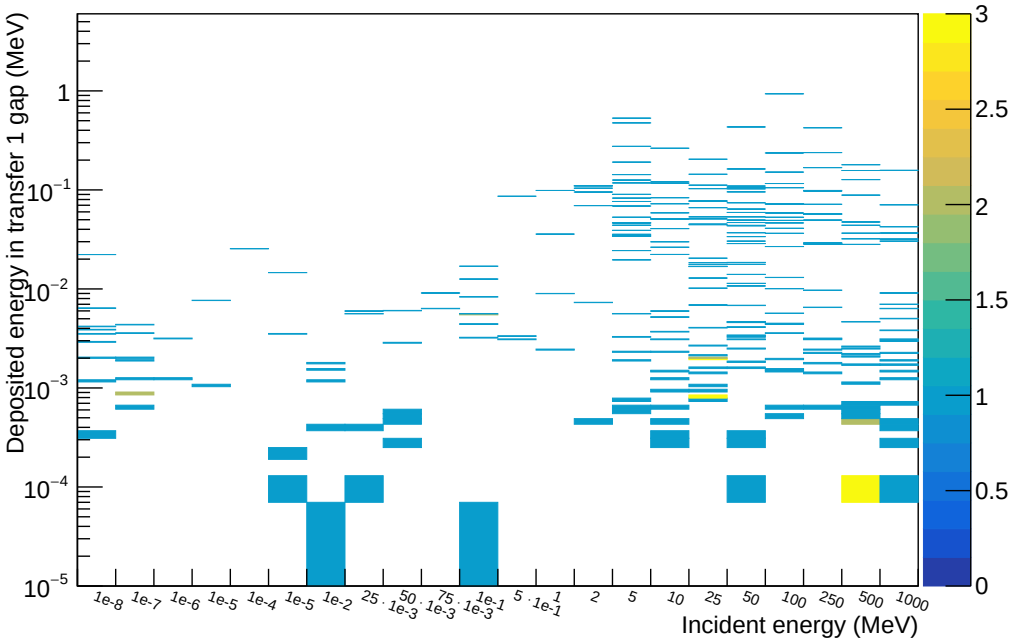

Fig. 6.34.: Deposited energy in the transfer 1 gap as a function of the incident energy of neutrons, for the "odd" configuration. The z-axis indicates the number of events per bin.

	neutrons	photons	electrons	positrons
even A	0.00257(6)	0.0153(2)	0.11(1)	0.12(1)
even B	0.00261(6)	0.0116(1)	0.048(8)	0.061(8)
odd A	0.00257(6)	0.0126(1)	0.048(8)	0.061(8)
odd B	0.00211(5)	0.0089(1)	0.10(1)	0.110(9)

Tab. 6.15.: Hit probabilities for Triple-GEM A and B in even and odd configuration assuming that the source is evenly spread on a sphere surrounding the super-chamber. The error is only statistical.

underestimated. This is why a series of simulations were performed assuming the worst case scenario, that is particles coming from every possible angle. In the GEANT4 simulation this is implemented by evenly distributing the source over a sphere surrounding the detector; all trajectories point at the center of the detector. The results are shown in Tab. 6.15 for every kind of particle. In fact the larger is the deviation from the perpendicular direction, the longest is the path that a particle may travel in the detector's volume. This is verified for neutral particles, not for charged ones, as they have a larger probability to lose their energy in the layers of solid materials without reaching the gas.

6.8.5 Results and uncertainties

In the previous sections, a series of possible sources of systematic errors was listed: the choice of the PL, the modelling of the holes in the kapton (that does not give significant contributions), the choice of the ionizing gas, the electronic threshold, and the angle distribution. Other sources exist but are not directly presented in this thesis: the geometry of the super-chamber is likely to be subjected to further modifications, especially concerning the position of the optohybrid and the layout of the cooling system. Independent results of GE1/1 sensitivities involving a different cooling system layout and few geometrical differences are presented elsewhere [65]. The results are reported in Tab. 6.16. These yields are taken into account in the final computation of the systematic errors shown in Tab. 6.17.

Another important source of error would be the incident flux given by FLUKA, which is currently not known. The kind of estimations available in former documents [40] were made from very simple CMS geometry models (300-400 elements only), but the latest FLUKA model has much more detail. It is currently not possible to build an equivalent geometry model for other codes, due to lack of resources. Therefore such up-to-date comparisons do not exist, as different codes are used for different purposes, in particular MARS [130], when the assumption that geometry detail is not necessary holds (S. Mallows, M. Guthoff, I. Azhgirey on behalf of BRIL Radiation Simulation, personal communication, 27 January 2016). Nevertheless the known

	Sensitivity (%)
neutrons	0.18 ± 0.05
photons	0.97 ± 0.04
electrons	8 ± 3
positrons	8 ± 3

Tab. 6.16.: GE1/1 sensitivity results obtained independently from the ones shown in this work, but with the same simulation framework and a few differences in the geometry and in the cooling system description. The errors shown include statistical and systematic errors coming from the different sensitivity depending on the chamber and the super-chamber configuration, with an additional systematic uncertainty related to the GEANT4 model used to simulate low energy neutron interactions.

particles	hit probability (%)
neutrons	$0.163 \pm 0.002(\text{stat.})^{+0.07}_{-0.05}(\text{syst.})$
photons	$0.884 \pm 0.004(\text{stat.})^{+0.2}_{-0.03}(\text{syst.})$
electrons	$9.2 \pm 0.3(\text{stat.}) \pm 3(\text{syst.})$
positrons	$9.8 \pm 0.3(\text{stat.}) \pm 3(\text{syst.})$

Tab. 6.17.: Hit probability values averaged over two orientation configurations and the two chambers forming one super-chamber. The statistical error is due to the limited amount of event generated by GEANT4, while the systematic ones are due to the different response of the PLs, the chosen gas, the presence of an electronic threshold, the uncertainty on the angle distribution of the incoming particles, and independent results with few different geometries [65].

contributions to the statistical and systematic error have been separately propagated. All results are shown in Tab. 6.17. The mean value of the sensitivity is taken as the weighted between the one obtained with PL `FTFP_BERT_HP` and `QGSP_BIC_HP`, as the validation phase did not allow to decide between them. Moreover, there are four chambers in total, taking into account two chambers forming a super-chamber, times the two configurations: therefore a further average is obtained from these four values.

6.9 Involved processes

Fig. 6.35 shows the physical processes with GEANT4 notation that generate a secondary particle satisfying the definition of sensitivity, as a function of the energy of the incident neutron. In the low-energy region ($E_\text{n} < 10^{-5}$ MeV) the neutron sensitivity is mostly due to the photons coming from (n,γ) capture reactions whose cross-section rises at lower neutron energies ($\sigma \propto 1/\sqrt{E_\text{n}}$). At higher energies ($E_\text{n} > 1$ MeV) the sensitivity rises rapidly and reaches a maximum as a consequence

of protons produced by elastic scattering on H and by (n,p) reactions on nuclei. At even higher energies, inelastic nuclear reactions occur, leading to the activation of certain materials, as testified by the presence of the decay processes for $E_{\mathrm{n}} \geq 250$ MeV. Secondary particles generated by these reactions, such as pions and muons, undergo inelastic processes or nuclear capture.
Fig. 6.36 provides an alternate view of this plot, encouraging a qualitative comparison between the shape of the sensitivity to neutrons as a function of incident energy – shown in Fig. 6.25 and 6.26 – and the contribution to this shape coming from the single processes. The ordering of processes is the same than in Fig. 6.35. One can then easily attribute the cause of the rising of the sensitivity to neutrons in the range $E_{\mathrm{n}} > 1$ MeV to the ionisation by electrons and delta ray production, and above all to the ionization by hadrons (typically protons resulting from nuclear reactions).

The same plots were produced for the sensitivity to photons, and are shown in Fig. 6.37 and 6.38. The latter allows to clearly identify the rise of sensitivity around 100 keV with the combined actions of the photoelectric effect and the ionization by electrons and delta rays.

Going on with electrons and positrons, respective plots are shown in Fig. 6.39 and 6.40, and in Fig. 6.41 and 6.42. One can notice the decisive contribution of the annihilation process in the positron case.

6.10 RPC hit rates in CMS

A last, effective way to assess the quality of the simulation is to apply the workflow presented above to detectors whose background hit rate is known. 2011 data convenient for this goal are available for the RPC detectors of the endcap region of CMS, installed in stations RE1/2 and RE1/3. Using the RPC geometry described in [127] along with RE1/2 active area information (Z. Aftab et al., "Geometrical Layout and Mechanical details of CMS End Cap RPCs", CMS Internal Note) it was possible to make a closure test between RPC data and GEANT4 predictions convoluted with FLUKA background fluxes. Despite the absence of systematic errors, data and simulation comparisons, reported in Fig. 6.43 show an excellent agreement.
In addition, a set of 4 RPC detectors was installed in 2008 in the inner ring of disk 1, in a station temporarily called RE1/1, now destined to the GE1/1 upgrade. However, these chambers were not connected to the gas nor powered until 2015. Moreover, the efficiency of such detectors is unknown, as no commissioning phase was ever performed. Therefore, (unpublished) data coming from them are very preliminary as they carry big uncertainties. Nevertheless, depending on their position their average

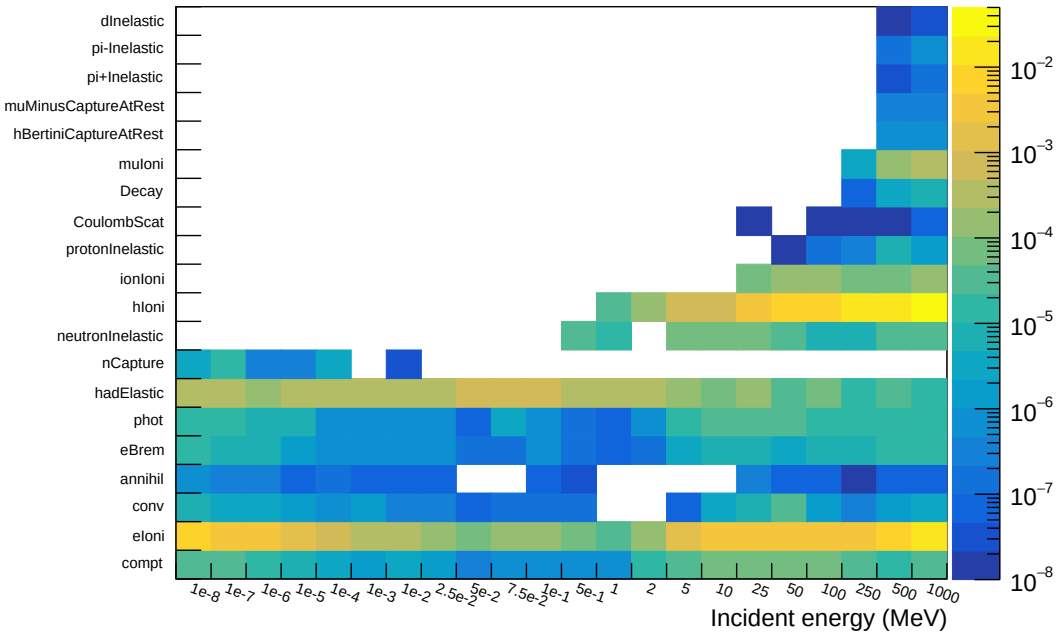

Fig. 6.35.: Processes that generate a secondary particle in a sensitive event, as a function of the incident neutron energy for the odd configuration. White cells indicate a process probability $< 10^{-8}$. The z-axis is normalized on the total number of secondary particles. The meanings of the physical processes listed on the y axis are the following. `dInelastic`: inelastic scattering of deuterons; `pi-Inelastic`: inelastic scattering of π^-; `pi+Inelastic`: inelastic scattering of π^+; `muMinusCaptureAtRest`: μ^- (hadronic) capture at rest; `hBertiniCaptureAtRest`: hadronic absorption at rest using Bertini Physics lists; `muIoni`: ionization and energy loss by μ^+ and μ^-; `Decay`: decay of unstable particles; `CoulombScat`: Coulomb elastic scattering; `protonInelastic`: inelastic scattering of protons; `ionIoni`: ionization and energy loss by ions; `hIoni`: ionization by hadrons; `neutronInelastic`: neutron inelastic scattering; `nCapture`: capture of at-rest neutrons; `hadElastic`: elastic scattering of hadrons; `phot`: photoelectric effect; `eBrem`: electron bremsstrahlung; `annihil`: matter-antimatter annihilation; `conv`: gamma conversion (also called pair production); `eIoni`: ionization by electrons and delta ray production; `compt`: Compton effect.

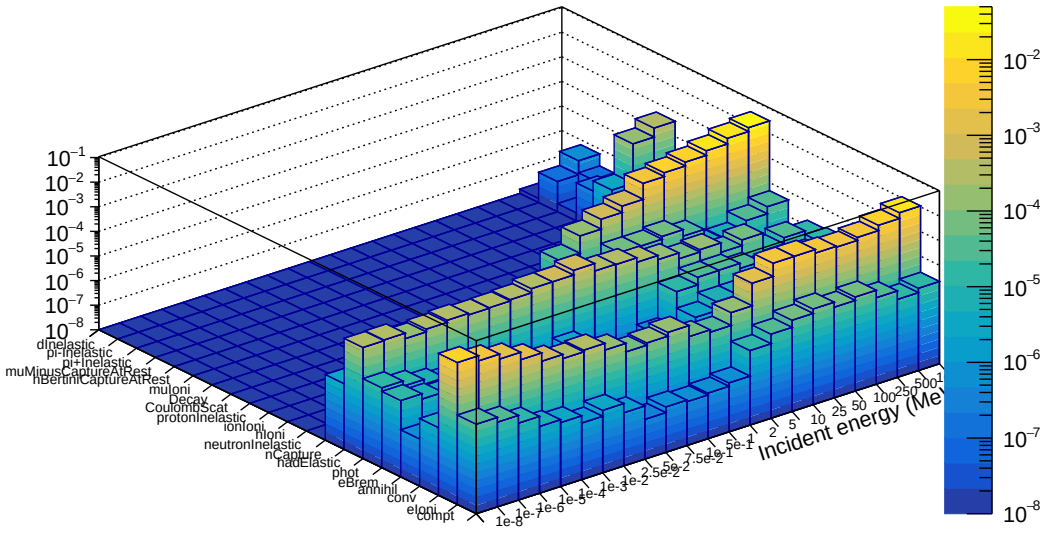

Fig. 6.36.: Partial 3D view of Fig. 6.35.

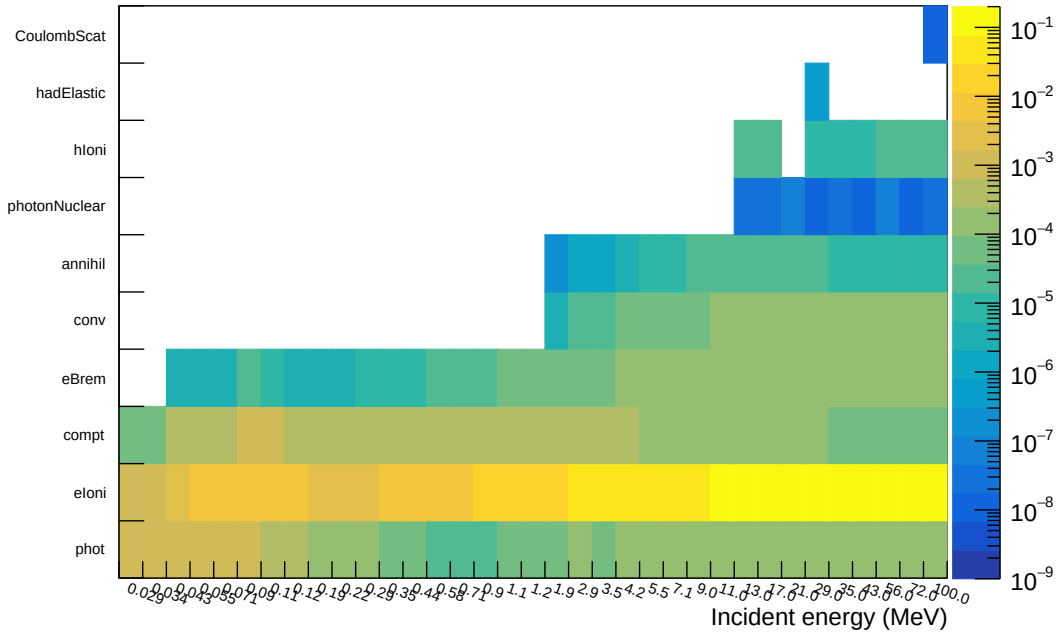

Fig. 6.37.: Processes that generate a secondary particle in a sensitive event, as a function of the incident photon energy for the odd configuration. The z-axis is normalized on the total number of secondary particles. The meanings of the physical processes listed on the y axis and not included in Fig. 6.35 is summarized by the presence of `photonNuclear`: photon-induced nuclear inelastic reaction.

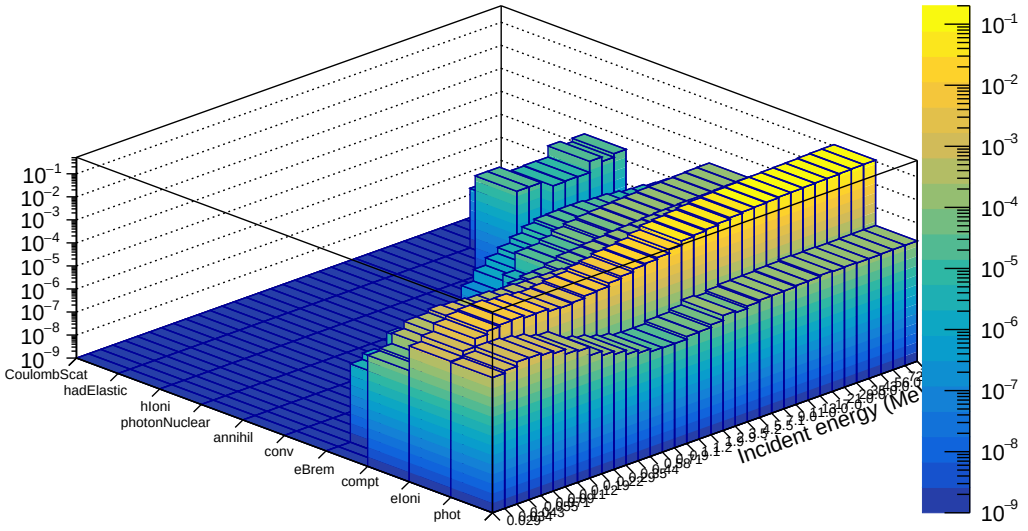

Fig. 6.38.: Partial 3D view of Fig. 6.37.

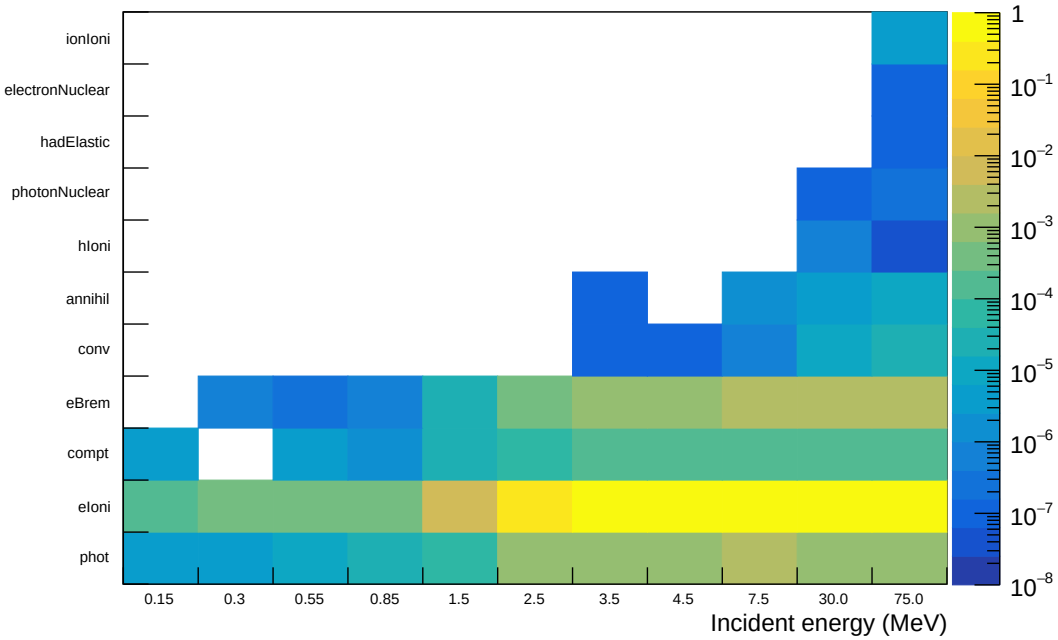

Fig. 6.39.: Processes that generate a secondary particle in a sensitive event, as a function of the incident electron energy for the odd configuration. The z-axis is normalized on the total number of secondary particles. The meanings of the physical processes listed on the y axis and not included neither in Fig. 6.35 neither in Fig. 6.37 is summarized by the presence of `electronNuclear`: electron-induced nuclear inelastic reaction.

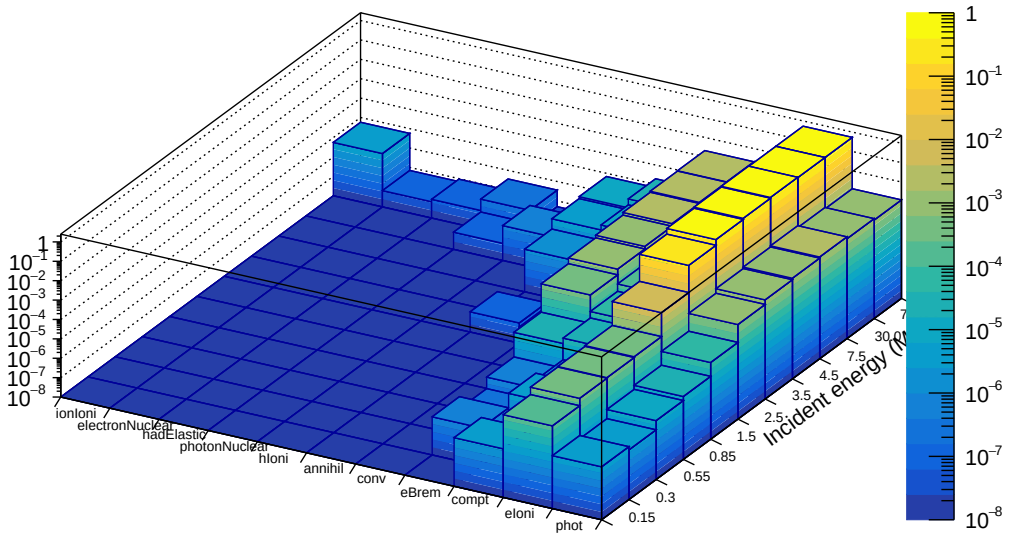

Fig. 6.40.: Partial 3D view of Fig. 6.39.

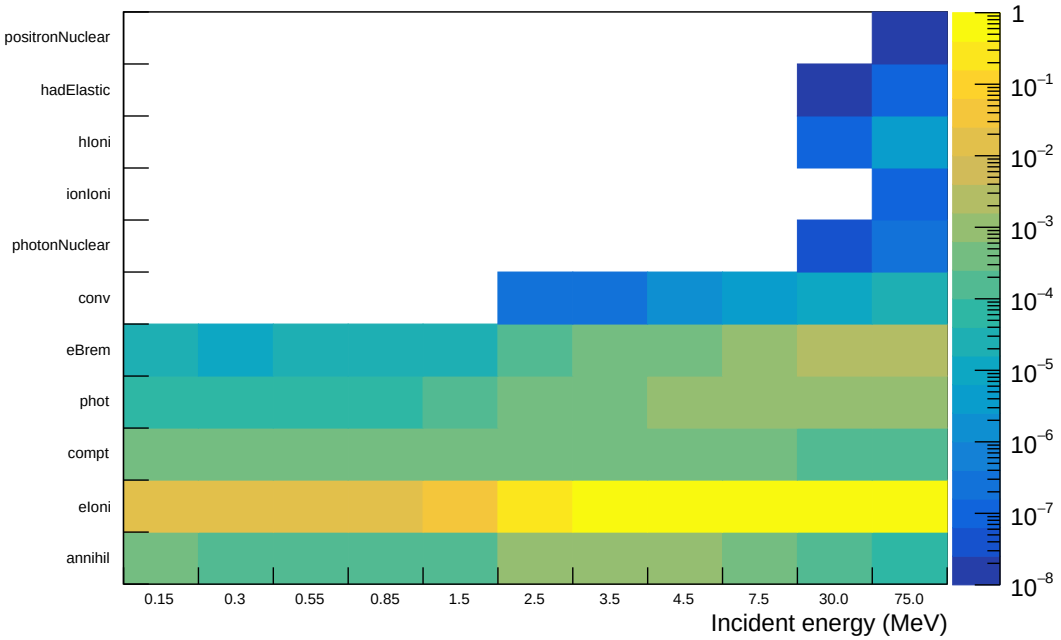

Fig. 6.41.: Processes that generate a secondary particle in a sensitive event, as a function of the incident positron energy for the odd configuration. The z-axis is normalized on the total number of secondary particles. The meanings of the physical processes listed on the y axis and not included neither in Fig. 6.35 neither in Fig. 6.37 neither Fig. 6.39 is summarized by the presence of `positronNuclear`: positron-induced nuclear inelastic reaction.

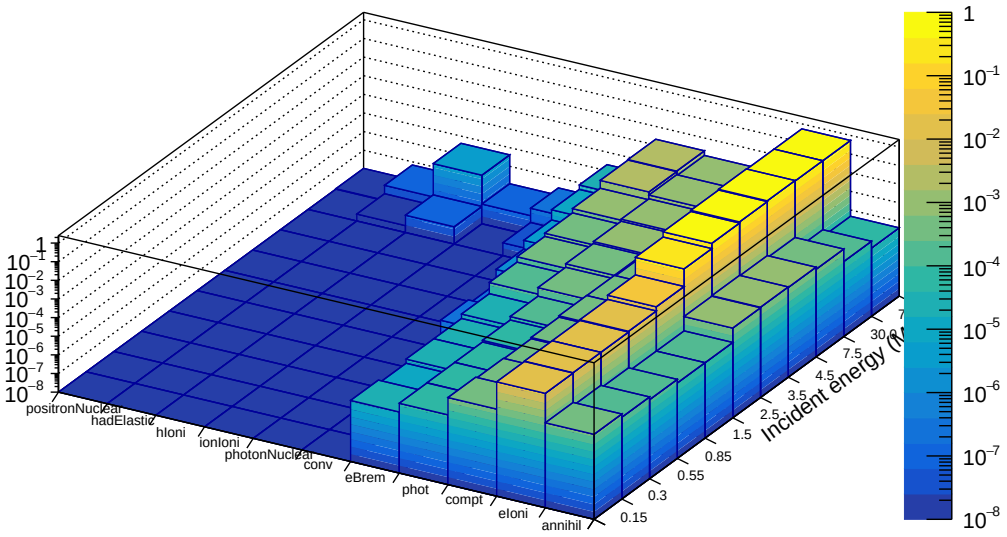

Fig. 6.42.: Partial 3D view of Fig. 6.41.

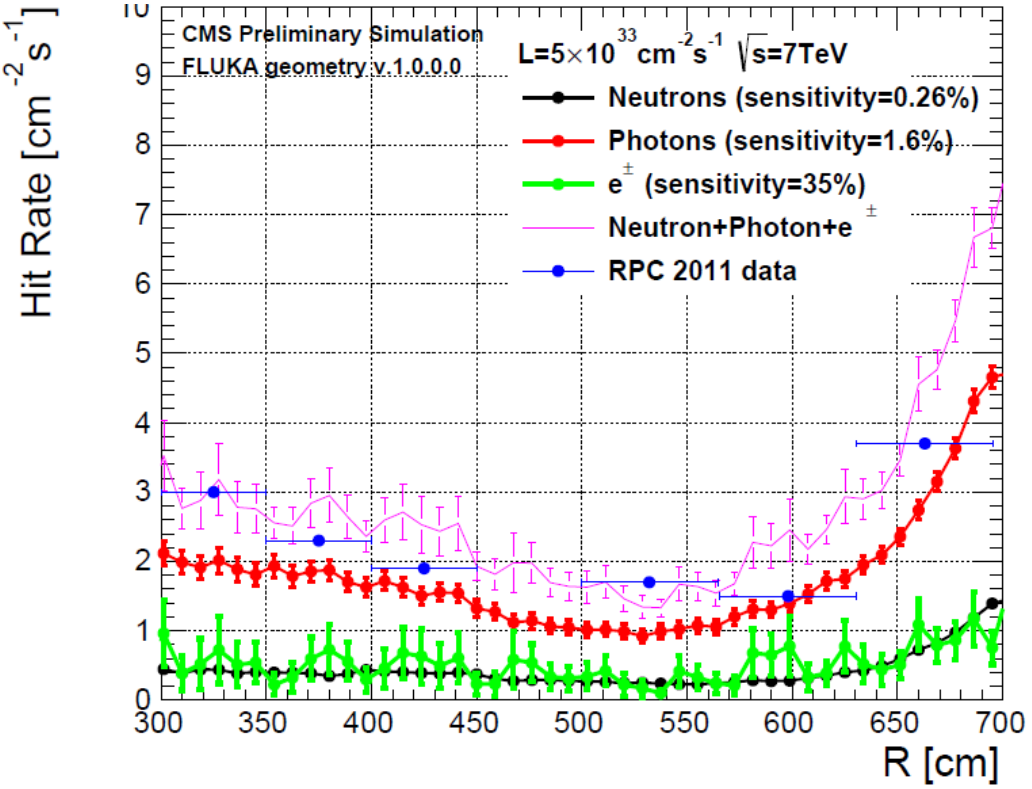

Fig. 6.43.: Background hit rate of RE1/2 and RE1/3 as a function of the radial coordinate predicted by GEANT4 and FLUKA, compared with corresponding 2011 data. Credits: Alfredo Castaneda, Silvia Costantini, Alice Magnani.

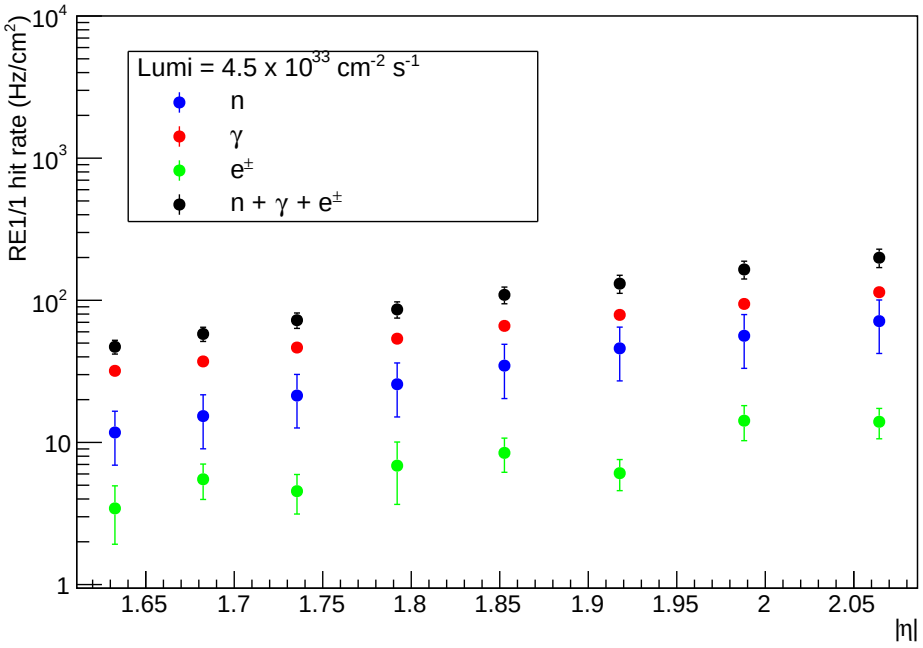

Fig. 6.44.: Background hit rate on RE1/1 station simulated with GEANT4 and FLUKA as a function of $|\eta|$. RE1/1 sensitivity values are a courtesy by Alice Magnani.

hit rate lie between 25 and 45 Hz/cm^2, that is a factor of at least 2 below GEANT4 predictions for these specific chambers, shown in Fig. 6.44.

6.11 Is it possible to reject background particles?

Given the inherent double-readout structure of the super-chamber, it is possible to collect some topology information about the signals coming from background sources. The goal is to search for differences between background and signals behaviour, with respect to muon detection, in order to establish a simple way to remove such background contributions. If it was established that given a super-chamber, neutral particles induce a signal in only one of the two Triple-GEM chambers at a time, it would therefore be an easy signature to detect. This would allow to better reject background signal during data analysis, or even at trigger level.
In Tab. 6.18, the fraction of events carrying a signature showing a signal in only one of the two Triple-GEM chambers is shown. This has been done for every kind of investigated particles, given energy and angle distribution at the CMS GE1/1 station coordinates. These values are normalized in the following way: the percentage of events in which chamber "A" ("B") and not "B" ("A") are hit is divided by the sensitivity of chamber "A" ("B").
The values show that it is highly likely that a neutral particle consumes its ionisation power within the volume of a single Triple-GEM detector. If compared with the

behaviour of a muon beam at 150 GeV, for which the probability to release a signal in both chambers is $> 99.9\%$, one can conclude that the neutron and photon signal feature can help to discriminate signal from (neutral) background by asking a coincidence between chambers "A" and "B". As expected, electrons and positrons don't share the same clear behaviour. Such an algorithm would certainly work in the removal of the majority of the charged background particle events, but with a minor impact.

		A not B	B not A
Neutrons	Odd	0.94(4)	0.93(4)
	Even	0.93(4)	0.94(4)
Photons	Odd	0.97(1)	0.96(1)
	Even	0.96(1)	0.96(1)
Electrons	Odd	0.58(6)	0.77(4)
	Even	0.77(4)	0.58(6)
Positrons	Odd	0.62(6)	0.78(4)
	Even	0.78(4)	0.60(6)

Tab. 6.18.: Fraction of events generating a signal in one Triple-GEM detector, and no signal in the associated Triple-GEM detector of the same super-chamber. Both super-chamber configurations were considered. Particles were simulated according to the energy and angles distributions at the CMS GE1/1 station coordinates.

6.12 Conclusions

In this Chapter a review of the interactions of with matter was first provided. Special attention was given to neutron physics from thermal energies up to the GeV scale. This was essential to the understanding of the simulation that was written, and executed with the usage of the GEANT4 framework. Our case of interest was then presented, and this lead to a research phase focused on the validation of the physics libraries, first electromagnetic and then hadronic. Any available source was analysed and efforts were done to reproduce experimental points and old simulations results alike. Sometimes, the ten years gap between physics libraries or the lack of information concerning the description of the environment – crucial when investigating neutron interactions – led to incompatibilities between the current results and the references. Nevertheless, the choice that was made consisted in conferring more trust to the state-of-the-art GEANT4 simulations, in light of the numerous independent validations with respect to data, and of the incessant updates released.

The question regarding how much the GE1/1 Triple-GEM detectors will suffer from the incident flux coming from the background particles has been provided an answer. The number of performed simulations allows a statistical error small enough to be

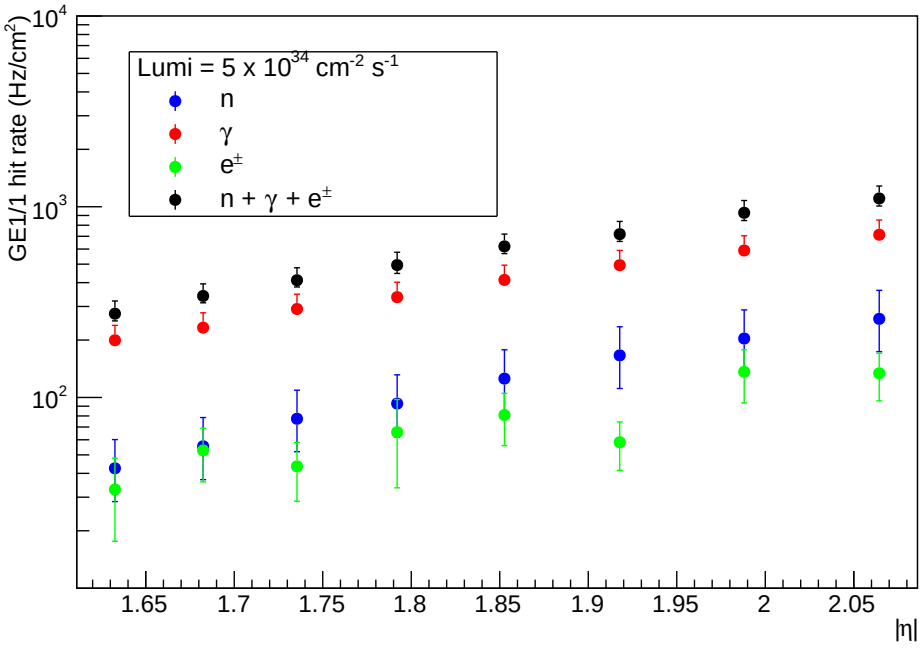

Fig. 6.45.: Hit rate of the simulated GE1/1 detector due to background particles as a function of $|\eta|$, in the harsh CMS environment corresponding to the instantaneous luminosity $\mathcal{L} = 5 \times 10^{34}$, typical of Phase II. The errors include statistical and systematic contributions. The plot was obtained by rescaling the curves in Fig. 6.8 by the sensitivities shown in Tab. 6.17. In the case of the electron/positron curve, an average of the two sensitivities has been computed.

negligible compared to the systematic uncertainties. Several sources of the latter have been investigated and the systematic contribution to the total uncertainty has been evaluated. The results were shown in Tab. 6.17. These values, once applied to the incident flux, allow to rescale the yields shown in Fig. 6.8. This operation provides the GE1/1 hit rate due to background particles as a function of $|\eta|$, shown in Fig. 6.45. This Figure shows that at the highest value of $|\eta|$, that is, the closest to the beam line, the total hit rate reaches a value of 1 kHz/cm^2. As explained in Sec. 5.4.3, the Triple-GEMs are required to have a rate capability of 10 kHz/cm^2 or better; experimental tests have proven that the gain stays constant up to 100 MHz/cm^2. Given the results of the simulations, the GE1/1 Triple-GEMs are guaranteed to operate in a safe enough environment throughout all Phase II.

Eventually the results of the simulations were critically analysed throughout the Chapter, and efforts were made to understand the physical processes underlying every one of them. This allowed to formulate an hypothesis about the possibility to discriminate between muon and background signals at a trigger level, by rejecting those events that do not fire the two Triple-GEM chambers forming one super-chamber.

In this area of research further developments may certainly involve similar simulations concerning GE2/1 detectors, and the more challenging ME0. In fact, having six planes of detection, ME0 needs special computing power in order to record all the processes providing signals in everyone of them.
On the longer term, one could wait for GEANT4 developments involving a reliable full chain of interaction and amplification in a gas detector, in order to simulate with a single software an event from the arrival of the incident particle to the detection and digitization of the signal.

7

Study of the forward-backward charge asymmetry of a potential spin 1 new dimuon resonance signal

7.1 Introduction

New heavy resonances decaying into a dimuon pair such as described in many Z' models – already presented in Sec. 2.5.2 – are low-background channels and good candidates for discoveries. In the search for such resonances, no significant excess above the Standard Model predictions was found using proton-proton collisions at $\sqrt{s} = 7$ and 8 TeV with the CMS detector. The lower limit on the mass of the resonance reaches values up to 3 TeV in some cases [131, 26]. Such a search was also performed by the ATLAS Collaboration and led to similar results [132, 25]. The current increase of the LHC beam energy from 4 TeV to 6.5 TeV, and up to 7 TeV in the upcoming years, will allow to probe higher mass values.
The goal of this section is to provide a projection of the CMS discrimination potential among different benchmark Z' models in the dimuon channel by looking at the forward-backward asymmetry, A_{FB}, a physical quantity discussed in Sec. 7.2. Three integrated luminosity scenarios are considered, corresponding respectively to the total integrated luminosity expected to be collected by the end of the two upcoming runs of the LHC – Run 2 and Run 3 – and by the end of the Phase II:

- 100 fb^{-1} at $\sqrt{s} = 13$ TeV corresponding to the foreseen center of mass and energy of the LHC Run 2 (2015-2018);

- 300 fb^{-1} at $\sqrt{s} = 14$ TeV corresponding to the foreseen center of mass and energy of the LHC Run 3 (2021-2023);

- 3000 fb^{-1} at $\sqrt{s} = 14$ TeV corresponding to the foreseen center of mass and energy of the LHC Phase II (2026 and beyond);

The estimations are first based on the analysis of the muon angular distributions and then with the addition of information coming from the dimuon pair rapidity. The analysis is designed to be as model independent as possible. This Chapter will eventually highlight the increases in luminosity of the LHC upgrades; the benefit to the analysis of the A_{FB} in the $\mathrm{Z}' \to \mu\mu$ decay channel will be shown. These studies include resolution effects but must still be extended to treat relevant sources of systematic uncertainties, such as effects due to misalignment, imperfect knowledge of the magnetic field, and theoretical uncertainties in the PDFs and K-factors used in Pythia.

7.2 Forward-backward charge asymmetry

7.2.1 Definition of the forward-backward charge asymmetry

The vector and axial-vector couplings in the neutral current annihilation process $\mathrm{q\overline{q}} \to \mathrm{Z}/\gamma^* \to \ell^+\ell^-$ lead to a forward-backward asymmetry A_{FB} in the polar angle distribution of the final state lepton ℓ^- with respect to the quark direction in the rest frame of the dilepton system. This is translated in a difference in the number of forward- versus backward-produced final state fermions. In fact, Eq. 2.67 is not invariant under parity transformation: right-handed and left-handed particles have different couplings to the Z boson. A_{FB} is defined as

$$A_{\mathrm{FB}} \equiv \frac{\sigma_{\mathrm{F}} - \sigma_{\mathrm{B}}}{\sigma_{\mathrm{F}} + \sigma_{\mathrm{B}}} = \frac{3}{8}\frac{c_2}{c_1}, \tag{7.1}$$

where

$$\sigma_{\mathrm{F}} \equiv \int_0^1 \frac{d\sigma(\mathrm{q\overline{q}} \to \ell^+\ell^-)}{d\cos\theta} d\cos\theta, \quad \sigma_{\mathrm{B}} \equiv \int_{-1}^0 \frac{d\sigma(\mathrm{q\overline{q}} \to \ell^+\ell^-)}{d\cos\theta} d\cos\theta, \tag{7.2}$$

and where θ is the angle in the dimuon center-of-mass reference frame between the negative lepton and the incident quark; c_1 and c_2 were defined in Eq. 2.68. A_{FB} is of special interest in the search for new physics: the angular differential cross-section of any spin 1 particle is proportional to $(1 + \cos^2\theta) + \frac{8}{3}A_{\mathrm{FB}}\cos\theta$. Therefore A_{FB} can help to distinguish signal from background or to identify a new signal.
The asymmetry arises then as a result of the interference between the vector couplings of the γ and the axial-vector coupling of the Z to the quarks and the final-state fermions. The $\cos\theta$ terms exactly cancel in purely electromagnetic (purely vector) interaction, while in the electroweak case the imbalance between the left and right chiral couplings destroys the cancellation.

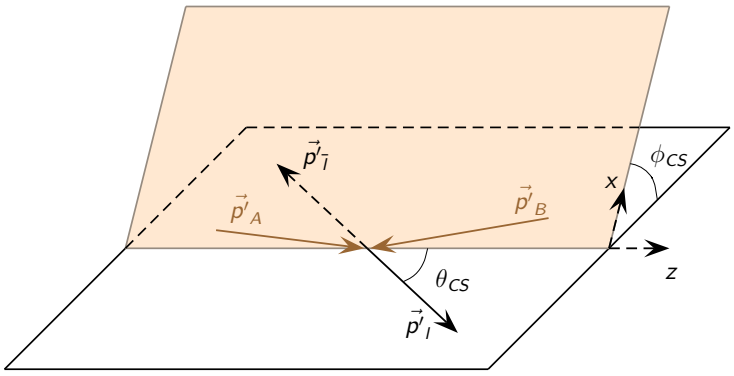

Fig. 7.1.: Definition of the Collins-Soper frame [134].

From a general point of view, the $\cos\theta$ distribution has the property to resolve the spin of the resonance. A spin 0 particle can be produced through gg or $\mathrm{q\overline{q}}$ fusion and will lead to a flat $\cos\theta$ distribution. For a spin 1 or 2 particle, the $\cos\theta$ is distributed according to the sum of an even polynomial, whose coefficients are univocally determined for a given production mode ($\mathrm{q\overline{q}}$ for spin 1, gg or $\mathrm{q\overline{q}}$ for a spin 0 or 2) and an odd polynomial, that leads to a forward-backward asymmetry and which is model dependent.

7.2.2 The Collins-Soper frame

The four-momentum of the incoming (anti-)quark is not known: as soon as the dilepton system transverse momentum p_{T} is non-zero, it is no longer collinear with the incoming beams. The impact of this effect on the asymmetry measurement is minimized by choosing a particular rest frame of the dilepton system, the Collins-Soper (CS) frame [133], in which the angle between the lepton and the quark, θ, is calculated. The CS frame (see Fig. 7.1 for a sketch) is defined as the frame in the center-of-mass of the dilepton pair for which:

- the z-axis bisects $\vec{p}'_A$ and $-\vec{p}'_B$;
- the x-axis is orthogonal to the z-axis, lies also in the plane spanned by $\vec{p}'_A$ and $\vec{p}'_B$ and its direction is chosen such that $\vec{p}'_{x,A}$ and $\vec{p}'_{x,B}$ are negative.

In this frame, one makes use of θ^*_{CS}, the angle between the negative lepton momentum and the z-axis, to approximate the value of θ. One can show that θ^*_{CS} can be expressed in term of the lepton variables in the laboratory frame:

$$|\cos\theta^*_{\mathrm{CS}}| = 2\left|\frac{(p_1^+ p_2^- - p_1^- p_2^+)}{m_{\ell\ell}\sqrt{m_{\ell\ell}^2 + p_{\mathrm{T},\ell\ell}^2}}\right|, \tag{7.3}$$

with

$$p_i^{\pm} = \frac{1}{\sqrt{2}(E_i \pm p_{z,i})}, \tag{7.4}$$

where E is the energy and p_z the longitudinal momentum of the lepton ($i = 1$) and anti-lepton ($i = 2$). The variables $p_{z,\ell\ell}$, $m_{\ell\ell}$ and $p_{\mathrm{T},\ell\ell}$ denote the longitudinal momentum, invariant mass and transverse momentum of the dilepton system, respectively. When the transverse boost of the lepton pair is small compared to its longitudinal boost, θ^*_{CS} provides a good approximation of θ.

The sign of $\cos\theta^*_{\mathrm{CS}}$ is defined with respect to the direction of the quark, which is, however, ambiguous in pp collisions. It is therefore chosen by measuring the longitudinal boost of the final-state dilepton system in the laboratory frame [135], and assuming that this is dominated by the direction of quark in the initial state, since a quark in a proton typically carries a larger momentum fraction x than does an antiquark. This assumption leads to a fraction of events with wrongly assigned quark direction, which causes a reduction ("dilution") of the observed asymmetry. The probability of correct quark direction assignment increases with the boost of the dilepton system, thus reducing the dilution for dileptons produced at large rapidities. With this assumption, and requiring the hadron A to provide the quark in the collision, it follows that

$$\cos\theta^*_{\mathrm{CS}} = \frac{p_{z,\ell\ell}}{|p_{z,\ell\ell}|} \frac{2(p_1^+ p_2^- - p_1^- p_2^+)}{m_{\ell\ell}\sqrt{m_{\ell\ell}^2 + p_{\mathrm{T},\ell\ell}^2}}, \tag{7.5}$$

The first factor in Eq. 7.5 defines the sign of $\cos\theta^*_{\mathrm{CS}}$ according to the longitudinal direction of flight of the dilepton system, as discussed above. The events with $\cos\theta^*_{\mathrm{CS}} \geq 0$ are classified as forward (F), while those having $\cos\theta^*_{\mathrm{CS}} < 0$ are classified as backward (B).

The reaction $\mathrm{pp} \to \ell^-\ell^+ + \ldots$ is dominated by virtual photons at low energy, by the Z^0 at $m(\ell^-\ell^+) = M_{\mathrm{Z}}$, and by photon-Z interference everywhere else. Here $\ell = (\mathrm{e}, \mu)$ stands for an isolated charged lepton, that is, one not due to charm or bottom semileptonic decay. For lepton pairs masses between about 60 and 80 GeV/c^2 [18], the similar magnitude of photon and Z contributions leads to an expected asymmetry of about -50%, with three out of four ℓ^+ having greater rapidity than ℓ^- in the direction of the incident quark. For pair masses above 100 GeV/c^2, one expects an asymmetry of about $+50\%$, with three out of four ℓ^- having greater rapidity than ℓ^+ in the direction of the quark. A new neutral gauge boson beyond the photon and the Z, such as the Z', will lead to deviations of the forward-backward asymmetry from that predicted in the SM. Each Z' setting of couplings to up quarks, down quarks and charged leptons induces a particular forward-backward asymmetry, as illustrated in Fig. 7.2.

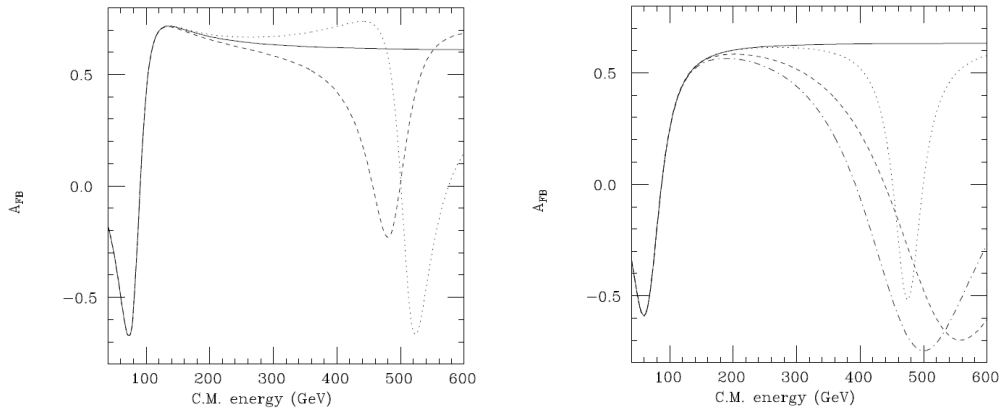

Fig. 7.2.: Parton-level forward-backward asymmetries for $u\bar{u} \to \mu^-\mu^+$ (left) and $d\bar{d} \to \mu^-\mu^+$, as a function of the center-of-mass energy. Solid line: SM. Dashed line: 500 GeV/c^2 Z'_χ added. Dotted line: 500 GeV/c^2 Z'_ψ added. Dot-dashed line: 500 GeV/c^2 Z'_I added; a Z'_I does not couple to u quarks and does not change the SM prediction [18].

7.3 Simulated samples and event selection

The samples studied in this section were privately produced with Pythia 8 generator [136] for proton-proton collisions at $\sqrt{s} = 13$ and 14 TeV, for scenarios corresponding to Run 2, Run 3 and Phase II of the LHC. Pythia is a general purpose program that, in addition to the hard process, also takes care of the parton showering, the hadronisation, and the description of the underlying event. For the matrix element calculation, Pythia only considers the leading order. The radiative corrections are not explicitly calculated but rather treated in the parton showering.

Run 2 geometry corresponds to the one currently in use by the CMS experiment, and has been already discussed in Ch. 4. As previously explained in Sec. 4.7.5, a series of major upgrades are planned through LS2. Among these the following ones are included in the simulated Run 3 geometry: the replacement of the pixel detector with a four-layer high-data-rate design, and an upgrade to the photo-detectors and electronics for the hadron calorimeters (HCAL) to reduce background signals and improve measurement of jets and missing-energy at high PU. To this list must be added the installation of Triple-GEM chambers in the GE1/1 stations, on which Ch. 5 was focused.

Concerning Phase II, the specific changes that the CMS collaboration proposes to carry out concern the muon system with the addition of GE2/1 and ME0 chambers. The two last CSC stations in the region $1.5 \leq |\eta| \leq 2.4$ will use low-resistivity RPC to mitigate background effects. The electromagnetic and hadronic endcap calorimeters will be replaced by an upgraded detector called High Granularity Calorimeter. The pixel and tracker system will be completely replaced, allowing to maintain and even improving the current level of tracking performance in the high occupancy

Process	σ at 13 TeV (fb)	σ at 14 TeV (fb)
Drell-Yan ($2.5 - 3.5$ TeV/c^2)	0.037 ± 0.001	0.051 ± 0.001
Drell-Yan ($3.5 - 4.5$ TeV/c^2)	0.0032 ± 0.0001	0.0049 ± 0.0001
Z'_{ψ} (3 TeV/c^2)	0.394 ± 0.009	0.539 ± 0.012
Z'_{ψ} (4 TeV/c^2)	0.051 ± 0.001	0.075 ± 0.002
Z'_{I} (3 TeV/c^2)	0.633 ± 0.013	0.912 ± 0.020
Z'_{I} (4 TeV/c^2)	0.078 ± 0.001	0.112 ± 0.002
Z'_{SSM} (3 TeV/c^2)	1.585 ± 0.032	2.095 ± 0.043
Z'_{SSM} (4 TeV/c^2)	0.240 ± 0.004	0.336 ± 0.006

Tab. 7.1.: List of simulated processes, such as the Drell-Yan, or Z$'$ particle decays, with their associated generated mass and their cross-section as they are provided by Pythia8.

environment of the upgraded LHC, with a reduced mass, a reduced innermost radius and increased lever arm. All of these upgrades are included in the geometry description used by the CMS software for the Phase II simulations.

The Drell-Yan process has also been considered in this study, as it represents the dominant and irreducible background in the high mass dilepton spectrum. It is the only considered SM process. The signal samples taken into exam are the Z'_{SSM}, the Z'_{ψ}, and the Z'_{I}. The chosen masses (3 and 4 TeV/c^2) and the couplings correspond to signals not already excluded and whose yields are large enough to provide sufficient statistics for the study performed here. In Tab. 7.1 is reported the list of simulated processes or particles (Drell-Yan to $\mu\mu$ and the models of Z$'$ decaying to $\mu\mu$) as well as their cross-sections such as they are provided by Pythia. In Tab. 7.2 are reported the names of the samples previously reported in Tab. 7.1.

The event selection is listed below and is directly taken from CMS internal note AN2015-223-v7. The same selection is applied to every considered scenario.

- The muon must be reconstructed as a “global” muon and a “tracker” muon.
- The offline muon p_{T} must be at least 53 GeV/c, so as to be in the plateau of the single-muon trigger efficiency.
- The relative p_{T} error $\delta p_{\mathrm{T}}/p_{\mathrm{T}}$ is required to be smaller than 0.3, to suppress grossly misreconstructed muons.
- The muon’s transverse impact parameter with respect to the primary vertex, as measured by the tracker-only fit, must be less than 0.2 cm.

Process	Dataset path
Z'_{SSM}	/ZpSSMtoMM_M3000_TuneCUETP8M1_13TeV/ryonamin-crab_Run2015-MCRUN2_71_V1-v4-c2aafb2acc3a48154facac2490c0d092/USER
	/ZpSSMtoMM_M3000_TuneCUETP8M1_14TeV/ryonamin-crab_GEM2019-DES19_62_V8-v3-35986fdb33276b6805c2e39b5e1ce4b5/USER
	/ZpSSMtoMM_M3000_TuneCUETP8M1_14TeV/ryonamin-crab_GEM2023-DES23_62_V1_v5-36eb384aacfb25612093d9d592bc52bc/USER
	/ZpSSMtoMM_M4000_TuneCUETP8M1_13TeV/ryonamin-crab_Run2015-MCRUN2_71_V1-v1-23e0dbda3d39d80da6f5a98c03f823ae/USER
	/ZpSSMtoMM_M4000_TuneCUETP8M1_14TeV/ryonamin-crab_GEM2019-DES19_62_V8-v2-f1d82f3c7ff5614b8264e176d39e91c0/USER
	/ZpSSMtoMM_M4000_TuneCUETP8M1_14TeV/ryonamin-crab_GEM2023-DES23_62_V1_v2_1-af2152723a3c9a511b9e4817147a3223/USER
Z'_{ψ}	/ZpPSItoMM_M3000_TuneCUETP8M1_13TeV/ryonamin-crab_Run2015-MCRUN2_71_V1-v1-7f41caa1dc361b85befd3b9727f6f7d7/USER
	/ZpPSItoMM_M3000_TuneCUETP8M1_14TeV/ryonamin-crab_GEM2019-DES19_62_V8-v3-b43c1e1e6c1fd1ffa400dd15764b4d71/USER
	/ZpPSItoMM_M3000_TuneCUETP8M1_14TeV/ryonamin-crab_GEM2023-DES23_62_V1_v1-1514e76b583b3bf16bd358aa33e27626/USER
	/ZpPSItoMM_M4000_TuneCUETP8M1_13TeV/ryonamin-crab_Run2015-MCRUN2_71_V1-v1-a34f27a5e3ed46352810304695abe54d/USER
	/ZpPSItoMM_M4000_TuneCUETP8M1_14TeV/ryonamin-crab_GEM2019-DES19_62_V8-v3_1-9ac8e40f552b02cba0c3e49edeab8848/USER
	/ZpPSItoMM_M4000_TuneCUETP8M1_14TeV/ryonamin-crab_GEM2023-DES23_62_V1_v2_1-f72d4d87e053e806d9a8a16881e9548e/USER
Z'_{I}	/ZpItoMM_M3000_TuneCUETP8M1_13TeV/ryonamin-crab_Run2015-MCRUN2_71_V1-v2-8a19a93392bc2df2c33321a3404b2ccd/USER
	/ZpItoMM_M3000_TuneCUETP8M1_14TeV/ryonamin-crab_GEM2019-DES19_62_V8-v4-1946322fba6925fe4b343d44f19e820a/USER
	/ZpItoMM_M3000_TuneCUETP8M1_14TeV/ryonamin-crab_GEM2023-DES23_62_V1-v1-011a63b380f90efb822d572c1077fa09/USER
	/ZpItoMM_M4000_TuneCUETP8M1_13TeV/ryonamin-crab_Run2015-MCRUN2_71_V1-v3-284a37602359593d30694df304716fcb/USER
	/ZpItoMM_M4000_TuneCUETP8M1_14TeV/ryonamin-crab_GEM2019-DES19_62_V8-v1-4585b608d5d529e8a32be8bfaca2f664/USER
	/ZpItoMM_M4000_TuneCUETP8M1_14TeV/ryonamin-crab_GEM2023-DES23_62_V1-v2_1-0fc5e105333a7fe409d5c7b088c5fdea/USER
Drell-Yan	/DYtoMM_M2500to3500_TuneCUETP8M1_13TeV/ryonamin-crab_Run2015-MCRUN2_71_V1-v1-df2218dd5ab9511977e6a6eb3cad81c9/USER
	/DYtoMM_M2500to3500_TuneCUETP8M1_14TeV/ryonamin-crab_GEM2019-DES19_62_V8-v3-3a86f60b4e274d27f9378ce6ea9200a4/USER
	/DYtoMM_M2500to3500_TuneCUETP8M1_14TeV/ryonamin-crab_GEM2023-DES23_62_V1_v2_1-c4560d8e2599110f7348d3f3319dd816/USER
	/DYtoMM_M2500to3500_TuneCUETP8M1_14TeV_PU140BX25/ryonamin-crab_GEM2023-DES23_62_V1_v2_1-512a96f6071df80e153222c4ae4a5bb6/USER
	/DYtoMM_M3500to4500_TuneCUETP8M1_14TeV/ryonamin-crab_GEM2023-DES23_62_V1-v1-ddd0e043c26ffcf51e41102b59e399cb/USER

Tab. 7.2.: A partial list of the samples analysed in this study.

	Run 2			Run 3			Phase II		
	gen	reco	r + 10%M	gen	reco	r + 10%M	gen	reco	r + 10%M
Z'_{ψ}	39.4	33.6	26.0	161.7	138.0	109.7	1617.0	1381.3	1115.8
Z'_{I}	63.3	53.8	39.4	273.6	233.3	176.6	2736	2331.2	1792.3
Z'_{SSM}	185.5	131.1	81.1	628.5	523.0	341.4	6285.0	5221.6	3464.2

Tab. 7.3.: Expected events for each considered Z′ model at a mass of 3 TeV/c^2, at generated level (gen), reconstructed level (reco), and reconstructed + a 10% windows (r + 10%M) selection around the generated mass of 3 TeV/c^2. Three integrated luminosity scenarios are considered. The error on the numbers falls on the last digit.

- The muon must pass a relative tracker-only isolation cut: the scalar sum of the p_{T} of all other tracks in a cone of $\Delta R = \sqrt{(\Delta\eta)^2 + (\Delta\phi)^2} < 0.3$ around but not including the muon's track must be less than 10% of the muon's p_{T}, also as measured by the tracker. To be used in the calculation of the tracker isolation, tracks have to be within $\Delta z = 0.2$ cm of the primary vertex with which the muon candidate is associated.

- The global muon track must have at least 6 tracker layers with hits in the fit.

- The global muon track fit must include at least one hit from each of the pixel detector and the muon system.

- The tracker muon must be matched to segments in at least two muon stations.

To form a dimuon, two muons of opposite charge that pass the above selection are taken. For the Z′ samples one last cut is applied to the dimuon mass, corresponding to the selection of a 10% window of the generated mass. Knowing the cross-section of each process and the expected integrated luminosity at the end of the chosen LHC runs, it is possible to predict the expected number of events at generated level. This yield is then reduced by the detector geometrical acceptance and the selection efficiency. The expected yields at generated (gen) level, reconstructed (reco) level and reco + 10% window of the generated mass (r + 10%M) are reported in Tab. 7.3 and Tab. 7.4 for masses of 3 and 4 TeV/c^2, respectively. Efficiencies on the selection cuts for Drell-Yan samples in Phase II scenario with $PU = 0$ and $PU = 140$ are reported in Tab. 7.5. The same is shown for Z'_{ψ} for the three luminosity scenarios in Tab. 7.6. Results presented in Sec. 7.5.5 show that pile-up has no impact on the reconstruction of the A_{FB}. Samples with pile-up were also considered: analysis of two Drell-Yan samples in the 2023 scenario, one with no pile-up and one with PU140BX25 ($\mathrm{PU} = 140$ with a bunch-crossing every 25 ns), was performed.

	Run 2			Run 3			Phase II		
	gen	reco	r + 10%M	gen	reco	r + 10%M	gen	reco	r + 10%M
Z'_{ψ}	5.1	4.3	3.1	22.5	19.0	14.2	225.0	190.0	144.7
Z'_{I}	7.8	6.4	4.0	33.6	28.0	19.0	336.0	279.3	190.9
Z'_{SSM}	24.0	19.0	9.08	100.8	81.0	43.4	1008.0	808.3	440.9

Tab. 7.4.: Expected events for each considered Z′ model at a mass of 4 TeV/c^2, at generated level (gen), reconstructed level (reco), and reconstructed + a 10% windows (r + 10%M) selection around the generated mass of 3 TeV/c^2. Three integrated luminosity scenarios are considered. The error on the numbers falls on the last digit.

Requirements	PU= 0	PU= 140
$p_{\mathrm{T}} > 53$	$1\ (0.936 \pm 0.001)$	$1\ (0.960 \pm 0.001)$
isGlobal and isTracker	$0.99980 \pm 5 \cdot 10^{-5}$	0.9997 ± 0.0001
track hits > 5	0.9990 ± 0.0001	0.9989 ± 0.0002
pixel hits ≤ 1	1 ± 0	1 ± 0
muon station hits > 0	0.9976 ± 0.0002	0.9976 ± 0.0003
matched station > 1	0.9878 ± 0.0004	0.9878 ± 0.0006
$\lvert d_{\mathrm{xy}} \rvert < 0.2$	1 ± 0	1 ± 0
isolation	$0.99975 \pm 6 \cdot 10^{-5}$	0.9996 ± 0.0001
$\delta p_{\mathrm{T}}/p_{\mathrm{T}} < 0.3$	0.9957 ± 0.0002	0.9956 ± 0.0004
total	0.917 ± 0.001	0.940 ± 0.001

Tab. 7.5.: List of cuts applied, one by one, to muons for Z/Drell-Yan events for both PU scenarios at Phase II conditions. The DY events are generated within $2500 < M < 3500$ GeV/c^2. The first row is set at 100% by definition, and every efficiency is computed with respect to the previous one. The p_{T} cut efficiency, as well as the total efficiency, are specified too.

Requirements	100 fb^{-1} $\sqrt{s} = 13$ TeV	300 fb^{-1} $\sqrt{s} = 14$ TeV	3000 fb^{-1} $\sqrt{s} = 14$ TeV
$p_{\mathrm{T}} > 53$ GeV/c^2	$1\ (0.934 \pm 0.001)$	$1\ (0.935 \pm 0.001)$	$1\ (0.9341 \pm 0.0001)$
isGlobal and isTracker	$0.99994 \pm 3 \cdot 10^{-5}$	$0.99988 \pm 3 \cdot 10^{-5}$	$0.99977 \pm 1 \cdot 10^{-5}$
track hits > 5	$0.99992 \pm 3 \cdot 10^{-5}$	$0.99983 \pm 3 \cdot 10^{-5}$	$0.99885 \pm 3 \cdot 10^{-5}$
pixel hits ≤ 1	0.9988 ± 0.0001	0.9984 ± 0.0001	1 ± 0
muon station hits > 0	0.9968 ± 0.0002	0.9972 ± 0.0001	$0.9975 \pm 4 \cdot 10^{-5}$
matched station > 1	0.9872 ± 0.0004	0.9865 ± 0.0003	$0.98686 \pm 9 \cdot 10^{-5}$
$\lvert d_{xy} \rvert < 0.2$	1 ± 0	1 ± 0	$0.999999 \pm 6 \cdot 10^{-7}$
isolation	$0.99953 \pm 7 \cdot 10^{-5}$	$0.99967 \pm 4 \cdot 10^{-5}$	$0.99968 \pm 1 \cdot 10^{-5}$
$\delta p_{\mathrm{T}}/p_{\mathrm{T}} < 0.3$	0.9929 ± 0.0003	0.9921 ± 0.0002	$0.99514 \pm 5 \cdot 10^{-5}$
total	0.911 ± 0.001	0.9104 ± 0.0007	0.9135 ± 0.0002

Tab. 7.6.: List of cuts applied, one by one, to muons for Z'_{ψ} events for three luminosity scenarios. The generated mass is equal to 3 TeV/c^2. The first row is set at 100% by definition, and every efficiency is computed with respect to the previous one. The p_{T} cut efficiency, as well as the total efficiency, are specified too. Other Z′ models provide very similar efficiencies.

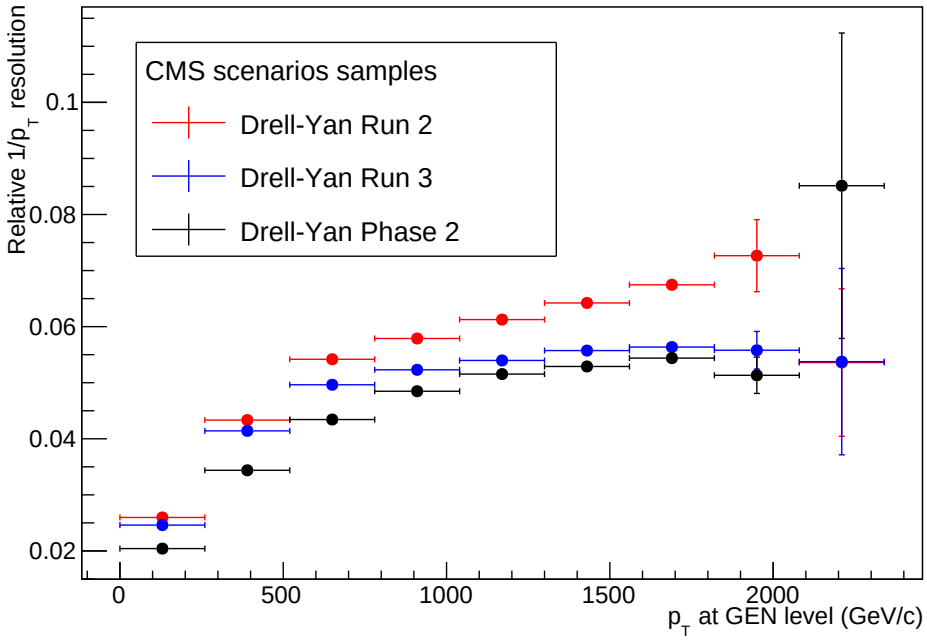

Fig. 7.3.: $1/p_{\mathrm{T}}$ relative resolution as a function of the generated muon p_{T} in the barrel region, for the Drell-Yan generated samples.

7.4 Control plots

The muon $1/p_{\mathrm{T}}$ resolution is studied from the relative residual distribution:

$$\sigma\left(1/p_{\mathrm{T}}\right) = \left(1/p_{\mathrm{T}}^{\mathrm{rec}} - 1/p_{\mathrm{T}}^{\mathrm{gen}}\right)/1/p_{\mathrm{T}}^{\mathrm{gen}}, \tag{7.6}$$

where gen means the true MC value and rec is the reconstructed value of the muon associated to the generated one by a geometrical matching. In the case of the Drell-Yan sample, Fig. 7.3 and 7.4 show the peak width and its RMS as a function of the generated muon $p_{\mathrm{T}}^{\mathrm{gen}}$, respectively for the barrel and the endcap regions. In the latter case the stabilization or even the improvement of the resolution for high values of p_{T} is due to kinematic effects: given a mass, a higher p_{T} implies a lower value of $|\eta|$; this allows a better p_{T} reconstruction due to a longer reconstructed track in the endcap in the x-y plane. Fig. 7.5 and 7.6 show the same quantity for the $\mathrm{Z}'_{\mathrm{SSM}}$ sample. The peak width is obtained from a Gaussian fit to the core of the distribution. The same has been performed for $\mathrm{Z}'_{\mathrm{SSM}}$ events. The mass resolution benefits from the Run 3 and Phase II upgrades recalled above. The same can be said for the $1/p_{\mathrm{T}}$ resolution, where the endcaps benefit from the upgrade in the muon system. Bins with tighter p_{T} selection can provide confusing fit results due to the lack of statistics; for this reason, in some cases the point was not reported.

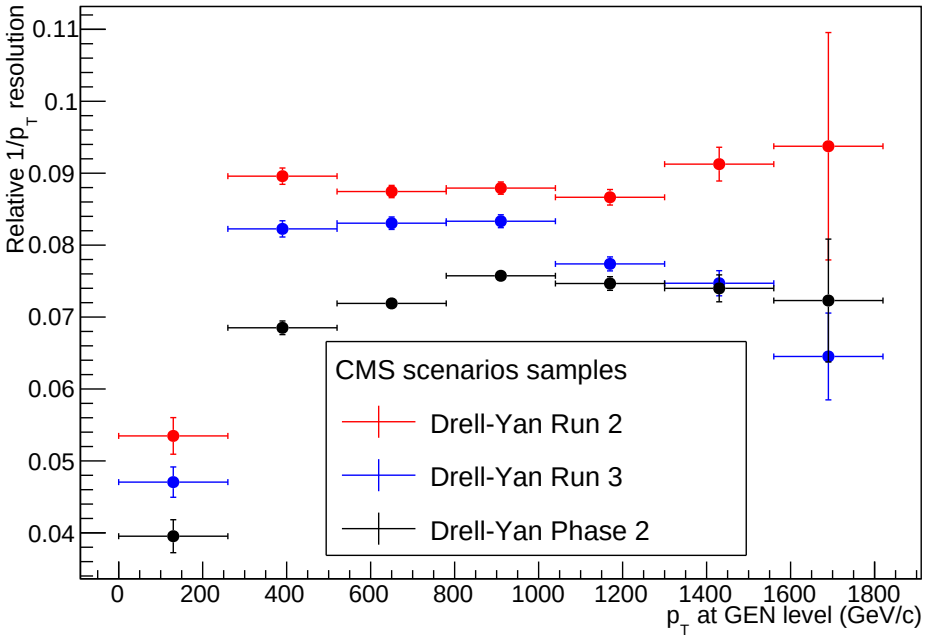

Fig. 7.4.: $1/p_{\mathrm{T}}$ relative resolution as a function of the generated muon p_{T} in the endcap region, for the Drell-Yan generated samples.

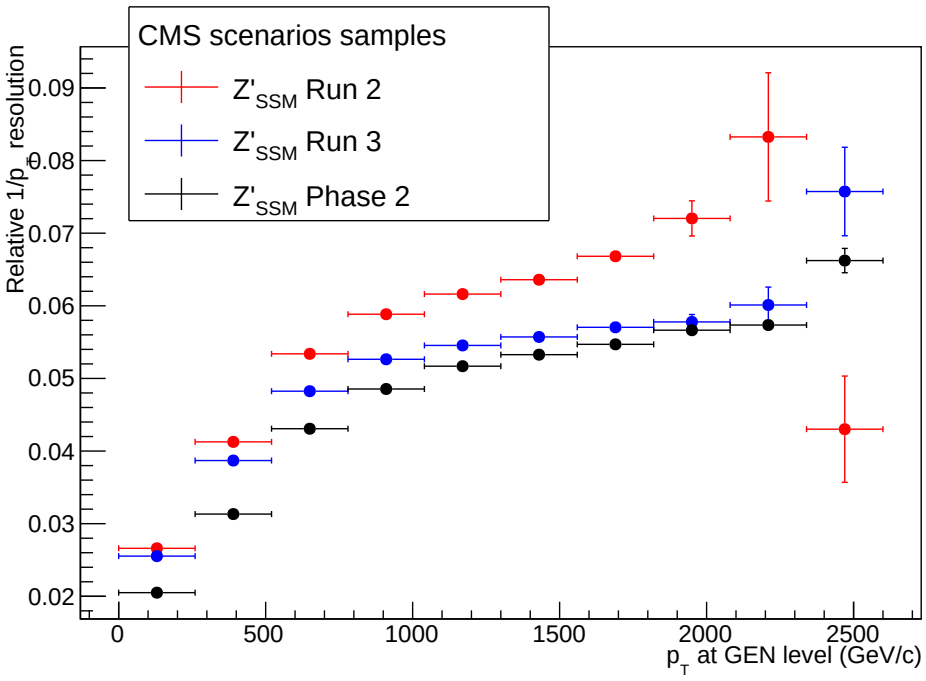

Fig. 7.5.: $1/p_{\mathrm{T}}$ relative resolution as a function of the generated muon p_{T} in the barrel region, for the $\mathrm{Z}'_{\mathrm{SSM}}$ generated samples.

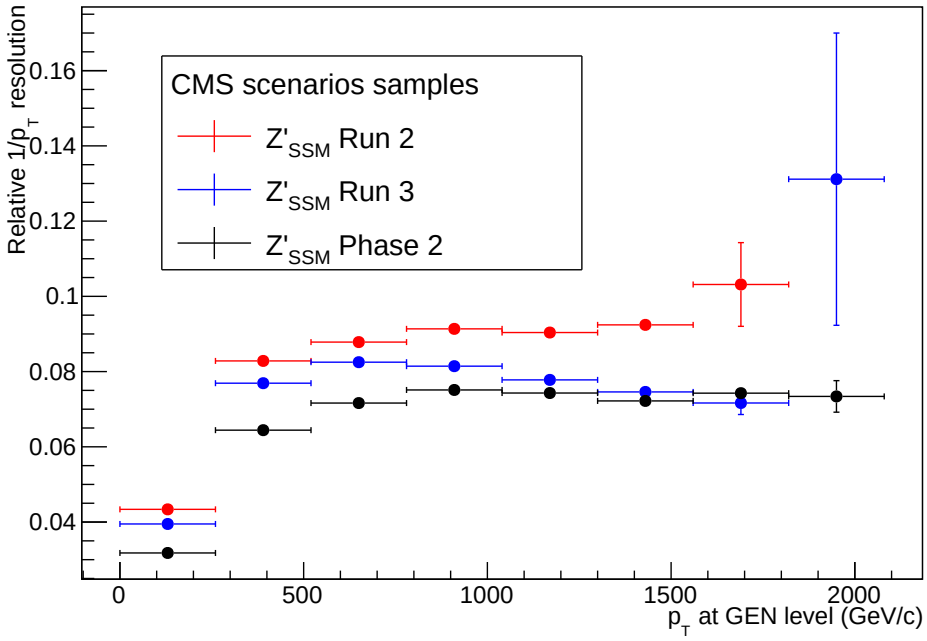

Fig. 7.6.: $1/p_{\mathrm{T}}$ relative resolution as a function of the generated muon p_{T} in the endcap region, for the $\mathrm{Z}'_{\mathrm{SSM}}$ generated samples. The stabilization or even the improvement of the resolution for high values of p_{T} is due to kinematic effects: given a mass, a higher p_{T} implies a lower value of $|\eta|$; this allows a better p_{T} reconstruction due to a due to a longer reconstructed track in the endcap in the x-y plane.

Fig. 7.7 shows the mass resolution as a function of the mass at the generated level for the Drell-Yan samples in the chosen scenarios. The reconstructed invariant mass of each dimuon is computed using the reconstructed muons geometrically matched with the ones from the Drell-Yan decay, and is compared to its true mass. The resolution is extracted by fitting the core of the distributions with a Gaussian. The generated masses were gathered in discrete bins. The same procedure has been followed for the $\mathrm{Z}'_{\mathrm{SSM}}$ samples, and is reported in Fig. 7.8. The improvements already shown for $1/p_{\mathrm{T}}$ resolutions are reflected in the mass resolution as:

$$\frac{\sigma(M)}{M} \sim \frac{\sigma(1/p_{\mathrm{T}})}{1/p_{\mathrm{T}}}. \tag{7.7}$$

As shown in Fig. A.5 the charge misidentification for muons is well below 1%. In the case of high energy muons, the charge misidentification is mainly caused by bremsstrahlung in matter, that leads to deflections and kinks in the track on the muon. This results in a wrong measurement of the sign of the curvature of the track. Appendix A includes other control plots, such as the spectra of the generated and reconstructed mass (Fig. A.1 and Fig. A.2, respectively), the rapidity distribution of the muon pair (Fig. A.3), and the p_{T} distribution of the Z' (Fig. A.4).

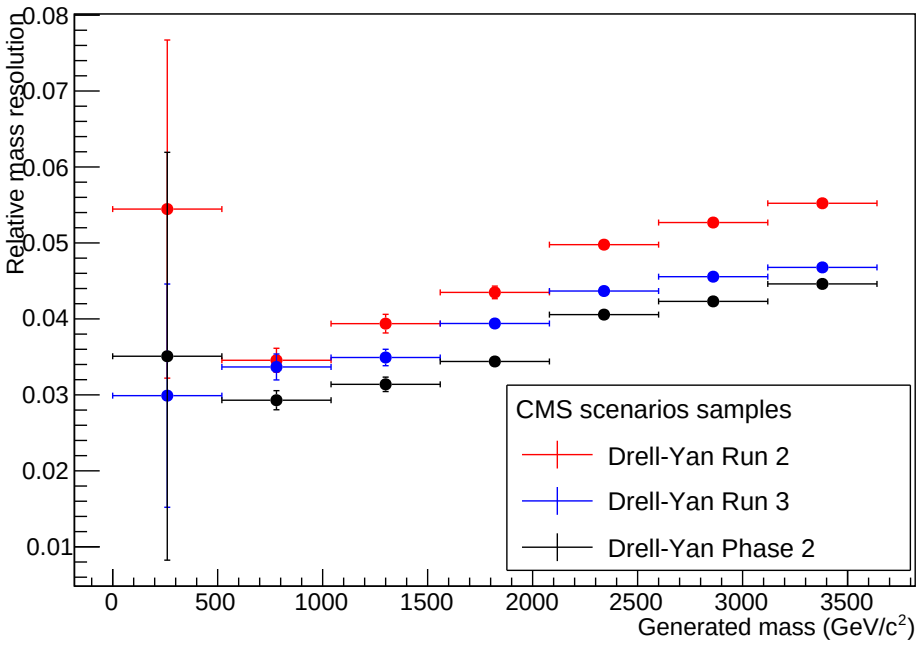

Fig. 7.7.: Mass resolution of Drell-Yan simulated signals (generated between 2.5 and 3.5 TeV/c^2 for scenarios representing the the amount of data taken at the end of Run 2, Run 3 and Phase II, as a function of the generated mass.

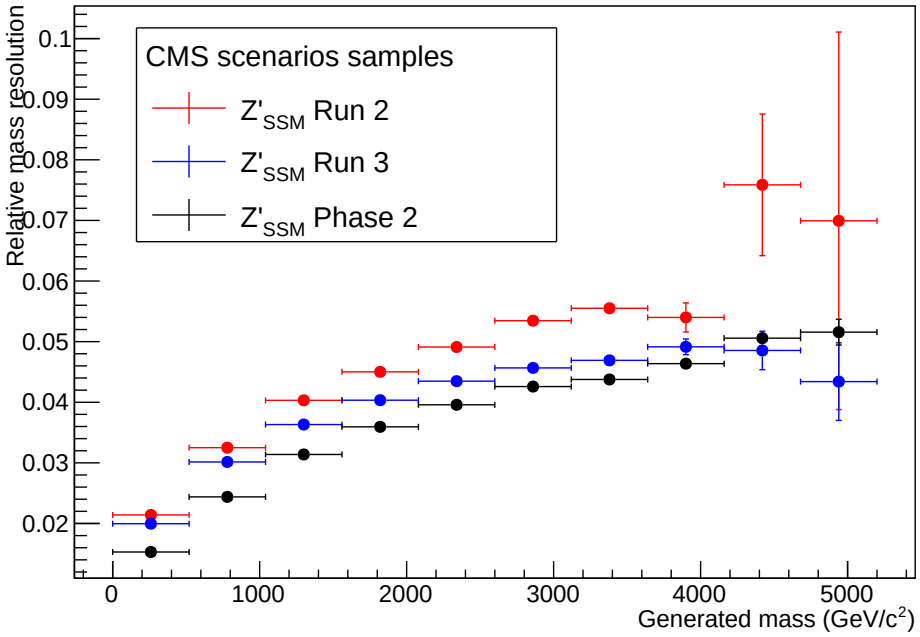

Fig. 7.8.: Mass resolution of Z'_{SSM} simulated signals with a generated mass of 3 TeV/c^2 for scenarios representing the amount of data taken at the end of Run2, Run3 and Phase II, as a function of the generated mass. The increasing error bars with increasing generated energies testifies the decrease in the population of the selected samples.

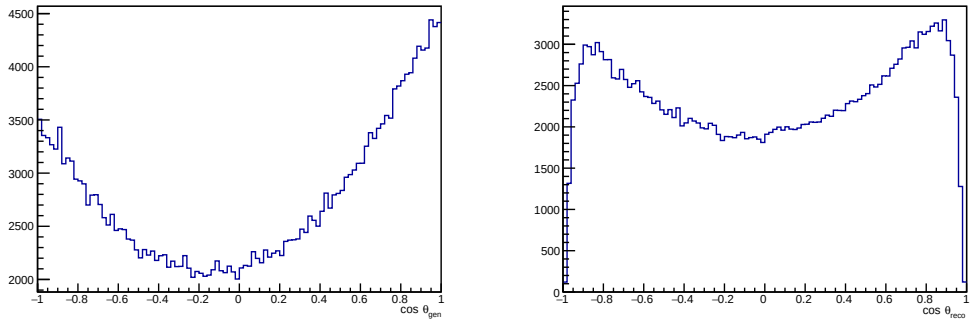

Fig. 7.9.: Left: distribution of the cosine of the Collins-Soper angle at the generated level for a simulated sample of a 3 TeV/c^2 Z'_{SSM} in the di-muon channel in a Run 2 scenario without pile-up. Right: distribution of the cosine of the Collins-Soper angle for the same sample at reconstructed level, requesting for each muon to pass the selection and to have opposite sign.

7.5 Results

7.5.1 Introduction

In case a new resonance is found, an interesting property to investigate is the forward-backward asymmetry (A_{FB}). As explained in Sec. 7.2, this quantity is extremely model-dependent and provides valuable information to understand the newly discovered particle. The A_{FB} measurement requires the correct identification of the quark and the negative lepton. At the reconstructed level the quark direction measurement is subject to errors: the wrong direction is selected when the antiquark carries a higher momentum fraction than the quark. As it will be further explained the use of the dimuon rapidity information reduces this uncertainty and is therefore expected to improve the precision on the result.

The study presented here is limited to the measurement of the expected A_{FB} and its uncertainty for several spin 1 resonances. No investigation about the spin measurement was performed. The A_{FB} measurement is achieved through a binned likelihood fit and through a strategy already presented in literature [134].
The distribution from which the A_{FB} is estimated is the cosine of the Collins-Soper angle, already defined in Eq. 7.5. In this Chapter, it is defined as θ^* for the sake of brevity. As an example, the generated and reconstructed distributions shown in Fig. 7.9 were obtained from a simulated sample of a 3 TeV/c^2 Z'_{SSM} at Run 2 conditions with no pile-up.
The theoretical asymmetry of the Z'_{SSM} is computed at generated level through a simple counting technique, by considering the number of values for which $\cos\theta^* > 0$ as forward events, and $\cos\theta^* < 0$ as backward events. The obtained result is ~ 0.096. The drop of events at high $\cos\theta^*_{\mathrm{reco}}$ is due to a detector effect: the negative muons in

events with $\cos\theta^*$ close to 1 are very forward and sometimes emitted at $|\eta|$ outside the tracker and muon system acceptance. The same counting technique applied to the reconstructed distribution provides a value around 0.04. It is closer to the perfect symmetry than the generated one because of the misreconstruction of the incident quark direction that translates into a dilution of the distribution itself. This is the main reason why a proper fit that takes into account the dilution and the detector effects is necessary to correctly estimate A_{FB}. It must be emphasised that the dilution depends on the Parton Distribution Functions (PDFs); hence in future work the effects of uncertainties in PDFs must be evaluated. To optimize the fit is must be noticed that the most important features of the distribution that help discriminating between one model of the other lie in the extreme values of $\cos\theta^*$. Indeed, a distribution based exclusively on the signals provided by the barrel detectors tends to be flat.
Considering the Phase II scenario, the $\cos\theta^*$ spectrum of the various Z' models and Drell-Yan samples are shown from Fig. 7.10 to Fig. 7.17 at the generated level in shades of blue – with a $|\eta| < 2.4$ acceptance cut – and at the reconstructed level in shades of green – after the full selection. The η regions in which the generated or reconstructed muons are detected are separately represented in the plots. The sum of these different contributions provide the total spectrum, shown by the black line. In addition, the events in which one muon lies in the barrel and the other in the η range corresponding to the GE1/1 station has been superimposed in red to the spectrum. This allows to underline the importance to have high-η detectors to optimize the description of the $\cos\theta^*$ spectrum. It is then evident that a fit based solely on the barrel-barrel information would hardly operate a discrimination between different models, or the background.

7.5.2 Procedure

To establish the fit parametrisation, one starts from the fact that the differential cross-section shown in Eq. 2.67 must be defined positive. If follows that for a spin 1 resonance, A_{FB} must be included in the range $[-0.75, 0.75]$. Let us define $p_{\mathrm{A_{FB}}=\pm 0.75}$ as the corresponding distributions for the experimental variable $\cos\theta^*_{\mathrm{reco}}$. It is possible to demonstrate that any spin 1 distribution is a linear combination of the two extreme cases:

$$p_\kappa = \kappa \times p_{\mathrm{A_{FB}}=+0.75} + (1-\kappa) \times p_{\mathrm{A_{FB}}=-0.75}, \tag{7.8}$$

where κ is a factor related to the forward-backward asymmetry:

$$A_{\mathrm{FB}} = \frac{3}{4}(2\kappa - 1). \tag{7.9}$$

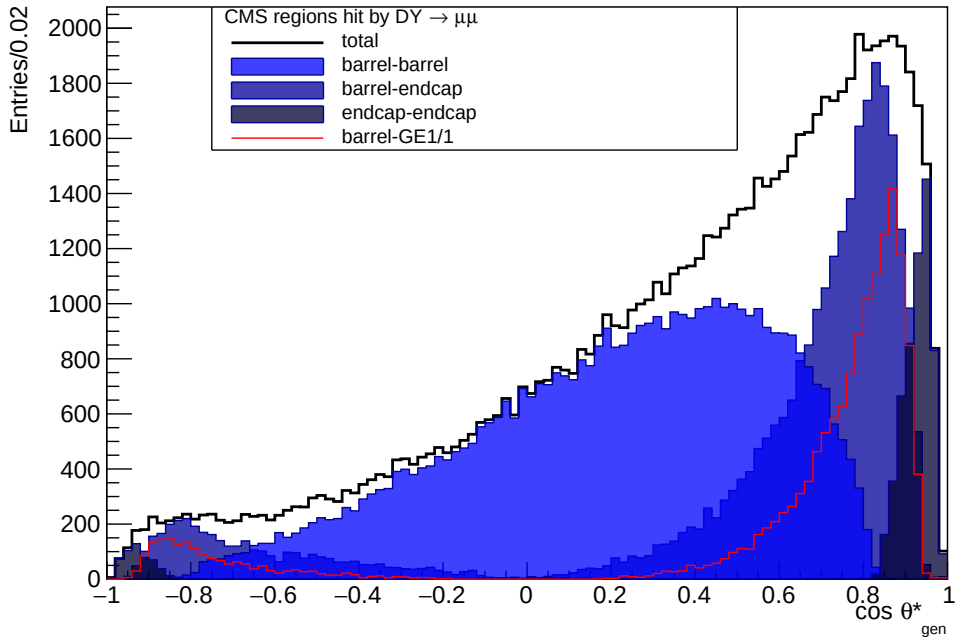

Fig. 7.10.: Distributions of $\cos\theta^*_{\mathrm{gen}}$ for a simulated sample of a Standard Model Drell-Yan process decaying in two muons, in a Phase II scenario at $\sqrt{s} = 14$ TeV, with a selected mass between 2500 and 3500 GeV/c^2. The light blue distribution shows the distribution obtained if two muons are reconstructed in the barrel; medium blue if one muon is reconstructed in the barrel and one in an endcap; dark blue if both muons are reconstructed in the endcaps. If summed, these three distributions provide the total distribution in black. The red superimposed distribution is built considering one muon in the barrel and one in the GE1/1 $|\eta|$ range.

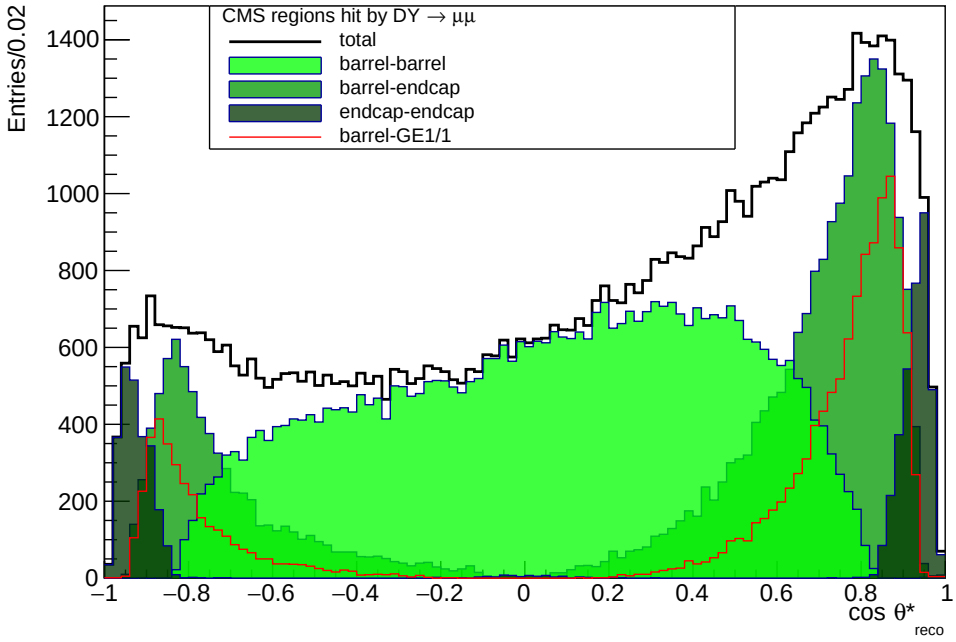

Fig. 7.11.: Distributions of $\cos\theta^*_{\mathrm{reco}}$ for a simulated sample of a Standard Model Drell-Yan process decaying in two muons, in a Phase II scenario at $\sqrt{s} = 14$ TeV, with a selected mass between 2500 and 3500 GeV/c^2. The same color code has in Fig. 7.10 holds, but with shades of green.

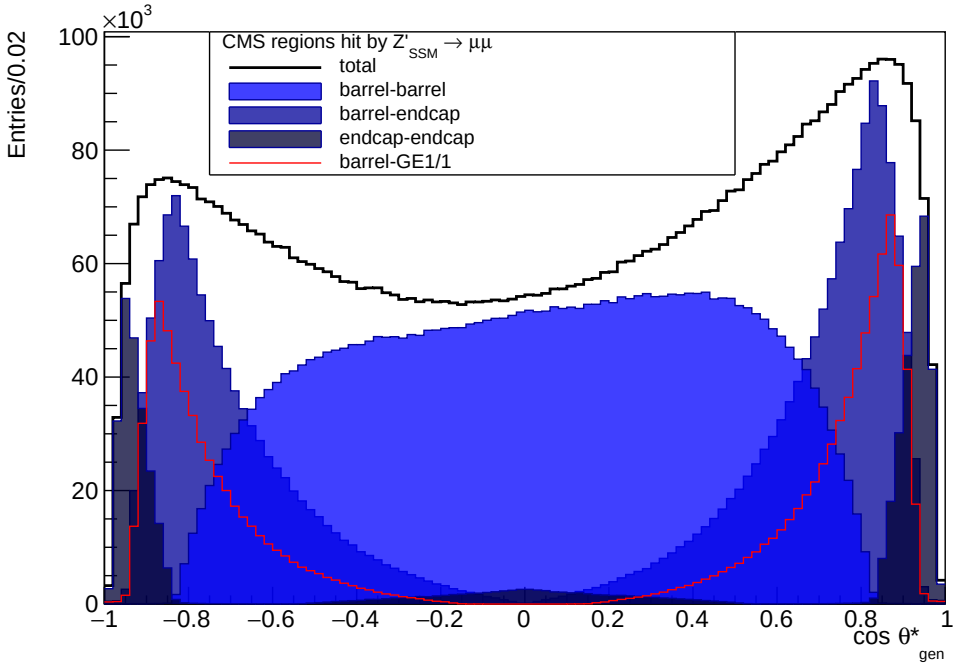

Fig. 7.12.: Distributions of $\cos\theta^*_{\mathrm{gen}}$ for a simulated sample of a 3 TeV/c^2 $\mathrm{Z'_{SSM}}$ decaying in two muons, in a Phase II scenario at $\sqrt{s} = 14$ TeV. The same color code has in Fig. 7.10 holds.

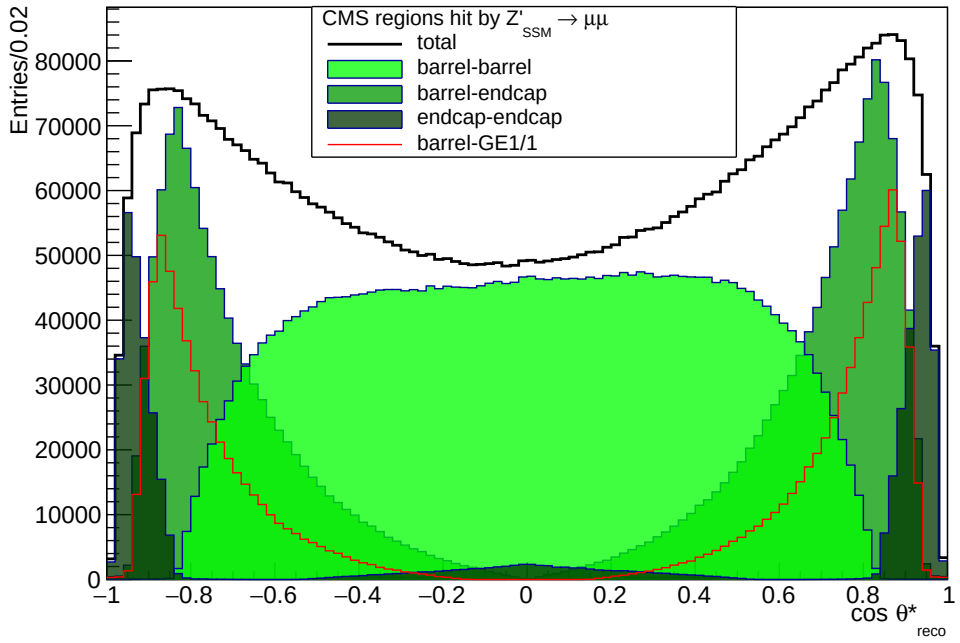

Fig. 7.13.: Distributions of $\cos\theta^*_{\mathrm{reco}}$ for a simulated sample of a 3 TeV/c^2 $\mathrm{Z'_{SSM}}$ decaying in two muons, in a Phase II scenario at $\sqrt{s} = 14$ TeV. The same color code has in Fig. 7.10 holds, but with shades of green.

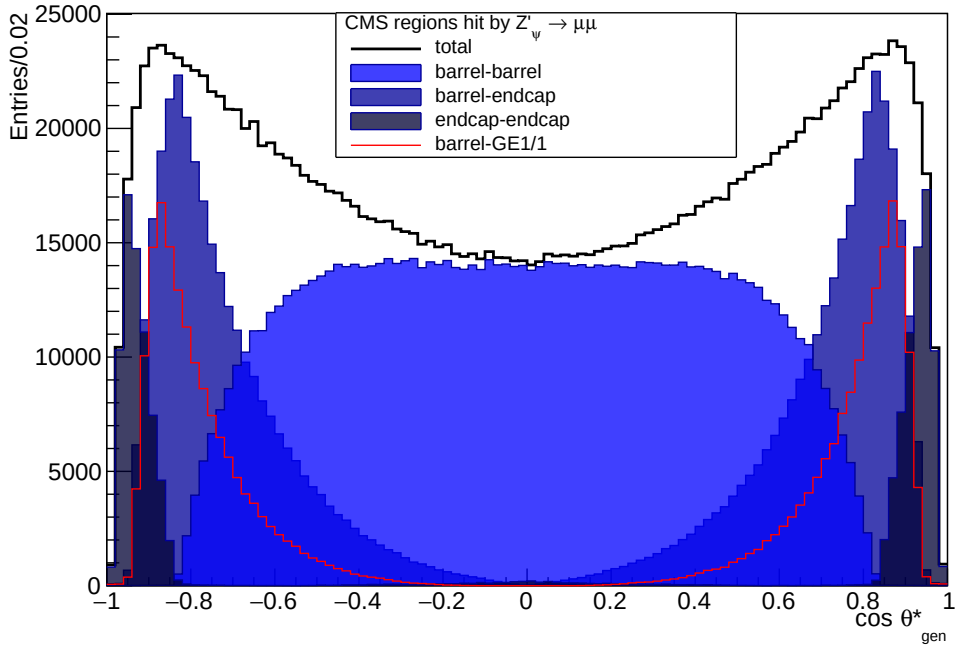

Fig. 7.14.: Distributions of $\cos\theta^*_{\mathrm{gen}}$ for a simulated sample of a 3 TeV/c^2 $\mathrm{Z'_{\psi}}$ decaying in two muons, in a Phase II scenario at $\sqrt{s} = 14$ TeV. The same color code has in Fig. 7.10 holds.

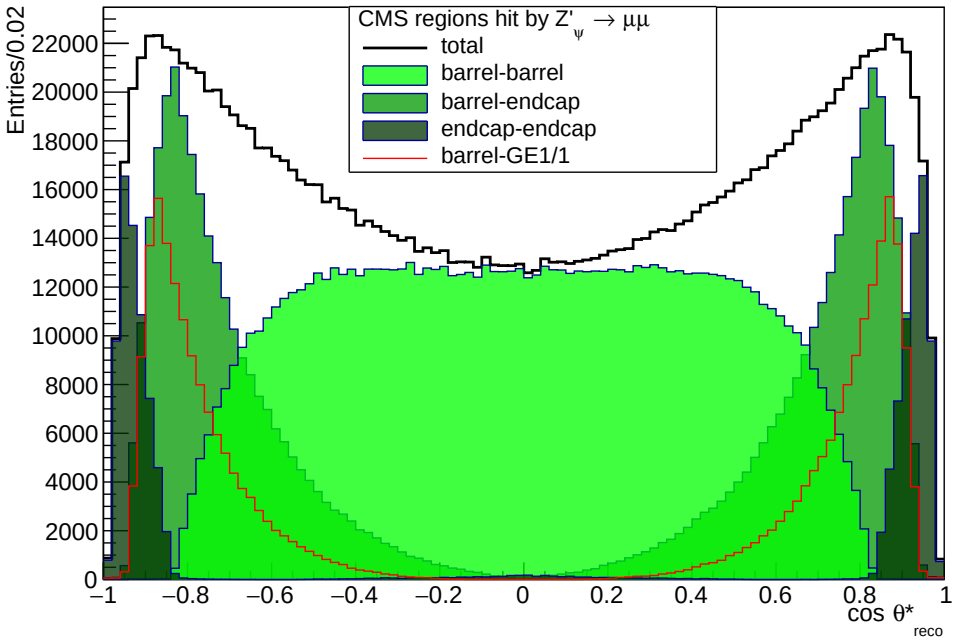

Fig. 7.15.: Distributions of $\cos\theta^*_{\mathrm{reco}}$ for a simulated sample of a 3 TeV/c^2 Z'_{ψ} decaying in two muons, in a Phase II scenario at $\sqrt{s} = 14$ TeV. The same color code has in Fig. 7.10 holds, but with shades of green.

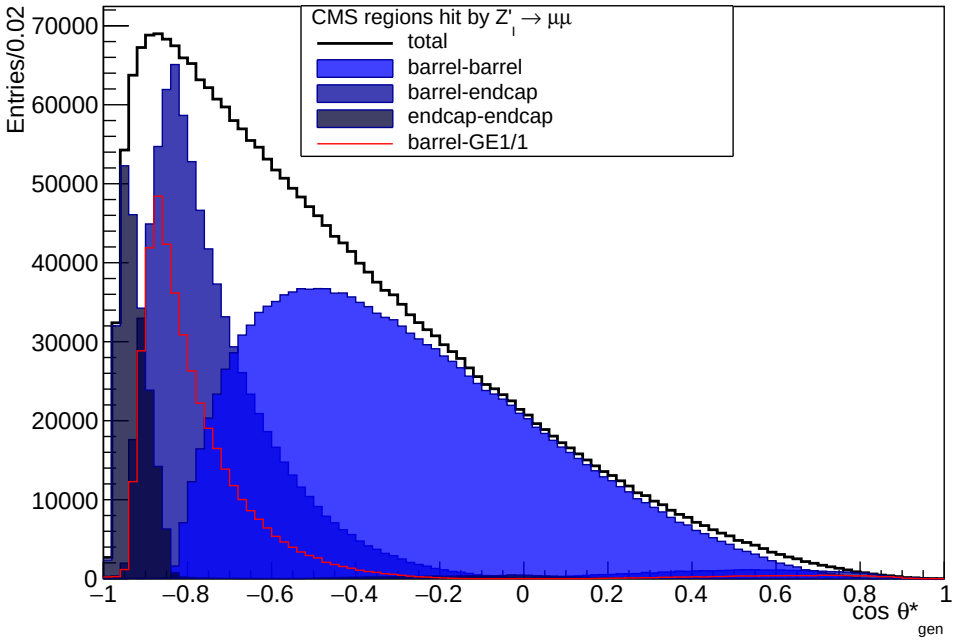

Fig. 7.16.: Distributions of $\cos\theta^*_{\mathrm{gen}}$ for a simulated sample of a 3 TeV/c^2 $\mathrm{Z}'_{\mathrm{SSM}}$ decaying in two muons, in a Phase II scenario at $\sqrt{s} = 14$ TeV. The same color code has in Fig. 7.10 holds.

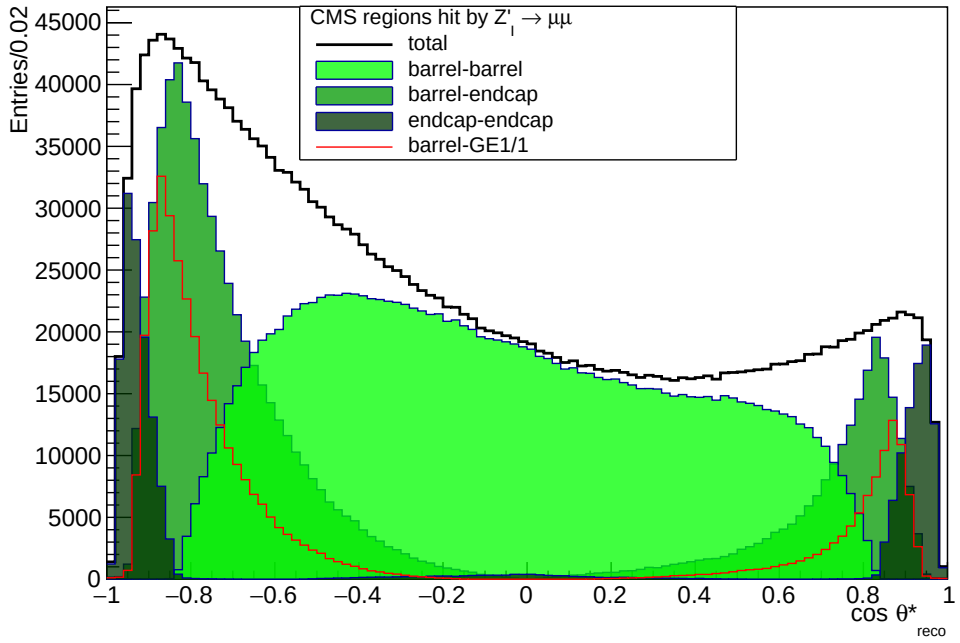

Fig. 7.17.: Distributions of $\cos\theta^*_{\text{reco}}$ for a simulated sample of a 3 TeV/c^2 Z'_I decaying in two muons, in a Phase II scenario at $\sqrt{s} = 14$ TeV. The same color code has in Fig. 7.10 holds, but with shades of green.

Then, starting from a particular sample one can randomly generate pseudo-experiments with a limited population and estimate the best κ value for each one of them. The average number of events generated during each pseudo-experiment corresponds to the column labelled as 'r + 10%M' in Tab. 7.3 and 7.4 and depends on the model and the integrated luminosity. This quantity represents the mean of a Poisson distribution on which the actual population of each pseudo-experiments is distributed. After repeating this procedure for a large amount of times (in this case 1000 iterations are generated), a Gaussian distribution is obtained: the median and uncertainty bands corresponding to 68.27% of the obtained A_{FB} distribution can then be extracted.
Two distributions corresponding to the two extreme cases ($A_{\text{FB}} = \pm 0.75$) are therefore built by re-weighting a $\cos\theta^*$ distribution at disposal. Fig. 7.18 shows such re-weighted distributions of the two aforementioned simulated samples: Drell-Yan and Z'_{SSM} at Run 2. The visible fluctuations for values of the re-weighted $\cos\theta^*_{\text{gen}}$ close to -1 in the Drell-Yan case are due to the decreased population of the corresponding values in the original distribution (see Fig. 7.10).
At this stage, a first test concerning the validity of the method can be done by fitting the distributions at the generated level, first through the re-weighted distributions from the original distribution itself, then with the ones coming from an independent signal. In this way, the κ parameter can be estimated, and therefore A_{FB}. The fit is performed through a binned likelihood fit, and the results are shown in Tab. 7.7. Every "crossed" fit is done with respect to the Z'_ψ, who has the same coupling to the

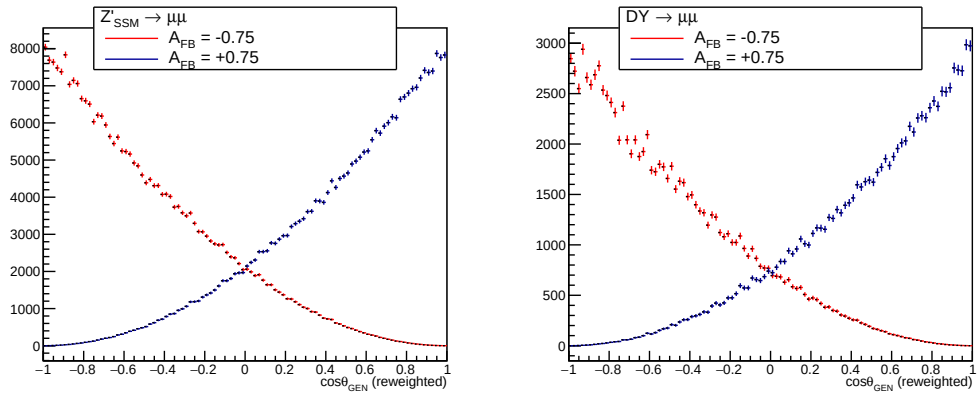

Fig. 7.18.: Left: re-weighted $\cos\theta_{\rm gen}$ distributions of the simulated 3 TeV/c^2 $\mathrm{Z'_{SSM}}$ sample at generated level, in order to obtain an $A_{\rm FB} = -0.75$ (red) and $+0.75$ (blue). The scenario corresponds to $\sqrt{s} = 13$ TeV at Run 2. Right: The same is performed with the Drell-Yan sample with the same CMS scenario.

$A_{\rm FB}$ GEN	Drell-Yan	$\mathrm{Z'_{\psi}}$	$\mathrm{Z'_{SSM}}$	$\mathrm{Z'_{I}}$
"Direct" fit	$0.611(2)$	$-0.004(3)$	$0.096(2)$	$-0.7499(3)$
"Crossed" fit	$0.612(2)$	$-0.004(3)$	$0.097(2)$	$-0.7499(3)$
Theoretical	$0.609(2)$	$-0.001(3)$	$0.096(2)$	$-0.743(2)$

Tab. 7.7.: Estimated values of $A_{\rm FB}$ at generated level through a "direct" fit (i.e. using pdf's obtained from the original distribution) and a "crossed" fit (i.e. using pdf's obtained from the $\mathrm{Z'_{\psi}}$ distribution. The theoretical value is obtained by counting forward and backward events.

u and d quarks, and has $A_{\rm FB} = 0$.

Once the weights are obtained at the generated level, one can apply them to the $\cos\theta^*_{\rm reco}$ distribution, in order to obtain the distributions shown in Fig. 7.19, reporting the two extreme $\cos\theta^*_{\rm reco}$ after the complete event selection. This method is still not immune to the misidentification of the incident quark direction. However, it can be shown that a cut on the rapidity of the muons pair improves a correct identification of the quark. The rapidity is defined as follows:

$$y = \frac{1}{2}\log\frac{E + p_z c}{E - p_z c}, \tag{7.10}$$

where p_z is the component of momentum along the beam axis. The highest the rapidity, the highest the probability that the dominant contribution of the momentum comes from the quark instead that from the anti-quark. Fig. 7.20 shows the probability of correctly identify the quark as a function of the efficiency of the muons pair rapidity selection: this means that an efficiency of 1 corresponds to no cut on the rapidity. Such a cut reduces the signal population; the process cross-section can be very low and one should reject the smallest possible number of signal events. The chosen strategy to exploit the rapidity cuts and still keeping the full signal population

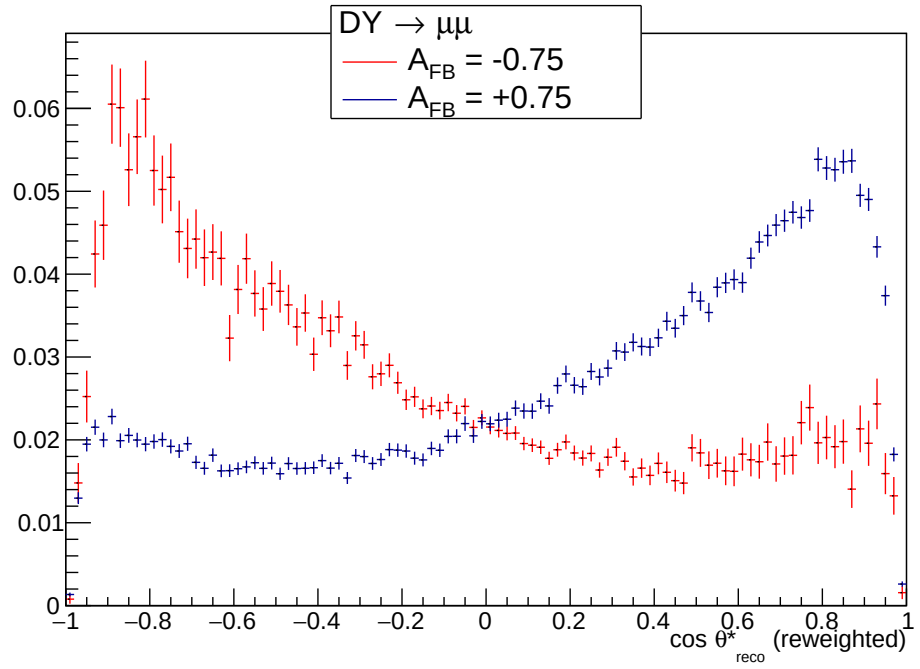

Fig. 7.19.: Re-weighted $\cos\theta_{\rm reco}$ distributions of the simulated Drell-Yan sample at reconstructed level, in order to obtain an $A_{\rm FB} = -0.75$ (red) and $+0.75$ (blue). The scenario corresponds to $\sqrt{s} = 14$ TeV at Phase II.

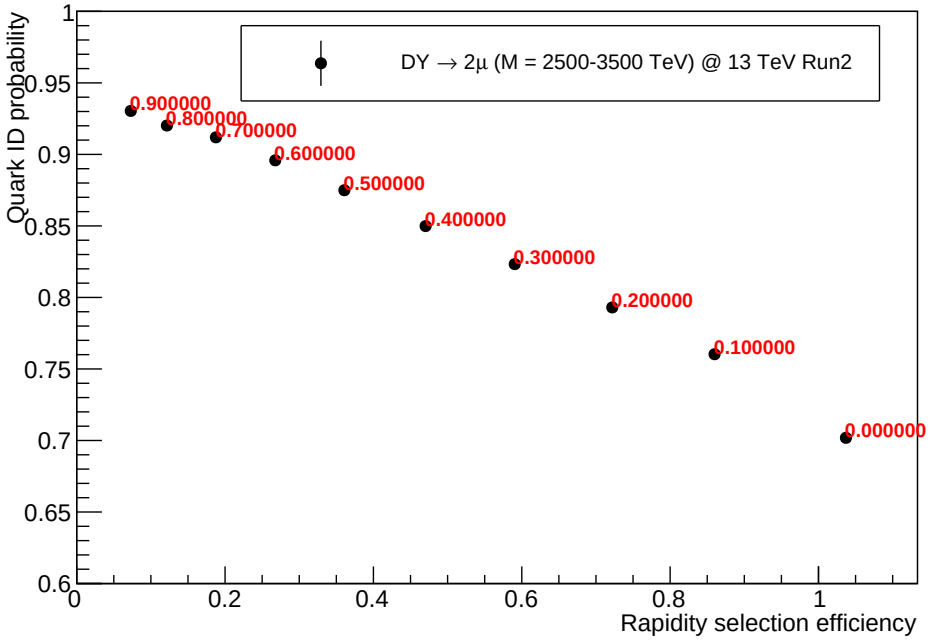

Fig. 7.20.: Probability of correctly identifying the quark direction as a function of the fraction of selected events when a condition $|y_{\mu\mu}| > y_{\rm cut}$ is applied for a Drell-Yan signal having a reconstructed mass 2.5 TeV/c^2 $< M <$ 3 TeV/c^2. Red labels associated to each point correspond to the applied pair rapidity cut. The errors are statistical and smaller than the marker size.

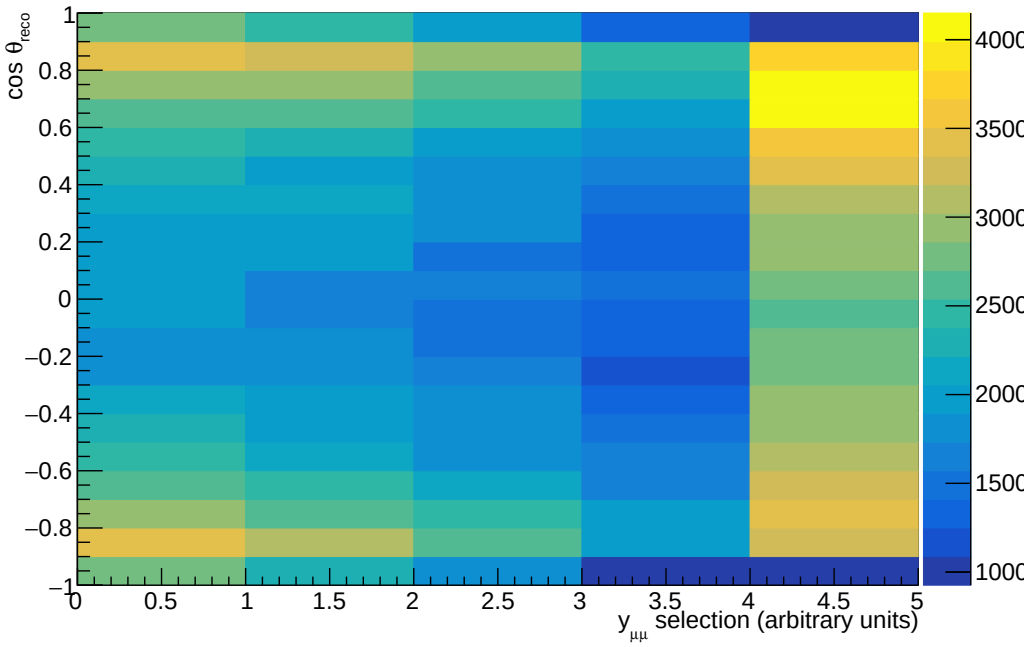

Fig. 7.21.: Z'_{SSM} $\cos\theta$ distributions on the y-axis, divided and numbered according to the selection shown in Tab. 7.8.

is to perform a fit in two dimensions to better estimate the parameter. The sample is divided in five different ranges, according to the muons pair rapidity. The width of each range was chosen in order to keep the population approximately constant from one to the other. The range limits are reported in Table 7.8.

Bin number	Rapidity range limits
1	$0 - 0.15$
2	$0.15 - 0.3$
3	$0.3 - 0.45$
4	$0.45 - 0.6$
5	$0.6 - 3$

Tab. 7.8.: Bin numbers and corresponding ranges of the muons pair rapidity. The bins correspond to the ones shown in Fig. 7.21, 7.22, and 7.23.

The two-dimensional distribution of $(\cos\theta_{\mathrm{reco}}, |y_{\mu\mu}|)$ for the Z'_{SSM} sample for Run 2 and no pile-up is shown in Fig. 7.21. Eq. 7.8 may also be applied in this case. The re-weighted distributions for $A_{\mathrm{FB}} = -0.75$ and $A_{\mathrm{FB}} = +0.75$, divided once again in vertical bins according to the muons pair rapidity, are respectively shown in Fig. 7.22 and 7.23. The choice to show Z'_{SSM} helps to better underline the difference between the original distribution and the re-weighted ones.

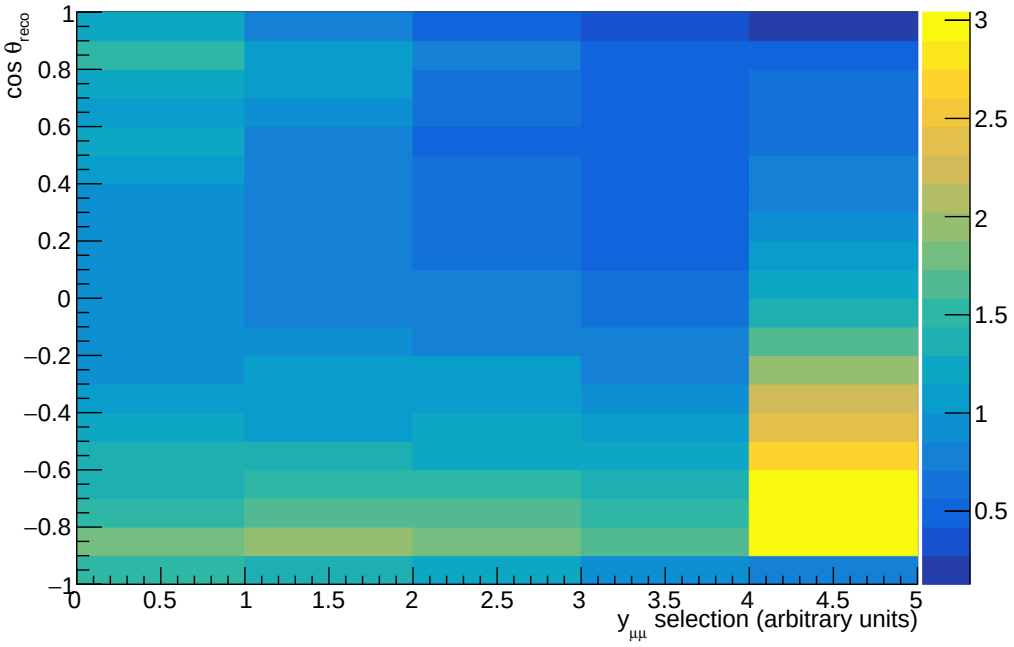

Fig. 7.22.: Re-weighted Z'_{SSM} $\cos\theta$ distributions on the y-axis, divided according to the selection shown in Tab. 7.8. The original distribution is re-weighted in order to have $A_{\mathrm{FB}} = -0.75$.

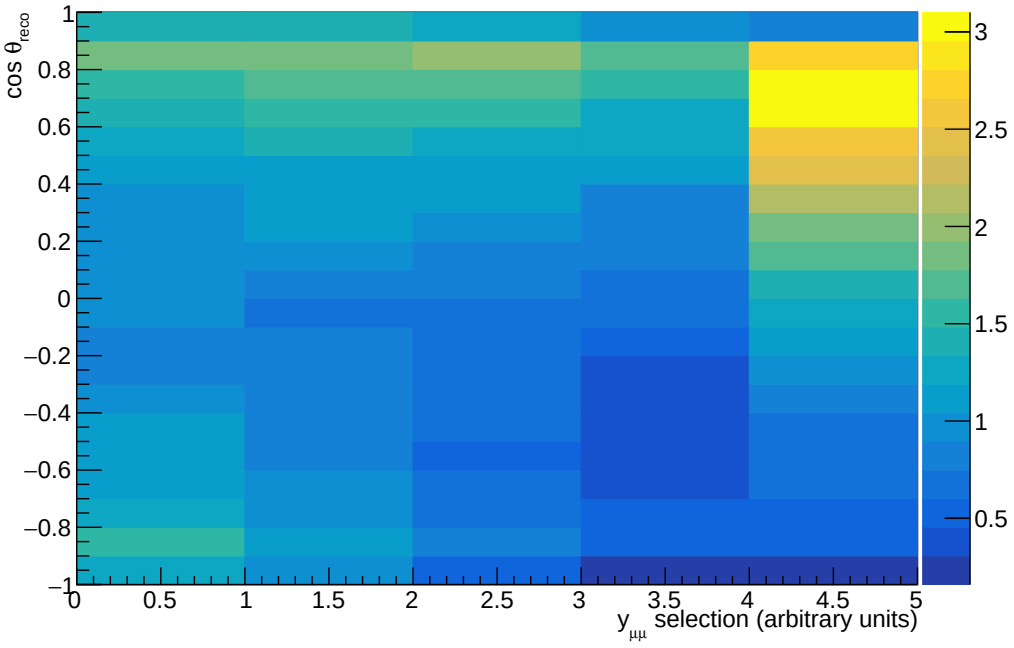

Fig. 7.23.: Re-weighted Z'_{SSM} $\cos\theta$ distributions on the y-axis, divided according to the selection shown in Tab. 7.8. The original distribution is re-weighted in order to have $A_{\mathrm{FB}} = -0.75$.

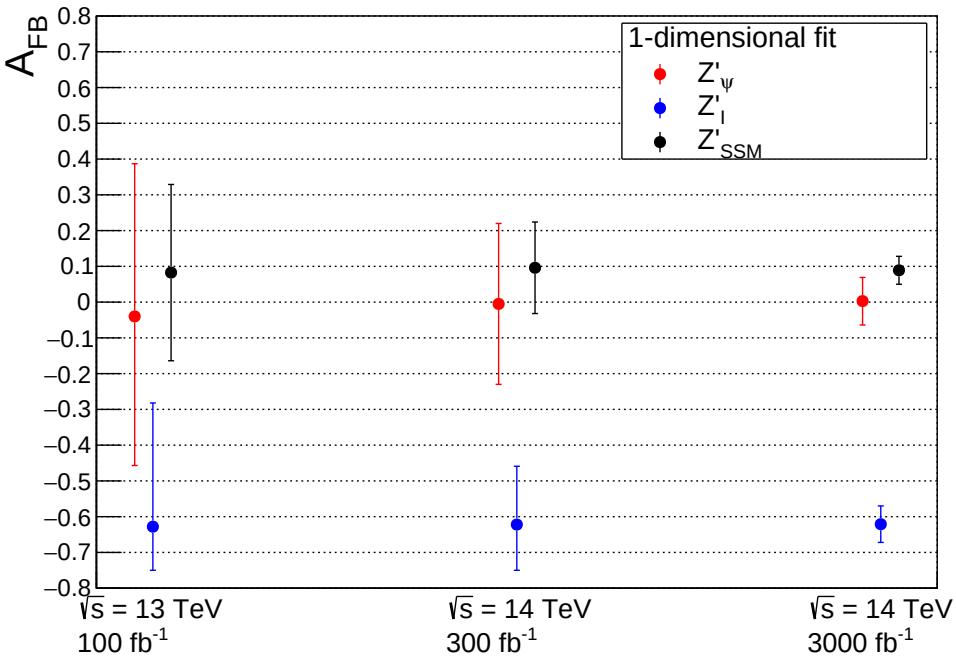

Fig. 7.24.: Estimated A_{FB} of three Z' models at a generated mass equal to 3 TeV/c^2 after 1000 pseudo-experiments, with a one-dimensional binned likelihood fit. Three CMS integrated luminosity scenarios are considered. The error bars represent a confidence interval of $\sim 68.27\%$.

Models such as the Z'_{I}, postulating a very asymmetric lepton distribution, return a pseudo-experiments central values very close to the physical boundaries at -0.75. This means that the uncertainty band can exceed the minimum physical value allowed for the model under consideration, in this case, for spin 1 particles. If one wants to state an interval that covers the unknown true value at exactly the stated confidence, this must be treated with care. Thus the estimation of the uncertainty errors in this study are based on the method presented by Feldman and Cousins in the reference [137].

7.5.3 A_{FB} estimations

The asymmetry estimations for $\mathrm{Z}'_{\mathrm{SSM}}$, Z'_{ψ}, and Z'_{I} at a generated mass of 3 TeV/c^2 are shown in Fig. 7.24 when the likelihood fit is based on 1D histograms, and Fig. 7.25 when it also involves the rapidity cut information. The same is shown for samples at 4 TeV/c^2 respectively in Fig. 7.26 and 7.27. The corresponding numerical values are reported in Tab. 7.9 and 7.10.

Regardless of the luminosity, all estimations keep the same median values depending on their model. The small discrepancies between the median values and the theo-

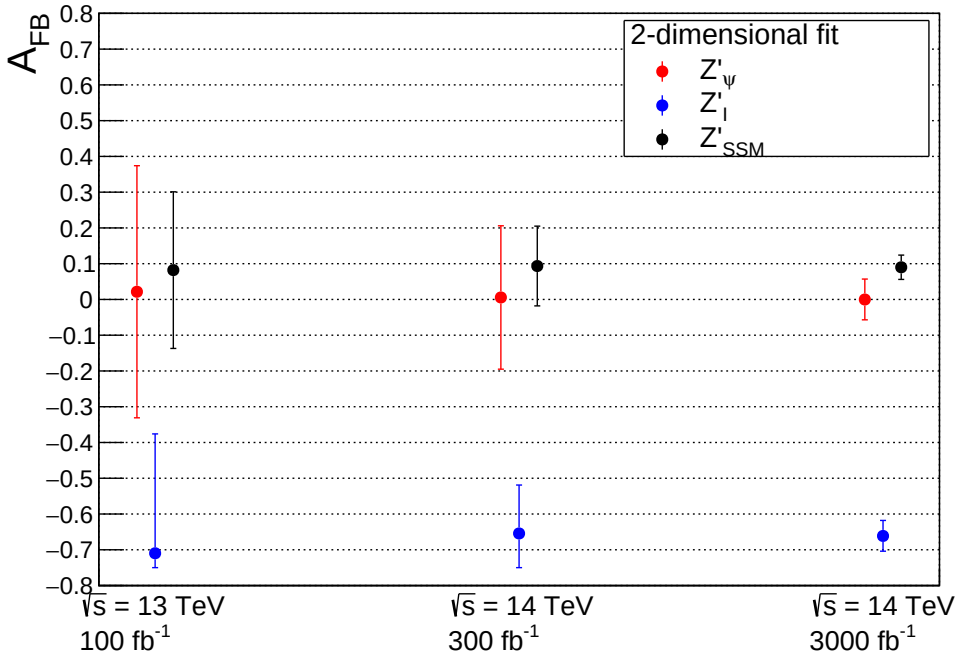

Fig. 7.25.: Estimated A_{FB} of three Z′ models at a generated mass equal to 3 TeV/c^2 after 1000 pseudo-experiments, with a two-dimensional binned likelihood fit. Three CMS integrated luminosity scenarios are considered. The error bars represent a confidence interval of $\sim 68.27\%$.

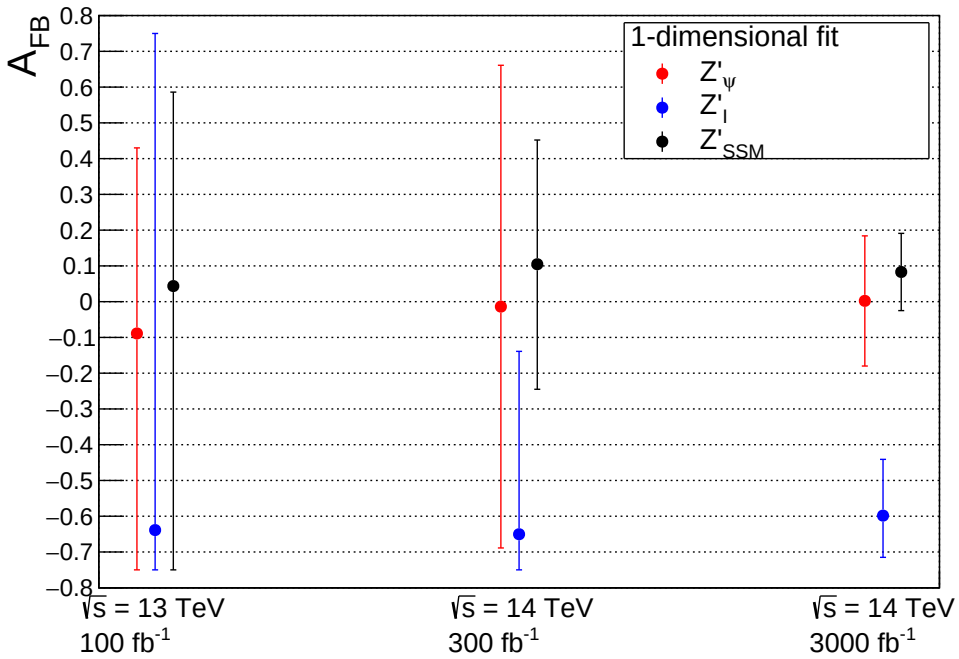

Fig. 7.26.: Estimated A_{FB} of three Z′ models at a generated mass equal to 4 TeV/c^2 after 1000 pseudo-experiments, with a one-dimensional binned likelihood fit. Three CMS integrated luminosity scenarios are considered. The error bars represent a confidence interval of $\sim 68.27\%$.

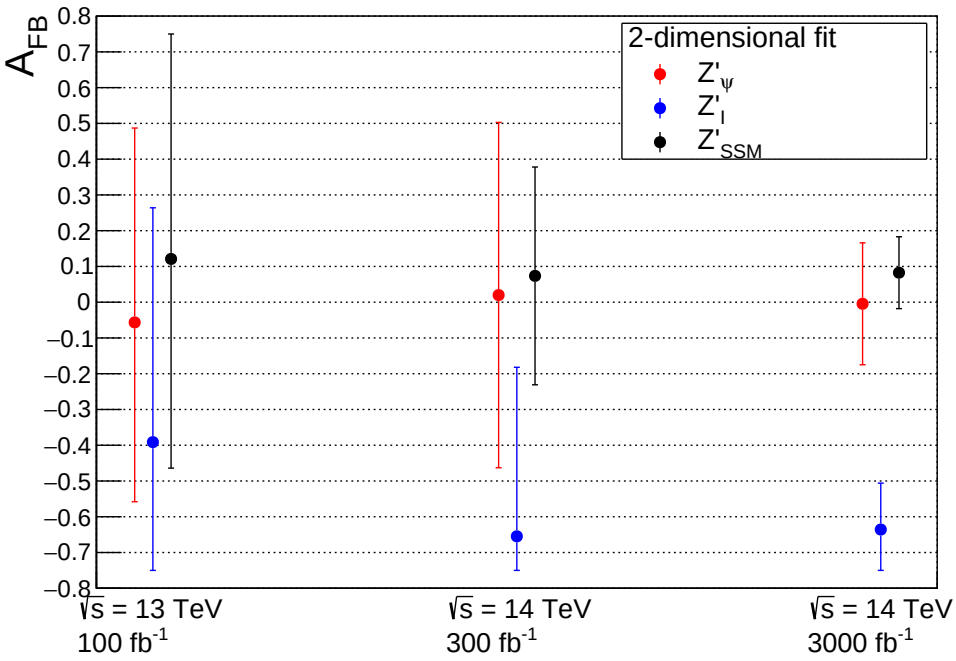

Fig. 7.27.: Estimated A_{FB} of three Z' models at a generated mass equal to 4 TeV/c^2 after 1000 pseudo-experiments, with a two-dimensional binned likelihood fit. Three CMS integrated luminosity scenarios are considered. The error bars represent a confidence interval of $\sim 68.27\%$.

Models	Generated mass	100 fb^{-1} $\sqrt{s} = 13$ TeV	300 fb^{-1} $\sqrt{s} = 14$ TeV	3000 fb^{-1} $\sqrt{s} = 14$ TeV
Z'_{ψ}	3 TeV/c^2	0.0 ± 0.4	0.0 ± 0.2	0.00 ± 0.07
Z'_{I}	3 TeV/c^2	$-0.61^{+0.4}_{-0.14}$	$-0.62^{+0.16}_{-0.11}$	-0.62 ± 0.05
$\mathrm{Z}'_{\mathrm{SSM}}$	3 TeV/c^2	0.1 ± 0.3	0.10 ± 0.12	0.09 ± 0.04
Z'_{ψ}	4 TeV/c^2	$0.1^{+0.5}_{-0.7}$	0.0 ± 0.7	0.0 ± 0.2
Z'_{I}	4 TeV/c^2	$-0.64^{+1.4}_{-0.11}$	$-0.65^{+0.51}_{-0.10}$	$-0.62^{+0.16}_{-0.12}$
$\mathrm{Z}'_{\mathrm{SSM}}$	4 TeV/c^2	$0.0^{+0.5}_{-0.8}$	0.1 ± 0.3	0.08 ± 0.11

Tab. 7.9.: Expected median and 1σ range on the A_{FB} measurement for a Z'_{ψ}, a Z'_{I} and a $\mathrm{Z}'_{\mathrm{SSM}}$ resonance for two different masses and for various integrated luminosities. The results presented here only use the $\cos\theta$ information.

Models	Generated mass	100 fb^{-1} $\sqrt{s} = 13$ TeV	300 fb^{-1} $\sqrt{s} = 14$ TeV	3000 fb^{-1} $\sqrt{s} = 14$ TeV
Z'_{ψ}	3 TeV/c^2	0.0 ± 0.4	0.0 ± 0.2	0.00 ± 0.06
Z'_{I}	3 TeV/c^2	$-0.64^{+0.30}_{-0.11}$	$-0.64^{+0.14}_{-0.09}$	-0.64 ± 0.04
Z'_{SSM}	3 TeV/c^2	0.1 ± 0.2	0.09 ± 0.11	0.09 ± 0.03
Z'_{ψ}	4 TeV/c^2	0.0 ± 0.5	0.0 ± 0.5	0.00 ± 0.2
Z'_{I}	4 TeV/c^2	$-0.4^{+0.7}_{-0.4}$	$-0.65^{+0.5}_{-0.10}$	$-0.64^{+0.13}_{-0.11}$
Z'_{SSM}	4 TeV/c^2	0.1 ± 0.6	0.1 ± 0.3	0.08 ± 0.10

Tab. 7.10.: Expected median and 1σ range on the A_{FB} measurement for a Z'_{ψ}, a Z'_{I} and a Z'_{SSM} resonance for two different masses and for various integrated luminosities. The results presented here use the $\cos\theta$ and the $y_{\mu\mu}$ information.

retical expectations are explained by the finite statistics in the simulated samples. In this study, the quantity of interest is the size of the 1σ band, which represents the expected statistical precision that can be reached on the forward-backward asymmetry measurement. It correctly follows a $1/\sqrt{N}$ dependence where N is the average signal population of a single pseudo-experiment. Two of the signals studied here, the Z'_{ψ} and the Z'_{SSM}, have a small or null asymmetry. However signals with strong asymmetries exist. An already mentioned example is the case of the Z'_{I} which only couples to left-handed leptons and right-handed down quarks and where the asymmetry is maximally negative.

7.5.4 Z'_{I} mismeasurement

As already illustrated in Sec. 2.5.2 and Tab. 2.2 the Z'_{I} has a maximally negative $A_{\mathrm{FB}} = -0.75$, due to its coupling to the sole down quark/anti-quark. However, in most cases the A_{FB} estimation provides values much closer to -0.6 than to its theoretical value. One of the main hypothesis formulated when the present fit method is applied is that the procedure is model-independent. Unfortunately it turns out that this is not entirely true. According to the parton density functions shown in Fig. 2.6, the momentum fractions carried by the quarks in a down-antidown interaction is different than the ones occurring in a up-antiup one. This results in the fact that a down-antidown interaction is more sensitive to a wrongful attribution of the quark direction. Such an effect results in a dilution of the $\cos\theta^*_{\mathrm{reco}}$ distribution. Fig. 7.28 shows a comparison between the re-weighted $p_{A_{\mathrm{FB}=-0.75}}$ distributions generated from Z'_{SSM}, Z'_{ψ} and Z'_{I} samples. While the ones coming from Z'_{SSM} and Z'_{ψ} are on top of each other, the dilution is clearly visible in the one coming from Z'_{I}. As a consequence, when Z'_{I} is estimated from $p_{A_{\mathrm{FB}=\pm 0.75}}$ re-weighted from a Z'_{ψ} sample, the adjustment of the fit requires a greater contribution from $p_{A_{\mathrm{FB}=+0.75}}$ instead of the purely negative one $p_{A_{\mathrm{FB}=-0.75}}$, as the nature of Z'_{I} would imply.
Possible solutions to this problem would imply to use an (independent) Z'_{I} sample

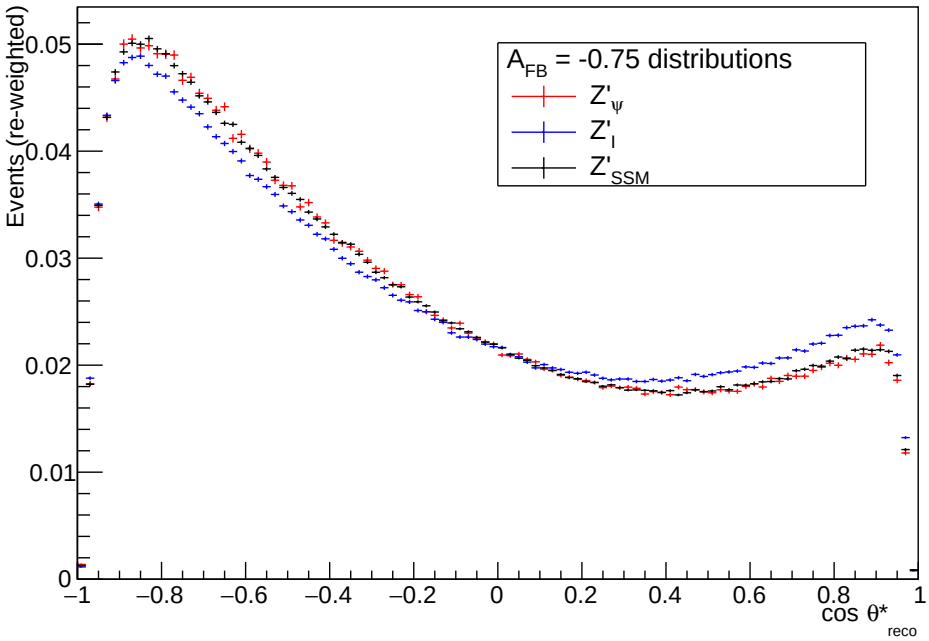

Fig. 7.28.: Re-weighted $\cos\theta^*_{\mathrm{reco}}$ distributions in order to have $A_{\mathrm{FB}} = -0.75$ coming from Z'_{ψ}, Z'_{I}, and $\mathrm{Z}'_{\mathrm{SSM}}$ samples at a generated mass of 3 TeV/c^2. While Z'_{ψ} and $\mathrm{Z}'_{\mathrm{SSM}}$ distributions are on top of each other, Z'_{I} shows a dilution due to the fact that this model foresees couplings only to down quarks/antiquarks.

to fit the Z'_{I} signal. Another possibility to estimate the systematic uncertainty of this error would be to select reconstructed Z'_{ψ} created only by $\mathrm{u\bar{u}}$ or $\mathrm{d\bar{d}}$ interactions, thanks to the information at the generated level.

7.5.5 Pile-up impact

The estimation of the impact of pile-up on the A_{FB} measurement was performed by comparing the results obtained in the Phase II scenario of a Drell-Yan sample (2.5 TeV/c^2 $< M <$ 3.5 TeV/c^2) with PU $= 0$ and one with PU $= 140$. The comparison is shown for both likelihood methods in Fig. 7.29. No difference in the 1σ interval has been observed. This leads to the conclusion that the applied muon selection does not suffer from the presence of pile-up.

7.6 Contributions of upgrades to A_{FB} estimation

The most direct strategy to evaluate the contribution of the upgrades between Run 2 and Phase II is to consider a Phase II sample and to generate pseudo-experiments having a population equivalent to the luminosity expected at the end of Run II, that

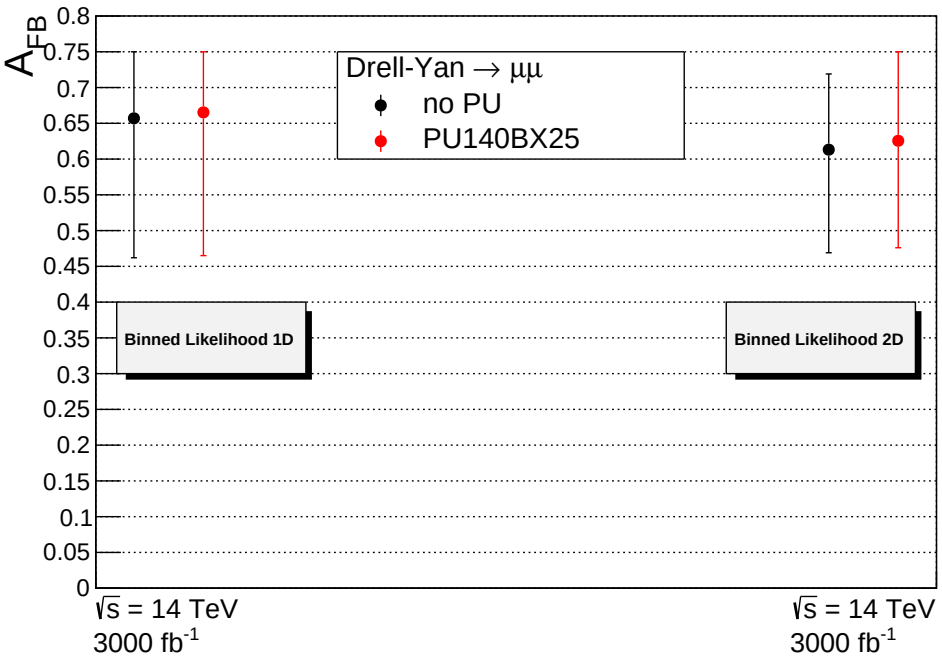

Fig. 7.29.: Estimated A_{FB} for Drell-Yan samples with PU $= 0$ and PU $= 140$ in the Phase II scenario. No difference in the 1σ interval has been observed.

is in this case 100 fb^{-1}. Phase II is expected to have a better selection efficiency, due to its better mass resolution (see Fig. 7.7 and 7.8), so this would allow to have more events per pseudo-experiment with respect to a Run 2 scenario with equal integrated luminosity. The results are shown in Tab. 7.11. The numbers show that despite a better p_{T} resolution, and hence a better mass resolution, the upgrades provide no significant improvement to the measurements. This can be explained by a simple statistics argument: the width of the Gaussian obtained in our case after 1000 pseudo-experiments follows a $1/\sqrt{N}$ trend, where N is the number of events in a single pseudo-experiment [138]. Let us assume that a given improvement in the mass resolution increases the number of events in the selected windows mass by a 10% factor. The ratio R between this newly obtained Gaussian and the original one (in the non-upgraded scenario) is equal to:

$$R = \frac{\sqrt{n \cdot (1.1)}}{\sqrt{n}} \approx 1.05, \tag{7.11}$$

where n is the population of the original selected events sample. The relative improvement in the A_{FB} statistical error is then approximately 5%.

	Z'_ψ		Z'_{SSM}	
Scenario	1D fit	2D fit	1D fit	2D fit
Run 2	-0.04 ± 0.42	0.20 ± 0.35	0.08 ± 0.25	0.08 ± 0.21
Phase II	0.01 ± 0.42	0.00 ± 0.36	0.08 ± 0.24	0.09 ± 0.21

Tab. 7.11.: Estimation of A_{FB} with 100 fb^{-1} of data generated by 1000 pseudo-experiments in two different CMS scenarios. No statistical difference is observed.

7.7 Distinguishing among Z' models

The asymmetry measurements can be used for discriminating among Z' models. The A_{FB} measurement is sensitive to the choice of the mass range and to the modelling of the mass resolution tails, neither of which has been optimized in the present studies. It is also possible to use the measured total cross-section to help distinguish among models. In this section, however, the determination of the couplings is done using A_{FB} independently of the total cross-section.

The discussion is here restricted to comparison taking only two models at a time. For instance, some measurements might be 3.5σ away from a second model. The method makes use of classical hypothesis testing developed by Neyman and Pearson [139]. When comparing two parameter-free hypotheses, one (say Z'_{I}) is taken as the "null" hypothesis H_0, and the other (say Z'_{SSM}) is taken as the "alternate" hypothesis H_1. An example of this method is illustrated by Fig. 7.30. Then A_{FB} is our test-statistics for which we construct the pdfs given H_0 and given H_1. It is assumed that the pdf for measured $A_{\mathrm{FB}}^{\mathrm{rec}}$ is a normalized Gaussian centred at $A_{\mathrm{FB}}^{\mathrm{count}}$ – the theoretical A_{FB} – for the given model. The width of the Gaussian is chosen to be the same as the value returned by the fit on Z'_{I}, as shown in Tab. 7.10. One usually fixes in advance the "significance level" of the test, that is the probability α of rejecting H_0 if it is not true. The region that rejects H_0, known as "critical region" is the best one if it maximises the power against H_1, represented by $1-\beta$. However, since in the current case, there is no reason for preferring a model or the other, a modification is implemented: one minimizes any given linear combination of α and β [140]. The value that divides the A_{FB} axis into the acceptance and critical region is called $A_{\mathrm{FB}}^{\mathrm{cut}}$. Such a minimization places the value of $A_{\mathrm{FB}}^{\mathrm{cut}}$ where the likelihood functions intersect; equivalently, it is the value that gives $\alpha = \beta$ [141]. Ultimately, the boundary of the critical regions $A_{\mathrm{FB}}^{\mathrm{cut}}$ is set to be halfway between the $A_{\mathrm{FB}}^{\mathrm{count}}$ of H_0 and H_1.
Each of the three models that were studied is taken in turn to be the null hypothesis H_0 and is tested against the alternative of each of the other two models, taken one at a time to be H_1. For each pair of models, the boundary of the critical region is set and the value of the significance level α (equal to β by construction) is calculated. α

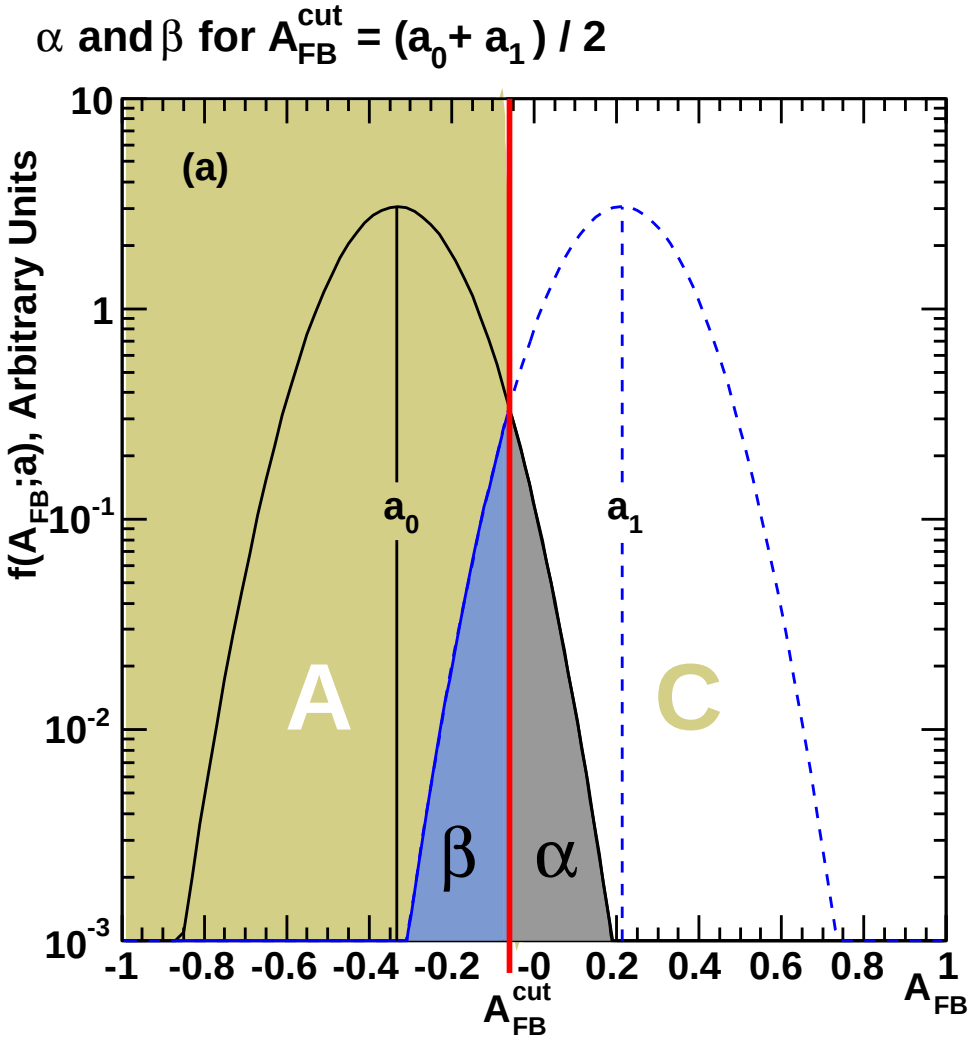

Fig. 7.30.: α and β for a placement of $A_{\mathrm{FB}}^{\mathrm{cut}} = (a_0 + a_1)/2$, indicated by the red vertical line. The shaded section with an "A" is the acceptance region; the section with a shaded "C" is the critical region. Reference: CMS Internal Note 2005/022.

	100 fb^{-1} $\sqrt{s} = 13$ TeV			300 fb^{-1} $\sqrt{s} = 14$ TeV			3000 fb^{-1} $\sqrt{s} = 14$ TeV		
Model	Z'_I	Z'_ψ	Z'_{SSM}	Z'_I	Z'_ψ	Z'_{SSM}	Z'_I	Z'_ψ	Z'_{SSM}
Z'_I	–	1.1	1.3	–	2.8	3.1	–	8.6	9.8
Z'_ψ	1.1	–	0.1	1.9	–	0.2	6.6	–	0.8
Z'_{SSM}	1.9	0.2	–	3.8	0.4	–	12	1.4	–

Tab. 7.12.: Significance level α (expressed in equivalent number of σ's) for pairwise comparisons of Z$'$ models at $M_{Z'} = 3$ TeV/c^2 for every integrated luminosity scenario.

	100 fb^{-1} $\sqrt{s} = 13$ TeV			300 fb^{-1} $\sqrt{s} = 14$ TeV			3000 fb^{-1} $\sqrt{s} = 14$ TeV		
Model	Z'_I	Z'_ψ	Z'_{SSM}	Z'_I	Z'_ψ	Z'_{SSM}	Z'_I	Z'_ψ	Z'_{SSM}
Z'_I	–	0.6	0.6	–	0.8	0.9	–	2.9	3.3
Z'_ψ	0.7	–	0.1	0.8	–	0.1	2.2	–	0.3
Z'_{SSM}	0.7	0.1	–	1.4	0.2	–	4.2	0.5	–

Tab. 7.13.: Significance level α (expressed in equivalent number of σ's) for pairwise comparisons of Z$'$ models at $M_{Z'} = 4$ TeV/c^2 for every integrated luminosity scenario.

is then calculated in terms of the equivalent number of standard deviation, that is the distance between A_{FB}^{cut} and A_{FB}^{count}, divided by the expected error on A_{FB}.
Of course, each Z$'$ model predicts a different dimuon production cross-section. This breaks the symmetry between H_0 and H_1: there is an ambiguity regarding what cross-section to use when choosing the statistical error on A_{FB}. Two values of the significance level are then obtained for each pair of models.
Tab. 7.12 gives a summary of the significance level α for pairwise comparisons of Z$'$ models at $M_{Z'} = 3$ TeV/c^2 for all luminosity scenarios; Tab. 7.13 contains α values for 4 TeV/c^2 Z$'$ bosons. The left column specifies the model taken as the null hypothesis H_0, which is tested against the alternative of each of the other two models in the adjacent columns.

Considering 3 TeV/c^2 models, one can see from Tab. 7.12 that no discrimination with $\alpha > 3\sigma$ is possible with 100 fb^{-1} of data among the three proposed models. Such a discrimination is however possible with 300 fb^{-1} of data between Z'_{SSM} and Z'_I. Finally, 3000 fb^{-1} of data allow to discriminate Z'_I versus any of the other two models at a very large significance level. At 4 TeV/c^2, the lower cross-sections allow to operate a discrimination at $\alpha > 3\sigma$ between Z'_{SSM} and Z'_I during Phase II scenario.

7.8 Conclusions

One of the straightforward ways to observe physics beyond the Standard Model at the LHC would be through the emergence of a new resonance in the dimuon mass spectrum at the TeV scale. The search for a signal in the data collected by CMS and ATLAS during the LHC Run 1 and early data from Run 2 did not lead to such a discovery [26, 28, 25, 27]. However, the first evidence after the LHC restart in 2015 characterized by the increase of the LHC beam energy, has shown interesting features [142, 143], although in another channel. In case a signal is observed in the dimuon or dielectron channel, the leptons angular distribution provide valuable information to distinguish between different new physics models and to measure the spin, and other properties of the observed signal. In this Chapter, assuming that the new discovery particle has spin 1, a method to estimate the forward-backward charge asymmetry based on $\cos\theta^*$ templates was applied, and the precision that could be reached in this was studied. Three resonant signal models were considered: the sequential Standard Model $\mathrm{Z'_{SSM}}$, the $\mathrm{Z'_{\psi}}$, and the $\mathrm{Z'_{I}}$. For a $\mathrm{Z'}$ with a mass of 3 TeV/c^2, and concerning the forward-backward asymmetry measurement, 300 fb^{-1} would lead to a discrimination level between 2 and 3σ between a 3 TeV/c^2 $\mathrm{Z'_{I}}$ and a $\mathrm{Z'_{\psi}}$ or $\mathrm{Z'_{SSM}}$, while 3000 fb^{-1} provide a very high discrimination power between models with very different asymmetry. At 4 TeV/c^2 the discriminations are more difficult due to much smaller cross-sections of the processes.
Eventually, an extension of this study would involve the analysis of resonant spin 2 particles, such as the Randall-Sundrum graviton G_{RS}. The spin measurement of the different models could be evaluated, as well as the measurement of the production mode – gg or $\mathrm{q\bar{q}}$ in the case of spin 2 resonances.

8 Conclusions

Decades of experiments and measurements have proven that the Standard Model of elementary particles is a very successful theory. Fundamental reasons, however, push researchers to move beyond its framework to find evidence of new physics. The thesis at hand is set in this context, both through the study of the MPGD known as Triple-GEMs, to be installed in the high-η region of the CMS muon spectrometer at the LHC, and through the simulated projection of the forward-backward asymmetry of a postulated resonance in the high-energy spectrum, called Z', in the dimuon channel.

The scheduled upgrades that the LHC will undergo in a few years will provide both unprecedented yields of energy in the center-of-mass and instantaneous luminosity in a man-made machine. The value of $2 \cdot 10^{34}$ cm^{-2}s^{-1} experienced after LS2 will ultimately increase up to $7.5 \cdot 10^{34}$ cm^{-2}s^{-1} around 2030 and beyond. Such an environment will provide harsh conditions that the CMS community must face, to keep providing excellent detectors performances at every stage of the data taking. This is why a series of upgrades are well under study since a few years. This thesis has focused on the Triple-GEM technology, officially approved to equip the GE1/1 muon chamber during LS2, in the range $1.5 < |\eta| < 2.1$ of the muon system. Triple-GEMs have proven to offer a rate capability exceeding 1 MHz/cm^2, well beyond the maximum expected hit rate in GE1/1 station during Phase II, and appropriate angular resolution of 130 μm and time resolution of less than 10 ns for a single chamber. The improvement of the L1 trigger rate is one of the crucial motivations for this upgrade. For all these reasons, an estimation of the response of the Triple-GEMs to the background particles is a fundamental step that leads to an appropriate muon trigger and muon reconstruction performance simulation.
Hence, this work was focused on the estimation, essentially through the GEANT4 toolkit, of the sensitivity of the Triple-GEMs to the main types of background particles: neutron, photons, electrons and positrons. The simulation were carried on by first validating the results with previous simulations found in literature and with data, when possible. Most of the time, a type of gas detector already installed in CMS, the Resistive Plate Chamber (RPC) was taken as a basis for comparison, due to its much longer employment in particle physics experiments and thus to the amount of available results. All along these studies, the most appropriate physics simulation libraries (called Physics Lists in GEANT4 environment) were put to the test. Two in

particular – FTFP_BERT_HP and QGSP_BIC_HP – were selected as they best describe the physics results in the energetic range, covering 11 order of magnitudes, that needs to be covered in this application. The interaction between charged or neutral particles and material has proven to be correctly included by both Physics Lists. The geometry of the detector was described to the best of our knowledge; several options, including the simulation of the holes in the GEM foils, were investigated; eventually, an up-to-date angular and energetic description of the background environment has been selected to be given as an input to the program. Statistical and systematic errors were then propagated and taken into account. They led to the following sensitivity results, convoluted with the incident Phase II flux on GE1/1 surface, and shown as probabilities.

particles	sensitivity (%)
neutrons	$0.163 \pm 0.002(\text{stat.})^{+0.07}_{-0.05}(\text{syst.})$
photons	$0.884 \pm 0.004(\text{stat.})^{+0.2}_{-0.03}(\text{syst.})$
electrons	$9.2 \pm 0.3(\text{stat.}) \pm 3(\text{syst.})$
positrons	$9.8 \pm 0.3(\text{stat.}) \pm 3(\text{syst.})$

These values provide an overall GE1/1 background hit rate less than 1 kHz/cm^2, well below Triple-GEM's hit rate capability.

The second part of the thesis was focused on the projected measurement of the forward-backward asymmetry of several models of postulated heavy bosons, known as Z$'$, decaying in a pair of muons. Such beyond-the-Standard-Model particles have been excluded up to masses of almost 3 TeV/c^2, in some cases. Samples of different models, such as Z$'_\psi$, Z$'_{\text{SSM}}$, and Z$'_{\text{I}}$ were generated at 3 and 4 TeV/c^2. It was determined if the measurement of a quantity known as forward-backward asymmetry could benefit from the Run 3 and Phase II upgrades. The distributions of the possible measurements were constructed thanks to a set of 1000 pseudo-experiments, for three different benchmark scenarios and integrated luminosities: 100 fb^{-1} at $\sqrt{s} = 13$ TeV reproducing the end of Run 2, 300 fb^{-1} at $\sqrt{s} = 14$ TeV reproducing the end of Run 3 and 3000 fb^{-1} at $\sqrt{s} = 14$ TeV reproducing the end of Phase II. Ultimately, it results that the propagation of the estimated improvement in the reconstructed mass resolution due to the muon upgrades and the tracker upgrades do not significantly contribute to the reduction of the observed 1σ band in the forward-backward asymmetry. Nevertheless, a discrimination power greater than 3σ is supposed to appear between Z$'_{\text{I}}$ and Z$'_\psi$ or Z$'_{\text{SSM}}$, postulating a Z$'$ at 3 TeV/c^2, once the full Phase I data acquisition will be accomplished. A similar performance can be reached after 3000 fb^{-1} of data if the mass of the postulated boson is equal to 4 TeV/c^2.

A Control plots

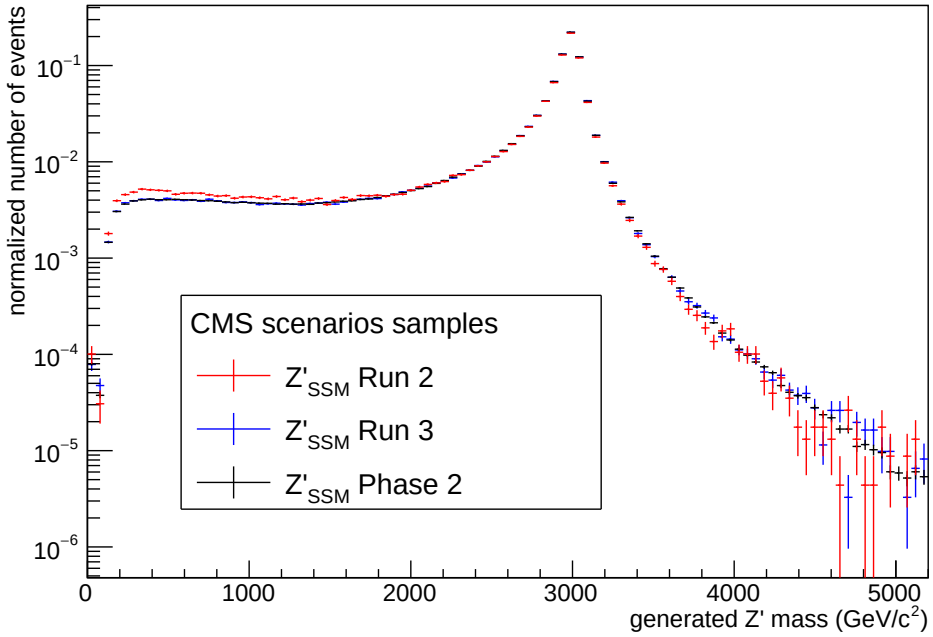

Fig. A.1.: Mass of the Z'_{SSM} at the generated level for three CMS scenarios. The larger off-shell contribution in the Run 2 scenario is due to the center-of-mass energy equal to 13 TeV instead of 14 TeV for the two other scenarios.

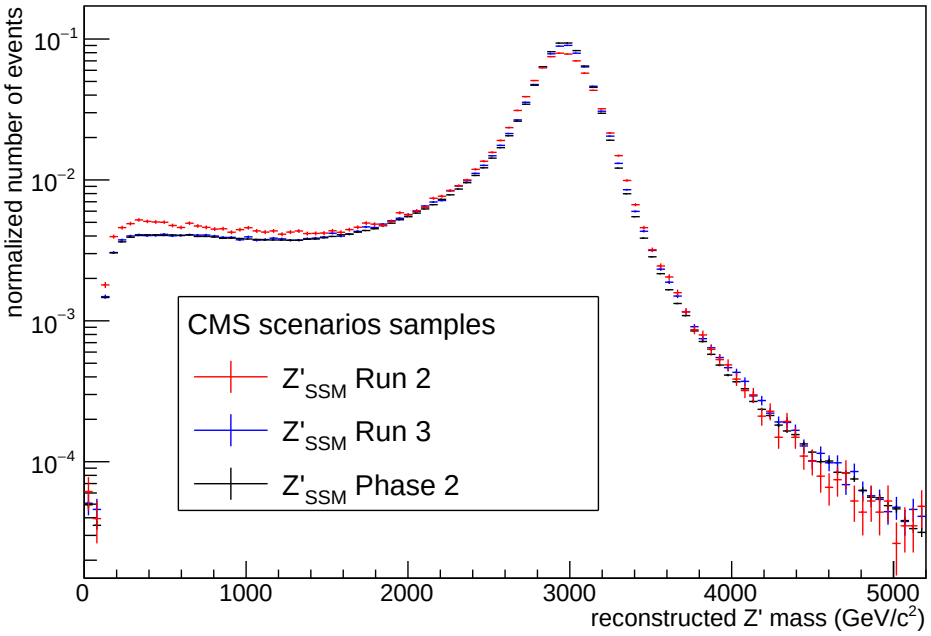

Fig. A.2.: Mass of the Z'_{SSM} at the reconstructed level for three CMS scenarios. The larger off-shell contribution in the Run 2 scenario is due to the center-of-mass energy equal to 13 TeV instead of 14 TeV for the two other scenarios, consistently with Fig. A.1.

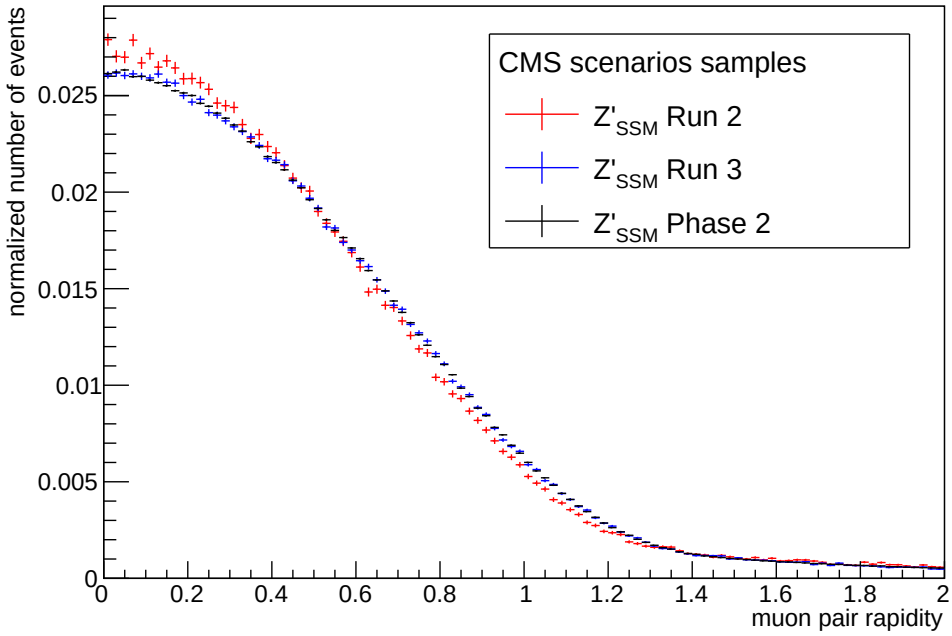

Fig. A.3.: Rapidity distribution of the muon pair coming from the decay of a 3 TeV/c^2 Z'_{SSM} at the generated level for three different CMS scenarios. The topology of the events is different in Run 2 due to the center-of-mass energy being at 13 TeV instead of 14 TeV.

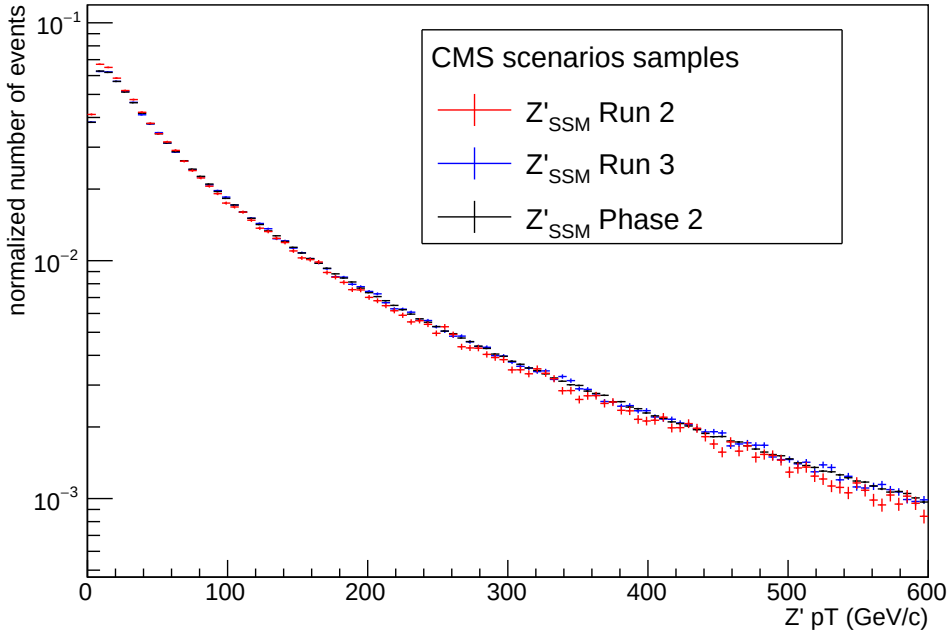

Fig. A.4.: p_{T} distribution of a 3 TeV/c^2 $\mathrm{Z}'_{\mathrm{SSM}}$ at the generated level.

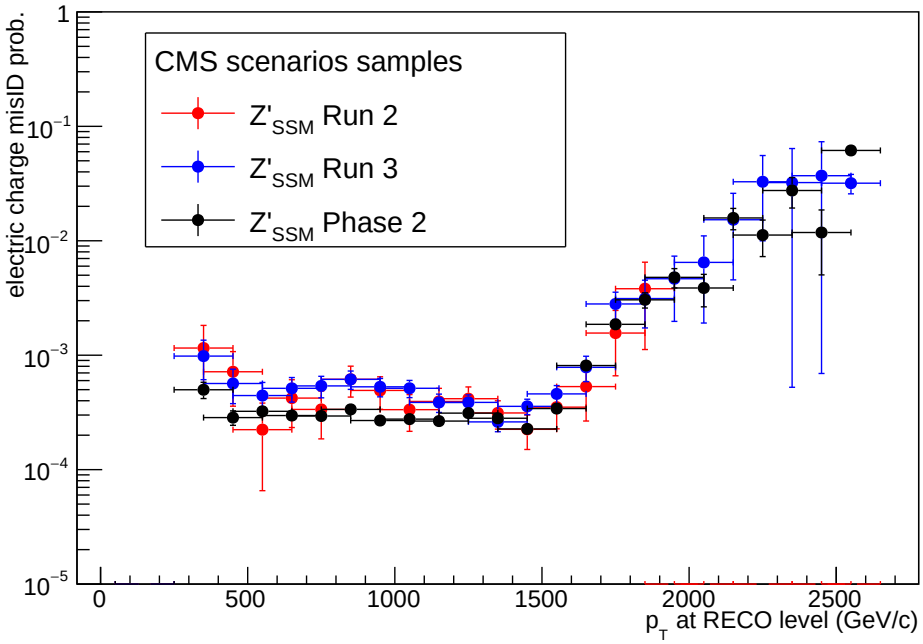

Fig. A.5.: Probability of muon charge mismeasurement as a function of the reconstructed p_{T} of the muon. The muons pass all the analysis selection and are required to come from a $\mathrm{Z}'_{\mathrm{SSM}}$ having a reconstructed mass within 10% of its theoretical value. The mismeasurement is larger as the p_{T} increases, as it becomes more and more challenging to reconstruct the curved trajectory.

Bibliography

[1] F. Englert and R. Brout. "Broken Symmetry and the Mass of Gauge Vector Mesons". In: *Phys. Rev. Lett.* 13 (9 1964), pp. 321–323 (cit. on p. 7).

[2] Peter W. Higgs. "Broken Symmetries and the Masses of Gauge Bosons". In: *Phys. Rev. Lett.* 13 (16 1964), pp. 508–509 (cit. on p. 7).

[3] G. S. Guralnik, C. R. Hagen, and T. W. B. Kibble. "Global Conservation Laws and Massless Particles". In: *Phys. Rev. Lett.* 13 (20 1964), pp. 585–587 (cit. on p. 7).

[4] ATLAS Collaboration. "Observation of a new particle in the search for the Standard Model Higgs boson with the ATLAS detector at the LHC". In: *Phys.Lett.* B716 (2012), pp. 1–29. arXiv: 1207.7214 [hep-ex] (cit. on p. 7).

[5] CMS Collaboration. "Observation of a new boson at a mass of 125 GeV with the CMS experiment at the LHC". In: *Phys.Lett.* B716 (2012), pp. 30–61. arXiv: 1207.7235 [hep-ex] (cit. on p. 7).

[6] I. J. R. Aitchison and A. J. G. Hey. *Gauge Theories in Particle Physics: A Practical Introduction (Graduate Student Series in Physics)*. 3rd Rev. Taylor & Francis, Sept. 2002 (cit. on p. 8).

[7] M. G. Green, S. L. Lloyd, P. N. Ratoff, and D. R. Ward. *Electron-Positron Physics at the Z (Studies in High Energy Physics Cosmology and Gravitation)*. Institute of Physics Publishing Bristol and Philadelphia, 1998 (cit. on p. 8).

[8] F. Halzen and A. D. Martin. *Quarks and Leptons: An Introductory Course in Modern Particle Physics*. New York, USA: Wiley, 1984 (cit. on p. 8).

[9] R. P. Feynman and M. Gell-Mann. "Theory of the Fermi Interaction". In: *Phys. Rev.* 109 (1 1958), pp. 193–198 (cit. on p. 11).

[10] Willem De Boer. *The Discovery of the Higgs Boson with the CMS Detector and its Implications for Supersymmetry and Cosmology*. Tech. rep. CMS-CR-2013-231. Comments: 26 pages, Conference Proceedings Time and Matter (TAM2013), Venice, Feb. 2013. Geneva: CERN, 2013 (cit. on p. 13).

[11] Michael E. Peskin. "On the Trail of the Higgs Boson". In: *Annalen Phys.* 528.1-2 (2016), pp. 20–34. arXiv: 1506.08185 [hep-ph] (cit. on pp. 18, 37).

[12] Roel Aaij et al. "Observation of the resonant character of the $Z(4430)^-$ state". In: *Phys. Rev. Lett.* 112.22 (2014), p. 222002. arXiv: 1404.1903 [hep-ex] (cit. on p. 21).

[13]Roel Aaij et al. “Observation of J/ψ p Resonances Consistent with Pentaquark States in $\Lambda_b^0 \to$ J/ψK$^-$p Decays”. In: *Phys. Rev. Lett.* 115 (2015), p. 072001. arXiv: 1507.03414 [hep-ex] (cit. on p. 21).

[14]A.D. Martin, W.J. Stirling, R.S. Thorne, and G. Watt. “Parton distributions for the LHC”. English. In: *The European Physical Journal C* 63.2 (2009), pp. 189–285 (cit. on p. 24).

[15]S. D. Drell and T.-M. Yan. “Massive Lepton-Pair Production in Hadron-Hadron Collisions at High Energies”. In: *Physical Review Letters* 25 (Aug. 1970), pp. 316–320 (cit. on p. 24).

[16]Thomas G. Rizzo. “Z$'$ phenomenology and the LHC”. In: *Proceedings of Theoretical Advanced Study Institute in Elementary Particle Physics : Exploring New Frontiers Using Colliders and Neutrinos (TASI 2006)*. 2006, pp. 537–575. arXiv: hep-ph/0610104 [hep-ph] (cit. on p. 27).

[17]H. Georgi and S. L. Glashow. “Unity of All Elementary Particle Forces”. In: *Phys. Rev. Lett.* 32 (1974), pp. 438–441 (cit. on p. 28).

[18]Jonathan L. Rosner. “Forward - backward asymmetries in hadronically produced lepton pairs”. In: *Phys.Rev.* D54 (1996), pp. 1078–1082. arXiv: hep-ph/9512299 [hep-ph] (cit. on pp. 29, 176, 177).

[19]P. Abreu et al. “A study of radiative muon-pair events at Z0 energies and limits on an additional Z$'$ gauge boson”. English. In: *Zeitschrift für Physik C Particles and Fields* 65.4 (1995), pp. 603–618 (cit. on p. 30).

[20]Ross Diener, Stephen Godfrey, and Ismail Turan. “Constraining extra neutral gauge bosons with atomic parity violation measurements”. In: *Phys. Rev. D* 86 (11 2012), p. 115017 (cit. on p. 30).

[21]Jens Erler, Paul Langacker, Shoaib Munir, and Eduardo Rojas. “Improved constraints on Z$'$ bosons from electroweak precision data”. In: *Journal of High Energy Physics* 2009.08 (2009), p. 017 (cit. on p. 30).

[22]J. Alcaraz et al. *A Combination of preliminary electroweak measurements and constraints on the standard model*. Tech. rep. CERN-PH-EP-2006-042, LEPEWWG-2006-01, ALEPH-2006-001-PHYSICS-2006-001, DELPHI-2006-014-PHYS-948, L3-NOTE-2833, OPAL-PR-419. Geneva: CERN, 2006. arXiv: hep-ex/0612034 [hep-ex] (cit. on p. 30).

[23]T. Aaltonen et al. “Search for High-Mass e^+e^- Resonances in $p\overline{p}$ Collisions at $\sqrt{s} = 1.96$ TeV”. In: *Phys. Rev. Lett.* 102 (3 2009), p. 031801 (cit. on p. 30).

[24]V.M. Abazov et al. “Search for a heavy neutral gauge boson in the dielectron channel with 5.4 fb^{-1} of collisions at $\sqrt{s} = 1.96$ TeV”. In: *Physics Letters B* 695.1–4 (2011), pp. 88 –94 (cit. on p. 30).

[25]Georges Aad et al. “Search for high-mass dilepton resonances in pp collisions at $\sqrt{s}$ = 8 TeV with the ATLAS detector”. In: *Phys. Rev. D* 90.5 (2014), 052005. 18 p (cit. on pp. 30, 173, 206).

[26]Vardan Khachatryan et al. “Search for physics beyond the standard model in dilepton mass spectra in proton-proton collisions at $\sqrt{s} = 8$ TeV”. In: *JHEP* 04 (2015), p. 025. arXiv: 1412.6302 [hep-ex] (cit. on pp. 30, 173, 206).

[27] *Search for new phenomena in the dilepton final state using proton-proton collisions at sqrt(s) = 13 TeV with the ATLAS detector*. Tech. rep. ATLAS-CONF-2015-070. Geneva: CERN, 2015 (cit. on pp. 30, 206).

[28] *Search for a Narrow Resonance Produced in 13 TeV pp Collisions Decaying to Electron Pair or Muon Pair Final States*. Tech. rep. CMS-PAS-EXO-15-005. Geneva: CERN, 2015 (cit. on pp. 30, 206).

[29] Lyndon Evans and Philip Bryant. "LHC Machine". In: *Journal of Instrumentation* 3.08 (2008), S08001 (cit. on pp. 33, 38, 41).

[30] Philippe Mouche. "Overall view of the LHC. Vue d'ensemble du LHC". General Photo. 2014 (cit. on p. 34).

[31] Vardan Khachatryan et al. "Pseudorapidity distribution of charged hadrons in proton-proton collisions at $\sqrt{s} = 13$ TeV". In: *Phys. Lett.* B751 (2015), pp. 143–163. arXiv: 1507.05915 [hep-ex] (cit. on p. 34).

[32] Jean-Luc Caron. "Accelerator complex of CERN: an overview of all accelerators of CERN. Vue d'ensemble de tous les accélérateurs du CERN". 2001 (cit. on p. 35).

[33] Fred Jegerlehner and Andreas Nyffeler. "The Muon g-2". In: *Phys. Rept.* 477 (2009), pp. 1–110. arXiv: 0902.3360 [hep-ph] (cit. on p. 36).

[34] P. A. R. Ade et al. "Planck 2013 results. I. Overview of products and scientific results". In: *Astron. Astrophys.* 571 (2014), A1. arXiv: 1303.5062 [astro-ph.CO] (cit. on p. 36).

[35] Michael Dine. "Naturalness Under Stress". In: *Ann. Rev. Nucl. Part. Sci.* 65 (2015), pp. 43–62. arXiv: 1501.01035 [hep-ph] (cit. on p. 37).

[36] Jean-Luc Caron. "LHC Layout. Schema general du LHC." AC Collection. Legacy of AC. Pictures from 1992 to 2002. 1997 (cit. on p. 40).

[37] The CMS Collaboration. "The CMS experiment at the CERN LHC". In: *Journal of Instrumentation* 3.08 (2008), S08004 (cit. on pp. 43, 46, 52, 55, 62).

[38] Tai Sakuma and Thomas McCauley. "Detector and Event Visualization with SketchUp at the CMS Experiment". In: *Journal of Physics: Conference Series* 513.2 (2014), p. 022032 (cit. on p. 45).

[39] The CMS Collaboration. "Description and performance of track and primary-vertex reconstruction with the CMS tracker". In: *Journal of Instrumentation* 9.10 (2014), P10009 (cit. on p. 47).

[40] *The CMS muon project: Technical Design Report*. Technical Design Report CMS. Geneva: CERN, 1997 (cit. on pp. 53, 54, 160).

[41] Serguei Chatrchyan et al. "The performance of the CMS muon detector in proton-proton collisions at $\sqrt{s} = 7$ TeV at the LHC". In: *JINST* 8 (2013), P11002. arXiv: 1306.6905 [physics.ins-det] (cit. on pp. 53, 56, 68, 69).

[42] Carlo Battilana. "Drift Tubes Trigger System of the CMS Experiment at LHC : Commissioning and Performances". PhD thesis. Bologna U., 2009 (cit. on p. 56).

[43] CMS Collaboration. "Performance of the CMS drift tube chambers with cosmic rays". In: *Journal of Instrumentation* 5 (Mar. 2010), p. 3015. arXiv: 0911.4855 [physics.ins-det] (cit. on p. 56).

[44]O. Prokofev et al. “Aging tests of full scale CMS muon cathode strip chambers”. In: *Nucl. Instrum. Meth.* A515 (2003). [,33(2001)], pp. 226–233 (cit. on p. 56).

[45]CMS Collaboration. “Performance of the CMS cathode strip chambers with cosmic rays”. In: *Journal of Instrumentation* 5 (Mar. 2010), T03018. arXiv: 0911.4992 [physics.ins-det] (cit. on p. 56).

[46]Michael Hoch. “Endcap assembly on ground level”. CMS Collection. 2007 (cit. on p. 57).

[47]Karol Bunkowski and Jan Krolikowski. “Optimization, Synchronization, Calibration and Diagnostic of the RPC PAC Muon Trigger System for the CMS detector”. Presented on Jul 2009. PhD thesis. Warsaw: Warsaw U., 2009 (cit. on p. 60).

[48]G L Bayatyan, N Grigorian, and V G Khachatrian. *CMS TriDAS project: Technical Design Report, Volume 1: The Trigger Systems*. Technical Design Report CMS (cit. on p. 60).

[49]Karol Bunkowski. “Optimization, Synchronization, Calibration and Diagnostic of the RPC PAC Muon Trigger System for the CMS detector”. PhD thesis. Warsaw U., 2009 (cit. on p. 61).

[50]G Bauer, B Beccati, U Behrens, et al. “The data-acquisition system of the CMS experiment at the LHC”. In: *Journal of Physics: Conference Series* 331.2 (2011), p. 022021 (cit. on p. 61).

[51]J Butler, D Contardo, M Klute, J Mans, and L Silvestris. *Technical Proposal for the Phase-II Upgrade of the CMS Detector*. Tech. rep. CERN-LHCC-2015-010. LHCC-P-008. Upgrade Project Leader Deputies: Lucia Silvestris (INFN-Bari), Jeremy Mans (University of Minnesota) Additional contacts: Lucia.Silvestris@cern.ch, Jeremy.Mans@cern.ch. Geneva. Geneva: CERN, 2015 (cit. on pp. 64, 104, 105).

[52]CMS Collaboration. *Technical proposal for the upgrade of the CMS detector through 2020*. Tech. rep. CERN-LHCC-2011-006. LHCC-P-004. Geneva: CERN, 2011 (cit. on p. 64).

[53]“Projected Performance of an Upgraded CMS Detector at the LHC and HL-LHC: Contribution to the Snowmass Process”. In: *Community Summer Study 2013: Snowmass on the Mississippi (CSS2013) Minneapolis, MN, USA, July 29-August 6, 2013*. 2013. arXiv: 1307.7135 (cit. on pp. 64, 72).

[54]D Acosta, N Adams, A Atamanchouk, et al. “Development and test of a prototype regional track-finder for the Level-1 trigger of the cathode strip chamber muon system of CMS”. In: *Nuclear Instruments and Methods in Physics Research Section A: Accelerators, Spectrometers, Detectors and Associated Equipment* 496.1 (2003), pp. 64 –82 (cit. on p. 68).

[55]A. Bodek. “Extraction of $\sin^2\theta_{\rm eff}^{\rm lept}$ and indirect measurement of m_w from the 9 fb^{-1} full run ii sample of $\mu^+\mu^-$ events at cdf”. In: *26th Rencontres de Blois on Particle Physics and Cosmology Blois, Loire Valley, France, May 18-25, 2014*. 2014. arXiv: 1409.5749 [hep-ex] (cit. on p. 69).

[56]A. Bodek, J. Han, A. Khukhunaishvili, and W. Sakumoto. “Using Drell-Yan forward-backward asymmetry to reduce PDF uncertainties in the measurement of electroweak parameters”. In: *Eur. Phys. J.* C76.3 (2016), p. 115. arXiv: 1507.02470 [hep-ex] (cit. on p. 69).

[57]M. Tytgat, A. Marinov, P. Verwilligen, et al. “The upgrade of the CMS RPC system during the first LHC long shutdown”. In: *Journal of Instrumentation* 8 (Feb. 2013), p. 2002. arXiv: 1209.1979 [physics.ins-det] (cit. on p. 70).

[58]A Dominguez, D Abbaneo, K Arndt, et al. *CMS Technical Design Report for the Pixel Detector Upgrade*. Tech. rep. CERN-LHCC-2012-016. CMS-TDR-11. Additional contacts: Jeffrey Spalding, Fermilab, Jeffrey.Spalding@cern.ch Didier Contardo, Universite Claude Bernard-Lyon I, didier.claude.contardo@cern.ch. Geneva: CERN, 2012 (cit. on p. 70).

[59]J Mans, J Anderson, B Dahmes, et al. *CMS Technical Design Report for the Phase 1 Upgrade of the Hadron Calorimeter*. Tech. rep. CERN-LHCC-2012-015. CMS-TDR-10. Additional contact persons: Jeffrey Spalding, Fermilab, spalding@cern.ch, Didier Contardo, Universite Claude Bernard-Lyon I, contardo@cern.ch. Geneva: CERN, 2012 (cit. on p. 72).

[60]A Tapper and Darin Acosta. *CMS Technical Design Report for the Level-1 Trigger Upgrade*. Tech. rep. CERN-LHCC-2013-011. CMS-TDR-12. Additional contacts: Jeffrey Spalding, Fermilab, Jeffrey.Spalding@cern.ch Didier Contardo, Universite Claude Bernard-Lyon I, didier.claude.contardo@cern.ch. Geneva: CERN, 2013 (cit. on p. 73).

[61]*PICMG Specification MTCA.0 R1.0*. July 2006 (cit. on p. 74).

[62]W. Adam et al. “The CMS high level trigger”. In: *Eur. Phys. J.* C46 (2006), pp. 605–667. arXiv: hep-ex/0512077 [hep-ex] (cit. on p. 75).

[63]K. A. Olive et al. “Review of Particle Physics”. In: *Chin. Phys.* C38 (2014), p. 090001 (cit. on pp. 80, 109).

[64]Y. Giomataris, Ph. Rebourgeard, J.P. Robert, and G. Charpak. “MICROMEGAS: a high-granularity position-sensitive gaseous detector for high particle-flux environments”. In: *Nuclear Instruments and Methods in Physics Research Section A: Accelerators, Spectrometers, Detectors and Associated Equipment* 376.1 (1996), pp. 29 –35 (cit. on p. 79).

[65]A Colaleo, A Safonov, A Sharma, and M Tytgat. *CMS Technical Design Report for the Muon Endcap GEM Upgrade*. Tech. rep. CERN-LHCC-2015-012. CMS-TDR-013. Geneva: CERN, 2015 (cit. on pp. 79, 84–86, 100, 160, 161).

[66]Nadir Daci and Alexandre Zabi. “Sélection des électrons et recherche du boson de Higgs se désintégrant en paires de leptons tau avec l’expérience CMS au LHC”. presented 30 Oct 2013. PhD thesis. Orsay, 2014 (cit. on p. 83).

[67]Y. Haddad, I. Laktineh, G. Grenier, N. Lumb, and S. Cauwenbergh. “High rate resistive plate chamber for LHC detector upgrades”. In: *Nuclear Instruments and Methods in Physics Research A* 718 (Aug. 2013), pp. 424–426. arXiv: 1211.5698 [physics.ins-det] (cit. on p. 85).

[68]F. Sauli. “GEM: A new concept for electron amplification in gas detectors”. In: *Nucl. Instrum. Meth.* A386 (1997), pp. 531–534 (cit. on p. 86).

[69]Marco Villa, Serge Duarte Pinto, Matteo Alfonsi, et al. “Progress on large area GEMs”. In: *Nucl. Instrum. Meth.* A628 (2011), pp. 182–186. arXiv: 1007.1131 [physics.ins-det] (cit. on p. 86).

[70]S Duarte Pinto, M Villa, M Alfonsi, et al. “Progress on large area GEMs”. In: *Journal of Instrumentation* 4.12 (2009), P12009 (cit. on p. 86).

[71]S. Bachmann et al. “Discharge mechanisms and their prevention in the gas electron multiplier (GEM)”. In: *Nucl. Instrum. Meth.* A479 (2002), pp. 294–308 (cit. on p. 88).

[72]F. Sauli. “Progress with the gas electron multiplier”. In: *Nuclear Instruments and Methods in Physics Research A* 522 (Apr. 2004), pp. 93–98 (cit. on p. 88).

[73]Archana Sharma. “Properties of some gas mixtures used in tracking detectors”. In: *ICFA Instrumentation Bulletin: Volume 16* (1998) (cit. on pp. 89, 90, 157).

[74]Fabio Sauli. “Principles of operation of multiwire proportional and drift chambers”. In: *CERN Academic Training Lecture no. 81, given in the CERN Academic Training Program 1975-1976*. CERN, Geneva, 1975 - 1976. Geneva, 1977, 92 p (cit. on p. 91).

[75]R. Veenhof. *Garfield*. `garfield.web.cern.ch/garfield` (cit. on pp. 92, 146).

[76]Alessandro Cardini, Giovanni Bencivenni, and Patrizia De Simone. “Operational Experience of the Triple-GEM Detectors of the LHCb Muon System: Summary of 2 years of data taking”. In: *Nuclear Science Symposium and Medical Imaging Conference (NSS/MIC), 2012 IEEE*. 2012 (cit. on p. 92).

[77]G. Antchev et al. “Performance of the TOTEM Detectors at the LHC”. In: *Int. J. Mod. Phys.* A28 (2013), p. 1330046. arXiv: `1310.2908 [physics.ins-det]` (cit. on p. 92).

[78]Rob Veenhof. “Garfield Version 6.05 - Forthcoming Release”. In: (1997) (cit. on p. 92).

[79]T. Zhao, Y. Chen, S. Han, and J. Hersch. “A study of electron drift velocity in Ar/CO2 and Ar/CO2/CF4 gas mixtures”. In: *Nuclear Instruments and Methods in Physics Research Section A: Accelerators, Spectrometers, Detectors and Associated Equipment* 340.3 (1994), pp. 485 –490 (cit. on p. 92).

[80]L. Benussi et al. “Candidate eco-friendly gas mixtures for MPGDs”. In: *4th International Conference on Micro Pattern Gaseous Detectors - MPGD2015 Trieste, Italy, October 12-15, 2015*. 2015. arXiv: `1512.08542 [physics.ins-det]` (cit. on p. 93).

[81]D. Abbaneo et al. “Test beam results of the GE1/1 prototype for a future upgrade of the CMS high-η muon system”. In: *Proceedings, 2011 IEEE Nuclear Science Symposium and Medical Imaging Conference (NSS/MIC 2011)*. 2011, pp. 1806–1810. arXiv: `1111.4883 [physics.ins-det]` (cit. on pp. 93, 99).

[82]Michael Tytgat et al. “The Triple-GEM Project for the Phase 2 Upgrade of the CMS Muon System”. In: *PoS* TIPP2014 (2014), p. 065 (cit. on p. 94).

[83]Paul Aspell. “VFAT2: A front-end system on chip providing fast trigger information, digitized data storage and formatting for the charge sensitive readout of multi-channel silicon and gas particle detectors”. In: *Electronics for particle physics. Proceedings, Topical Workshop, TWEPP-07, Prague, Czech Republic, September 3-7, 2007*. 2007, p. 63 (cit. on p. 95).

[84]Paulo Moreira. “The GBT, a proposed architecture for multi-Gbps data transmission in high energy physics”. In: *Electronics for particle physics. Proceedings, Topical Workshop, TWEPP-07, Prague, Czech Republic, September 3-7, 2007*. 2007, p. 71 (cit. on p. 95).

[85]A Xiang, D Gong, S Hou, et al. “A Versatile Link for High-Speed, Radiation Resistant Optical Transmission in LHC Upgrades”. In: *Phys. Procedia* 37 (2012), 1750–1758. 9 p (cit. on p. 95).

[86]M Barros Marin, S Baron, V Bobillier, et al. “A GLIB-based uTCA demonstration system for HEP experiments”. In: *Journal of Instrumentation* 8.12 (2013), p. C12011 (cit. on p. 95).

[87]Davide Cieri. *L1 Track Finding for a Time Multiplexed Trigger*. Tech. rep. CMS-CR-2015-106. Geneva: CERN, 2015 (cit. on p. 95).

[88]P. Abbon et al. “The COMPASS experiment at CERN”. In: *Nucl. Instrum. Meth.* A577 (2007), pp. 455–518. arXiv: hep-ex/0703049 [hep-ex] (cit. on p. 98).

[89]D. Abbaneo et al. “Characterization of GEM Detectors for Application in the CMS Muon Detection System”. In: *Proceedings, 2010 IEEE Nuclear Science Symposium and Medical Imaging Conference (NSS/MIC 2010)*. 2010, pp. 1416–1422. arXiv: 1012.3675 [physics.ins-det] (cit. on p. 99).

[90]D. Abbaneo et al. “Beam test results for new full-scale GEM prototypes for a future upgrade of the CMS high-η Muon System”. In: *Proceedings, 2012 IEEE Nuclear Science Symposium and Medical Imaging Conference (NSS/MIC 2012): Anaheim, California, USA, October 29-November 3, 2012*. 2012, pp. 1172 –1176. arXiv: 1211.3939 [physics.ins-det] (cit. on p. 99).

[91]D. Abbaneo et al. “Performance of a Large-Area GEM Detector Prototype for the Upgrade of the CMS Muon Endcap System”. In: *2014 IEEE Nuclear Science Symposium and Medical Imaging Conference and 21st Symposium on Room-Temperature Semiconductor X-ray and Gamma-ray Detectors (NSS/MIC 2014 / RTSD 2014) Seattle, WA, USA, November 8-15, 2014*. 2014. arXiv: 1412.0228 [physics.ins-det] (cit. on p. 99).

[92]M. Raymond, M. French, J. Fulcher, et al. “The APV25 0.25 μm CMOS readout chip for the CMS tracker”. In: *Nuclear Science Symposium Conference Record, 2000 IEEE*. Vol. 2. 2000, 9/113–9/118 vol.2 (cit. on p. 99).

[93]*Estimates of the Radiation Levels in Run II, MARS and FLUKA Simulations*. Tech. rep. CMS-DP-2015-010. CERN, 2015 (cit. on p. 107).

[94]William R Leo. *Techniques for nuclear and particle physics experiments: a how-to approach; 2nd ed.* Berlin: Springer, 1994 (cit. on pp. 108, 109).

[95]Glenn F Knoll. *Radiation detection and measurement; 4th ed.* New York, NY: Wiley, 2010 (cit. on p. 108).

[96]J. F. Ziegler. “Stopping of energetic light ions in elemental matter”. In: *Journal of Applied Physics* 85 (Feb. 1999), pp. 1249–1272 (cit. on p. 109).

[97]H.H. Andersen and J.F. Ziegler. *Hydrogen. Stopping powers and ranges in all elements.* Pergamon Press, New York, 1977 (cit. on p. 110).

[98]James F. Ziegler and Jochen P. Biersack. “The Stopping and Range of Ions in Matter”. English. In: *Treatise on Heavy-Ion Science*. Ed. by D. Allan Bromley. Springer US, 1985, pp. 93–129 (cit. on p. 110).

[99]M.J. Berger et al. *XCOM: Photon Cross Section Database (version 1.5)*. http://physics.nist.gov/xcom/, National Institute of Standards and Technology, Gaithersburg, MD. Online; accessed 1-November-2015. National Institute of Standards and Technology, Gaithersburg, MD, 2010 (cit. on pp. 112, 129).

[100]R. Serber. “Nuclear Reactions at High Energies”. In: *Phys. Rev.* 72 (1947), pp. 1114–1115 (cit. on p. 117).

[101]M. L. Goldberger. “The Interaction of High Energy Neutrons and Heavy Nuclei”. In: *Phys. Rev.* 74 (10 1948), pp. 1269–1277 (cit. on p. 117).

[102]M.P. Guthrie, R.G. Alsmiller, and H.W. Bertini. “Calculation of the capture of negative pions in light elements and comparison with experiments pertaining to cancer radiotherapy”. In: *Nuclear Instruments and Methods* 66.1 (1968), pp. 29 –36 (cit. on p. 117).

[103]Aatos Heikkinen, Nikita Stepanov, and Johannes Peter Wellisch. “Bertini intranuclear cascade implementation in GEANT4”. In: *eConf* C0303241 (2003), MOMT008. arXiv: nucl-th/0306008 [nucl-th] (cit. on pp. 117, 121).

[104]V. Weisskopf. “Statistics and Nuclear Reactions”. In: *Phys. Rev.* 52 (4 1937), pp. 295–303 (cit. on p. 119).

[105]Karl Heinrich Lieser. *Nuclear and Radiochemistry: Fundamentals and Applications*. Weinheim: Wiley-VCH, 2001 (cit. on p. 119).

[106]S. Agostinelli et al. “Geant4 - A simulation toolkit”. In: *Nuclear Instruments and Methods in Physics Research Section A: Accelerators, Spectrometers, Detectors and Associated Equipment* 506.3 (2003), pp. 250 –303 (cit. on pp. 119, 120, 136).

[107]John Allison et al. “Geant4 developments and applications”. In: *IEEE Trans. Nucl. Sci.* 53 (2006), p. 270 (cit. on pp. 119, 121).

[108]J.S. Coursey, D.J. Schwab, J.J. Tsai, and R.A. Dragoset. *Atomic Weights and Isotopic Compositions (version 4.1)*. [Online] Available: http://physics.nist.gov/Comp [2015, October, 29]. National Institute of Standards and Technology, Gaithersburg, MD, 2015 (cit. on p. 120).

[109]G. Folger and J. P. Wellisch. “String parton models in GEANT4”. In: *eConf* C0303241 (2003), MOMT007. arXiv: nucl-th/0306007 [nucl-th] (cit. on p. 121).

[110]“Development of the Fritiof Model in Geant4”. In: *Joint International Conference on Supercomputing in Nuclear Applications and Monte Carlo 2010 (SNA + MC2010)*. 2010 (cit. on p. 121).

[111]G. Folger, V.N. Ivanchenko, and J.P. Wellisch. “The Binary Cascade”. In: *The European Physical Journal A - Hadrons and Nuclei* 21.3 (2004), pp. 407–417 (cit. on p. 121).

[112]J. Apostolakis, M. Asai, A.G. Bogdanov, et al. “Geometry and physics of the Geant4 toolkit for high and medium energy applications”. In: *Radiation Physics and Chemistry* 78.10 (2009). Workshop on Use of Monte Carlo Techniques for Design and Analysis of Radiation Detectors, pp. 859 –873 (cit. on pp. 121, 122).

[113]A. Ribon, J. Apostolakis, A. Dotti, et al. “Transition between hadronic models in Geant4”. In: *Proceedings, 2009 IEEE Nuclear Science Symposium and Medical Imaging Conference (NSS/MIC 2009)*. 2009, pp. 526–529 (cit. on p. 121).

[114]A. Bolshakova et al. “Cross-Sections of Large-Angle Hadron Production in Proton- and Pion-Nucleus Interactions. III. Tantalum Nuclei and Beam Momenta from +-3 GeV/c to +-15 GeV/c”. In: *Eur. Phys. J.* C63 (2009), pp. 549–609. arXiv: 0906.0471 [hep-ex] (cit. on p. 122).

[115]Julia Yarba. “Recent developments and validation of Geant4 hadronic physics”. In: *J. Phys. Conf. Ser.* 396 (2012), p. 022060 (cit. on pp. 122, 132).

[116]T.T. Böhlen, F. Cerutti, M.P.W. Chin, et al. “The FLUKA Code: Developments and Challenges for High Energy and Medical Applications”. In: *Nuclear Data Sheets* 120 (2014), pp. 211 –214 (cit. on p. 124).

[117]A Ferrari, Paola R Sala, A Fassò, and Johannes Ranft. *FLUKA: A multi-particle transport code (program version 2005)*. Geneva: CERN, 2005 (cit. on p. 124).

[118]Alfredo Castaneda et al. “Impact of the radiation background on the CMS muon high-eta upgrade for the LHC high luminosity scenario”. In: *PoS* TIPP2014 (2014), p. 086 (cit. on p. 124).

[119]R. Brun, F. Bruyant, M. Maire, A. C. McPherson, and P. Zanarini. *GEANT3 user’s guide*. CERN, Geneva. Sept. 1987 (cit. on p. 130).

[120]S. Altieri, G. Belli, G. Bruno, et al. “Simulation of Resistive Plate Chamber sensitivity to neutrons”. In: *Nuclear Instruments and Methods in Physics Research Section A: Accelerators, Spectrometers, Detectors and Associated Equipment* 461.1–3 (2001). 8th Pisa Meeting on Advanced Detectors, pp. 57 –59 (cit. on pp. 130, 132, 133).

[121]M. Abbrescia, S. Altieri, V. Baratti, et al. “Experimental results on RPC neutron sensitivity”. In: *Nuclear Instruments and Methods in Physics Research Section A: Accelerators, Spectrometers, Detectors and Associated Equipment* 508.1–2 (2003). Proceedings of the Sixth International Workshop on Resistive Plate Chambers and Related Detectors, pp. 79 –82 (cit. on pp. 130, 134–136).

[122]M. Jamil, J.T. Rhee, Steve Hall, Christopher Chun, and Y.J. Jeon. “Study of neutron sensitivity in CMS–RPC using MC simulation for two different setups”. In: *Nuclear Instruments and Methods in Physics Research Section A: Accelerators, Spectrometers, Detectors and Associated Equipment* 556.1 (2006), pp. 192 –196 (cit. on pp. 130, 134, 137, 138).

[123]A A Borio Di Tigliole, A Cesana, R Dolfini, et al. “FLUKA simulations for low-energy neutron interactions and experimental validation”. In: *Nucl. Instrum. Methods Phys. Res., A* 469.3 (2001), pp. 347–353 (cit. on p. 132).

[124]N Colonna and G Tagliente. “Response of liquid scintillator detectors to neutrons of $E_{\mathrm{n}} < 1$ MeV”. In: *Nuclear Instruments and Methods in Physics Research Section A: Accelerators, Spectrometers, Detectors and Associated Equipment* 416.1 (1998), pp. 109 –114 (cit. on p. 132).

[125]V. N. Ivanchenko et al. “Geant4 Electromagnetic Physics for LHC Upgrade”. In: *J. Phys. Conf. Ser.* 513 (2014), p. 022015 (cit. on p. 132).

[126]Anton V. Ivantchenko, Vladimir N. Ivanchenko, Jose-Manuel Quesada Molina, and Sebastien L. Incerti. “Geant4 hadronic physics for space radiation environment”. In: *International Journal of Radiation Biology* 88.1-2 (2012), pp. 171–175. eprint: `http://www.tandfonline.com/doi/pdf/10.3109/09553002.2011.610865` (cit. on pp. 133, 141).

[127]J.T. Rhee, M. Jamil, B. Hong, et al. “Study of the neutron sensitivity for the double gap RPC of the CMS/LHC by using GEANT4”. In: *Journal of the Korean Physical Society* 48.1 (2006), pp. 33–39 (cit. on pp. 136, 139, 162).

[128]M Jamil, J T Rhee, and Y J Jeon. “Simulation of the neutron response of a glass-resistive plate chamber in the energy range 10^{-10} MeV $< E_{\mathrm{n}} < 10$ GeV”. In: *Physica Scripta* 76.4 (2007), p. 287 (cit. on p. 139).

[129]M Abbrescia, S Altieri, V Baratti, et al. “Resistive plate chamber neutron and gamma sensitivity measurement with a 252Cf source”. In: *Nuclear Instruments and Methods in Physics Research Section A: Accelerators, Spectrometers, Detectors and Associated Equipment* 506.1–2 (2003), pp. 101 –109 (cit. on pp. 140–142).

[130]Nikolai V. Mokhov. *The MARS code system user's guide version 13(95)*. FERMILAB-FN-0628. 1995 (cit. on p. 160).

[131]Serguei Chatrchyan et al. “Search for heavy narrow dilepton resonances in pp collisions at $\sqrt{s} = 7$ TeV and $\sqrt{s} = 8$ TeV”. In: *Phys. Lett.* B720 (2013), pp. 63–82. arXiv: 1212.6175 [hep-ex] (cit. on p. 173).

[132]Georges Aad et al. “Search for high-mass resonances decaying to dilepton final states in pp collisions at $\sqrt{s} = 7$ TeV with the ATLAS detector”. In: *JHEP* 11 (2012), p. 138. arXiv: 1209.2535 [hep-ex] (cit. on p. 173).

[133]John C. Collins and Davison E. Soper. “Angular distribution of dileptons in high-energy hadron collisions”. In: *Phys. Rev. D* 16 (7 1977), pp. 2219–2225 (cit. on p. 175).

[134]Laurent Thomas and Barbara Clerbaux. “Search for new heavy narrow resonances decaying into a dielectron pair with the CMS detector”. PhD thesis. Université Libre de Bruxelles, 2015 (cit. on pp. 175, 186).

[135]Michael Dittmar. “Neutral current interference in the TeV region: The experimental sensitivity at the CERN LHC”. In: *Phys. Rev. D* 55 (1 1997), pp. 161–166 (cit. on p. 176).

[136]Torbjörn Sjöstrand, Stefan Ask, Jesper R. Christiansen, et al. “An Introduction to PYTHIA 8.2”. In: *Comput. Phys. Commun.* 191 (2015), pp. 159–177. arXiv: 1410.3012 [hep-ph] (cit. on p. 177).

[137]Gary J. Feldman and Robert D. Cousins. “Unified approach to the classical statistical analysis of small signals”. In: *Phys. Rev. D* 57 (7 1998), pp. 3873–3889 (cit. on p. 197).

[138]G. Cowan. *Statistical Data Analysis*. Oxford science publications. Clarendon Press, 1998 (cit. on p. 202).

[139]J. Neyman and E. S. Pearson. “On the Problem of the Most Efficient Tests of Statistical Hypotheses”. In: *Philosophical Transactions of the Royal Society of London Series A* 231 (1933), pp. 289–337 (cit. on p. 203).

[140]Robert Bartoszyński and Magdalena Niewiadomska-Bugaj. *Probability and statistical inference*. English. "A Wiley-Interscience publication." New York : Wiley, 1996 (cit. on p. 203).

[141]Robert L. Wolpert James O. Berger Lawrence D. Brown. “A Unified Conditional Frequentist and Bayesian Test for Fixed and Sequential Simple Hypothesis Testing”. In: *The Annals of Statistics* 22.4 (1994), pp. 1787–1807 (cit. on p. 203).

[142]*Search for resonances decaying to photon pairs in 3.2 fb^{-1} of pp collisions at $\sqrt{s}$ = 13 TeV with the ATLAS detector*. Tech. rep. ATLAS-CONF-2015-081. Geneva: CERN, 2015 (cit. on p. 206).

[143]*Search for new physics in high mass diphoton events in proton-proton collisions at $\sqrt{s} = 13$ TeV*. Tech. rep. CMS-PAS-EXO-15-004. Geneva: CERN, 2015 (cit. on p. 206).

List of Figures

List of Tables

Colophon

This thesis was typeset with LaTeX 2_ε. It uses the *Clean Thesis* style developed by Ricardo Langner. The design of the *Clean Thesis* style is inspired by user guide documents from Apple Inc.

Download the *Clean Thesis* style at `http://cleanthesis.der-ric.de/`.

Declaration

You can put your declaration here, to declare that you have completed your work solely and only with the help of the references you mentioned.

Brussels, April 2016

Florian Zenoni